POLITECNICO DI MILANO
DEPARTMENT OF ENERGY
DOCTORAL PROGRAMME IN:
ENERGY AND NUCLEAR SCIENCE AND TECHNOLOGY

DESIGN AND MODELING OF A MICRO GAS TURBINE WITH A BOTTOMING ORGANIC RANKINE CYCLE: STEADY-STATE AND DYNAMIC APPROACH

Doctoral Dissertation of:
Sonia Laura Gómez Aláez

Cosupervisor:
Andrea Giostri
Supervisor:
Prof.Paolo Silva
The Chair of the Doctoral Program:
Prof. Vincenzo Dossena

Year 2019 – XXXI Cycle

To everyone who has been by my side helping me directly or indirectly.

Muchas gracias.

Contents

Figures

Tables

Nomenclature

A	area/ system Matrix
a	speed of sound
B	input matrix
C	output matrix
c_p	specific heat at constant pressure
C	heat capacity
D	diameter/ feedforward matrix
E	total energy
e	control error
f	friction factor
G	process transfer function
g_{ij}	gain value of the process transfer function
h	enthalpy
I	identity matrix
K	decoupler matrix
K_c	concentrated coefficient
k_p	proportional gain constant
L	length
MM	molecular mass
M	mass
$\dot{m}$	mass flow rate
N	Rotational speed
$\overline{n}$	normal vector
$\dot{n}$	molar flow rate
P	power
p	pressure
Q	heat
R	constant of the gas
$\vec{r}$	vector
S	surface
s	entropy
T	temperature
T_i	Integral time constant
T_d	derivative time constant
t	time
U	global heat transfer coefficient
u	internal energy/ inputs vector
V	volume
$\dot{V}$	volume flow rate
v	velocity
$\overline{v}$	velocity vector
W	width
x	state variables vector
x_i	molar fraction of component i
y	outputs vector
y_i	Mass fraction of component i
Δp	pressure drop

ΔT_{lm} log mean temperature difference

Greek symbols

α off-design coefficient

Λ RGA matrix

β pressure ratio/ chevron angle

δ thickness

κ similarity law coefficient

λ distance between channels

λ_{ij} element of the RGA matrix

γ convective heat transfer coefficient

ϵ effectiveness

η efficiency

ρ density

Subscripts

amb ambient

comb combustion chamber

comp compressor

cond condenser

desh desuperheating

eco economizer

el electric

evap evaporator

filt filter

h hydraulic

in inlet

iso isentropic

liq liquid phase

mech mechanical

nom nominal

off off-design

out outlet

pp pinch point

r reduced

ref reference

reg regenerator

sh superheater

turb turbine

vap vapor phase

wf working fluid

Superscripts

$*$ chocked conditions

- averaged values

Acronyms

FVM	Finite Volume Discretization Method
GWP	Global Warming Potential
ICE	Internal Combustion Engine
LHV	Lower Heating Value
mGT	micro Gas Turbine
ODP	Ozone Depletion Potential
OECD	Organization of Economic Cooperation and Development
ORC	Organic Rankine Cycle
OTEC	Ocean Thermal Energy Conversion
PHE	Primary Heat Exchanger
PI	Proportional Integral Controller
PID	Proportional Integral Derivative Controller
PV	Photovoltaic
RES	Renewable Energy Sources
RGA	Relative Gain Array
SP	Set Point
SP	Size Parameter
TIT	Turbine Inlet Temperature
TOT	Turbine Outlet Temperature
TPES	Total Primary Energy Supply
VR	Volume Ratio
WHR	Waste Heat Recovery

Summary

This PhD dissertation deals with the integration of a bottoming Organic Rankine Cycle (ORC) cycle to recover heat from the flue gases of a commercial micro gas turbine (mGT) for the production of electricity. The off-design behavior is modelled with a steady-state approach and, in addition, the transient response is analyzed. The application of this system aims to instantaneously satisfy the electricity demand of a set of 150 houses in Cologne (Germany).

First, the design of the energy system under study (i.e. mGT coupled with the bottoming ORC) is performed. A commercial mGT (on-design electric power output equal to about 100 kWe) is selected for this application and a thermodynamic optimization of the design of the bottoming ORC is performed aiming to maximize the electric power output. The most promising working fluid for the ORC is an environmentally friendly one, the R1233zd. The total electric output is equal to 119.7 kW at ambient temperature of15°C, split in 93.9 kW from the mGT and 25.8 kW from the ORC. The ORC equipment is sized subsequently after the complete design.

Second, the part-load performance of the designed energy system is studied through steady-state models developed in Matlab®. The off-design study aims to analyze how the system behaves when the operating conditions (i.e ambient temperature, power demand) differ from the nominal ones. In addition, the results obtained with the steady-state part-load approach are used to validate the dynamic model results once steady-state conditions are reached.

Third, the dynamic response of the energy system is analyzed when the ambient temperature and the electricity demand vary along the two most critical days of the year (i.e. maximum and minimum load). For that purpose, dynamic models are developed in Modelica (in Dymola environment) and validated with the match of the results with the steady-state part-load performance. A control system is designed aiming to guarantee good operational conditions, controlling the electric output, the TOT of the mGT and the TIT of the ORC.

The dynamic simulations are performed considering a time step of one second, however, two types of electricity-demand profiles are imposed: real demand conditions and one-minute averaged demand conditions. After analyzing the transient response, it is concluded that the proposed system formed by the mGT and ORC cannot work in stand-alone conditions to satisfy the demand instantaneously, as there is a difference in the demanded electricity and the given electricity. Therefore, a fast, parallel system (e.g. a battery or the electric grid) should be coupled to fulfill instantaneously the demand. The results show that taking an averaged profile

helps to get considerably smoother results, therefore, the equipment would suffer less as the temperature gradients are lower.

Chapter 1. Introduction

Fortunately, learning never ends

1.1. Primary energy sources and energy consumption

The industrial development of the countries comes with the consumption of primary energy resources. With the growth of the population and the industrial development of the countries, the demand of energy keeps on increasing.

Figure 1.1-1 shows how the Total Primary Energy Supply (TPES) has changed along the years between 1990 and 2016. The TPES keeps the tendency of increasing along the years due to the continuous development, with the exception of the economic crisis of 2008. This graphic shows the absolute energy supply divided by the energy source. It can be highlighted that the highest share of TPES comes from fossil fuel source (i.e. coal, natural gas and primary and secondary oil). Even if the oil (in its main form, primary, or as a derivate, secondary) has been the principal source of energy, the amount of coal consumption has increased since the year 2001, mainly influenced by the high industrial development and energy consumption in Asiatic countries (especially in China) [1], [2].

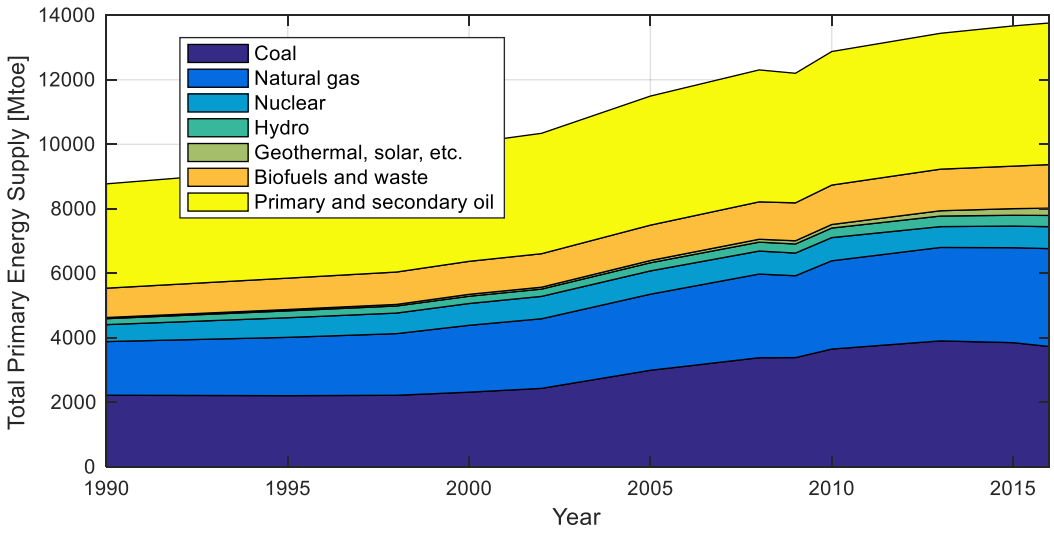

Figure 1.1-1 Total Primary Energy Supply divided by source [1], [2]

Energy demand has evolved differently across the regions along the years. Figure 1.1-2 shows how the TPES is distributed among the different regions in a frame of time of 45 years. The Organization of Economic Cooperation and Development (OECD) is historically an organization of developed countries from different parts of the world with high-income economy. As stated before, the economy and the industrial development imply a high consumption of energy. Therefore, in 1971, nearby the initial creation of the OECD, most of the TPES share was for the countries with high development, with more than the 60% of the global amount. The scenario has changed over the years, and the countries which are not part of OECD represent a continuously growing share of the world energy consumption. For example, in 2016, the great industrial development of Asia implies a higher energy consumption in this region, almost tripling the share of 1971.

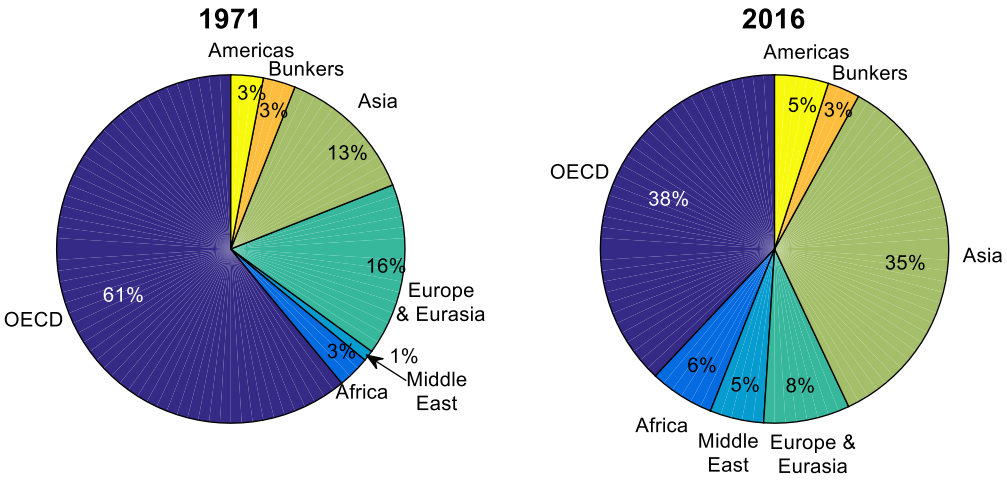

Figure 1.1-2 Total primary energy supply by region [1], [2]

The population is growing along the years, and the energy consumption per capita is also increasing. Also considering the electricity consumption, the continuous development has yield to an increase of the consumption higher than 3 MWh/capita in 2016, 50% more than the value registered in 1990, around 2 MWh/capita. Figure 1.1-3 shows how the electricity consumption per capita varies along the years. It presents the same tendency to grow as seen in Figure 1.1-1, with the exception of 2008, in which the economic crisis stopped the development and it is the only moment in which a reduction of energy consumption is registered.

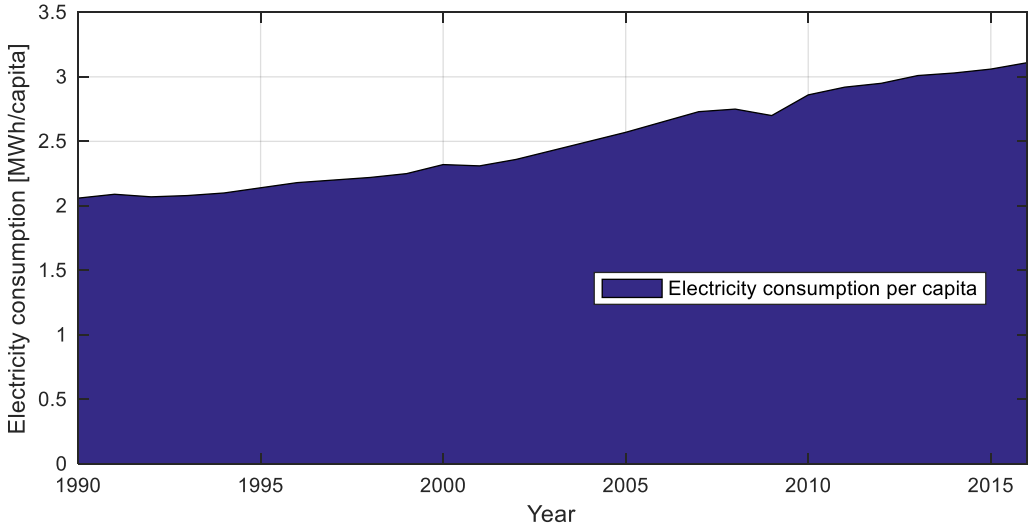

Figure 1.1-3 Variation of the electricity consumption per capita along the years [1], [2]

Although the total final consumption has increased over the years, from 4244 Mtoe in 1971 to 9555 Mtoe in 2016, so it was multiplied by 2.25, the energy division by most economic sectors did not change drastically. It has kept stable over the years, with the only significant increase in the energy consumption dedicated to the transport [1], [2].

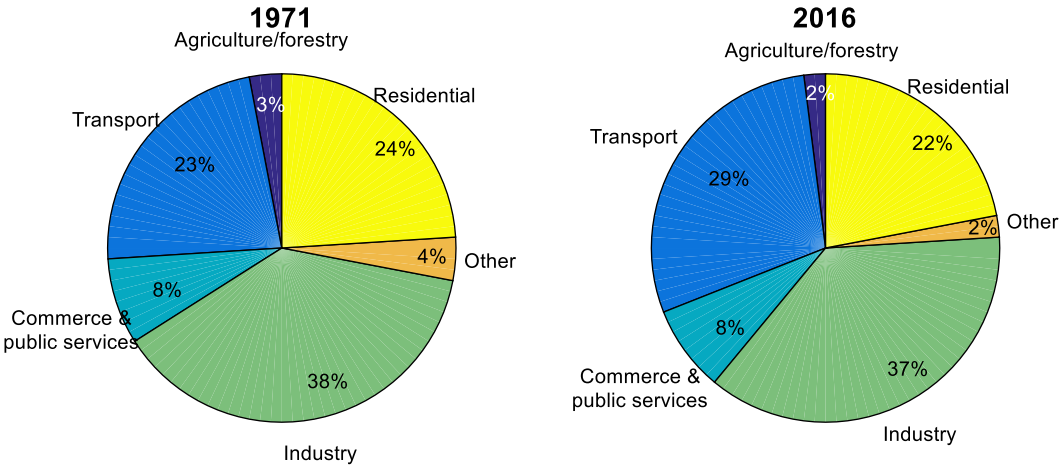

Figure 1.1-4 Total final consumption by sector

1.2. Energy policy in Europe

It is a fact that the energy consumption is increasing, as it has been shown in the previous section. However, the European Commission is building the 2030 climate and energy goals to reduce green-house gas emissions, to achieve energy savings and to promote the deployment of renewable energy. The energy policy adopted by the European Council on 24 October 2014 sets the following achievements by 2030 [3]:

- A reduction of at least 40% in greenhouse gas emissions compared to 1990 levels. This addresses the scarce environmental sustainability of the energy system, on both the demand and supply sides
- An increase to 27% of the share of renewable energies in energy consumption. This mostly promotes the security of supply, and consequently the political and economic stability of the region
- An improvement of 20% in energy efficiency as a minimum, aiming at achieving 30% if possible.
- A development to at least 15% of electricity interconnection, aiming at opening up the internal market by supporting the diversification of energy sources and routes of supply within Europe.

This framework is more demanding than the previous one, the Europe 2020 Strategy. The targets of this framework were:

- 20% reduction of greenhouse gases emissions by 2020, compared to 1990 levels.
- Increase of the production from renewable energy sources, in order for renewable energy to achieve 20% share in the overall EU energy consumption.
- 20% reduction in the primary energy consumption, compared to 2020 projections, through energy efficiency measures.

By comparing the targets of the both strategy plans, it can be concluded that the aim is to reduce drastically the primary energy consumption in terms of improving the energy efficiency, the improvement of the sustainability of the energy systems in order to importantly reduce the greenhouse gases emissions and a great introduction of renewable energy sources (RES) in the share of EU energy consumption.

1.2.1. Renewable energy sources

On one hand, the energy policy promotes the use of RES. In order to do it, the European Commission aims at acting in different areas [4]:

- Further deploying renewables in the electricity sector. In order to fulfill this objective, the European Union pursues as its primary objective the construction of electricity infrastructure which fits for the large-scale installation of renewables.
- Mainstreaming renewables in the heating and cooling sector. The European Commission has imposed to the fuel suppliers to provide a minimum share of 6.8% of low-emission and renewable fuels by introducing bioenergy in the heating and cooling sector.
- Decarbonizing and diversifying the transport sector (with a renewables target for 2030 of at least 14% of total energy consumption in transport)
- Empowering and informing customers.
- Strengthening the EU sustainability criteria for bioenergy. The European Parliament plays an important role by defining the sustainability criteria in order to avoid conflicts of the introduction of biofuels with social sustainability, land-use rights and effects on food security and prices.
- Making sure the EU-level binding target is achieved on time and in a cost-effective way.

1.2.2. Energy efficiency

On the other hand, the energy policy promotes the boosting of energy efficiency. This is valuable as it aims at reducing the primary energy consumption and it decreases the energy imports.

As stated by Miguel Arias Cañete, European Commissioner for Climate Action and Energy [5]:

¨The cheapest energy, the cleanest energy, the most secure energy is the energy that is not used at all.¨

As a consequence of reducing the primary energy consumption, the greenhouse gas emissions are reduced as well. Moreover, with the directive of increasing the energy efficiency, it is expected the development of innovative technological solutions and an improvement of competitiveness of the industry of the European Union [6], [7].

Figure 1.2-1 shows the number of measures implemented in states members of the European Union to boost the energy efficiency classified by the policies adopted by topics [8]. It can be highlighted that the measures on energy efficiency and renewable energy in buildings account for almost 50% of the total measures implemented. This is due to the fact that European buildings represent approximately the 40% of the

total energy consumption of the European Union. Therefore, great improvements in energy efficiency in buildings yield to high reductions of energy consumption.

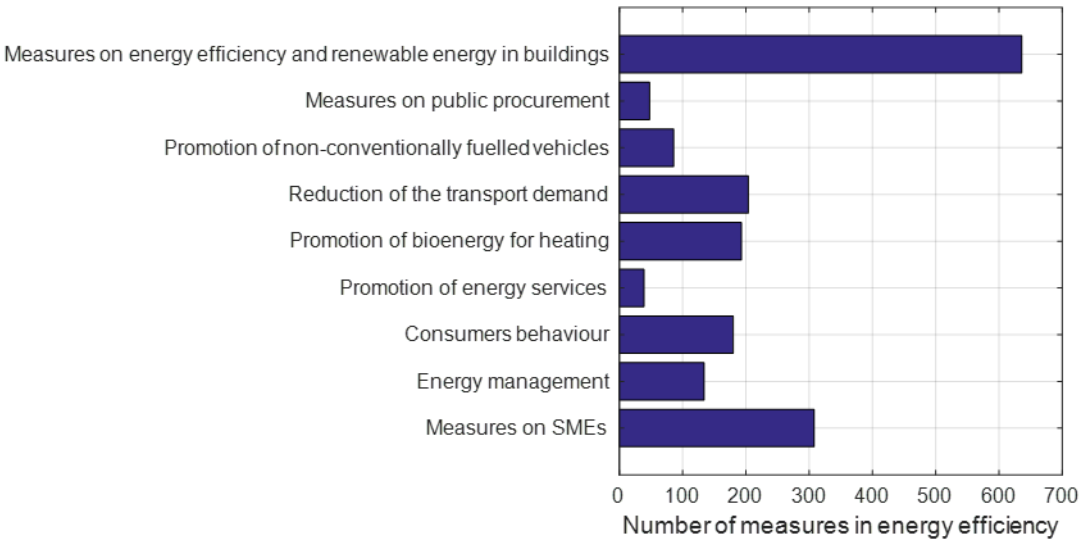

Figure 1.2-1 Measures on energy efficiency in Europe

In industry, the final energy consumption has decreased by 15% from 2005 till 2013. This is a consequence of the awareness that energy is an important cost in the process. Therefore, any measure that aims at reducing the energy consumption has an important weight in the overall cost of the products. Waste heat recovery is one of the measures which has contributed to the reduction of energy consumption, as well as the continuous improvement of energy systems efficiency.

1.3. Energy systems and flexibility

Due to the energy policies and measures, in which the RES starts playing a significant role, the power systems in Europe are suffering a significant change. The introduction of weather-dependent sources as wind or solar, with less controllable and predictable output than the conventional power plants, is driving changes in the composition and operation of the entire power grid [9]–[11].

Matching the generation and consumption requires flexibility in the system. The term flexibility has different meanings according to the different players involved in the energy supply. According to planners, it describes the extent to which an electricity system can adapt the pattern of electricity generation and consumption in order to balance supply and demand. But according to generation companies and power plant operators, it defines the ability of a power plant to vary its generation output as fast as possible, without harming the components.

Traditionally, in power systems, the flexibility was provided almost entirely by monitoring the supply side and controlling the generation. The complexity increases

when the flexibility is needed not only due to a non-constant demand of energy, but also an unpredictable energy generation due to variable renewable energy sources.

Table 1.3-1 describes the different types of flexibility needs due to the addition of RES in the energy supply framework [11].

Table 1.3-1 Description of the different types of flexibility needs [11]

Occurrence	**Yearly**	**Weekly**	**Daily**	**Intra-hour**
Historical stakes	Peak demand due to temperature (heating in winter or cooling in summer)	Higher demand during working days compared to weekend	Demand variation between peak and off-peak hours	Unit outages and demand forecast errors
New stakes with high RES shares	Needs to back-up renewable variable energy with firm capacity	Variation of wind energy generation (at national level) over periods of a few days	Daily cycle of PV generation	RES generation forecast errors
Corresponding markets	Capacity market or scarcity prices	Day-ahead market	Day-ahead and intraday market	Balancing market
Flexibility characteristics requirements	3-6h for countries with high PV share 6-12 h otherwise	> 12h	3-6h	High reactivity
Flexibility value	High in most countries as it can replace investments in peak units	High values for country with high wind energy share and low interconnection capacity	Low value for most countries in Europe by 2030. Benefits appear for PV shares higher than 12%	High in European countries

The need for flexibility over a given period can be defined as the amount of energy that has to be shifted in order that the energy demand minus the variable renewable

energy generation would be constant. Therefore, the end result is to avoid peaks. The need of flexibility depends on the considered time framework. If short amount of time is considered, the flexibility characteristics requirements demand high reactivity of the system. If the time framework increases, reactivity should be less intense, till a certain point, because there may be fluctuations that should be compensated.

There are three important terms in energy flexibility:

- Up regulation: which means that the additional power should be provided because it is needed to maintain the system balance.
- Down regulation: which means that the power availability in the system should be reduced.
- Ramping capability: which means how fast flexible resources can change demand or supply of power.

Flexibility plays an important role in the competitiveness of the energy systems, as it defines their capability of meeting the demand especially when non-programmable renewable energy sources are involved in satisfying the demand. This is particularly relevant for the development of smart grids and for off-grid applications (like rural villages development).

1.4. Importance of the research

In conclusion, the future energy policy will be increasingly oriented towards improving the efficiency of energy systems, as well as towards increasing the flexibility i.e. the dynamic response of the electricity production to be combined with rising amounts of energy produced from renewable sources. Renewable energy sources cause an increase of the importance of the small-scale distributed generation with respect to the traditional large-scale generation. This is particularly relevant for the development of smart grids and for off-grid applications (like rural villages development), in which the study of the dynamic behavior is really important.

The studied energy system in this work is classified as small-scale generation. The present research aims to create a methodology to study the dynamic behavior of an energy system, starting from the steady-state conditions.

The energy system that will be analyzed is a plant formed by a commercial micro Gas Turbine (mGT) coupled with an optimized bottoming Organic Rankine Cycle (ORC). By coupling the mGT with the bottoming ORC, the energy efficiency of the overall system increases in comparison to the mGT working by its own. This thesis is focused on the proper modeling and simulation of both systems, in steady-state as well as in dynamic conditions.

By studying the dynamic behavior of the energy system, the response time can be analyzed and that would help to study the integration of conventional systems with renewable systems. The best way to increase the flexibility in the energy supply is to be aware of the dynamics present in the energy system.

In order to analyze the dynamics of the system, a real electricity-demand profile consisting in a set of 150 houses in Cologne (Germany) is studied. By imposing the electricity demand, the flexibility of the system formed by the mGT with the ORC can be analyzed. The flexibility is analyzed in terms of dynamic response to the fluctuations.

Chapter 2. Methodology

Don’t try to be the best, just try to give your best

2.1. Objectives

The final objective of the thesis is analyzing the possibility of the implementation of the combined system formed by the mGT and the ORC by studying the dynamic behavior of the whole system. This would allow determining whether the system is able to correctly respond to the electricity demand of the aggregation of a set of houses. In order to reach this final objective, different intermediate steps have to be completed:

- Identifying the performance at nominal conditions of a commercial mGT: AE-T100 (nameplate electric power out equal to 100 kWe).
- mGT steady-state modeling to study the behavior in part load conditions while varying the ambient temperature and the requested power load.
- Optimizing the design of the bottoming ORC by maximizing the net power produced.
- Steady-state modeling to analyze the part-load behavior of the ORC when the mGT operates in off-design conditions.
- Modeling of the mGT regenerator to obtain the characteristics (i.e. metal mass) needed to analyze the dynamic response.
- Dimensioning the heat exchangers of the bottoming ORC using Aspen Exchanger Design& Rating®.
- Dynamic modeling of the whole system mGT+ORC in Modelica language.
- Implementing a dedicated control system to handle the operation of the mGT+ORC system.
- Analyzing the system response.

In Figure 2.1-1, the layout of the system under study is depicted, showing the components which have been considered and the numeration of the streams.

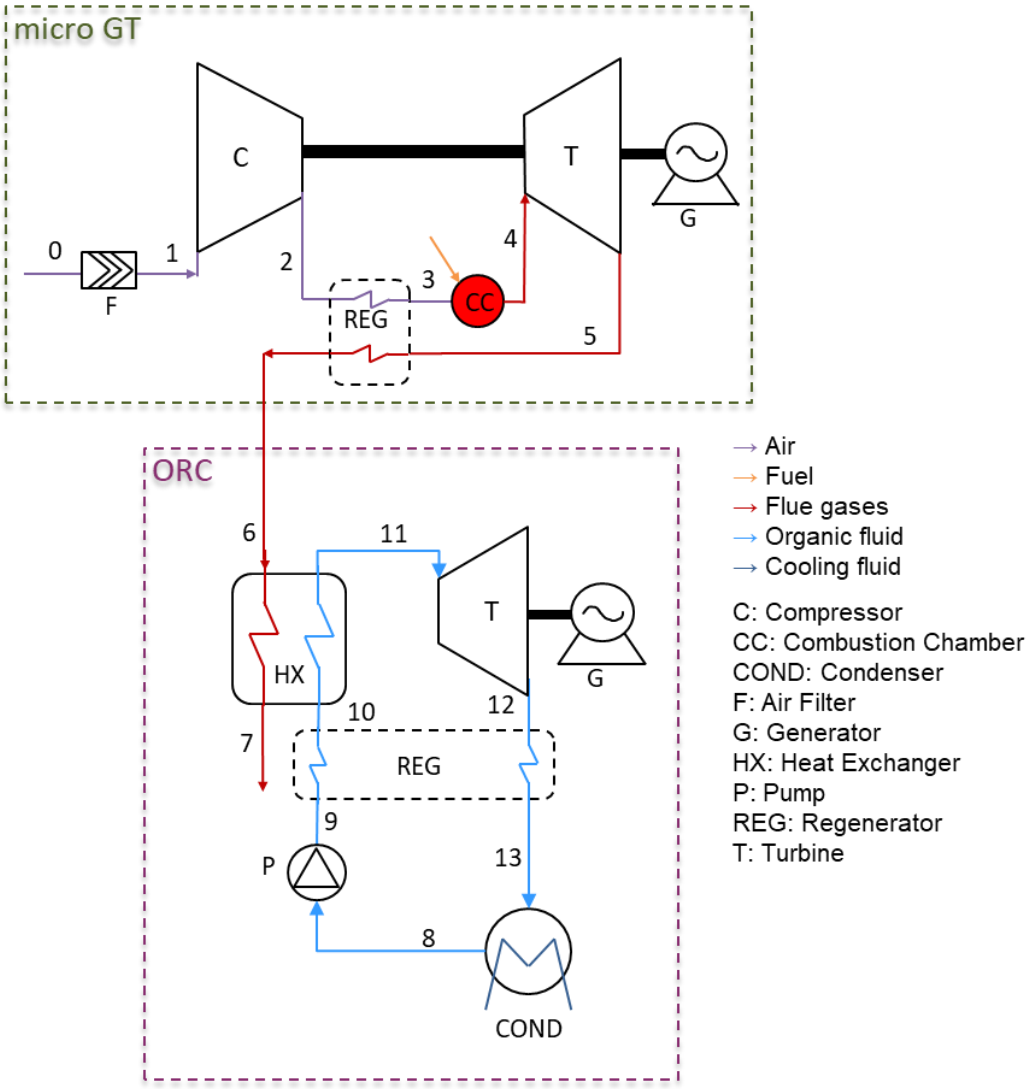

Figure 2.1-1 Layout of the studied system (mGT+ORC)

2.2. Description of the structure of the thesis

In this section, the structure of the thesis is described. As stated before, the main objective of this work is the study of the performance of the combined cycle composed by a commercial mGT with a bottoming ORC in both steady-state and dynamic conditions considering the variation of ambient temperature and electricity demand. To reach that goal, a suite of in-house models has been developed.

In Chapter 3. , after the description of the mGT technology, it is explained the way the design model has been developed considering the real performance of the mGT AE-T100 as well as the considerations taken to perform the part-load simulations while describing the off-design models.

Chapter 4. has the same structure as Chapter 3. . First, an overview of the ORC technology is introduced. Once the technology is described, it is presented the way the ORC has been designed, considering the optimization process to maximize the net power output evaluating the feasibility of different working fluids. In addition, the considerations taken to carry out the part load simulations are explained by describing the off-design models implemented.

Chapter 5. deals with the dynamic modeling and the considerations taken into account to study the transient behavior. In addition, in this chapter the control strategy and how the parameters of the controllers are obtained are described.

After the description of how the models are performed, the results are presented and discussed in Chapter 6.

Figure 2.2-1 shows how the solutions of the models are interrelated.

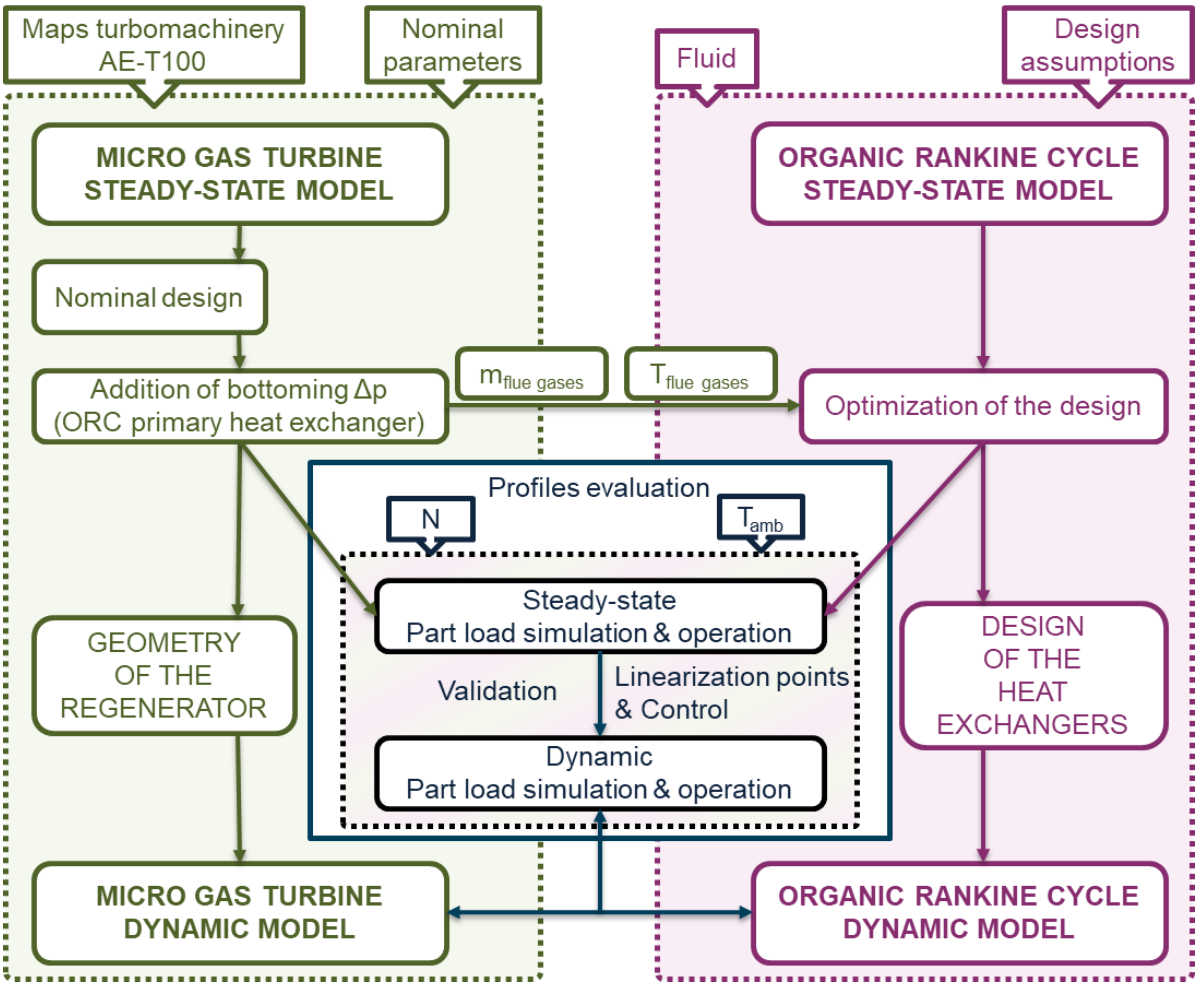

Figure 2.2-1 Description of the interrelations among the models and simulations

When looking at the figure, in green is represented the part related to the mGT and, in pink, to the ORC. Two design models have been developed in Matlab® for steady-state conditions. The first one introducing the already-known data (e.g. turbomachinery maps, entering air mass flow rate, turbine outlet temperature) to validate the performance at nominal conditions of the existing mGT. The second one, to optimize the design of the bottoming ORC. Once the nominal performance of the mGT has been obtained, a representative pressure drop has been added in order to simulate the pressure drop caused by the primary heat exchanger of the bottoming ORC. After adding the pressure drop, the corrected values of mass flow rate and temperature of the flue gases exiting the turbine of the mGT at nominal conditions have been taken as input for the design of the ORC.

Once the behavior of the whole system at nominal conditions has been determined, the heat exchangers could be sized. For the mGT, the regenerator is an existing one, therefore, a 3-D model of it has been developed in Matlab® using the characteristic dimensions, in order to calculate the volume, surface and steel mass that are fundamental to evaluate the dynamic performance of the system (they characterize the thermal capacitance). In the case of the ORC, the heat exchangers have been sized with Aspen Exchanger Design & Rating® by indicating the design process conditions. Moreover, the sized heat exchangers of the ORC have been simulated independently to analyze the part load behavior of them in stand-alone conditions and retrieve specific correlations that have been used in the part-load system model.

After the heat exchangers have been sized, steady-state models for the off-design conditions have been developed considering the whole system and including the information of turbomachinery and heat exchangers at part load conditions. The simulations have been performed by varying the ambient temperature and the rotational speed of the mGT turbomachinery (as indirect way to evaluate a reduction of requested power). The variation of those parameters affects the performance of the mGT and, as a consequence, the performance of the bottoming ORC. These results have been taken as a reference to validate the performance of the dynamic model when reaching steady-state conditions.

The dynamic model has been developed with an object-oriented language (i.e. Modelica, through Dymola platform). Therefore, each component (e.g. turbine, heat exchanger) has been modeled independently. Then, the components have been coupled together describing the system mGT+ORC. The response of the dynamic model reaching steady-state conditions has been validated with the results obtained from the steady-state models. Moreover, the solution of the steady-state models plays a fundamental role not only for the validation of the dynamic models, but also, to evaluate different off-design points in which the dynamic model should be linearized. To design the control system, obtaining the transfer functions of the

system (i.e. the way the outputs of the process vary with a modification of the inputs) was needed. To do so, it was required to perform the linearization of the system at different equilibrium conditions (different off-design conditions).

Finally, the control system has been designed, and the evaluation of the transient conditions has been performed by dynamically changing the electricity demand, considering the two most critical days of the year.

2.3. Software

In order to fulfill the modeling requirements to properly reach the objectives of this thesis, five main softwares have been used. On one hand, for the design and part-load operation models in steady state conditions, the software selected to implement the models is Matlab®, which was coupled to REFPROP to calculate the properties of the organic fluid. To calculate the properties of the mGT fluids (i.e. air, fuel and flue gases), the NASA polynomials formulation was implemented in Matlab®, as they properly describe the thermodynamic properties of the fluids involved, facilitating the computations. On the other hand, Dymola® has been chosen to develop the dynamic models, coupled to CoolProp to evaluate the properties of the organic fluid. The motivation to use different software to evaluate the properties of the fluids was the proper compatibility between them.

In addition to the software mentioned above, the dimensioning of the heat exchangers of the ORC module has been done by using Aspen Exchanger Design & Rating®.

Chapter 3. Micro Gas Turbine

There are always reasons to feel lucky, make those reasons your strengths.

3.1. Introduction to the technology

In this section, a brief introduction to the micro gas turbine (mGT) is reported, considering which mGT can be found in the market and the thermodynamics ruling the process. In addition, a brief comparison to its main competitor in small scale, namely internal combustion engine is reported too.

3.1.1. Thermodynamic properties of the ideal cycle and modifications from the ideality

A gas turbine is based on the open Brayton cycle, which ideally consists in 4 transformations: an isentropic compression till the maximum pressure of the cycle, an isobaric heating of the fluid till the maximum temperature of the cycle followed by an isentropic expansion till the minimum pressure and the isobaric heat rejection. Figure 3.1-1-left shows the layout of the ideal simple gas turbine considering an external heat input (no combustion chamber is considered) while Figure 3.1-1-right shows the T-s diagram considering air as working fluid, with a molecular mass equal to 29 kg/kmol, with a pressure ratio equal to 5, with ambient air temperature of 15ºC and the turbine inlet temperature equal to 1000ºC.

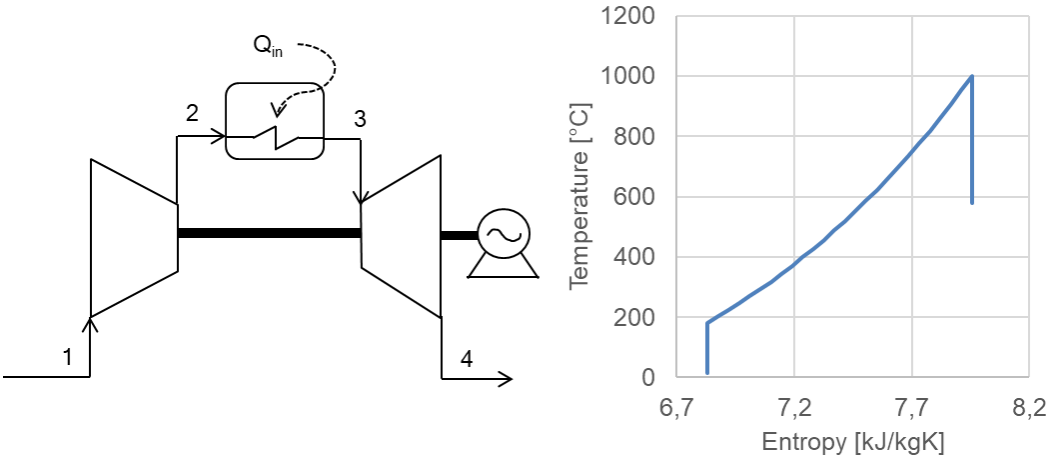

Figure 3.1-1 Ideal simple gas turbine layout (left) and T-s diagram (right) using air as working fluid considering a pressure ratio equal to 5, air inlet temperature equal to 15ºC and turbine inlet temperature equal to 1000ºC

The ideal regenerative gas turbine is based on the same basis of the ideal simple one, but the hot fluid exiting the turbine preheats the fluid after the compressor in order to reduce the heat input. In Figure 3.1-2-left, the layout of the regenerative gas turbine is depicted and in Figure 3.1-2-right represents the ideal regenerative Joule-Brayton cycle in T-s space considering the same assumptions adopted for the simple gas turbine and an ideal regenerator. Therefore, considering that the mass flow and fluid are the same, the hot fluid is cooled down till the inlet temperature of the cold fluid and the cold fluid is heated up till the temperature of the hot fluid at the inlet of the regenerator. As it can be seen from both T-s diagrams, considering the same assumptions for both cycles, the net work is the same[1], while the heat input in the regenerative case is lower, implying higher efficiency.

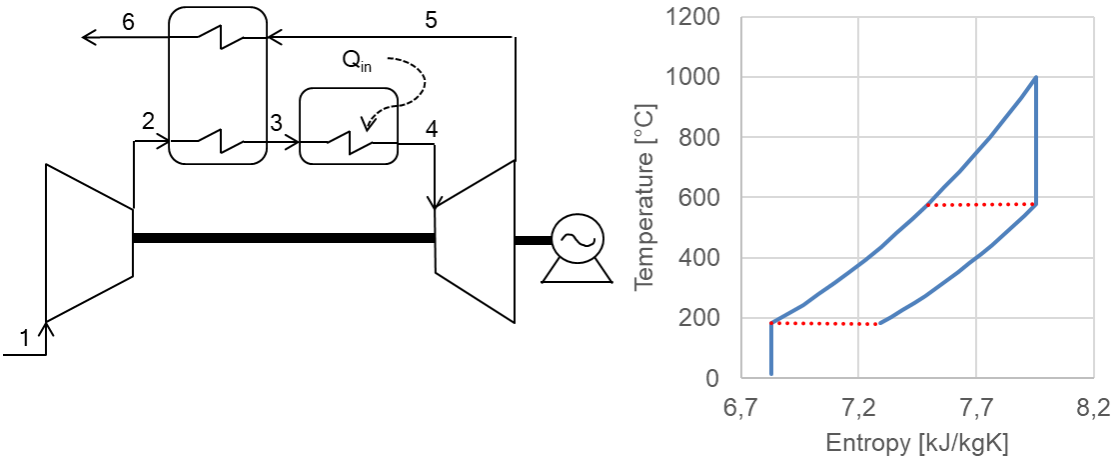

Figure 3.1-2 Ideal regenerative gas turbine layout (left) and T-s diagram (right) using air as working fluid considering a pressure ratio equal to 5, air inlet temperature equal to 15ºC and turbine inlet temperature equal to 1000ºC

After defining qualitatively the performance of the cycle, here the evaluation of the efficiency of both cycles is developed.

Considering a perfect gas, with a specific heat (c_p) and constant of the gas (R^*), the variation of entropy affecting the fluid can be expressed as:

$$ds = c_p \frac{dT}{T} - R^* \frac{dp}{p} \qquad \text{Eq. 1}$$

By defining θ as

$$\Theta = \frac{R^*}{c_p} \qquad \text{Eq. 2}$$

[1] Since the thermodynamic transformations of the ideal regenerative Joule-Brayton cycle are reversible, the net work is represented by the area contained by the cycle in T-s space.

Considering isentropic conditions, the outlet temperature after the compression can be computed with Eq. 3 and, after the expansion, with Eq. 4. β is the pressure ratio between the pressure at the outlet with respect to the inlet.

$$T_{out,comp} = T_{in,comp}\beta^{\Theta} \quad \text{Eq. 3}$$

$$T_{out,turb} = T_{in,turb}\beta^{-\Theta} \quad \text{Eq. 4}$$

The efficiency (η) is defined as the ratio between the net work obtained (l_{net}) and the heat input to the system (q_{in}). For a simple gas turbine with a perfect gas, it can be expressed as:

$$\eta_{simple} = \frac{l_{net}}{q_{in}} = \frac{c_p(T_3 - T_4) - C_p(T_2 - T_1)}{c_p(T_3 - T_2)} = 1 - \frac{T_4 - T_1}{T_3 - T_2} \quad \text{Eq. 5}$$

Considering isentropic conditions for the turbomachinery, it can be expressed as:

$$\eta_{simple} = 1 - \frac{T_3\beta^{-\Theta} - T_1}{T_3 - T_1\beta^{\Theta}} = 1 - \beta^{-\Theta} \quad \text{Eq. 6}$$

For a regenerative Joule-Brayton cycle, also considering a perfect gas as working fluid, the efficiency can be expressed as:

$$\eta_{regenerative} = \frac{l_{net}}{q_{in}} = \frac{C_p(T_4 - T_5) - C_p(T_2 - T_1)}{C_p(T_4 - T_3)} = 1 - \frac{T_2 - T_1}{T_4 - T_3} \quad \text{Eq. 7}$$

And considering isentropic conditions, it can be expressed as:

$$\eta_{regenerative} = 1 - \frac{T_1\beta^{\Theta} - T_1}{T_4 - T_4\beta^{-\Theta}} = 1 - \frac{T_1}{T_4}\beta^{\Theta} \quad \text{Eq. 8}$$

Looking at Eq. 6, the efficiency of an ideal gas turbine based on a simple cycle just depends on pressure ratio and fluid: an increment of the pressure ratio implies an increment of efficiency. When analyzing Eq. 8, the efficiency of an ideal regenerative gas turbine depends on the pressure ratio and both on the inlet and maximum temperature. Differently from the simple gas turbine, an increment of the pressure ratio would deal to a decrease in the efficiency. While an increment of the maximum temperature results in an increment of the efficiency.

In Figure 3.1-3, how the efficiency varies with the pressure ratio (left) and how the efficiency varies with the net specific work (right) are represented considering two different maximum temperatures equal to 800ºC (top) and 1000ºC (bottom) for both simple (black lines) and regenerative (blue lines) gas turbine. The continuous lines represent the ideal cases, while the dashed lines represent a more real behavior considering isentropic efficiency of the turbomachinery equal to 90%, pressure drop on the heat exchangers equal to 2% with respect to the inlet pressure, and effectiveness of the regenerator equal to 90%.

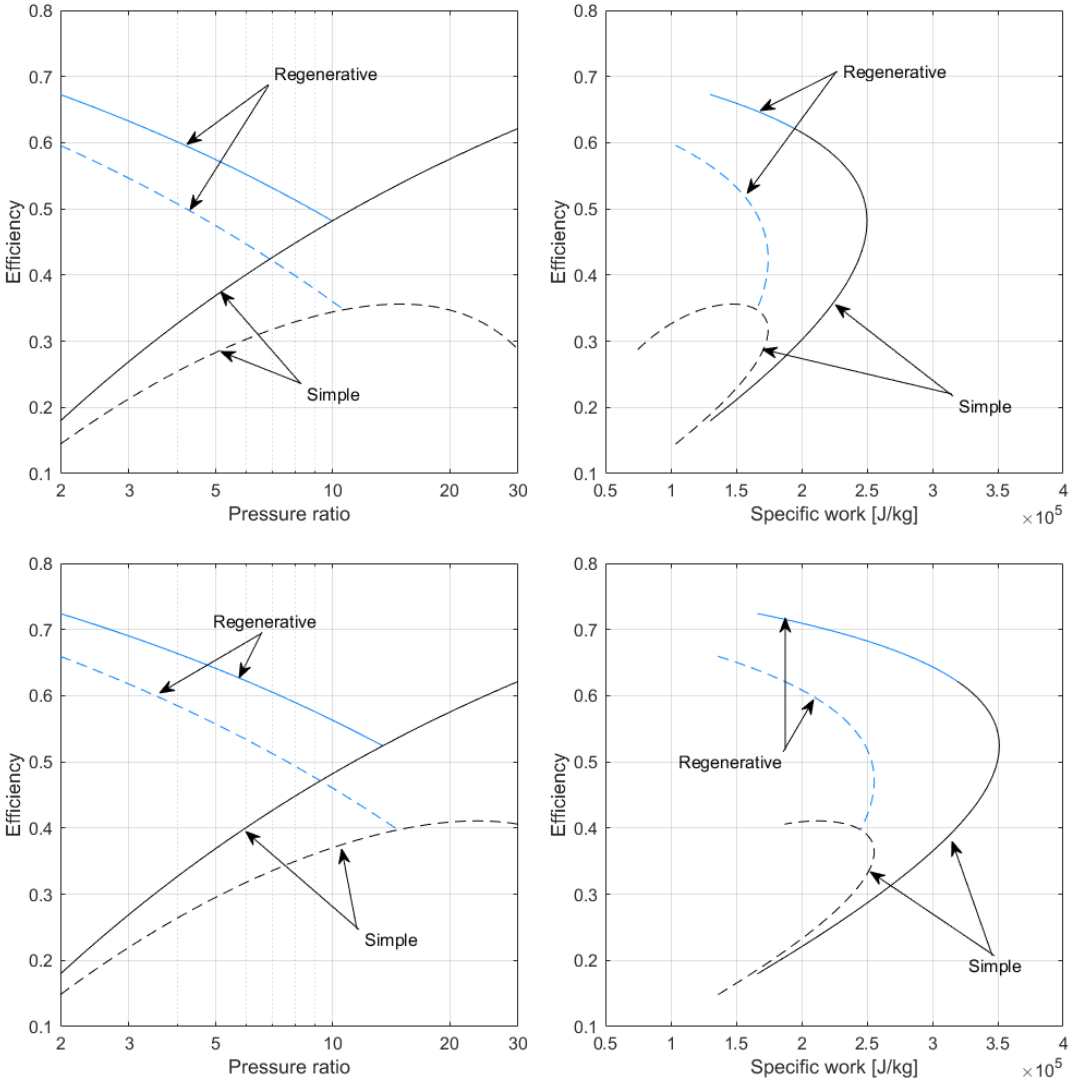

Figure 3.1-3 Efficiency vs pressure ratio (left) and efficiency vs specific work (right) for maximum temperature equal to 800ºC (top) and 1000ºC (bottom) for both simple (black lines) and regenerative gas turbine (blue lines)

As predicted before, the efficiency of the ideal simple gas turbine does not change with the maximum temperature, but the specific work increases with the temperature. In the regenerative case, the efficiency decreases with the decrease of the maximum temperature. The maximum temperature influences the simple gas turbine when considering real conditions, obtaining a higher efficiency with higher values of maximum temperature. In addition, the effect of the pressure ratio on the efficiency can be seen for both cycles. As stated before, for the ideal regenerative gas turbine, the efficiency decreases with the pressure ratio while it increases for an ideal simple gas turbine. However, in this last case, the different losses could modify that behavior highlighting the presence of an optimum value of pressure ratio which maximizes the efficiency.

Moreover, the net specific work increases with the maximum temperature for both cycle configurations.

3.1.2. Categories of gas turbines

The gas turbine (GT) technology is classified in five different groups [12]:

- Frame type Heavy-Duty gas turbines. This type of gas turbine represents the largest power generation units, within a range from 3 MW to 480 MW with efficiencies varying between 30-46%. They employ axial-flow compressors and turbines.
- Aircraft-Derivative gas turbines. Originated originally as aircraft mover, they turned to be also power generation units, with a production between 2.5 MW to 50 MW, with an efficiency range from 35-45%. They consist of an aircraft derivative gas generator and a free-power turbine.
- Industrial Type gas turbines. This kind of gas turbine are widely used in petrochemical plants. With a nominal power between 2.5 MW and 15 MW but penalized in efficiency (with respect to the others mentioned before) at values around 30%, which could be boosted using a regenerator.
- Small gas turbines. In this case, the nominal power ranges between 0.5 MW and 2.5 MW. The design of this type of gas turbine includes the use of centrifugal compressor (or a combination of centrifugal and axial compressors) and a radial-inflow turbine.
- Micro gas turbines. Within this category, the gas turbines with a nominal power lower than 350 kW are included. They use radial-flow turbine and compressor and a regenerative cycle.

The gas turbine used in this work belongs to the latter mentioned category.

3.1.3. Comparison with internal combustion engines

A good alternative to a combined cycle composed by a micro gas turbine with a bottoming ORC for electricity generation, is substituting the GT with a diesel engine. Indeed, the diesel engine has the advantage of having a faster starting response with respect to the GT and a higher efficiency. However, it has some disadvantages while comparing it to a gas turbine [13]:

- The diesel engine has a higher level of vibration than a gas turbine.
- The diesel engine cannot compete in terms of NO_x emissions, at least without a catalyst, as the gas turbine emits one order of magnitude less NO_x than the diesel engine (~40 mg/Nm^3 against 500 mg/Nm^3 at 5% O2) [14].
- Usually, maintenance costs are lower for a gas turbine, mainly due to the lower oil consumption and lower wear of components.
- Typically, the volume occupied by a diesel engine is higher than a gas turbine for the same nominal power.

So even if the efficiency is higher with a diesel engine, it can be considered that the increment of efficiency while combining the GT with the bottoming ORC fulfills the requirements of high efficiency for electricity generation, while keeping the advantages of the gas turbine.

3.1.4. AE T100

The gas turbine selected to be studied is the Turbec T100, manufactured by Ansaldo Energia (recalled AE T100). The AE T100 is a micro gas turbine designed to produce 100 kWe when working just in power mode (no cogeneration is considered). There are two different models: the AE T100 Power, which just produces electricity, and the AE T100 Power and Heat, which produces both electricity and heat (i.e. an additional heat exchange is present). With the second one, a higher first principle efficiency is obtained, but a penalization exists in the production of electricity due to the additional bottoming recovery heat exchanger (i.e additional pressure drops at the turbine outlet) [15]. Figure 3.1-4 shows the mGT selected.

The AE T100 is composed by a single-stage radial centrifugal compressor, a single-stage radial turbine, a lean premix combustion chamber, a permanent magnet electrical generator (which acts as an electric starter when doing the start-up of the GT by giving the power needed to the system to be self-stable) and a flue gas-air regenerator [15]–[17]. The rotating elements (i.e. electrical generator, compressor and turbine) are mounted on the same shaft, and the whole system is contained in the same housing. Table 3.1-1 collects the nominal performance of the gas turbine under study.

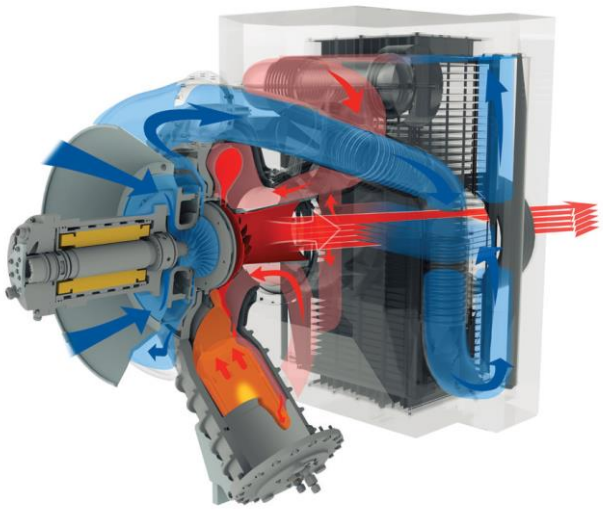

Figure 3.1-4 mGT AE T100 [17]

Table 3.1-1 Nominal performances of the AE T100 [17]

MICROTURBINE	
Nominal speed	70000 rpm
Turbine Inlet Temperature	≈ 950ºC
Turbine Outlet Temperature	645ºC
Pressure ratio of compressor	≈ 4.5
Fuel	Natural gas
PERFORMANCES	
Electrical output	100 kW (±3)
Electrical efficiency	30 % (±2)
Exhaust gas flow	≈ 0.79 kg/s
Exhaust gas temperature	≈ 270 ºC
Average sound pressure	≈ 72 dB (A) @ 1 m
NOx	≤ 15 ppm(v) ≈ 31 mg/Nm^3
CO	≤ 15 ppm(v) ≈ 19 mg/Nm^3

3.2. Design modeling

After introducing the technology itself, the way the micro gas turbine has been modeled at nominal conditions is described in this section. It is mandatory for the completeness of this thesis to know how the micro GT behaves. The technical information given by the manufacturer is not enough either to study the part-load behavior of the mGT itself and/or to properly design the bottoming ORC plant. Therefore, the complete thermodynamic performance should be evaluated. Figure 3.2-1 shows the layout of the micro GT.

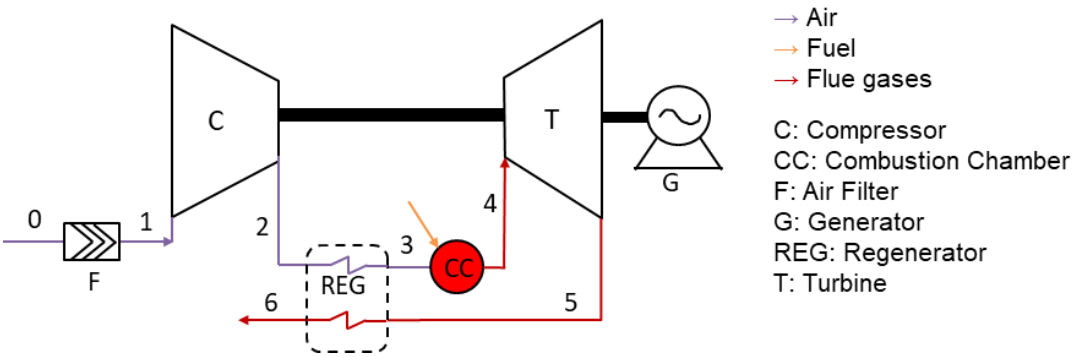

Figure 3.2-1 Layout of the considered micro gas turbine

The model to evaluate the nominal conditions collects the information available in literature [18], [19]. However, not all the information of the performance of the T100 is given in the literature, namely, the pressure drop of the filter of air entering the system and the pressure drop in the regenerator, because the experimental layouts do not consider the micro gas turbine T100 in standalone conditions, but usually it is modified according to the requirements of the research institution (e.g. coupled with volume modules [19], in an hybrid configuration with fuel cell [20], [21] or modifying it to operate like micro-Humid gas turbine [22]). Those modifications constitute a perturbation of the pressure drops of the system, modifying the performance of the gas turbine. Therefore, to validate the performance and establish the whole model of the micro gas turbine evaluating each thermodynamic state, the pressure drops are considered as independent variables which are modified in order to obtain the declared electric power, namely 100 kWe. Figure 3.2-2 shows the concept here explained. The nominal conditions already known from literature are taken as parameters, a tailored-made model has been developed in Matlab® considering each component independently and the pressure drops are the iteration variables to validate the nominal conditions. In order to evaluate the properties of the fluids, the NASA polynomials formulation is implemented (see Appendix B), as they properly

describe the characteristics (i.e. specific heat and enthalpy) of the fluids considered in the gas turbine (air, fuel and flue gases)[2].

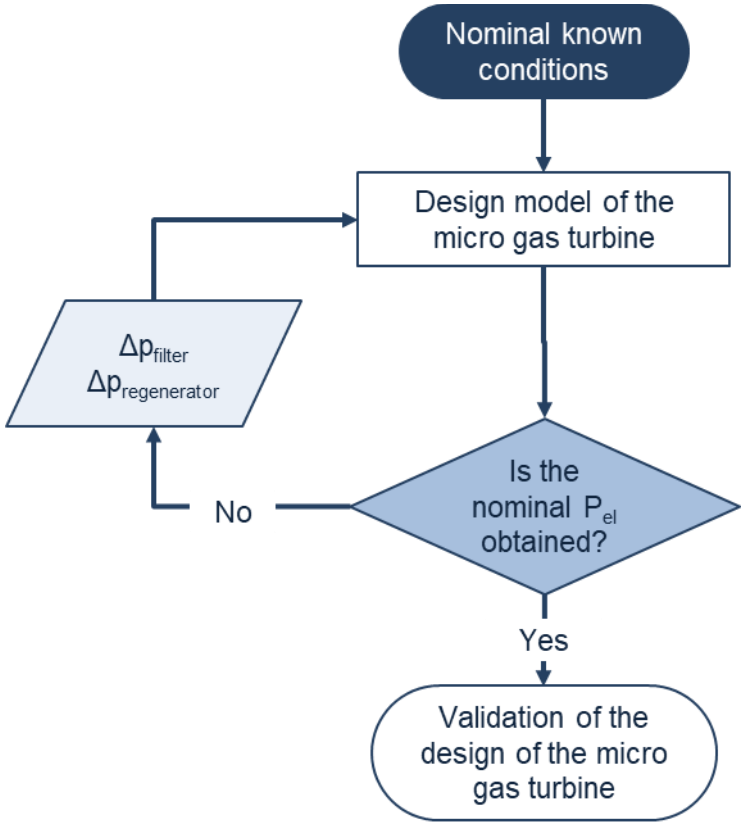

Figure 3.2-2 General logic to evaluate the nominal conditions of the mGT

In the next paragraphs, each component is described, and the characteristic equations are discussed. At the end, the way the equations are coupled together to perform the mGT simulation is defined.

3.2.1. Filter

Before the compressor, a filter is installed. The main function of the filter is avoiding the entrance of particles and bodies that could produce the erosion and damage of the compressor blades [23]. However, the filter reduces the performance of the system by adding a pressure drop, thus the air entering the compressor (p_1) is not at atmospheric pressure (p_0), but at a lower pressure (See Eq. 9).

$$p_1 = p_0 - \Delta p_{filter} \quad \text{Eq. 9}$$

In addition, the filter can be considered isothermal as there are no heat exchanged and the air is ideal, which means that isenthalpic corresponds to an isothermal.

[2] The behavior of air, fuel and flue gases can be approximated as ideal in the range of temperature and pressure typical of gas turbine applications

Therefore, the temperature of the air entering the compressor is the same as the ambient temperature.

$$T_1 = T_0 \qquad \text{Eq. 10}$$

3.2.2. Compressor

After the eventual particles have been removed from the air with the filter, the air is compressed in a single-stage centrifugal compressor to the maximum pressure in the cycle. The way the air is compressed is described by the compressor characteristic maps. These maps describe not only how the compressor works at nominal conditions, but also at part load operation. Following the common approach in turbomachinery, reduced variables are considered: reduced rotational speed (N_r) and reduced mass flow rate (m_r). The definition of these variables is expressed with Eq. 11 and Eq. 12.

$$N_{r-comp} = \frac{N}{\sqrt{T_1}} \qquad \text{Eq. 11}$$

$$m_{r-comp} = \dot{m}_{air} \cdot \frac{\sqrt{T_1}}{p_1} \qquad \text{Eq. 12}$$

The compressor characteristic maps (shown in Figure 3.2-3) represent two functions which correlates the pressure ratio (β) and the isentropic efficiency (η) with the reduced mass flow rate and the reduced rotational speed [24], [25].

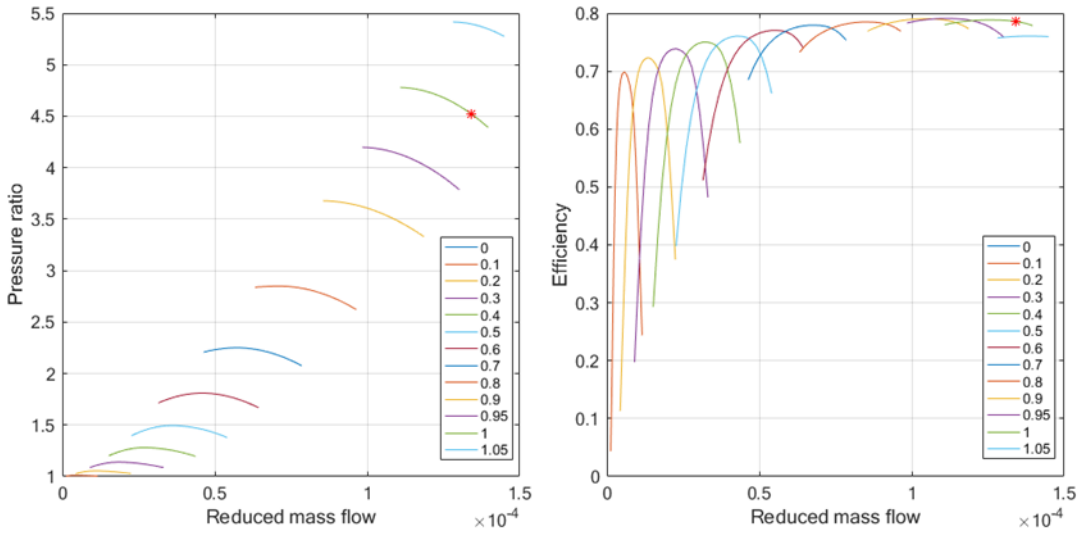

Figure 3.2-3 Characteristic map of the centrifugal compressor (left) and efficiency trend (right) of the AE T100 for different ratios of reduced rotational with respect to the nominal

The compressor characteristic maps are also used for the off-design and dynamic model, so in order to have a wider range of values nearby the sub-idle zone, the procedure explained in Appendix A is used to extrapolate the original curves at lower values of reduced rotational speed.

The pressure ratio (β) can be expressed as:

$$\beta_{comp} = f\left(m_{r-comp}, N_{r-comp}\right) \quad \text{Eq. 13}$$

$$\beta_{comp} = \frac{p_2}{p_1} \quad \text{Eq. 14}$$

With the isentropic efficiency, the enthalpy at the outlet of the compressor can be calculated. It can be expressed as:

$$\eta_{comp} = f\left(m_{r-comp}, N_{r-comp}\right) \quad \text{Eq. 15}$$

$$\eta_{comp} = \frac{h_{2iso} - h_1}{h_2 - h_1} \quad \text{Eq. 16}$$

$$h_{2iso} = h(p_2, s_1) \quad \text{Eq. 17}$$

In addition, the mechanical power absorbed by the compressor is expressed as:

$$P_{comp} = m_{air} \cdot (h_2 - h_1) \quad \text{Eq. 18}$$

3.2.3. Regenerator

The AE-T100 is a regenerative gas turbine, which means that after the air has been compressed in the compressor, the air is preheated before entering the combustion chamber. In this case, the regenerator is a corrugated heat exchanger, described in the section 3.4. On one hand, the presence of the regenerator reduces the amount of fuel required in the combustion chamber [12]. On the other hand, to preheat the air, a part of the heat of the turbine exhaust flue gases is exploited; thus, reducing the available heat that could be exploited by the bottoming cycle. Considering the enthalpy of the working fluids (h), the heat exchanged between the two fluids (Q) can be expressed as:

$$Q_{reg} = \dot{m}_{air} \cdot (h_3 - h_2) = \dot{m}_{flue} \cdot (h_5 - h_6) \quad \text{Eq. 19}$$

And considering the global heat transfer coefficient (U) and the exchange area (A), the exchanged heat can also be expressed as:

$$Q_{reg} = UA \cdot \Delta T_{lm} \quad \text{Eq. 20}$$

Where the logarithm mean temperature difference (ΔT_{lm}) is computed as:

$$\Delta T_{lm} = \frac{(T_5 - T_3) - (T_6 - T_2)}{\ln\left(\frac{T_5 - T_3}{T_6 - T_2}\right)} \quad \text{Eq. 21}$$

A good parameter describing the performance of the regenerator is the effectiveness (ϵ). The effectiveness represents the ratio between the actual heat exchanged and the maximum heat that could be exchanged in an ideal heat exchanger (i.e. infinite heat exchanger area) [23], [26].

$$\epsilon_{reg} = \frac{T_3 - T_2}{T_5 - T_2} \quad \text{Eq. 22}$$

Even if the heat transfer would be better with higher values of effectiveness, increasing the effectiveness of the regenerator has the drawback of an increment of the surface required, dealing to higher costs, higher pressure drop and higher inertia of the system [12]. In this case, the nominal value of effectiveness is equal to 88.9% [18].

Moreover, the pressure drops need to be taken into account as the real regenerator is not isobaric.

$$p_3 = p_2 - \Delta p_{reg,cold} \quad \text{Eq. 23}$$

$$p_5 = p_6 + \Delta p_{reg,hot} \quad \text{Eq. 24}$$

For the validation of the micro gas turbine, the regenerator discharges directly to the atmosphere and not to the evaporator of the bottoming cycle, so the outlet pressure is the atmospheric one. The pressure drop of the filter at the outlet of the mGT is included in the pressure drop of the regenerator.

3.2.4. Combustion chamber

The heat input to the gas turbine is provided by the combustion chamber. The combustion chamber is the component in which the combustion reaction takes place. The pressurized air enters the combustion chamber and it reacts with the fuel leading

to a flue gas exiting the combustion chamber with a different composition, temperature and pressure. In order to take this fact into account, the reaction of combustion is implemented, considering a generic natural gas, with the composition indicated in Table 3.2-1 [27] and the composition of dry air, indicated in Table 3.2-2.

Table 3.2-1 Molar composition of the natural gas

CH_4	[% mol]	91.397
CO_2	[% mol]	1.392
C_2H_6	[% mol]	4.979
C_3H_8	[% mol]	0.79
C_4H_{10}	[% mol]	0.342
N_2	[% mol]	1.1

Table 3.2-2 Molar composition of the air

O_2	[% mol]	20.96
N_2	[% mol]	78.12
Ar	[% mol]	0.92

The combustion is assumed to be complete, as the amount of oxygen is always higher than the stoichiometric one required by the fuel. However, in the model both reactions, complete and incomplete, have been implemented depending on the amount of oxygen entering with the air, here the complete reaction is reported.

As the natural gas considered consists of a mixture of hydrocarbons (i.e. CH_4, C_2H_6 etc.) and inert gases (i.e. N_2,Ar, CO_2) the generic combustion reaction is considered See Eq. 25).

$$C_\alpha H_\beta + \frac{2\alpha + \frac{\beta}{2}}{2} O_2 \rightarrow \alpha\, CO_2 + \frac{\beta}{2} H_2O \qquad \text{Eq. 25}$$

Where α and β are the mole coefficients which create a fictitious macromolecule allowing the definition of a generic combustion reaction. These coefficients take into account the number of moles of each substance reacting in one mole of fuel.

$$\alpha = \sum_{j=1}^{J} n_{C,j} x_{j,fuel} \qquad \text{Eq. 26}$$

$$\beta = \sum_{j=1}^{J} n_{H,j} x_{j,fuel}$$ Eq. 27

Where

$n_{C,j}$ is the amount of atoms of carbon in the reactive compound j of the fuel

$n_{H,j}$ is the amount of atoms of hydrogen in the reactive compound j of the fuel

$x_{j,fuel}$ is the mole fraction of the reactive compound j in the fuel

By knowing the coefficients which define the generic fuel, the stoichiometric coefficients of production and consumption of reactants can be calculated following the reaction in Eq. 25.

It is possible to evaluate the amount of each component reacting.

$$\dot{n}_{i,flue\ gas} = \dot{n}_{air} \cdot x_{i,air} + \dot{n}_{fuel} \cdot x_{i,fuel} + \nu_i \cdot \dot{n}_{fuel}$$ Eq. 28

In Eq. 28, the mole balance is represented, the number of moles of each substance exiting with the flue gases is the amount of it entering with the air and with the fuel plus the production of that substance due to the reaction. ν_i represents either the production (positive value) or consumption (negative value) coefficient of each component. As the evaluation of the consumption and production uses moles, it is needed the transformation from mass to moles by using Eq. 29 and Eq. 30.

$$MM_{fuel} = \sum_{i=1}^{I} MM_i \cdot x_{i,fuel}$$ Eq. 29

$$\dot{n}_{fuel} = \frac{\dot{m}_{fuel}}{MM_{fuel}}$$ Eq. 30

The combustor mass balance is indicated in Eq. 31.

$$\dot{m}_{flue} = \dot{m}_{fuel} + \dot{m}_{air}$$ Eq. 31

Finally, the combustor energy balance is considered, considering the presence of thermal losses equal to 1% of the inlet heat ($\eta_{comb} = 0.99$):

$$\left(\dot{m}_{fuel} \cdot h_{fuel} + \dot{m}_{air} \cdot h_{air}\right) \cdot \eta_{comb} = \dot{m}_{flue} \cdot h_{flue}$$ Eq. 32

To evaluate the efficiency of the cycle, the heat input is computed with the corresponding lower heating value of the fuel (LHV_{fuel}), which in this case it corresponds to 45.92 MJ/kg:

$$Q_{in} = \dot{m}_{fuel} \cdot LHV_{fuel} \quad \text{Eq. 33}$$

Pressure drops are computed as:

$$p_4 = p_3 - \Delta p_{comb} \quad \text{Eq. 34}$$

3.2.5. Expander

Once the flue gases exit the combustion chamber, they are expanded in the radial turbine. The way the turbine behaves is described by the characteristics maps of the turbine. Following a procedure similar to the one described for compressor, the characteristic maps of the turbine (shown in Figure 3.2-4) represent two functions which correlates the reduced mass flow and the efficiency with the pressure ratio and the reduced rotational speed [24], [25].

$$m_{r-turb} = f(\beta_{turb}, N_{r-turb}) \quad \text{Eq. 35}$$

$$\eta_{turb} = f(\beta_{turb}, N_{r-turb}) \quad \text{Eq. 36}$$

Also in this case, reduced variables are used, and to calculate them, the conditions at the inlet should be considered as reflected in Eq. 37 and Eq. 38.

$$N_{r-turb} = \frac{N}{\sqrt{T_4}} \quad \text{Eq. 37}$$

$$m_{r-turb} = \dot{m}_{flue} \cdot \frac{\sqrt{T_4}}{P_4} \quad \text{Eq. 38}$$

As in the case of the compressor, also these maps are implemented to study the off-design performance of the turbine while varying the external conditions and the load. As they are used to study the off-design, they have been extrapolated to lower values in the sub-idle region following the procedure explained in Appendix A.

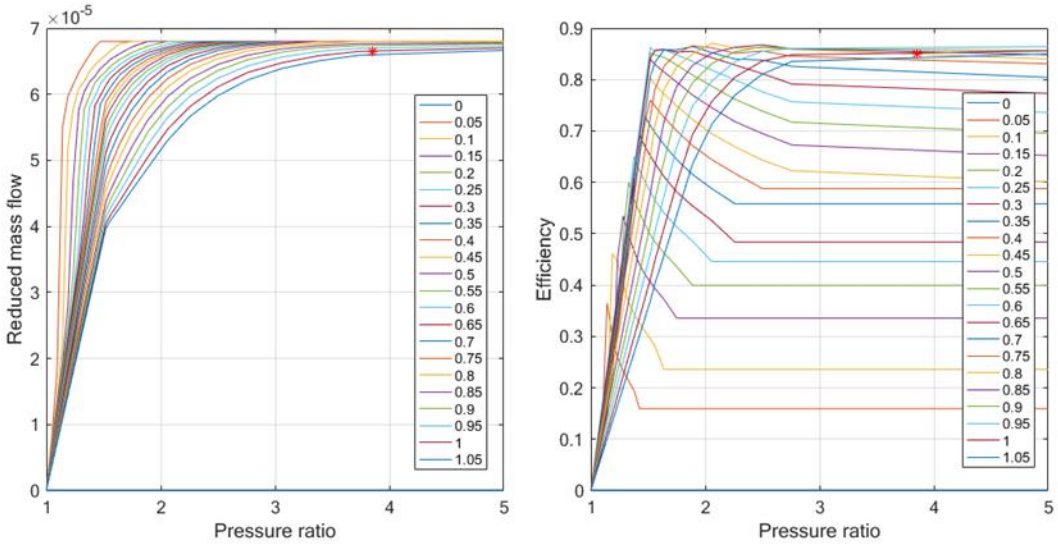

Figure 3.2-4 Characteristic map of the turbine (left) and efficiency trend (right) of the AE-T100 for different ratios of reduced rotational with respect to the nominal one

The pressure ratio for the turbine can be expressed as:

$$\beta_{turb} = \frac{p_4}{p_5} \quad \text{Eq. 39}$$

By knowing the efficiency, the actual enthalpy at the outlet of the turbine can be calculated:

$$\eta_{turb} = \frac{h_4 - h_5}{h_4 - h_{5iso}} \quad \text{Eq. 40}$$

$$h_{5iso} = h(p_5, s_4) \quad \text{Eq. 41}$$

Once the thermodynamic properties are known, it is possible to compute the mechanical power that could be obtained with the turbine:

$$P_{turb} = \dot{m}_{flue} \cdot (h_4 - h_5) \quad \text{Eq. 42}$$

3.2.6. Generator

The net mechanical power of the micro gas turbine considers the power produced by the turbine and the one consumed by the compressor, as expressed in Eq. 43.

$$P_{mech} = P_{turb} - P_{comp} \quad \text{Eq. 43}$$

However, the real electrical power produced contemplates the presence of losses due to the power electronic conversion (i.e. inverter and rectifier), auxiliary units energy demands (which are approximatively constant) and bearing friction. These losses can be computed with Eq. 44 [28], [29]

$$P_{loss\ generator}[kW] = 0.0806 \cdot P_{mech}[kW] + 7.5\ [kW] \qquad \text{Eq. 44}$$

After computing the losses, the electric power produced by the system can be calculated by subtracting the losses to the net mechanical power produced.

$$P_{el} = P_{mech} - P_{loss\ generator} \qquad \text{Eq. 45}$$

Finally, the electric efficiency is defined as the ratio between electric power output and the heat input:

$$\eta_{el} = \frac{P_{el}}{m_{fuel} LHV} \qquad \text{Eq. 46}$$

3.2.7. Micro gas turbine overall system

Figure 3.2-5 represents the way the model for the validation of nominal conditions of the micro gas turbine has been developed. The white boxes represent the equations shown in the sections before (from 3.2.1 to 3.2.6); the dark blue boxes, the inputs already known of the system; the light blue trapezoids, the thermodynamic states of the stream indicated and in green, the unknown variables which are modified to obtain the electric power indicated by the manufacturer (100 kWe).

At nominal conditions, the air inlet conditions are known (i.e. mass flow of entering air is equal to 0.8 kg/s, the temperature is equal to 15ºC and the pressure is 1 bar), the turbomachinery rotates at 70000 rpm, the effectiveness of the regenerator is 88.9% and the temperature at the outlet of the turbine is measured and kept fixed by the control system at 645 ºC [18]. With these parameters and the characteristic maps describing the performance of the turbomachinery (Figure 3.2-3 and Figure 3.2-4), the system could be evaluated. However, the pressure drops are variables which cannot be found in the literature for the stand-alone micro gas turbine. Therefore, they are taken as iteration variables to obtain the electric power declared by the manufacturer (100 kWe).

By knowing the conditions of the air entering the system and by establishing the pressure drop in the filter, it is possible to evaluate the conditions at the inlet of the compressor using the equations in the section 3.2.1. With the equations indicated in

the section 3.2.2, the performance of the compressor is analyzed so the outlet conditions can be obtained.

As the effectiveness of the regenerator at nominal conditions and the outlet temperature of the turbine are known, by using Eq. 22 and Eq. 23 the temperature and pressure at the outlet of the regenerator in the cold side can be calculated. Once the inlet conditions of the combustor have been calculated, it is needed to evaluate the performance of the combustion chamber by using the model specified in the section 3.2.4. In order to do it, first, an initial value for the outlet temperature of the combustor is needed. With this initial value, there is just one value of mass flow of fuel which satisfies both the mass and energy balances. However, as the composition of the flue gases changes with the amount of fuel introduced, there is an iterative process to find that value. Once both mass and energy balances of the combustor are satisfied, the conditions of the flue gases are known. Therefore, the reduced rotational speed and reduced mass flow can be computed (by using Eq. 37 and Eq. 38). With them, and the characteristic maps of the turbine, the outlet conditions of the turbine are determined. As the outlet temperature of the flue gases exiting the turbine is a parameter known, it needs to be checked whether the value of temperature obtained with the turbine model is the same or not. If that value does not match, a new value of temperature at the outlet of the combustor should be taken into consideration, recalculating the required amount of fuel with the model of the combustor and afterwards, the performance of the turbine. This process converges when the value of temperature matches, indicating the amount of fuel required to obtain the performance indicated. At this point, the whole regenerator can be evaluated and the outlet temperature, determined.

Finally, the electric power is evaluated. If it is equal to 100 kWe, the assumed pressure drops are the ones taken as nominal. If not, new values of pressure drops are assumed, and the process starts again till the convergence.

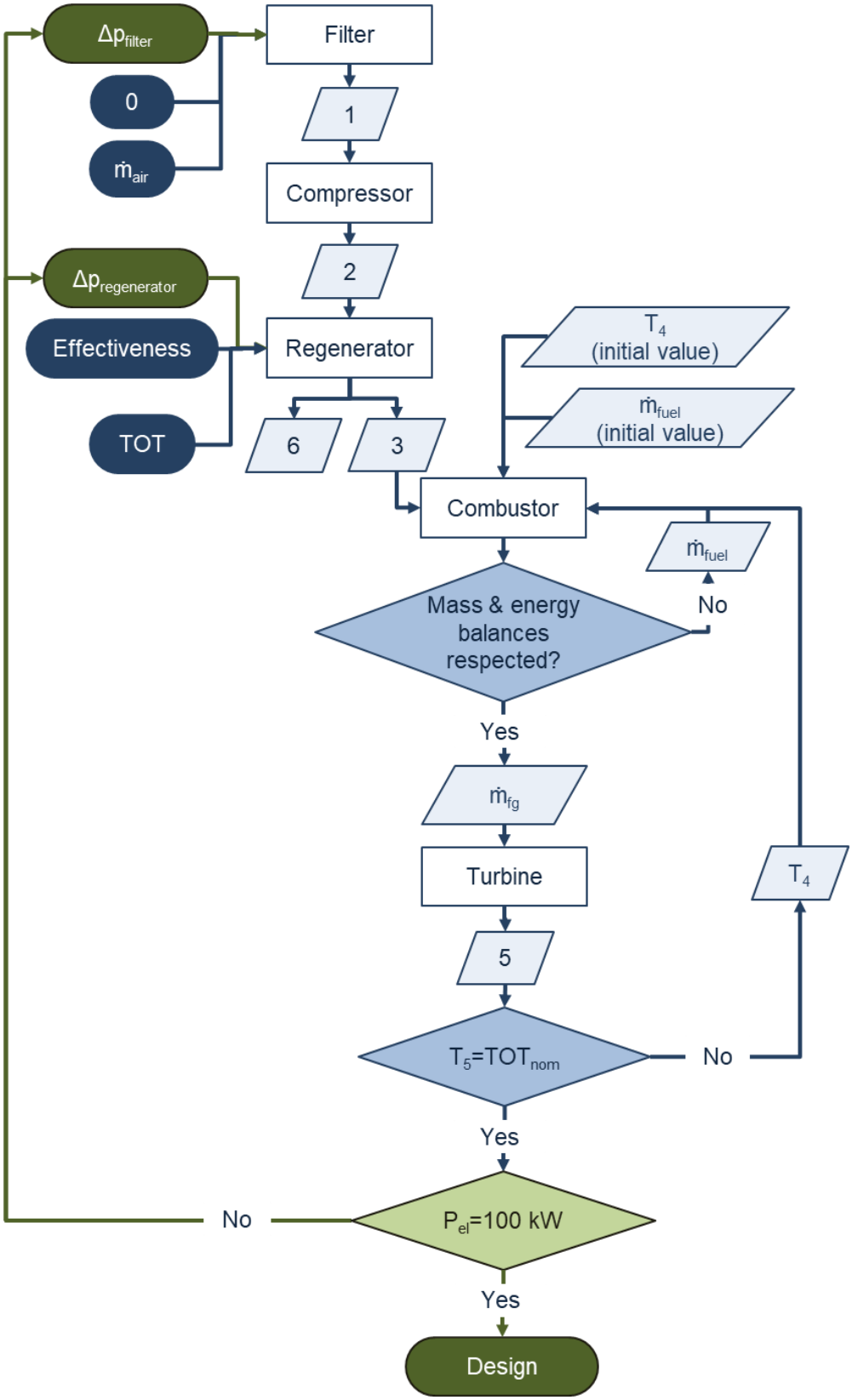

Figure 3.2-5 Extended logic of the evaluation of nominal conditions of the mGT

3.3. Off-design modeling

During real operation, the ambient temperature changes, as well as the power required by the user (e.g. the request of a group of houses). In order to study the transient behavior and how the system changes during the day, first, different part-load cases have been studied in steady-state conditions. This approach helps to validate the reached steady-state conditions of the dynamic model.

A tailored-made model has been developed taking into account the nominal performance obtained after the validation of design conditions and a set of non-linear equations that characterizes the behavior of each component.

Table 3.3-1 collects the known thermodynamic properties in off-design conditions.

Table 3.3-1 Fixed thermodynamic properties of the mGT

Fluid	N. stream	Description	Mass flow	Composition	Temperature	Pressure
Air	0	in, filt	✗	✓	✓	✓
	1	in,comp/out filt			✗	✗
	2	in,reg cold/out comp			✗	✗
	3	in,comb/out, reg cold			✗	✗
Flue gases	4	in,turb/out,comb	✗	✗	✗	✗
	5	in,reg hot/out,turb			✓	✗
	6	in,evap/ out, reg hot			✗	✗
	7	out,evap			✗	✓
Fuel			✗	✓	✓	✓

There are three different fluids: air, the fuel, and the flue gases resulting after the combustion. Among them, the composition of inlet air and fuel are known beforehand; but not the one of the flue gases as it depends on the reaction of combustion. Regarding to other thermodynamic properties, just the entering conditions of both air and fuel do not depend on the performance of the gas turbine, thus, known beforehand. In addition, the turbine outlet temperature is controlled at a constant value of 645ºC (as stated by the manufacturer). By fixing the TOT, the regenerator does not suffer thermal damages. If the TIT is fixed, in partial conditions, the TOT would increase so much that the regenerator should be designed for higher temperatures or it would suffer thermal damages. Moreover, it is easier to control the TOT instead of the TIT as the temperature is lower, so cheaper accurate thermocouples can be used for the measurements [19], [30], [31]. The last fixed condition is the discharge pressure after the flue gases have heated the working fluid

of the bottoming cycle as it discharges to the atmosphere. After analyzing the initial conditions, and as it can be seen in Table 3.3-1, there are 16 unknowns which should be determined to evaluate the performance of the system.

Table 3.3-2 Equations defining the part load model of the mGT

Components	Nº equations	Description
Filter	2	Pressure drop Isoenthalpic
Compressor	2	Compressor map Polytrophic compression
Regenerator	4	Energy balance Heat transfer equation Pressure drop (cold side) Pressure drop (hot side)
Combustion chamber	4	Mass balance Reaction Energy balance Pressure drop
Turbine	2	Turbine map Polytrophic expansion
Evaporator	2	Pressure drop Energy balance with ORC
Total components equations	16	

As there are 16 unknowns, 16 equations are needed to solve the system, which are aggregated in Table 3.3-2. Most of the equations described in the table, are described in the sections from 3.2.1 to 3.2.6. However, in this case, the pressure drops are not the nominal ones, but taking the nominal pressure drop as reference, they depend on the variation of the velocity of the fluid (i.e. air and flue gases). Thus, for each component, the new pressure drop (Δp_{off}) can be determined by using Eq. 47 with the nominal values and the off-design ones of mass flow rate ($\dot{m}$) and density (ρ) [24]

$$\Delta p_{off} = \Delta p_{nom} \left(\frac{\dot{m}_{off}}{\dot{m}_{nom}}\right)^2 \left(\frac{\rho_{nom}}{\rho_{off}}\right) \quad \text{Eq. 47}$$

Another characteristic equation of the part load behavior is how the heat transfer varies with the process conditions with respect to the nominal ones. The heat

exchanged in the regenerator can be expressed in terms of the global heat transfer coefficient, the exchanging surface and the logarithm mean temperature difference, as seen in Eq. 48. That expression is valid either for nominal or part load conditions.

$$Q_{heat\ exchanger} = UA \cdot \Delta T_{lm} \qquad \text{Eq. 48}$$

It is possible to evaluate the product UA at nominal conditions as all the system is already determined. Thus, it is possible to say in a general way, and without additional information regarding the part load conditions for that specific heat exchanger that the variation of the UA product follows Eq. 49 [24].

$$UA_{off} = UA_{nom}\left(\frac{\dot{m}_{off}}{\dot{m}_{nom}}\right)^{0.6} \qquad \text{Eq. 49}$$

Regarding the part load behavior of the compressor and turbine, they behave in the same way as explained in the sections 3.2.2 and 3.2.5, considering the different performance maps.

The part load model is more difficult to solve than the design one, due to the dependence of the part-load behavior on the thermodynamic properties at those conditions (i.e. pressure drop with mass flow and temperature). This fact converts the system in a highly non-linear one. The model implemented follows the logic explained in Figure 3.3-1, where the design conditions are introduced to evaluate the off-design ones. The part load simulations have been performed by varying the ambient temperature and the rotational speed of the turbomachinery (as indirect way to study the variation of the electric power produced). The selection of changing the rotational speed of the turbomachinery instead of the electric power output is motivated by the reduction of iterations for obtaining the solution, as it is easier to study the performance of the turbomachinery by knowing the rotational speed, thus, interpolating in the characteristic maps. However, the variables indicated in Figure 3.3-1 are the variables which are modified with the solver function of Matlab® to reach the convergence of the whole system respecting the mass and energy balances of each component.

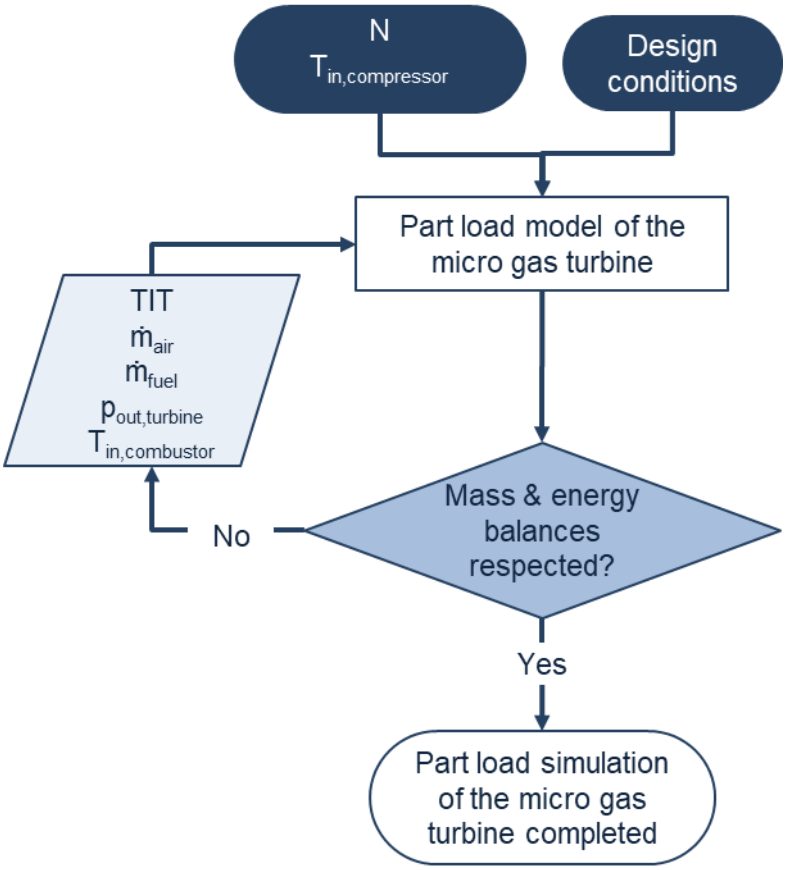

Figure 3.3-1 General algorithm of the off-design model of the mGT

3.4. Dimensioning of the regenerator

To analyze the dynamic performance of the system, the thermal capacitance plays a fundamental role, as it determines how fast the system reacts. Therefore, the dimensions of the regenerator should be determined, namely the volume of the channels through which the fluids flow, the mass and volume of the metal through which the heat exchange happens and the effective surface of the regenerator.

The regenerator used in the micro gas turbine AE-T100 is a Stainless steel SS-347 [32] corrugated plate heat exchanger [33]–[35].

To the author's knowledge, no complete information about the whole regenerator geometry can be found in the literature. Moreover, discordances with the calculation of lengths and surfaces of a corrugated plate heat exchanger have been found in the literature [36]–[39]. Thus, a complete 3D model has been developed with Matlab® collecting the information available in the literature and a purely mathematic calculation has been conducted to evaluate the real surfaces and volumes. The parameters used to do the calculations are shown in Figure 3.4-1 and Figure 3.4-2.

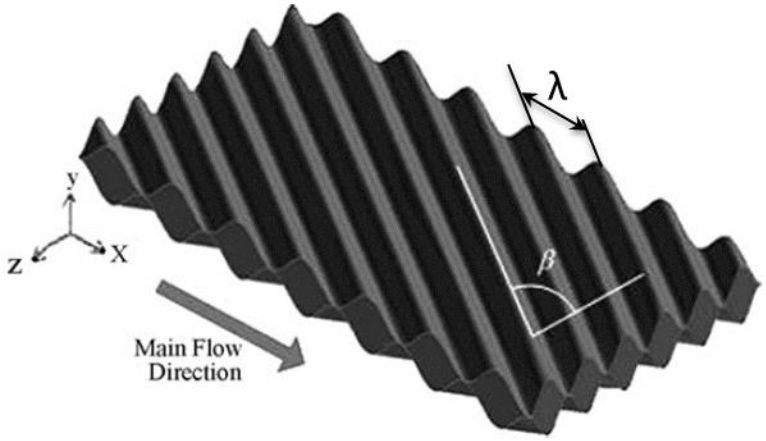

Figure 3.4-1 Representation of one channel of the regenerator [40]

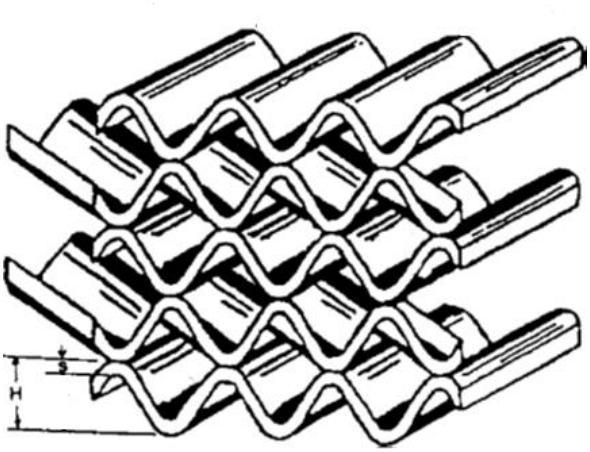

Figure 3.4-2 Representation of the channels configuration of the regenerator [38], [41]

The corrugations are described by a sine curve in the main flow direction (x) and they are displaced with the chevron angle (β) in the z direction [40] as in Eq. 50.

$$y = \frac{b}{2} \cdot sen\left(\left(x - \frac{\lambda}{4} + z \cdot \tan(\beta)\right) \cdot \frac{2\pi}{\lambda}\right) + \frac{b}{2} \qquad \text{Eq. 50}$$

By knowing the three dimensions describing the surface of the corrugations, the exchanging area can be computed with of Eq. 51 [42]:

$$\iint dS = \iint |\vec{r}_x \times \vec{r}_z| dx dz \qquad \text{Eq. 51}$$

Where $\vec{r}$ is the vector describing the surface of the corrugations and the subscripts x and z indicate the partial derivatives of $\vec{r}$ with x and z, respectively.

The vector $\vec{r}$ can be expressed as:

$$\vec{r} = x\vec{\imath} + \left(\frac{b}{2} \cdot sen\left(\left(x - \frac{\lambda}{4} + z \cdot \tan(\beta)\right) \cdot \frac{2\pi}{\lambda}\right) + \frac{b}{2}\right)\vec{\jmath} + z\vec{k} \qquad \text{Eq. 52}$$

To calculate the surface, it is required to calculate the module of cross product of the partial derivative of $\vec{r}$ with respect to x and z ($|\vec{r}_x \times \vec{r}_z|$). The partial derivatives can be expressed as shown in Eq. 53 and Eq. 54.

$$\vec{r}_x = \frac{\partial \vec{r}}{\partial x} = \vec{\imath} + \frac{b}{2} \cdot \frac{2\pi}{\lambda} \cdot cos\left(\left(x - \frac{\lambda}{4} + z \cdot \tan(\beta)\right) \cdot \frac{2\pi}{\lambda}\right)\vec{\jmath} \qquad \text{Eq. 53}$$

$$\vec{r}_z = \frac{\partial \vec{r}}{\partial z} = \frac{b}{2} \cdot \frac{2\pi}{\lambda} \cdot \tan(\beta) \cdot cos\left(\left(x - \frac{\lambda}{4} + z \cdot \tan(\beta)\right) \cdot \frac{2\pi}{\lambda}\right)\vec{\jmath} + \vec{k} \qquad \text{Eq. 54}$$

So the cross product of them ($\vec{r}_x \times \vec{r}_z$) is expressed in Eq. 55, with a final result declared in Eq. 56.

$$\vec{r}_x \times \vec{r}_z = \begin{vmatrix} \vec{\imath} & \vec{\jmath} & \vec{k} \\ 1 & \frac{b}{2} \cdot \frac{2\pi}{\lambda} \cdot cos\left(\left(x - \frac{\lambda}{4} + z \cdot \tan(\beta)\right) \cdot \frac{2\pi}{\lambda}\right) & 0 \\ 0 & \frac{b}{2} \cdot \frac{2\pi}{\lambda} \cdot \tan(\beta) \cdot cos\left(\left(x - \frac{\lambda}{4} + z \cdot \tan(\beta)\right) \cdot \frac{2\pi}{\lambda}\right) & 1 \end{vmatrix} \qquad \text{Eq. 55}$$

$$\vec{r}_x \times \vec{r}_z = \frac{b}{2} \cdot \frac{2\pi}{\lambda} \cdot cos\left(\left(x - \frac{\lambda}{4} + z \cdot \tan(\beta)\right) \cdot \frac{2\pi}{\lambda}\right)\vec{\imath} - \vec{\jmath} + \frac{b}{2} \cdot \frac{2\pi}{\lambda} \cdot \tan(\beta) \cdot cos\left(\left(x - \frac{\lambda}{4} + z \cdot \tan(\beta)\right) \cdot \frac{2\pi}{\lambda}\right)\vec{k} \qquad \text{Eq. 56}$$

Therefore, the module of the cross product is expressed in Eq. 57

$$|\vec{r}_x \times \vec{r}_z| = \sqrt{\left(\frac{b}{2} \cdot \frac{2\pi}{\lambda} \cdot cos\left(\left(x - \frac{\lambda}{4} + z \cdot \tan(\beta)\right) \cdot \frac{2\pi}{\lambda}\right)\right)^2 + (-1)^2 + \left(\frac{b}{2} \cdot \frac{2\pi}{\lambda} \cdot \tan(\beta) \cdot cos\left(\left(x - \frac{\lambda}{4} + z \cdot \tan(\beta)\right) \cdot \frac{2\pi}{\lambda}\right)\right)^2} \qquad \text{Eq. 57}$$

After substituting the result of Eq. 57 in Eq. 51, it is possible to evaluate the heat exchange surface of one corrugated plate.

The volume of the channels can be directly evaluated by doing the double integral of the corrugations equations in both dimensions: x and z.

$$V_{channel} = 2 \cdot \int_0^x \int_0^z \left(\frac{b}{2} \cdot sen\left(\left(x - \frac{\lambda}{4} + z \cdot \tan(\beta) \right) \cdot \frac{2\pi}{\lambda} \right) + \frac{b}{2} \right) dzdx \qquad \text{Eq. 58}$$

To evaluate the volume of metal between the channels, the thickness should be added to the value of y.

$$V_{metal} = \int_0^x \int_0^z (y + \delta)\, dzdx - \int_0^x \int_0^z y\, dzdx \qquad \text{Eq. 59}$$

The nominal parameters of the regenerator of AE-T100 are reported in Table 3.4-1 [43].

Table 3.4-1 Parameters of the regenerator

Assumptions of the dimensions	
L [mm]	250
W [mm]	300
δ [mm]	0,15
λ [mm]	2
h [mm]	1
N plates	770
β [º]	75

Chapter 4. Organic Rankine Cycle

The only one who must believe in you is just yourself.

4.1. Introduction to the technology

In this section, a brief introduction to the ORC technology is made. Some of the available applications are presented, the advantages of the technology are highlighted, the main classification of the cycle configurations is presented and a remark to the influence of the fluid is done.

4.1.1. Applications

There are a lot of applications for which the steam cycles do not offer a viable solution, and on those applications, the ORC technology can be a good competitor. In Figure 4.1-1, the different applications in which the ORC technology is suitable according to the temperature of the heat source and the power output of the module are shown in Figure 4.1-1 [44]. It can be highlighted the high potentiality for a wide selection of different applications. The case under study in this work is positioned in the small waste heat recovery (WHR) classification with a power output below than 50 kW and with temperature of the heat source between 200°C and 400 °C.

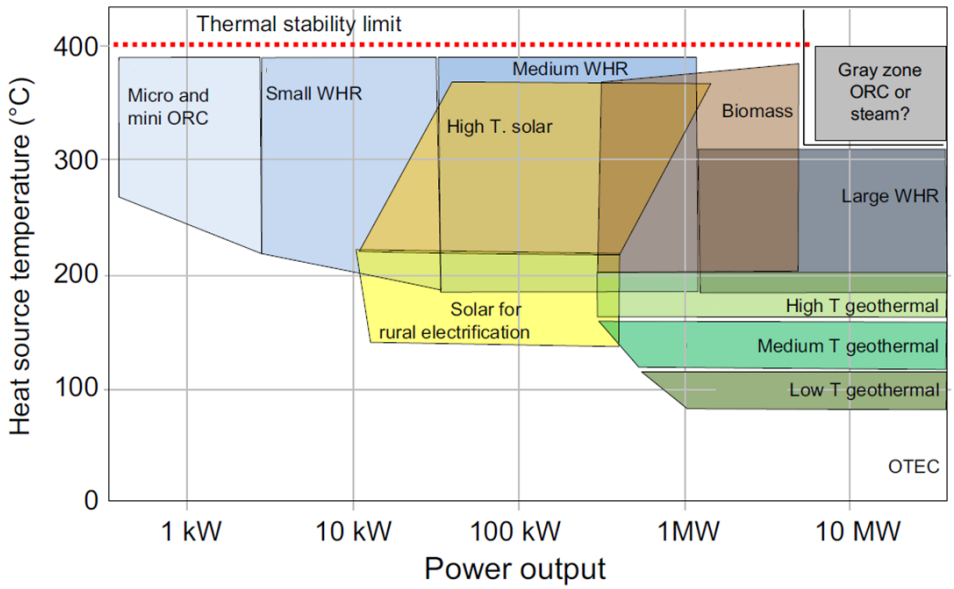

Figure 4.1-1 ORC applications field considering the heat source temperature and the power output [44]

A brief description of each application is mentioned in the following sections.

4.1.1.1. Biomass

The biomass is an energy source originated from living organisms. Even if the fossil fuels are also originated from living organisms, the main difference between biomass and fossil fuels is the fact that the latter ones have been produced and trapped underground in very long times. The main advantage of the biomass is that the power production with this source has limited carbon dioxide emissions into the atmosphere thanks to its production chain.

The use of biomass is usually coupled with cogenerative ORC plants, usually with a net electrical efficiency in the 15-20% range, able to reach a total first principle efficiency of 90%. In Europe, more than 200 ORC power plants fueled with various types of solid biomass have been installed, making this application one of the fields of major success for ORCs. Many of these power plants are in the MW_{el} power range and adopt a superheated cycle configuration. Usually high complexity fluids as hydrocarbons, fluorinated fluids, light siloxanes and MDM are adopted in this kind of application [45].

4.1.1.2. Concentrated solar power

Concentrated solar power plants use a technology based on the conversion of the direct component of solar radiation into medium-high temperature thermal energy and then into electricity, heat or mechanical work. To obtain a higher level of energy per unit area, mirrors are used. An opportune heat transfer fluid (e.g. molten salts or synthetic oil) is heated up in solar collectors and then the fluid transfers the accumulated heat to the ORC working fluid [44].

An interesting application for this kind of system is the stand-alone configuration for remote areas, for final users not connected to the electric grid. Usually, the plant size is small for those cases. Due to the small capacity of the engines, volumetric expanders are usually used [45].

Moreover, recently, instead of using a heat transfer fluid, the idea of heating up directly the ORC working fluid has been studied. The idea consists in avoiding the evaporation in the solar field, and in storing the heated organic fluid directly in tanks. Electricity is then produced through a flash triangular cycle or one level cycle with laminated admission [46].

In addition, there are studies considering the possibility of combining the concentrated solar power plant with biomass to provide the heat input to the ORC [47]. This gives more flexibility to the electricity production and heat generation, if present.

4.1.1.3. Geothermal

The properties of the geothermal fluid strongly depend on the location, characterizing the heat source with a temperature which can vary from about 80ºC to 200ºC. ORC power plants are mainly adopted for the conversion of liquid-dominated geothermal reservoirs characterized by temperatures around 120-150ºC [45]. The geothermal fluid may contain a non-negligible amount of incondensable gases, which may originate corrosive compounds, dealing to the need of more expensive equipment. The most common configuration for the geothermal exploitation is the saturated cycle one with an alkane (e.g. propane, isopentane, isobutane) as working fluid, which may include a regenerator.

When two-phase geothermal fluid is extracted from the reservoir, the steam and the brine are separated: the steam is used to evaporate the ORC working fluid, while the brine is used to preheat the ORC working fluid.

When working with steam-dominated geothermal reservoirs of large capacity, usually steam power plant is used to recover the available heat. However, a bottoming ORC system is an optimal solution to increase the overall efficiency, by exploiting the hot discharge from the steam turbine.

4.1.1.4. Ocean Thermal Energy Conversion (OTEC)

Even if no commercial application exists, ORC power plants could be adopted for the conversion of ocean energy deriving from the temperature difference between surface and deep water. OTEC engines have a really limited efficiency due to the low thermal gradient and, in order to be effective, the minimum temperature difference between the ocean surface layers should be around 20°C [45], [48].

4.1.1.5. Waste heat recovery

The potential of recover the waste heat is countless. Nowadays, the use of ORC systems has become an efficient and convenient solution to recover part of that released heat to produce electricity [45], [48], [49].

GTs and internal combustion engines (ICEs) are two sources of waste heat. The integration of ORCs with ICEs is a common commercial practice to improve the power output and efficiency of these systems and it can be found as a commercial solution by many ICE manufacturers [50]. Depending on the place where the heat is recovered (either from the engine water jacket or from the hot flue gases), the power increment would be in a range between the 3% and 10%. Similarly, the waste heat of the flue gases of the GTs with a power output range between 3 and 30MWel (too small for a steam bottoming cycle) can be recovered by an ORC, with an increment of the power output around 20-35% [45], [51], [52]. An example of this is the WHR from GTs which mechanically drive the compressors in the natural gas compressor

stations [53]. Usually, these stations are isolated so thermal energy is not needed. However, a bottoming ORC could mechanically drive a compressor or produce electricity. Moreover, the combination of a micro gas turbine with a bottoming ORC is of great interest. And it is the application under study in this work.

In addition to GTs and ICEs, many industrial sectors are characterized by large quantities of waste thermal energy available in the process fluids in a wide range of mass flow rates and temperatures. After using some part of the available thermal energy for the processes, the remaining heat could be exploited to produce additional power instead of being released to the environment. The sectors with a relevant amount of waste heat, so the more interesting ones, are the cement industry, the metal industry (e.g. iron, steel, copper, aluminum), the glass industry, the petrochemical sector and food and beverage processing industry. In general, ORC technology enables heat recovery from any industrial process where the available waste thermal power and temperature are sufficiently high to guarantee a cycle design with adequate efficiency at a reasonable cost.

According to the temperature level, the waste heat sources can be classified in three categories: low temperature (<230 °C), medium temperature (230–650 °C) and high temperature (>650 °C). The temperature determines the efficiency of the energy recovery process. Generally, the steam cycles have been used for the medium and high temperature sources and medium to large power, so an innovative cycle cannot compete with the maturity of the steam cycles. However, for low and medium temperature heat sources and small to medium plant size, the ORC is an optimal alternative.

However, only in recent years this huge potential has attracted interest and the first waste heat recovery ORC power plants have been installed, especially in cement industry. Waste heat streams are available in a 200-400 ºC range of temperatures depending on the cement plant configuration and in a range of available thermal powers between 5 and 100 MW_{th}. This range of available thermal energy pushes the competition of both technologies. The heat exchangers of the steam cycles are cheaper, but a larger number of stages in the turbine is required. Therefore, there is a chance of optimizing the ORC system to be competitive in comparison to the small steam cycle [45].

Therefore, ORC growth potential is particularly strong in all those sectors where there is the possibility of recovering waste heat and the use of a steam cycle is not economically feasible [48], [52].

4.1.2. Advantages of the technology

The steam Rankine cycle is one of the dominant power generation technology. The ORC represents a modified version of it in which the working fluid is not water but

another fluid. As encountered advantages can be highlighted: the reduction of the needed heat for the evaporation process at lower values of temperature and pressure with respect to the steam; the use of simple single or double stage turbines due to a relatively low pressure ratio between the evaporation and condensation pressure; the adaptability to different heat sources with the selection of the optimal fluid; and the dry expansion in the turbine avoiding the blades erosion when condensation occurs [44], [48], [50], [52], [54]–[56].

4.1.3. Selection of the fluid

The possibility of selecting the proper working fluid which is able to fit the external conditions to maximize the electric power by recovering maximum heat available is one of the main advantages of the ORC technology. This degree of freedom makes the ORC a flexible system in terms of suitability to different heat sources at medium-low temperature. Therefore, the working fluid has to be carefully selected in order to obtain the best performance of the cycle. The optimal working fluid should have [44]:

- Vapor saturation curve with zero or positive slope (ds/dT), respectively isentropic and dry fluids to avoid wet-expansion in the turbine.
- Suitable molecular mass. Large molecular mass benefits the turbine design as the number of stages is reduced (the molecular mass is inversely proportional to the turbine enthalpy drop), but it worsens the heat transfer coefficients, bringing to larger heat exchangers.
- Low environmental impacts (low Ozone Depletion Potential (ODP) and low Global Warming Potential (GWP). The ODP gives a relative measure of the impact on ozone layer degradation when a certain mass of gas is emitted in comparison with the effect that the emission of the same amount of CFC-11 has [57], integrated over time. The GWP measures how much heat the emissions of 1 ton of gas will absorb (over a period of time) relative to the amount of absorbed energy by 1 ton of carbon dioxide during the same period of time [58].
- Good safety properties (non-flammable and non-toxic). Hydrocarbons are often adopted as working fluid even if they are flammable, bringing complications to the system and additional costs related to safety reasons.
- Suitable thermal stability for the studied application.
- Suitable molecular complexity (i.e. number of atoms per molecule and the structure of the atoms in it). The molecular complexity affects the shape of the Andrews curve, with the positive consequences of the dry expansion and large fractions of heat input at variable temperature; but with the drawbacks of the requirement of a regenerator and small temperature drops in the expansion phase. Figure 4.1-2 shows three saturated cycles (with same maximum and minimum temperature) considering fluids with different

molecular complexity (namely water, benzene and MDM). It can be highlighted that the temperature drop between the turbine outlet temperature and the temperature of condensation in the case of the MDM is very high, pushing to the presence of a regenerator to recover part of the heat.

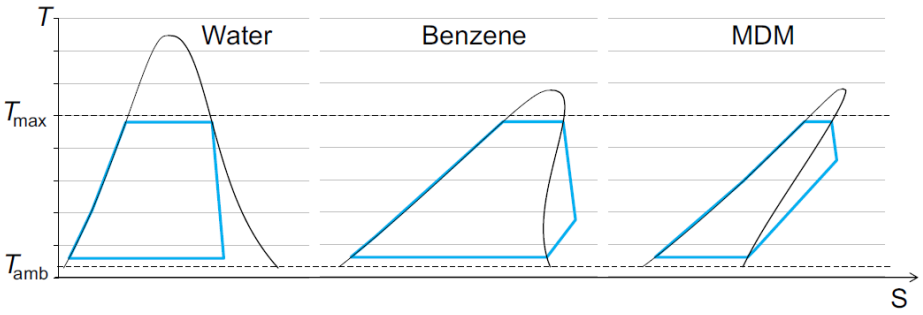

Figure 4.1-2 T-s diagrams for saturated cycles considering fluids with different molecular complexity [44]

4.1.4. Plant layout

In comparison to the conventional steam Rankine cycles, the ORC layout is usually simplified. The limited power output pushes to less complex layouts. Various pressure levels cycles can only be found where the heat source has a high cost (e.g. geothermal) that the investment cost of the ORC is not relevant to the overall cost and higher efficiencies of the plant would make feasible the exploitation of the source.

The single pressure level cycle is the simplest layout that can be found, requiring the smallest number of components, namely a primary heat exchanger, an expander, a condenser and a pump. A regenerator is optional depending on the fluid itself and the heat input conditions. The pressure of the saturated liquid exiting the condenser is increased with a pump till the maximum pressure of the cycle. Afterwards, if a regenerator exists, the fluid is preheated before entering the primary heat exchanger. In this latter one, the fluid absorbs the heat available for the heat source till the maximum temperature. Once the fluid is heated up till the maximum temperature, it is expanded in the expander, producing mechanical work, which is converted into electrical work by a generator connected to the shaft. If the regenerator is present, the hot fluid exiting the expander is used to preheat the fluid exiting the pump. Finally, the cycle is closed with the condenser. This configuration is divided into two families depending on the maximum pressure: subcritical and supercritical cycles [44], [49].

The maximum pressure in a subcritical cycle is lower than the critical one. They are the most common ones. Within this category, two subclassifications can be made according to the maximum temperature: saturated and superheated. Usually, if the working fluid has a critical temperature higher than the temperature of the heat source, the superheating penalizes the performance of the cycle, as there is a

reduction of the working mass flow rate. If the critical temperature of the fluid is small, then superheating is preferred to achieve a higher average temperature of heat introduction and reduce the entropy generation in the primary heat exchanger (PHE) [44], [45].

The supercritical or transcritical cycle consists in a cycle with a maximum pressure higher than the critical one. In a supercritical cycle, the change of phase from liquid to vapor is gradual, improving the heat introduction process. These cycles have the advantage that they can properly match the variable temperature heat source, reducing the overall logarithmic temperature difference, thus reducing the irreversibilities. As main disadvantage, the pressure is usually higher than the subcritical cycles. This fact deals to two main consequences: it is required more expensive devices and multi-stage centrifugal pumps are used, with a higher power consumption. Some examples of experimental plants have been installed [59]–[61], however, subcritical cycles are still ruling the ORC market.

Therefore, currently, the most common configurations are the saturated and superheated cycles, while the supercritical cycle configuration are adopted only in few cases. As mentioned before, the adoption of two or more pressure level cycles is only justified where the heat source cost is so high (e.g. geothermal source), that the investment cost of the ORC is not relevant to the overall cost [44].

Independently of the maximum pressure of the cycle, regenerative cycles are adopted where the working fluid is highly complex, presenting a high turbine discharge temperature and a huge difference between the turbine outlet temperature and the condensation temperature.

4.2. Design modeling

In this section, it will be described how the ORC module is designed considering optimal thermodynamic performance maximizing the electric output. The bottoming ORC module has been designed considering the flue gas conditions of the mGT at nominal conditions (i.e. temperature of flue gases around 275 ºC and mass flow around 0.8 kg/s).

As it has been said before, the bottoming cycle has to be designed and optimized. Differently from the micro gas turbine, in which the validation of the performance has been performed, in this case, the main objective is to obtain the maximum net power output with the exploitation of the heat available. It has to be taken into account, that the optimization performed is a thermodynamic one, not an economic one.

The layout of the system studied is shown in Figure 4.2-1, where the numeration of the streams is reported.

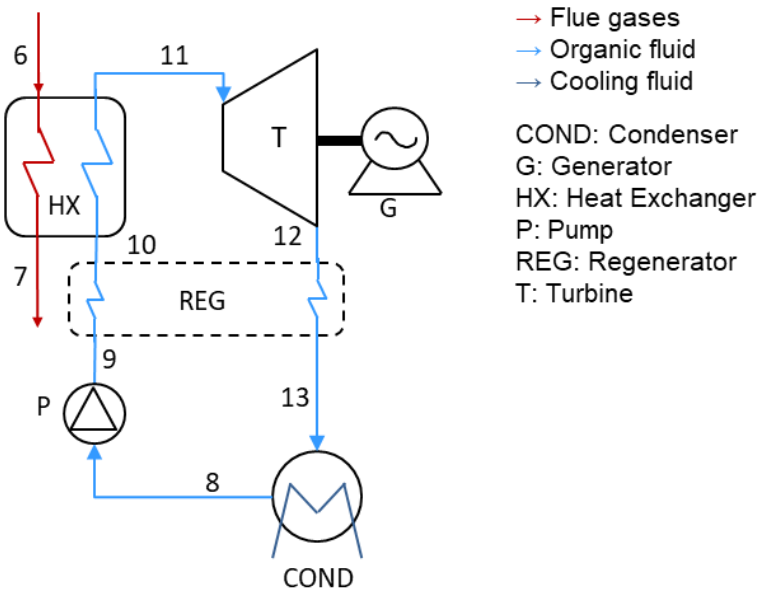

Figure 4.2-1 Layout of the ORC

A full tailored-made model has been developed in Matlab® considering each component of the system. The independent inputs to the model are the mass flow rate and the temperature of the gas turbine exhaust gases and the temperature of the cooling fluid of the condenser.

In order to perform the optimization, three variables are modified, namely the maximum temperature of the cycle (T_{11}), the pressure at the inlet of the turbine (p_{11}) and the approach temperature difference of the condenser (i.e. difference between the temperature at the inlet of the condenser and the outlet temperature of the cooling fluid). Water cooled condenser is considered in this study. The cycle optimization, once it has been modeled with Matlab®, has been performed by the *patternsearch* algorithm available in the optimization ToolBox of Matlab®. Other authors consider more variables (e.g. pinch point temperature) in the optimization [62]–[64]. In this work it has been decided to limit the number of optimization variables, as the output power of the ORC module is limited in comparison with the whole energy system.

As stated above, the ORC offers another degree of freedom, namely the working fluid. In this case, different fluids have been studied, preselecting them according to their maximum stability temperature and their condensation pressure (above 0.8 bar at a condensation temperature of 15ºC to avoid air infiltrations).

The general logic followed by the optimization of the design is shown in Figure 4.2-2.

In the next sections, the way each component has been designed is described with the equations characterizing them. At the end, the way the components have been connected is described.

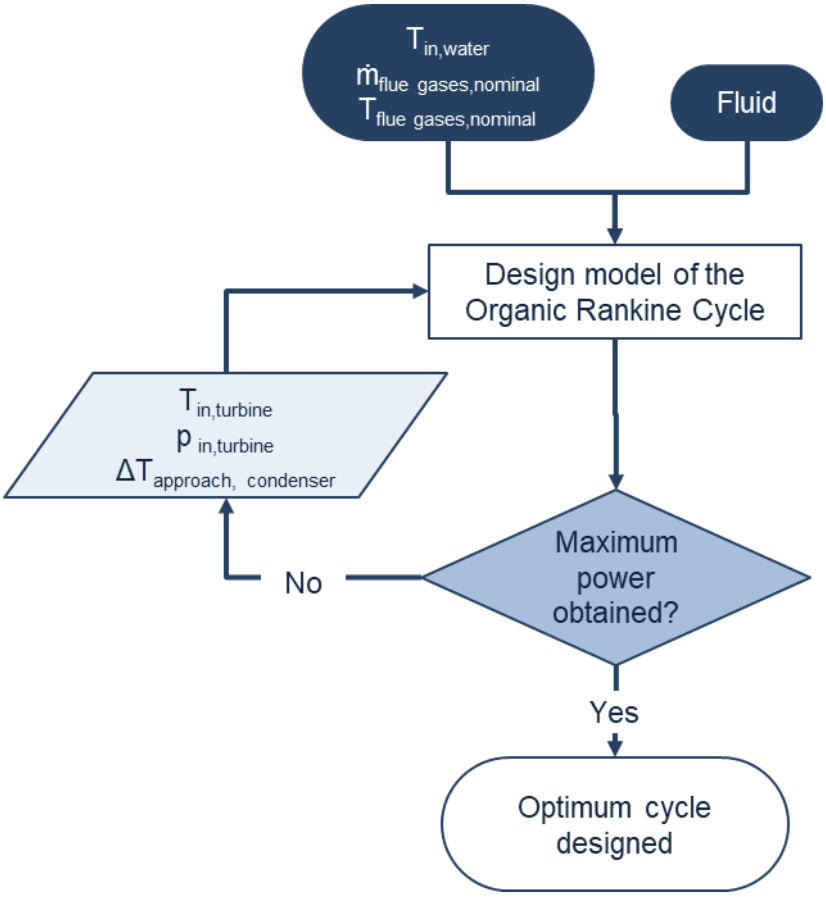

Figure 4.2-2 General logic to optimize the design of the ORC

4.2.1. Turbine

Considering the temperature (~275 ºC) and mass flow of the exhaust flue gases (~0.8 kg/s), it is possible to know the thermal input (approximatively 170 kW) to the bottoming cycle. With that thermal input, the ORC module designed is a small-scale one and the most suitable turbine is a radial inflow one [65].

Initially, the development of a complete model of the turbine was considered, by following the procedure indicated in [66]. However, strong assumptions have to be taken to evaluate the losses and to select the proper airfoil of the blades [67]–[70], without assuring a proper behavior with the organic fluid if CFD analysis or experimental studies are not performed [71], [72]. Finally, it has been selected a theoretical work (experimentally verified), which considers the possibility of varying the working fluid and predicts the maximum achievable efficiency of a single-stage radial inflow turbine evaluating the losses [73]. This work predicts the optimum specific speed (N_s) and the efficiency of the turbine (η_s) considering the size parameter (SP) and the volume ratio (VR). This approach allowed the possibility of

considering different fluids and obtaining the best design of the turbine while allowing the external optimization of the cycle by varying the pressure ratio.

$$\eta_s = f(VR, SP) \quad \text{Eq. 60}$$

$$N_s = f(VR, SP) \quad \text{Eq. 61}$$

Where the volume ratio and size parameter are defined as indicated in Eq. 62 and Eq. 63

$$VR = \frac{\dot{V}_{out,iso}}{\dot{V}_{in}} = \frac{\rho_{11}}{\rho_{12,iso}} \quad \text{Eq. 62}$$

$$SP = \frac{\sqrt{\dot{V}_{out,iso}}}{\Delta h_{iso}^{0.25}} = \frac{\sqrt{\frac{\dot{m}}{\rho_{12,iso}}}}{\Delta h_{iso}^{0.25}} \quad \text{Eq. 63}$$

Different values of volume ratio and size parameter combination deals to different optimum designs by varying the optimum specific rotational speed. Figure 4.2-3 has been implemented in the model, predicting the efficiency and the optimum specific speed for each couple of VR and SP.

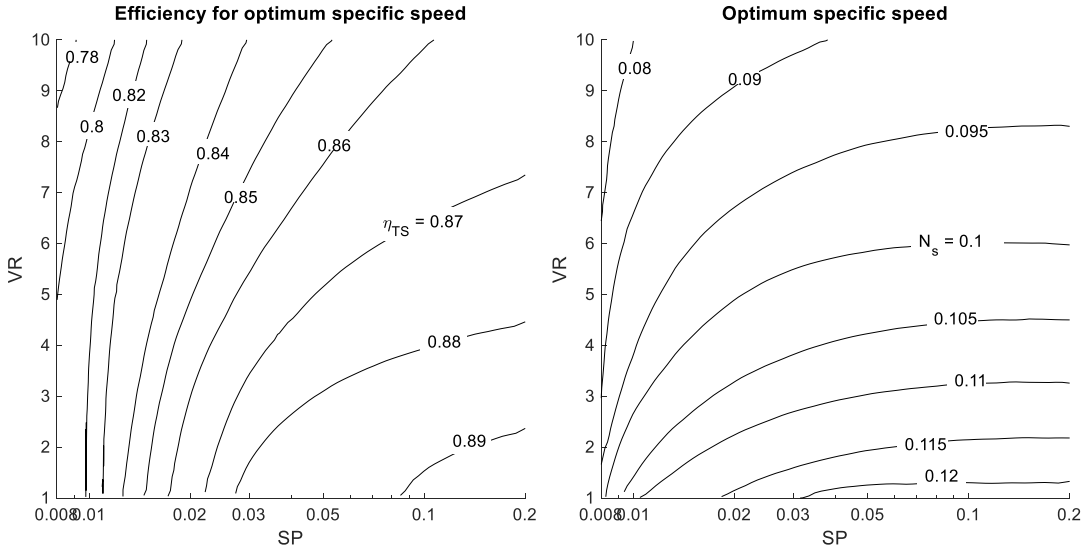

Figure 4.2-3 Efficiency prediction (left) and optimum specific speed (right) for a single-stage radial inflow turbine [73]

At the end, the optimum specific speed and the maximum efficiency are obtained with the maps, thus, the optimum single-stage radial inflow turbine design.

The rotational speed at nominal conditions can be calculated by using Eq. 64.

$$N = N_s \cdot 60 \frac{\Delta h_{iso}^{0.75}}{\sqrt{\frac{\dot{m}}{\rho_{12,iso}}}} \quad \text{Eq. 64}$$

And with the value of efficiency obtained, it was possible to calculate the enthalpy at the outlet of the turbine

$$\eta_{turb} = \frac{h_{11} - h_{12}}{h_{11} - h_{12iso}} \quad \text{Eq. 65}$$

$$h_{12iso} = h(p_{12}, s_{11}) \quad \text{Eq. 66}$$

In addition, the electric power produced by the turbine can be computed as indicated in Eq. 67.

$$P_{turb,ORC} = \dot{m}_{ORC} \cdot (h_{11} - h_{12}) \cdot \eta_{mec,el} \quad \text{Eq. 67}$$

4.2.2. Pump

The selected pump is a variable speed centrifugal pump, giving flexibility to obtain the required mass flow rate of fluid for the indicated pressure difference.

The fluid entering the pump is saturated liquid (i.e. condenser outlet). The process of increasing the pressure of the fluid is not isentropic, but there are some losses, considered by the hydraulic efficiency, as seen in Eq. 68.

$$\eta_{pump} = \frac{h_{10iso} - h_9}{h_{10} - h_9} \quad \text{Eq. 68}$$

$$h_{10iso} = h(p_{10}, s_9) \quad \text{Eq. 69}$$

And the electrical consumption of the pump is

$$P_{pump,ORC} = \frac{\dot{m}_{ORC} \cdot (h_{10} - h_9)}{\eta_{mec,el}} \quad \text{Eq. 70}$$

4.2.3. Primary heat exchanger

The exiting flue gases from the mGT heat up the ORC working fluid till the maximum temperature of the cycle. The heat available for the cycle is expressed in Eq. 71.

$$Q_{evap} = \dot{m}_{\text{flue}} \cdot (h_6 - h_7) = \frac{\dot{m}_{ORC} \cdot (h_{11} - h_{10})}{\eta_{evap}} \quad \text{Eq. 71}$$

But as some thermal losses have been considered, the actual heat received by the fluid is smaller.

The pressure drops have been modelled differently considering the status of the fluid, for liquid streams, it has been considered an absolute pressure drop, while for vapor streams, the pressure drop has been considered proportional to the inlet pressure. Moreover, when the fluid evaporates, the pressure drop has been indirectly considered with a temperature difference while evaporating [53], [74], [75]. This is the most suitable way to evaluate the pressure drops, considering that the model has been implemented to evaluate different configurations and different fluids.

As the optimization has been carried out, the type of cycle was not known beforehand, so both, subcritical and supercritical cycles have been considered. When the cycle is subcritical, the three main units (i.e. economizer, evaporator and superheater) are considered.

If the cycle is subcritical, the different sections have different pressure drops due to the fact that the conditions are different for the liquid (Eq. 74), for the two-phase zone (Eq. 73) and for the vapor (Eq. 72).

$$p_{11} = p_{10-11,v} - \Delta p_{sh} \quad \text{Eq. 72}$$

$$T_{10-11,l} = T_{10-11,v} + \Delta T_{evap} \quad \text{Eq. 73}$$

$$p_{10} = p_{10-11,l} + \Delta p_{eco} \quad \text{Eq. 74}$$

If the cycle is supercritical, just one pressure drop is considered (Eq. 75).

$$p_{11} = p_{10} - \Delta p_{exchanger} \quad \text{Eq. 75}$$

Table 4.2-1 collects the values of the pressure drop adopted for both types of cycle: subcritical (divided on the three sections) and supercritical.

Table 4.2-1 Assumptions of pressure drop adopted at the evaporator [53]

Δp_{sh} [bar]	$0.02 \cdot p_{11}$
ΔT_{eva} [ºC]	1
Δp_{eco} [bar]	0.5
$\Delta p_{supercritical}$ [bar]	$0.05 \cdot p_{11}$

To do the design, a fixed pinch point ($\Delta T_{pp,evap}$) has been adopted as a designing parameter. As the position of the pinch point was not known at the beginning, especially for the supercritical cycles, the heat exchanger has been analyzed by dividing it into multiple sections. The way it has been divided considers the same enthalpy difference and pressure variation for each section [53], [62], [76]. Therefore, the temperature of both ORC fluid and flue gases can be determined and the difference between them calculated. This would allow imposing the design pinch point wherever it is positioned along the heat exchanger (Eq. 76).

$$\Delta T_{pp,evap} = \min\left(T_{i,evap,flue\ gas} - T_{i,evap,ORC}\right) \quad \text{Eq. 76}$$

To analyze the part load performance, it is mandatory to compute the heat exchanger area. The exchanged heat can also be expressed in terms of the area, the global heat transfer coefficient and the logarithm mean temperature difference (Eq. 77). The evaluation of the exchanged heat has been done considering the multiple sections in which the heat exchanger has been divided. In addition, the global heat transfer coefficient depends on the properties of the fluid. Anticipating that the optimal solution is a subcritical cycle, here it is explained how it has been computed in the model.

$$Q_i = UA_i \Delta T_{lm,i} \quad \text{Eq. 77}$$

The logarithm mean temperature difference can be computed considering each calculation section with Eq. 78

$$\Delta T_{lm,i} = \frac{\Delta T_i - \Delta T_{i-1}}{\ln\left(\frac{\Delta T_i}{\Delta T_{i-1}}\right)} \quad \text{Eq. 78}$$

Figure 4.2-4 shows how the subdivision of the heat exchanger has been implemented and what temperature differences have been considered in Eq. 78.

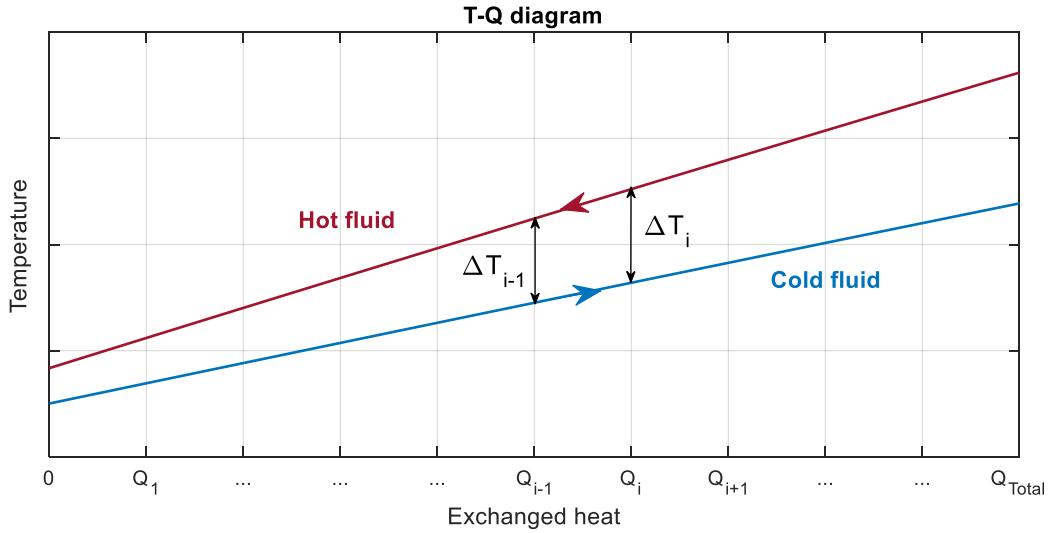

Figure 4.2-4 Subdivision of the heat exchanger expressed in the T-Q diagram

Once the heat has been computed, with the values of logarithm mean temperature difference, the product of the area and the global heat transfer coefficient can be determined. Thus, in order to evaluate the area of each section, the global heat transfer can be evaluated with Eq. 79, Eq. 80 and Eq. 81. Three different values have to be considered as the cold fluid enters as a liquid, evaporates and then it is heated till the maximum temperature, so the convective heat transfer coefficient of the cold fluid (i.e. working fluid) cannot be taken as constant. The values of the convective heat transfer coefficients (γ) and the ratio between the hot and cold surfaces have been taken from the design performed with Aspen Exchanger Design & Rating®. The assumption of neglecting the conductive resistance and the fouling has been taken to calculate the global heat transfer coefficient, as they have less influence for the cases under study.

$$U_{eco} = \frac{1}{\frac{1}{\gamma_{hot} \cdot \frac{A_{hot,evap}}{A_{cold,evap}}} + \frac{1}{\gamma_{liq,cold}}}$$ Eq. 79

$$U_{evap} = \frac{1}{\frac{1}{\gamma_{hot} \cdot \frac{A_{hot,evap}}{A_{cold,evap}}} + \frac{1}{\gamma_{evap,cold}}}$$ Eq. 80

$$U_{sh} = \frac{1}{\frac{1}{\gamma_{hot} \cdot \frac{A_{hot,evap}}{A_{cold,evap}}} + \frac{1}{\gamma_{vap,cold}}}$$ Eq. 81

After evaluating the global heat transfer coefficient, it was possible to calculate the surface of each section and by adding them, the whole area of the primary heat exchanger was determined.

$$A_{eco} = \frac{UA_{eco}}{U_{eco}}$$ Eq. 82

$$A_{evap} = \frac{UA_{evap}}{U_{evap}}$$ Eq. 83

$$A_{sh} = \frac{UA_{sh}}{U_{sh}}$$ Eq. 84

$$A_{PHE} = A_{eco} + A_{evap} + A_{sh}$$ Eq. 85

4.2.4. Regenerator

The regenerator is an option in the model. As the optimization has been performed, the cycle could or not have the regenerator. Usually, the regenerator improves the performance of the system, as the fluid is preheated before entering the evaporator, and less heat is rejected to the cooling fluid. Therefore, as initial hypothesis, the presence of it is always considered. However, the feasibility of it is studied, as it may happen that the fluid starts evaporating in the regenerator, damaging it. In that case, the regenerator would be deleted as component of the cycle.

The hot fluid leaving the turbine releases some heat to the pressurized cold fluid exiting the pump. The heat taken by the cold fluid is expressed in Eq. 86.

$$\dot{Q}_{reg} = \dot{m}(h_{10} - h_9)$$ Eq. 86

However, the heat released with the hot fluid is higher due to the existing thermal losses.

$$\dot{Q}_{reg} = \dot{m}(h_{12} - h_{13})\eta_{reg}$$ Eq. 87

Also the pressure drops have been considered for both sides:

$$p_{10} = p_9 - \Delta p_{reg,cold} \quad \text{Eq. 88}$$

$$p_{13} = p_{12} - \Delta p_{reg,hot} \quad \text{Eq. 89}$$

Table 4.2-2 collects the values of pressure drop taken for the regenerator.

Table 4.2-2 Assumptions of pressure drop adopted at the regenerator

$\Delta p_{reg,liq}$ [bar]	0.5
$\Delta p_{reg,vap}$ [bar]	$0.02 \cdot p_{13}$

As in the evaporator, the pinch point is a design parameter, but the position of it is not known since the beginning. Also in this case, the heat exchanger has been divided in multiple sections considering the same pressure and enthalpy differences for each section. This allows taking into account how the thermodynamic properties change through the heat exchanger and computing the real pinch point wherever it happens along the regenerator. The first attempt considers that the pinch point at the inlet of the regenerator, but that assumption is checked while computing.

$$\Delta T_{pp,reg} = \min\left(T_{i,reg,vap} - T_{i,reg,liq}\right) \quad \text{Eq. 90}$$

As it has been done in the primary heat exchanger, the model should evaluate the area of the regenerator (using Eq. 77 and Eq. 78). Therefore, after obtaining the performance of the process at nominal conditions, the dimensioning of the heat exchanger has been done considering a fin-plate heat exchanger with Aspen Exchanger Design & Rating® and the convective heat transfer coefficients were computed, allowing the calculation of the area with the Matlab® model.

$$U_{reg} = \frac{1}{\frac{1}{\gamma_{hot} \cdot \frac{A_{hot,reg}}{A_{cold,reg}}} + \frac{1}{\gamma_{cold}}} \quad \text{Eq. 91}$$

$$A_{reg} = \frac{UA_{reg}}{U_{reg}} \quad \text{Eq. 92}$$

4.2.5. Condenser

A water-cooled condenser is chosen to avoid the impact of the ambient temperature in the performance of ORC, this could have happened with the selection of an air fan. The heat exchanged is indicated for both sides, the hot one (Eq. 93) and the cold one (Eq. 94). In this case, the thermal losses have not been included, as the effect of them would be improving the performance of the condenser.

$$Q_{cond} = \dot{m}_{\mathrm{ORC}} \cdot (h_{13} - h_8) \quad \text{Eq. 93}$$

$$Q_{cond} = \dot{m}_{\mathrm{water}} \cdot C_{p_{water}} \left(T_{out,water} - T_{in,water}\right) \quad \text{Eq. 94}$$

In this case, as with the evaporator when the cycle is subcritical, two different pressure drops have been considered, taking into account the desuperheating (Eq. 95) and the phase changing (Eq. 96):

$$p_{8-13} = p_{13} - \Delta p_{desh} \quad \text{Eq. 95}$$

$$T_{8-13} = T_8 + \Delta T_{cond} \quad \text{Eq. 96}$$

Table 4.2-3 collects the values of pressure drop adopted at the condenser.

Table 4.2-3 Assumptions of pressure drop adopted at the condenser

Δp_{desh} [bar]	$0.01 \cdot p_{8,13}$
ΔT_{cond} [ºC]	0.3

In addition, a modified pinch point ($\Delta T^*_{pp,cond}$) has been considered as design parameter, imposing the outlet temperature of the cooling fluid equal to the temperature in which the condensation starts minus the modified pinch point (Eq. 97).

$$T_{out,water} = T_{8-13} - \Delta T^*_{pp,cond} \quad \text{Eq. 97}$$

One of the parameters modified with the *patternsearch* algorithm to maximize the power output is the approach temperature. The outlet temperature of the ORC fluid at the outlet of the condenser has been computed considering the temperature of the cooling fluid and the approach temperature.

$$T_8 = T_{in,water} + \Delta T_{approach} \quad \text{Eq. 98}$$

Following with the motivations indicated while explaining the primary heat exchanger and the regenerator, also the area of the condenser has to be computed by the model, especially to evaluate the part load performance. In this case, the condenser has not been divided into multiple sections to evaluate the pinch point, but just in two: the two-phase (Eq. 99) and the desuperheating zone (Eq. 100).

$$Q_{bip,cond} = \dot{m}_{ORC}(h_{8-13} - h_8) = UA_{bip}\Delta T_{lm,bip} \quad \text{Eq. 99}$$

$$Q_{desh,cond} = \dot{m}_{ORC}(h_{13} - h_{8-13}) = UA_{desh}\Delta T_{lm,desh} \quad \text{Eq. 100}$$

The logarithm mean temperature difference can be computed as indicated in Eq. 78 for both sections, considering the respective temperatures.

As in the primary heat exchanger, where the fluid is not at the same state, in the condenser there is a desuperheating zone, in which the temperature of the vapor is reduced till reaching the saturated vapor conditions, and the actual condensing zone, in which the fluid changes phase. The convective heat transfer coefficients are strongly dependent on the properties of the fluid. Hence, different global heat transfer coefficients should be evaluated for each zone considering the design results of Aspen Exchanger Design & Rating®.

$$U_{bip,cond} = \frac{1}{\frac{1}{\gamma_{bip,hot} \cdot \frac{A_{hot,cond}}{A_{cold,cond}}} + \frac{1}{\gamma_{cold}}} \quad \text{Eq. 101}$$

$$U_{desh,cond} = \frac{1}{\frac{1}{\gamma_{desh,cond} \cdot \frac{A_{hot,cond}}{A_{cold,cond}}} + \frac{1}{\gamma_{cold}}} \quad \text{Eq. 102}$$

After computing the global heat transfer coefficients, the areas of both sections can be evaluated, obtaining the total area by adding both of them.

$$A_{bip} = \frac{UA_{bip}}{U_{bip}} \quad \text{Eq. 103}$$

$$A_{desh} = \frac{UA_{desh}}{U_{desh}} \quad \text{Eq. 104}$$

$$A_{cond} = A_{bip} + A_{desh}$$ Eq. 105

Finally, the consumption of the pump of the cooling fluid (i.e. water) is computed with Eq. 106

$$P_{pump,water} = \frac{\dot{m}_{water} \cdot \Delta p_{water}}{\rho_{water} \cdot \eta_h \cdot \eta_{mec-el}}$$ Eq. 106

4.2.6. ORC overall system

Figure 4.2-5 represents the way the model has computed the nominal conditions of the ORC module. The white boxes represent the equations shown in the sections before (from 4.2.1 to 4.2.5); the dark blue boxes, the inputs of the system (which can be both known inputs or inputs from the optimizer); the light blue trapezoids, the thermodynamic states of the stream indicated or assumed initial values.

As stated before, three parameters have been modified by the *patternsearch* algorithm to maximize the net power produced, namely the temperature and pressure at the inlet of the turbine and the approach temperature of the condenser.

On one hand, with the inlet conditions of the turbine and with an initial value of mass flow of working fluid, by using the equations shown in section 4.2.1, the radial-inflow turbine can be dimensioned, and a value of efficiency is a result from that dimensioning. After dimensioning the turbine, the thermodynamic properties at the outlet of the turbine can be computed.

On the other hand, considering the temperature of approach of the condenser and the inlet temperature of the cooling fluid, the temperature of the working fluid at the outlet of the condenser is determined with Eq. 98. As it is saturated liquid, also the condensation pressure is known. Therefore, with the equations shown in the pump section (4.2.2) the conditions at the outlet of the pump (inlet of the cold side of the regenerator) are known.

Once the thermodynamic conditions at the outlet of the turbine and at the outlet of the pump are computed, the inlet conditions of both sides of the regenerator are known. By adopting an initial value of temperature at the outlet of the hot side of the regenerator, the whole conditions of the regenerator can be determined by using the equations described in section 4.2.4. The pinch point value is checked and the initial value considered at the outlet of the hot side is iteratively modified till the convergence of the pinch point is reached.

After the performance of the regenerator is computed, both sides outlets of the regenerator are known. Therefore, the inlet conditions of the evaporator (cold side) and the inlet conditions of the condenser (hot side) are determined.

When taking the inlet conditions of the condenser, with the equations described in the section 4.2.5, the mass flow and outlet temperature of the cooling fluid are completely determined.

Finally, the performance of the evaporator has to be evaluated. The mass flow and temperature of the hot source are known, as the hot source is the flue gases exiting the mGT at nominal conditions. As the inlet conditions of the evaporator are known after evaluating the regenerator, with the equations described in section 4.2.3, the performance of the evaporator can be established. Once they are determined, the pinch point is calculated. If it is the one imposed at the design, the cycle is completely determined, if not, the value of mass flow of working fluid adopted at the beginning will be modified till the convergence is reached.

It has to be remarked that following the procedure here mentioned, the performance of the cycle is computed. However, this performance changes when modifying the three optimization parameters, allowing the maximization of the net power produced (computed with Eq. 107).

$$P_{net,ORC} = P_{turb,ORC} - P_{pump,ORC} - P_{pump,water} \qquad \text{Eq. 107}$$

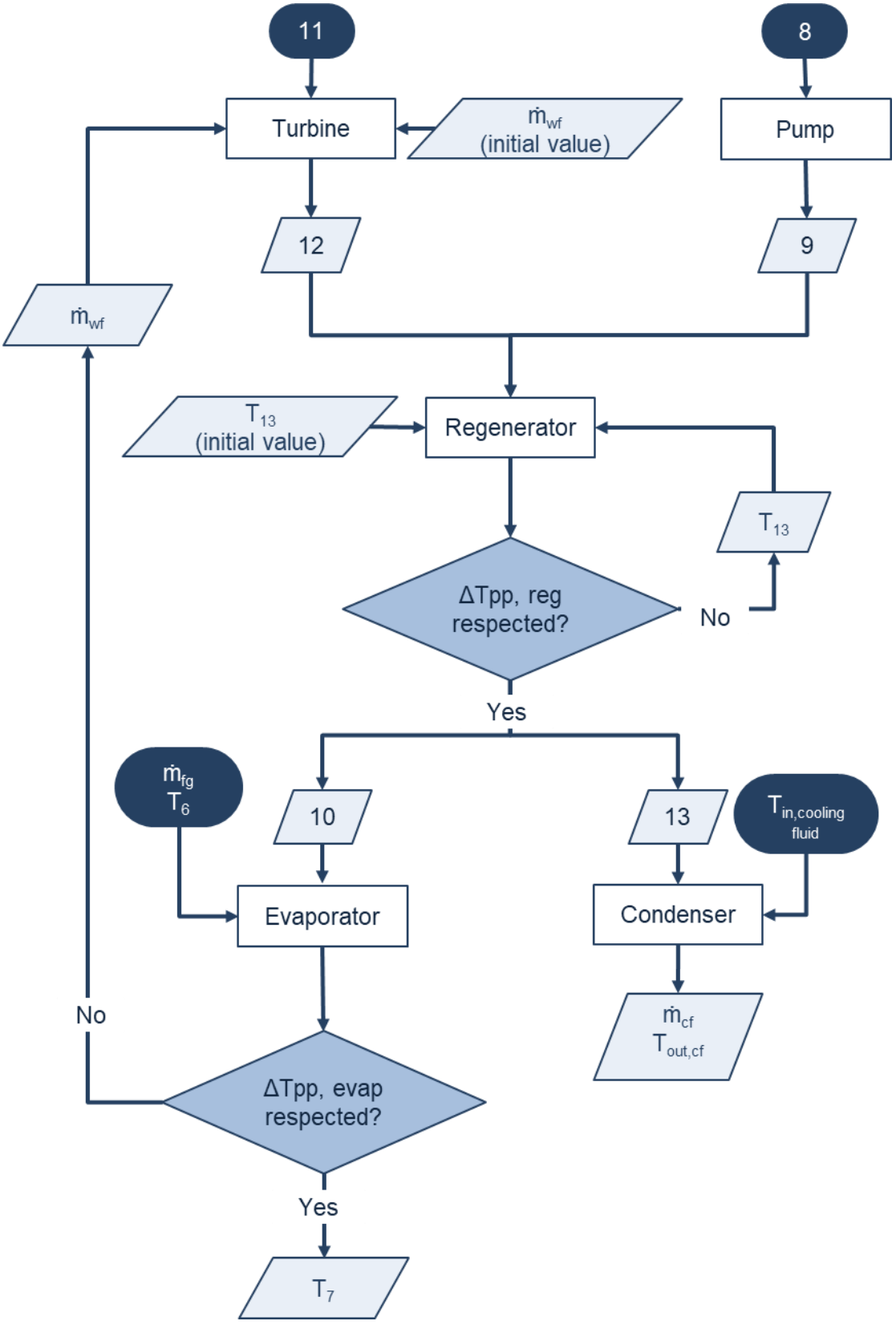

Figure 4.2-5 Extended procedure of the sizing of the ORC

4.3. Off-design modeling

As the performance of the mGT changes with the ambient temperature and the electric power requested, the temperature and mass flow of the flue gases exiting the mGT change, thus, the thermal input to the ORC varies. Therefore, it is necessary not only dimensioning the ORC, but also studying its part load operation, as during the real operation the conditions change.

A tailored-made model has been developed in Matlab® taking into consideration the nominal performance obtained after the optimization of the cycle and the set of non-linear equations that characterizes the whole ORC system.

Table 4.3-1 collects the thermodynamic properties at initial conditions.

Table 4.3-1 Thermodynamic properties at initial conditions of the ORC

Fluid	N. stream	Description	Mass flow	Temperature	Pressure	Quality
Organic fluid	8	in,pump/ out,cond	✗		✓	✓
	9	in,reg cold/out,pump		✗	✗	
	10	in,evap/out reg cold		✗	✗	
	11	in,turb/out,evap		✓	✗	
	12	in,reg hot/out,turb		✗	✗	
	13	in,cond/out,reg hot		✗	✗	
Flue gases	6	in,evap hot	✓	✓	✓	
	7	out, evap hot		✗	✓	
Water		in,cond cold	✗	✓	✓	
		out,cond cold		✗	✗	

There are three different fluids also in this case: the organic fluid, the flue gases exiting the mGT and the cooling fluid. Differently from the mGT model, the composition of all of them is known beforehand. Regarding to other thermodynamic properties, once the ambient temperature and rotational speed of the mGT are imposed, with the model evaluating the part load performance of the micro gas turbine, the flue gases conditions are determined, thus, the hot source of the ORC. Moreover, the maximum temperature of the cycle is imposed as it is a variable that will be controlled in the dynamic system. In order to maximize the efficiency of the cycle, the maximum temperature has been fixed at the nominal value when feasible

[69]. However, when the system is far away from nominal conditions and the temperature and the mass flow of flue gases decrease, it may happen that keeping the same maximum value of temperature is not feasible, therefore, it will be iteratively reduced till reaching feasible conditions. In addition, another parameter is fixed, which can be either the mass flow of cooling fluid or the condensing pressure. If the mass flow of cooling fluid is fixed to the nominal value, then the condensing pressure will vary. If the condensing pressure is fixed, then the mass flow of cooling fluid will be varied to reach the imposed pressure (case shown in Table 4.3-1). Both cases are implemented on the model, giving the possibility to analyze the differences between both of them.

After the imposition of the maximum temperature of the ORC fluid and the condensing pressure or mass flow rate of cooling fluid, there are 14 unknowns to solve the part load of the ORC. Table 4.3-2 collects the 14 equations to solve the system.

Table 4.3-2 Equations defining the part load model of the ORC

Components	Nº equations	Description
Condenser	4	Heat transfer equation Energy balance Pressure drop (hot side) Pressure drop (cold side)
Pump	1	Compression
Regenerator	4	Heat transfer equation Energy balance Pressure drop (hot side) Pressure drop (cold side)
Evaporator	3	Heat transfer equation Energy balance Pressure drop (cold side)
Turbine	2	Turbine maps Polytrophic expansion
Total components equations	14	

Most of the equations described in the table, are described in the sections from 4.2.1 to 4.2.5. However, in this case, the pressure drops are not the nominal ones, but taking the nominal pressure drop as reference, they depend on the variation of the velocity of the fluid. Thus, for each component, the new pressure drop can be

determined by Eq. 108 using the nominal values and the new ones of mass flow rate and density [24]

$$\Delta p_{off} = \Delta p_{nom} \left(\frac{\dot{m}_{off}}{\dot{m}_{nom}}\right)^2 \left(\frac{\rho_{nom}}{\rho_{off}}\right) \quad \text{Eq. 108}$$

Another characteristic equation of the part load behavior is the one describing how the convective heat transfer varies with the process conditions with respect to the nominal ones. Once the heat exchangers have been dimensioned with Aspen Exchanger Design & Rating®, different simulations have been performed with that software modifying the mass flows of the different fluids, so at part load conditions. The off-design coefficients (α) are computed for each coefficient involved in the study, so the new heat transfer coefficients can be computed using Eq. 109.

$$\gamma = \gamma_{nom} \left(\frac{\dot{m}}{\dot{m}_{nom}}\right)^{\alpha} \quad \text{Eq. 109}$$

After computing the new convective heat transfer coefficients, the global heat transfer coefficients can be calculated at part load conditions with the same equations described in 4.2.3, 4.2.4 and 4.2.5.

Regarding to the part load behavior of the turbine, it has not been considered a constant efficiency. Some works describe the part load of the turbine considering the geometry of it and evaluating the losses [70], [77]. However, the way the turbine has been dimensioned does not consider the size of each component, but the way it behaves. Therefore, performance maps have been considered [78]–[82] based on similitude theory. The performance maps (Figure 4.3-1) represent two functions which correlates the reduced flow coefficient (Eq. 110) with the reduced head coefficient (Eq. 111) and the turbine efficiency with the reduced head coefficient for different values of reduced rotational speed (Eq. 112). The reduced flow coefficient depends on the mass flow ($\dot{m}$) and density (ρ) and speed of sound (a) at chocked conditions, the reduced head coefficient depends on the isentropic enthalpy difference (Δh_{iso}) and the speed of sound of the fluid at chocked conditions and the reduced rotational speed (N_{red}) depends on the rotational speed and the speed of sound of the fluid at chocked conditions. All the parameters can be computed at nominal conditions; therefore, the dimensional performance maps can be obtained for different designs and fluids.

$$Reduced\ flow\ coefficient = \frac{\dot{m}}{\rho^* a^*} \quad \text{Eq. 110}$$

$$Reduced\ head\ coefficient = \frac{\Delta h_{iso}}{a^{*2}}$$ Eq. 111

$$N_{red} = \frac{N}{a^*}$$ Eq. 112

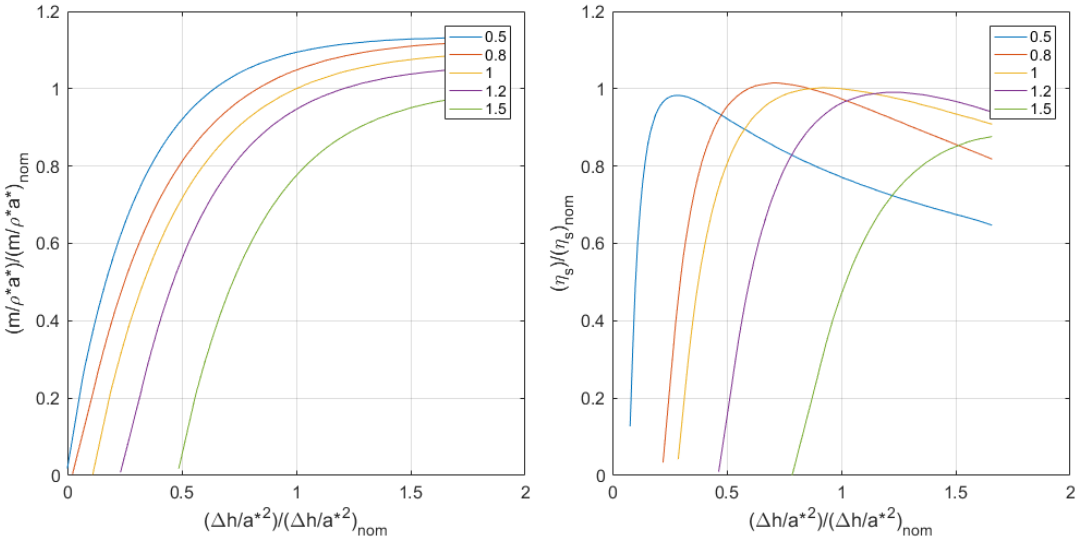

Figure 4.3-1 Dimensionless performance maps of the ORC turbine: reduced flow coefficient (left) and efficiency (right) with respect to the reduced head coefficient at different values of dimensionless reduced rotational speed with respect to the nominal one

The part load model is more complicated to solve than the sizing one. This is due to the highly dependence of the partial behavior on the thermodynamic properties at those conditions (i.e. pressure drop with mass flow and temperature, convective heat transfer coefficients with the circulating mass flow and the behavior of the turbine with the circulating mass flow too). Thus, the system is highly non-linear. The model implemented solves the mass and energy balances with the solver algorithm of Matlab® modifying the variables indicated in Figure 4.3-2 till reaching the convergence. The part load simulations consider as inputs the mass flow and temperature of the flue gases exiting the micro gas turbine resulted after studying the part load of it when the ambient temperature and rotational speed is modified.

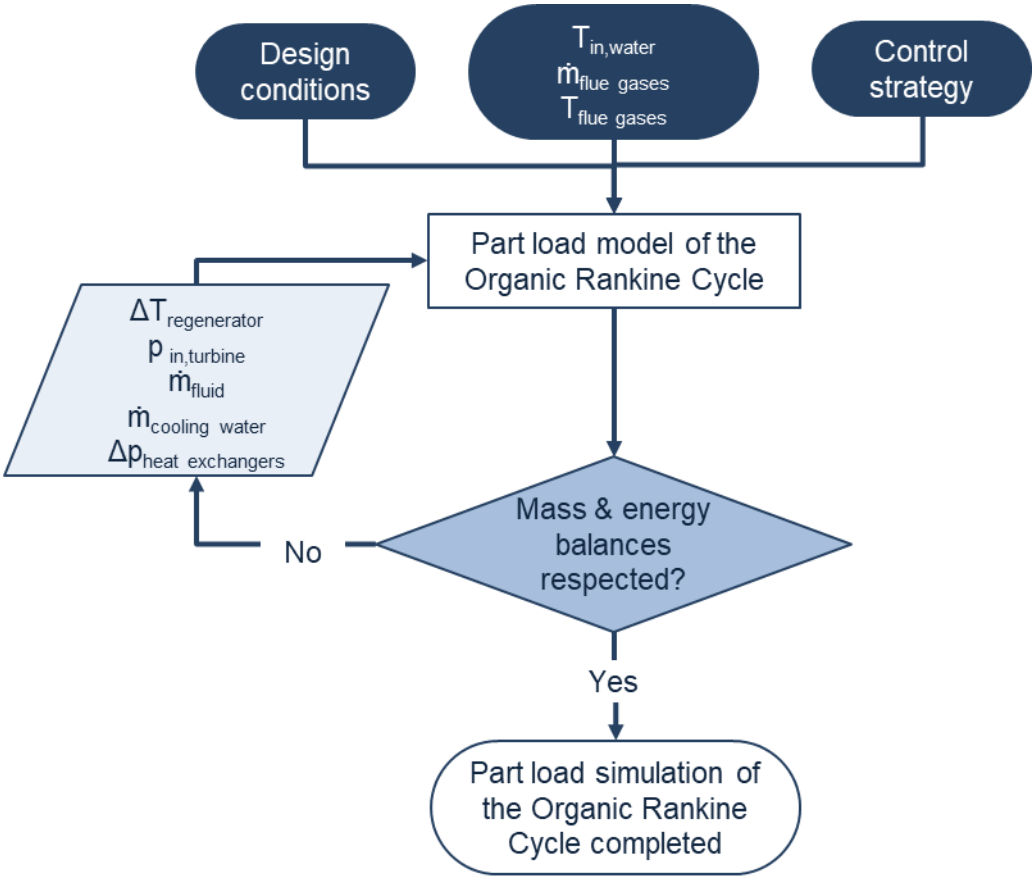

Figure 4.3-2 General algorithm for the off-design model of the ORC

4.4. Dimensioning of the heat exchangers

Plate fin heat exchangers are characterized by a large heat transfer surface in a compact volume. The fins increment additionally the surface with respect to normal plate heat exchangers, improving the heat transfer between both sides. The fluid flows in the passages created by the two plates where the fins are inserted. There are different types of fins available for this type of heat exchanger, namely plain fins, offset strip fins and louvered films. Usually, the louvered fins are used for air flows, but when single and two-phase applications are considered, the fins used are either plain or offset strip ones [83].

Initially, these compact heat exchangers were developed for the aerospace industry due to the large area of heat transfer with low weight and volume. However, plate fin heat exchangers are getting more attention also in the industry thanks to their compactness and high performance [84]. Moreover, they are suitable for small scale ORC modules [44]. Their proper suitability for waste heat recovery from an engine with an organic fluid changing phase as well as for the rest of the heat exchangers of

the ORC cycle (i.e. condenser and regenerator) has been demonstrated experimentally [85], [86].

Some works can be found in literature aiming to optimize the dimensioning and performance of this type of heat exchangers [87]–[91]. However, for the sizing of all the heat exchangers of the ORC module, it has been decided to use Aspen Exchanger Design & Rating®. Once the nominal process conditions are known after performing the design of the ORC system and the optimal fluid has been selected, all the parameters needed to perform the sizing are determined.

In order to perform the sizing, the process conditions are taken as inputs for the sizing. In addition, the maximum values of pressure drop are established and the counter-current configuration has been selected. The optimal sizing is performed by the software by modifying the different parameters defining the geometry (e.g. length, type of fins, number of fins, distributors). The output is the proper sizing of the heat exchanger with all the thermodynamic properties of both streams with the specification of the convective heat transfer coefficients and fin efficiency. Therefore, it can be evaluated how the convective heat transfer coefficient varies according to the conditions of the fluid along the heat exchanger.

Moreover, after sizing the heat exchangers, the part load is studied keeping the obtained geometry and modifying first the mass flow of the hot fluid and then, the mass flow of the cold fluid. By performing these simulations, a correlation between the effective heat transfer coefficient (thus the convective heat transfer coefficient affected by the fin efficiency) and the mass flow is obtained (Eq. 109). The results of the obtained geometries for the three heat exchangers are described in Chapter 6. , while the results correlating the part load effective heat transfer coefficients with the mass flow rates are shown in section 6.3.1.

Chapter 5. Dynamics

The life is dynamic, but sometimes, steady-state conditions are needed to get perspective.

5.1. Introduction

This chapter describes the way the dynamics of the system has been studied, by defining the power system and afterwards, by implementing the preliminary control system.

First, a description of the language used for the modeling (i.e. Modelica) is done. Second, the characteristic equations of each component and the relevant assumptions to model them are presented. Third, the way each component is connected to form the power system is described. And fourth, all the considerations adopted to implement a simple control system are specified.

5.2. Modelica language

The platform used to model and perform the dynamic simulations is Dymola, which uses the Modelica language. The Modelica language is an object-oriented language originated to model physical systems considering the algebraic and differential equations describing the system. The main features which describe the characteristics of the language are mentioned in this section [92], [93].

The Modelica language is a-casual. This means that the physical model is described by the set of equations without specifying how they have to be solved. In addition, the boundary conditions are not necessarily declared a-priori. Therefore, modules can be created with the set of equations describing the system and the modules can be connected if compatible connectors are implemented. It allows a great flexibility and the possibility of communicating among different models.

Moreover, it is based on the concept of transparency, allowing the modeler to see all the equations, even those implemented in other libraries by other people, giving the possibility to analyze how other people have modeled the component and decide whether to use it or modify it according to the specific requirements.

In addition, the models can be formed by different submodels, having a hierarchical structure. It allows creating complex models starting from simple ones. Moreover, different complex models can be defined using the same basis describing the component (e.g. valves, pumps, compressors).

Furthermore, it can be connected to other software (i.e. CoolProp and Refprop) to evaluate the properties of the fluids through the ExternalMedia library [94].

Finally, it has to be said that all these characteristics lead to the reusability of the models. Different systems can be modeled and studied by connecting different components.

5.3. Components modeling

In this section, the way the components have been modeled is described, starting from the equations characterizing the performance of a one-dimensional flow model, continuing with the components themselves, and finally, explaining the modeling of the overall system.

5.3.1. Conservation equations

The mass conservation principle states that the variation of the mass inside a control volume is equal to the mass flux entering that volume minus the mass flux exiting that volume. By calling V the control volume and S the surface of the control volume exchanging mass with the exterior, the mass conservation equation for a compressible fluid can be written as expressed in Eq. 113.

$$\frac{d}{dt}\int_V \rho\, dV + \int_S \rho(\overline{v}\cdot\overline{n})\, dS = 0 \qquad \text{Eq. 113}$$

The first integral represents the net variation of mass contained inside V during time. According to the finite volume method, even if it is a compressible fluid, the density is assumed to be constant along the control volume. Considering that the control volume does not change with the time and the density evaluated in the cell centre, the first term of Eq. 113 can be written as:

$$\frac{d}{dt}\int_V \rho\, dV \cong V\frac{d\overline{\rho}}{dt} \qquad \text{Eq. 114}$$

Considering that it is necessary to express the fluid property terms as a function of the state variables variations to reduce the complexity of the problem and the number of variables to be solved, the variation of density with time can be approximated to:

$$\overline{\rho} = \rho\left(\overline{h},\overline{p}\right) \quad \rightarrow \quad \frac{d\overline{\rho}}{dt} = \frac{\partial\overline{\rho}}{\partial\overline{h}}\frac{d\overline{h}}{dt} + \frac{\partial\overline{\rho}}{\partial\overline{p}}\frac{d\overline{p}}{dt} \qquad \text{Eq. 115}$$

Therefore, the first term of the mass conservation equation can be written as:

$$\frac{d}{dt}\int_V \rho\, dV \cong V\left(\frac{\partial\overline{\rho}}{\partial\overline{h}}\frac{d\overline{h}}{dt}+\frac{\partial\overline{\rho}}{\partial\overline{p}}\frac{d\overline{p}}{dt}\right) \quad \text{Eq. 116}$$

The second term of the Eq. 113 represents the net mass flux through the boundaries of the control volume exchanging mass. By separating the inlet and outlet mass fluxes, it could be written as:

$$\int_S \rho(\overline{v}\cdot\overline{n})\, dS = \dot{m}_{in} - \dot{m}_{out} \quad \text{Eq. 117}$$

By substituting the terms of Eq. 113 with the expressions obtained in Eq. 115 and Eq. 117, the mass conservation equation for a defined control volume V considering one-dimensional flow can be expressed as shown in Eq. 118.

$$V\left(\frac{\partial\overline{\rho}}{\partial\overline{h}}\frac{d\overline{h}}{dt}+\frac{\partial\overline{\rho}}{\partial\overline{p}}\frac{d\overline{p}}{dt}\right) = \dot{m}_{in} - \dot{m}_{out} \quad \text{Eq. 118}$$

The energy conservation equation states that the total energy of a system is conserved, so the only way that the amount of energy could vary is by crossing the boundaries of the system. For an open control volume, there are three terms involved on exchanging energy: heat transfer through the boundaries, work done on or by the system and mass fluxes entering or exiting the system carrying the associated energy. Considering that in a pipe the work is equal to zero and the variations of kinetic and potential energy are neglected because they are small compared to static enthalpy variation, the energy balance can be expressed as stated in Eq. 119.

$$\frac{d}{dt}\int_V \rho u\, dV = \dot{m}_{in}h_{in} - \dot{m}_{out}h_{out} + \dot{Q}^{\leftarrow} \quad \text{Eq. 119}$$

The first integral represents the variation of energy inside the adopted control volume during time. According to the finite volume method, average values can be adopted for each control volume. Moreover, the volume does not change in time. Therefore, the first term of the energy balance can be written as:

$$\frac{d}{dt}\int_V \rho u\, dV \cong V\frac{d(\overline{\rho u})}{dt} = V\left(\overline{\rho}\,\frac{d\overline{u}}{dt}+\overline{u}\,\frac{d\overline{\rho}}{dt}\right) \quad \text{Eq. 120}$$

As the variation of density is less influent in comparison to the variation of the internal energy, it can be neglected. So by substituting the result of Eq. 120 in Eq. 119, the energy balance equation can be written as:

$$\overline{\rho}V\frac{d\overline{u}}{dt} = \dot{m}_{in}h_{in} - \dot{m}_{out}h_{out} + \dot{Q}^{\leftarrow} \qquad \text{Eq. 121}$$

For resolution purposes, the variation of internal energy (*u*) should be expressed in terms of the state variables of the system (i.e. enthalpy and pressure):

$$u = h - \frac{p}{\rho} \qquad \text{Eq. 122}$$

The energy balance can be finally expressed as:

$$\overline{\rho}V\frac{d\overline{h}}{dt} = \dot{m}_{in}h_{in} - \dot{m}_{out}h_{out} + \dot{Q}^{\leftarrow} + V\frac{dp}{dt} \qquad \text{Eq. 123}$$

Where the heat transfer through the boundaries can be written considering the Newton's law as:

$$\dot{Q}^{\leftarrow} = \gamma A(T_{wall} - T) \qquad \text{Eq. 124}$$

In order to be coherent with the steady-state off-design model, the convective heat transfer coefficient is computed considering the nominal one and the variation of the mass flow rate with respect to the nominal conditions considering an exponential coefficient:

$$\gamma = \gamma_{nom} \cdot \left(\frac{\dot{m}}{\dot{m}_{nom}}\right)^{\alpha} \qquad \text{Eq. 125}$$

Both the mass and energy balances constitute the behaviour of the fluid flowing. In the next sections, the models of each component are described.

5.3.2. Sink and sources

In order to impose the boundary conditions for the flow streams, the models sink and source of the ThermoPower library are used [95]. There are two types of sink and source models implemented: pressure boundaries and mass flow rate boundaries.

The source models impose either the pressure or the mass flow rate (depending on the selected model) and the temperature (or enthalpy) of the upstream fluid of a component as inlet boundary conditions.

The sink models just set either the pressure or the mass flow rate (according to the selected model). In this case, the temperature (or enthalpy) is an output of the simulations.

5.3.3. Pressure drops

The dynamic momentum equation has been neglected in all the components, but the variations of the pressure along the pipe and components of the cycle have been computed with a specific component representing the pressure drop.

The pressure drops can be classified in two categories: distributed (as a consequence of friction with the walls) and concentrated (as a consequence of discontinuities in the pipes) pressure drops, depending both of them on the velocity of the fluid and the density (see Eq. 126).

$$\Delta p = \begin{cases} f \dfrac{L}{D} \rho \dfrac{v^2}{2} & (distributed) \\ K_c \rho \dfrac{v^2}{2} & (concentrated) \end{cases} \qquad \text{Eq. 126}$$

In the calculation of the distributed pressure drops appears the dependence on the friction factor (f), the hydraulic diameter (D) and the pipe length (L); while the concentrated pressure drop depends on the concentrated coefficient (K_c)

In both cases, there is a dependence of the pressure drop on the velocity that could be expressed as a dependence of the pressure drop with the mass flow rate:

$$\Delta p \sim \rho v^2 \sim \frac{\dot{m}^2}{\rho} \qquad \text{Eq. 127}$$

Considering that the nominal conditions are known, the pressure drops of the components are computed with respect to the nominal values.

$$K_{nom} = \Delta p_{nom} \frac{\rho_{nom}}{\dot{m}_{nom}^2} \qquad \text{Eq. 128}$$

$$\Delta p = K_{nom} \frac{\dot{m}^2}{\rho} \qquad \text{Eq. 129}$$

Across the component, an isenthalpic process has been considered, as the purpose of this model is just to represent the pressure drops. This model was taken completely from the library ThermoPower [96].

5.3.4. Turbomachinery

The dynamics of the turbomachinery is much faster than the thermal dynamics of the heat exchangers. As the main objective of this work is to study the dynamics of the overall system, the influence of the transients of the turbomachinery can be neglected in comparison to the rest of the components. Therefore, the behavior of the turbomachinery (i.e. turbine, compressor, pump) is described by steady-state equations [92], [97], [98].

The equations defining each component are described considering the mass and energy balances and the characteristic maps of the turbomachinery. The reader should refer to section 3.2.5 for the equations characterizing the turbine of the mGT; 3.2.2, for the characterization of the mGT compressor; 4.2.1, for the description of the ORC radial-inflow turbine. As the dynamics of the pump is also very fast, the way it has been modeled is considering that it can be designed as a variable speed pump, giving the required mass flow rate of ORC working fluid. Therefore, a further step has been considered in the modeling by imposing directly the mass flow rate; as the design of the pump is out of the scope of this thesis, it does not affect the dynamic of the system. In order to compute the consumption of the pump, the enthalpy difference has been computed and constant efficiencies have been assumed.

5.3.5. Combustion chamber

The combustion chamber model is based on the base model available in the library ThermoPower describing the combustion chamber [95], [96].

It is assumed that the metal wall temperature and the heat transfer coefficient between the wall and the fluid are uniform. The wall is thermally insulated from the outside. It has been assumed that inlet gases are premixed before entering in the volume. The original model considers that the fuel is composed just by methane, carbon dioxide and nitrogen. An extension of this model has been made considering the actual composition of the fuel entering the combustion chamber (CH_4, CO_2, C_2H_6, C_3H_8, C_4H_{10}, N_2). The reactions that take place are:

$$CH_4 + 2\,O_2 \rightarrow CO_2 + 2\,H_2O \qquad \text{Eq. 130}$$

$$C_2H_6 + \frac{7}{2}\,O_2 \rightarrow 2\,CO_2 + 3\,H_2O \qquad \text{Eq. 131}$$

$$C_3H_8 + 5\,O_2 \rightarrow 3\,CO_2 + 4\,H_2O \qquad \text{Eq. 132}$$

$$C_4H_{10} + \frac{13}{2}\,O_2 \rightarrow 4\,CO_2 + 5\,H_2O \qquad \text{Eq. 133}$$

The variation of mass of each component (M_i) during time considers the amount of that component entering the combustion chamber both with the air and the fuel, the amount which is exiting and the production of consumption [99].

$$\frac{dM_i}{dt} = \dot{m}_{air}y_{i,air} + \dot{m}_{fuel}y_{i,fuel} - \dot{m}_{flue}y_{i,flue} + \nu_i\frac{\dot{m}_{fuel}}{MM_{fuel}}MM_i \qquad \text{Eq. 134}$$

The coefficient ν_i represents either the production or consumption coefficient, which is computed in the model according to the stoichiometric coefficients of the reactions (Eq. 25 - Eq. 133) considering the molar fraction of each component entering with the fuel.

The overall mass variation in the system could be expressed either by the sum of the variation of all the components, or considering the combustion chamber as a black box and analyzing the overall inputs and outputs to the system:

$$\frac{dM}{dt} = \dot{m}_{air} + \dot{m}_{fuel} - \dot{m}_{flue} \qquad \text{Eq. 135}$$

Considering the combustion chamber as a well-mixed reactor with uniform conditions equal to the ones exiting the combustor, the mass contained can be calculated by knowing the density of the flue gases exiting and the volume of the combustion chamber (Eq. 150).

$$M = \rho_{flue}V_{comb} \qquad \text{Eq. 136}$$

The energy accumulated in the combustion chamber (E) is equal to the total internal energy that the mass inside the combustion chamber has (Eq. 137).

$$E = Mu_{flue} \qquad \text{Eq. 137}$$

The variation of the energy accumulated in the combustion chamber considers the energy entering and exiting the combustion chamber. The thermal losses have been considered by introducing the thermal efficiency ($\eta_{comb} = 0.99$): in fact, the possibility

of directly calculating the losses is not possible, as there is no information about the geometry and materials.

$$\frac{dE}{dt} = \dot{m}_{air} h_{air} \eta_{comb} + \dot{m}_{fuel} LHV_{fuel} \eta_{comb} - \dot{m}_{flue} h_{flue} \qquad \text{Eq. 138}$$

5.3.6. Heat exchanger

All the heat exchangers have been modeled in the same way, considering the method of finite volume discretization, with the exception of the condenser of the ORC. The heat exchangers have been modeled considering basic models taken from the ThermoPower library [100].

The schematic representation with the submodels which form the evaporator is shown in Figure 5.3-1. The scheme here described of the evaporator is representative of all the heat exchangers.

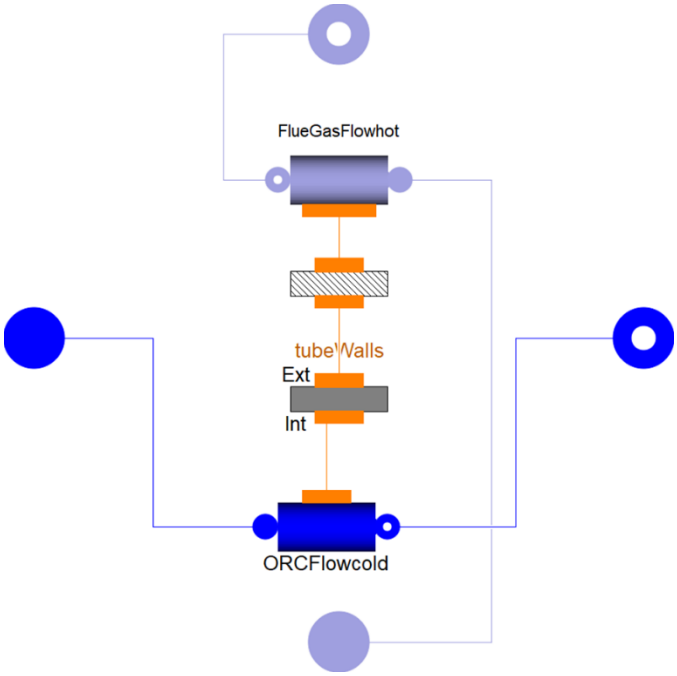

Figure 5.3-1 Model of the evaporator in Dymola

Before explaining the submodels themselves, a first description is given here. The gray icons represent the flue gases, while the blue ones, the ORC working fluid and the orange icons represent the heat ports. The lines represent the connection between the submodels, with the same colors as the description; therefore, the blue lines represent the ORC working fluid flux; the gray ones, the flue gases flux; and the orange ones, the heat flux connections. The circle shapes represent the input and output mass flux connections with the rest of the cycle. The box with the inclined lines

is the “CounterCurrentFV” model, the gray box is the “MetalTubeFV” model and the blue and grey boxes are the “Flow1DFV” model; all from the ThermoPower library. A deep explanation should be given to understand how the combination of all of these submodels can model the whole heat exchanger.

The main model describing the dynamics of the fluid inside the heat exchanger is the Flow1DFV model. It describes the flow using a finite volume discretization method (FVM). This approach considers that the flow path is divided into different control volumes with uniform state properties along the control volume. Each of these volumes is governed by fundamental equations and influenced by upstream, downstream, and lateral elements (in terms of heat exchange through lateral boundaries). Results are improved as the number of discretisation is increased, at cost of more computation expenditure.

For each control volume of the discretization, the thermodynamic conditions are computed and the mass and energy balances described in Eq. 118 and Eq. 123 in the section 5.3.1 are implemented in the model. Even if the momentum equation is implemented in the model Flow1DFV, it has been neglected for the simulations. However, the pressure drops have been considered in the whole system (with the model described in the section 5.3.3 and the implementation is shown in Figure 5.3-2 and Figure 5.3-4). This assumption helps the numerical stability of the system while simulating, without decreasing significantly the dynamic performance of the whole power plant.

After explaining how the dynamics of the fluid are modelled with the submodel Flow1DFV, the way the energy is transferred and accumulated in the solid walls is considered with the MetalTubeFV model. This component models the behavior of a metal tube wall in terms of energy accumulation and thermal resistance to heat transfer processes through the wall itself.

The MetalTubeFV model also uses the FVM; therefore, it is discretized in the same number of discretization elements as the Flow1DFV. For each control volume, the wall average temperature T_w is evaluated with Eq. 139.

$$\rho_{wall} c_{wall} V \frac{dT_{wall}}{dt} = \dot{Q}_{int}^{\leftarrow} + \dot{Q}_{ext}^{\leftarrow} \qquad \text{Eq. 139}$$

The energy balance considers the density (ρ_{wall}) and specific heat capacity (c_{wall}) of the wall. As well as the thermal power exchanged through the internal ($\dot{Q}_{int}^{\leftarrow}$)and external ($\dot{Q}_{ext}^{\leftarrow}$) ports (assuming positive if it enters the component).

Finally, the last and easiest submodel is the CounterCurrentFV model. It is just a mathematical component that has the task of connecting in the right way the control

volumes of the two physical models. When connecting two thermal ports, Modelica automatically connects components having the same index in a co-current configuration. Hence, to model a counter-current configuration, it is necessary to insert an additional mathematical component that writes down the equations arising from a thermal connection switching the indexes of one of the components.

As stated at the beginning of this section, all the heat exchangers are modeled with the approach here indicated with the exception of the condenser of the ORC. The approach considered to model the condenser assumes that it works at constant pressure, the model “PrescribedPressureCondenser” from the ThermoPower library has been used. This model acts as a sink of constant pressure. This approach is a typical one to model the condenser as the low values of pressure in a condenser, modeled in the same way as explained with the evaporator, may deal to numerical instabilities [98]. In addition, with the off-design simulations, in the studied range of operability in this work, the performance of the ORC increases by keeping the pressure constant (varying the mass flow of the cooling fluid), rather than by following a sliding pressure strategy in which the condensation pressure varies (keeping constant the mass flow of the cooling fluid) [98].

5.3.7. Technologies scheme

In this section, the way the components have been connected together to form both power systems (i.e. mGT and ORC) is depicted.

In Figure 5.3-2 is shown the scheme of the mGT while in Figure 5.3-4 is shown the scheme of the ORC.

The components which constitute the mGT are shown in Figure 5.3-3. The overall scheme of the mGT has three inputs (namely the fuel mass flow rate, the ambient temperature and the rotational speed of the turbomachinery) which are given from outside of the model; and two outputs (namely the electric power produced by the system and the TOT).

While the components which constitute the ORC are shown in Figure 5.3-5. The overall scheme of the ORC has two inputs (i.e. the mass flow rate of the ORC working fluid and the hot flue gases coming from the mGT) coming from the outside of the system and two outputs (namely the net electric power produced by ORC module and the TIT).

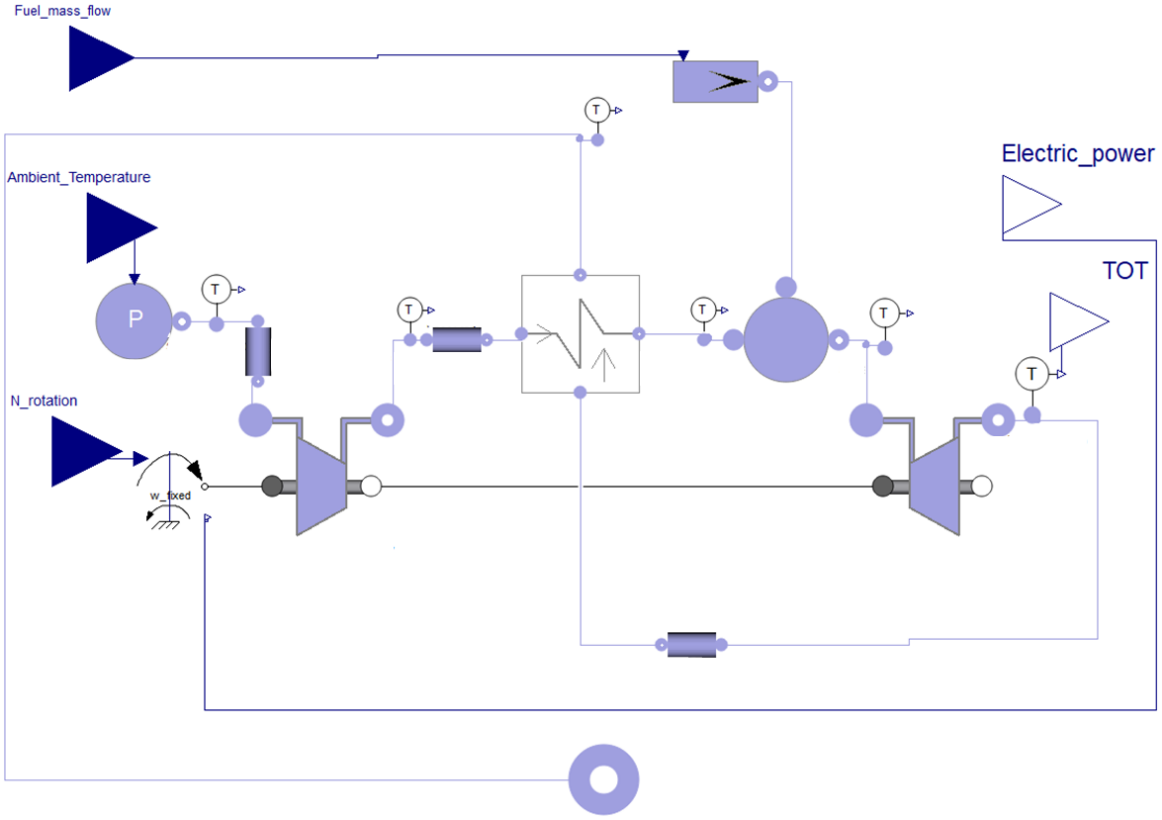

Figure 5.3-2 mGT layout in Dymola

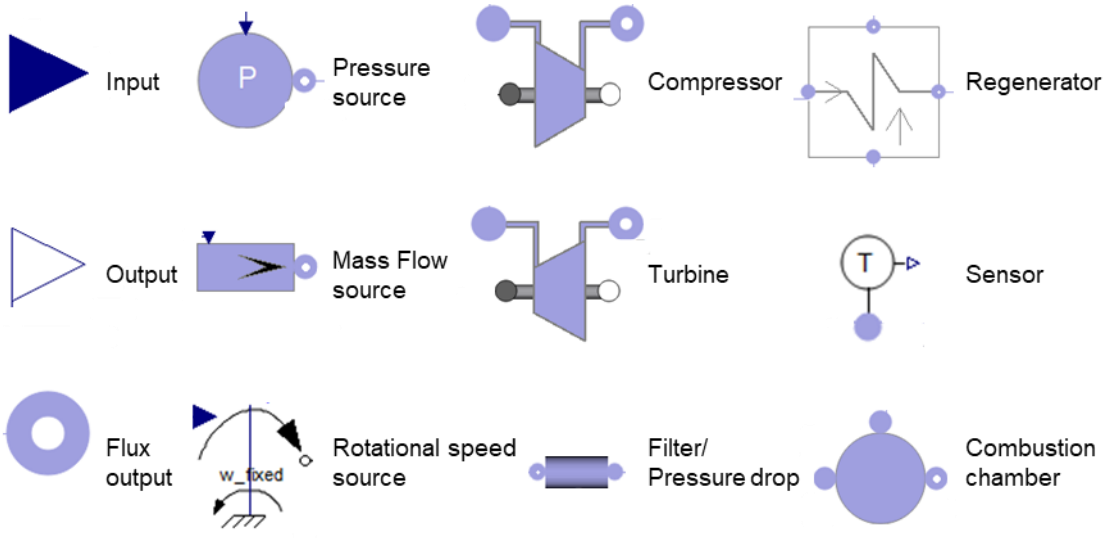

Figure 5.3-3 Representation of the mGT components in Dymola

An explanation of Figure 5.3-2 is given here. The pressure source represents the environment, in which the pressure is fixed (ambient pressure is considered as a constant along the whole day) and the temperature is given from an external input as

it varies continuously, the air mass flow entering the system is determined according to the characteristic maps of the turbomachinery. Then the air enters the filter and afterwards, the compressor. The pressure drops of the cold side of the regenerator and combustion chamber are concentrated in the module pressure drop between the compressor and the regenerator to simplify the convergence of the simulations. After being preheated in the regenerator, the air reacts with the fuel entering through the mass flow source in the combustion chamber. The flue gases are expanded and then, they preheat the air exiting the compressor in the regenerator. Also in this case, the pressure drops of the regenerator are concentrated and evaluated before entering the regenerator. The exit of the regenerator ends on a flux output which will be connected to the flux input in the ORC module. The rotational speed of the turbomachinery is always imposed through the rotational speed source module.

After seeing the components forming the mGT, the ORC module is shown in Figure 5.3-4.

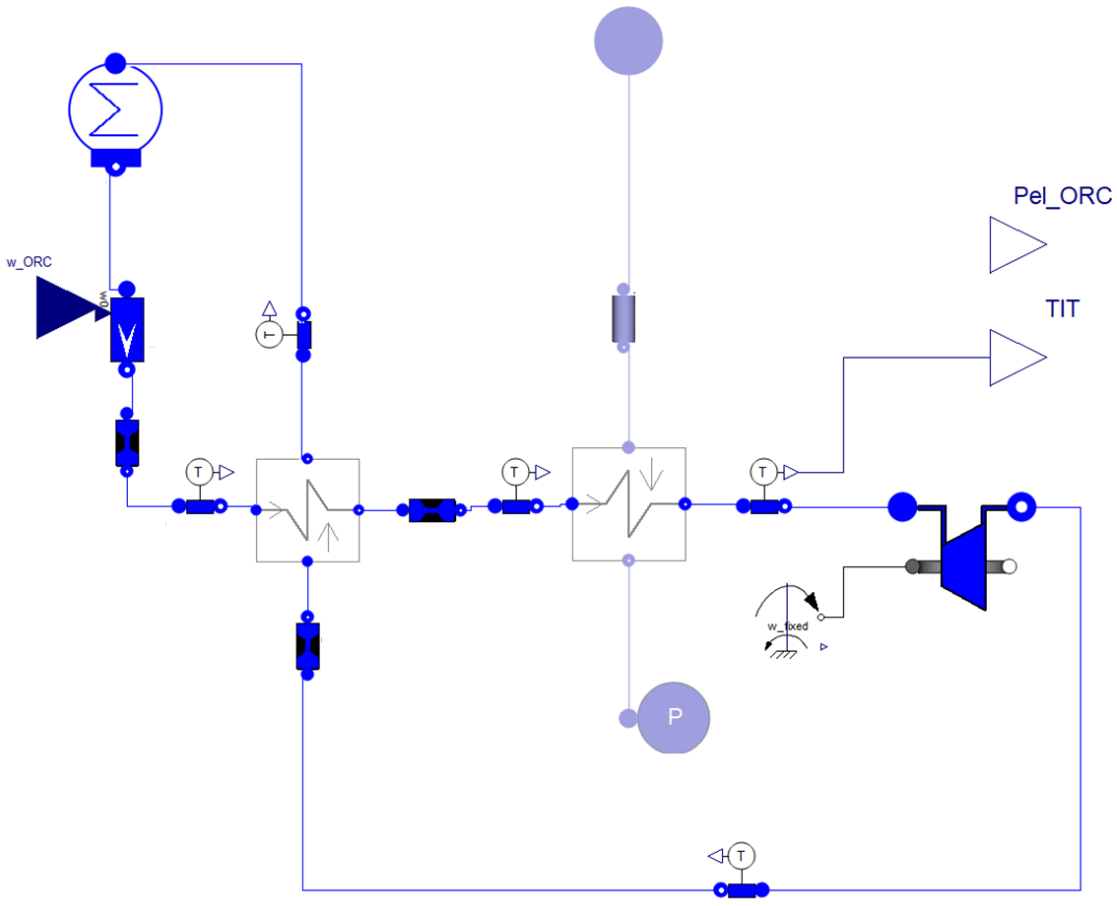

Figure 5.3-4 ORC layout in Dymola

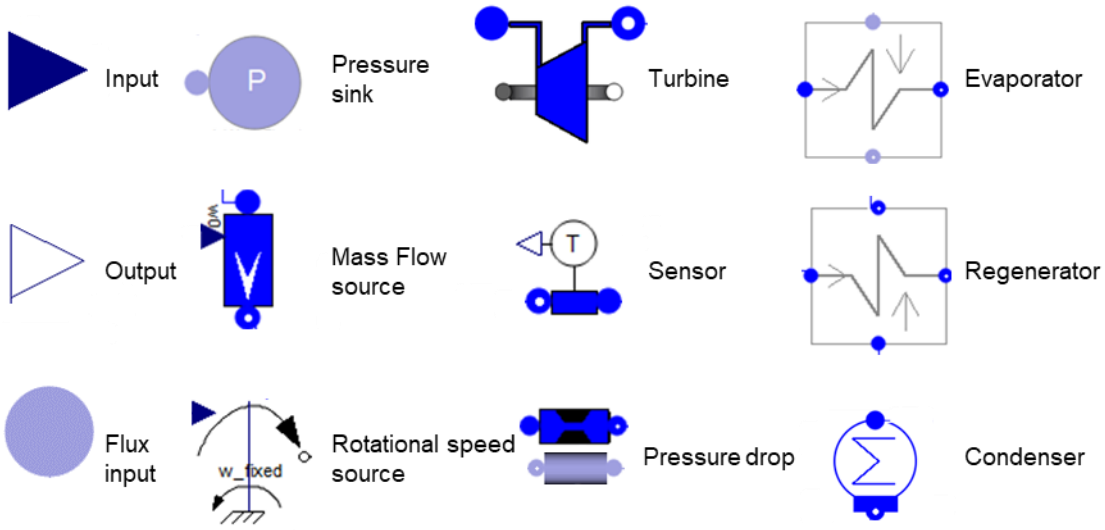

Figure 5.3-5 Representation of the ORC components in Dymola

As it has been done with the mGT, here, an explanation of the ORC module is done. The heat input to the system comes with the flux input (which is connected to the flux output of the mGT). The pressure drops of the evaporator are concentrated before it, and then the flue gases enter the evaporator to heat up the ORC working fluid till the maximum temperature. The ambient in which the flue gases are discharged is modeled with the pressure sink, by fixing the ambient pressure. If the focus stands on the ORC working fluid, it is heated up in the primary heat exchanger till the maximum temperature and then it is expanded in the turbine which rotates at the nominal rotational speed imposed with the module “Rotational speed source”. The pressure drops of the working fluid across the regenerator and the condenser are concentrated in the module “Pressure drop”. The hot fluid exiting the turbine enters the regenerator to preheat the fluid before entering the evaporator. Afterwards, the fluid is condensed in a condenser working at constant pressure. Then the module mass flow source imposes the ORC working fluid mass flow rate flowing in the system.

5.4. Control system design

After explaining the way the system mGT+ORC has been modeled, in this section of the chapter, the control system design and the considerations taken into account for its modeling are described. The main focus of this part is to design a control system which allows the system formed by the mGT+ORC to follow the electricity demand while keeping the mGT turbine outlet temperature and the ORC turbine inlet temperature at the values guaranteeing the performance dictated in the steady-state part (i.e. mGT TOT equal to 645°C and ORC TIT equal to the design one or to a lower one if the thermal load to the ORC is really low).

5.4.1. Basis of the control system

A control system has an input, a process and an output. Two types of control system can be found: open-loop and closed-loop. Open-loop systems modify the input entering the system without monitoring the output response; while closed-loop systems modify the input monitoring the response of the output and analyzing whether the output is the desired or not, correcting the differences. Therefore, the closed-loop systems correct possible disturbances of the system and guarantee the output response.

The main objectives of a control system are three: reducing the steady-state errors from the desired response of the output, producing the desired transient response and achieving stability [101].

5.4.2. Linearization of the system

In order to proceed with the design of the control system, it is more convenient to work in the frequency domain rather than the time domain as working in the frequency domain provides stability and transient response information. Therefore, from the time variant equations, the transfer functions using the Laplace transformations have to be obtained. As drawback of working in the frequency domain, it can only be applied to linear, time-invariant systems [101]–[104].

The dynamic model which has been performed in this work is characterized by non-linear equations. A generic time-invariant dynamic system can be described by non-linear differential equations derived from first-principle laws as seen in the sections before (i.e. mass, energy and momentum balances). Generally, it can be expressed in the state-space[3] as:

$$\begin{cases} \dot{x} = f(x(t), u(t)) \\ y = g(x(t), u(t)) \end{cases} \qquad \text{Eq. 140}$$

Where $x \in \mathbb{R}^n$ is the state variables vector, $u \in \mathbb{R}^m$ is the inputs vector and $y \in \mathbb{R}^p$ is the outputs vector. Considering that linear multivariable control has been selected to design the control system, the time-dependent non-linear system should be linearized around a certain equilibrium point. For control purposes, it is needed to move from the time domain towards the frequency domain; thus, a linear system is needed. A linear system possesses two important properties for the control: superposition and homogeneity. The property of superposition means that the output

[3] The state-space approach is a unified method for modeling, analyzing and designing the systems. It consists of the first-order differential equations from which the state variables can be solved and the algebraic output equation from which all other system variables can be found.

response of a system to the different inputs is the sum of the effects that each input independently has on the output. While the property of homogeneity means that if an input is multiplied by a factor, the output will be multiplied by the same factor. To linearize the system, the nominal point and different points of off-design have been considered as equilibrium points. By using a first order Taylor's approximation, the linearized state equation and the linearized output equation can be as:

$$\begin{cases} \Delta\dot{x} = f(\bar{x},\bar{u}) + \dfrac{\partial f}{\partial x}\Delta x + \dfrac{\partial f}{\partial u}\Delta u + h.o.t \\ \bar{y} + \Delta y = g(\bar{x},\bar{u}) + \dfrac{\partial g}{\partial x}\Delta x + \dfrac{\partial g}{\partial u}\Delta u + h.o.t \end{cases} \quad \text{Eq. 141}$$

Taking into account that at the equilibrium point:

$$\begin{cases} f(\bar{x},\bar{u}) = 0 \\ \bar{y} = g(\bar{x},\bar{u}) \end{cases} \quad \text{Eq. 142}$$

If higher order terms are neglected, with Eq. 141 substituting the considerations taken at the equilibrium point shown in Eq. 142, it is obtained the linear system.

$$\begin{cases} \Delta\dot{x} = \dfrac{\partial f}{\partial x}\Delta x + \dfrac{\partial f}{\partial u}\Delta u \\ \Delta y = \dfrac{\partial g}{\partial x}\Delta x + \dfrac{\partial g}{\partial u}\Delta u \end{cases} \rightarrow \begin{cases} \Delta\dot{x} = A\Delta x + B\Delta u \\ \Delta y = C\Delta x + D\Delta u \end{cases} \quad \text{Eq. 143}$$

Where A ϵ $\mathbb{R}^{nxn}$ is the system matrix, B ϵ $\mathbb{R}^{nxm}$ is the input matrix C ϵ $\mathbb{R}^{pxm}$ is the output matrix and D ϵ $\mathbb{R}^{pxm}$ is the feedforward matrix. All of them are the Jacobian matrices evaluated at the equilibrium point.

Applying the Laplace transformation to the system shown in Eq. 143 to change from the time to the frequency domain, it is obtained:

$$\begin{cases} sX(s) = AX(s) + BU(s) \\ Y(s) = CX(s) + DU(s) \end{cases} \quad \text{Eq. 144}$$

Solving for X:

$$(sI - A)X(s) = BU(s) \quad \text{Eq. 145}$$

$$X(s) = (sI - A)^{-1}BU(s) \quad \text{Eq. 146}$$

By substituting the result of X:

$$Y(s) = C(sI - A)^{-1}BU(s) + DU(s) = [C(sI - A)^{-1}B + D]U(s) \quad \text{Eq. 147}$$

Considering that the process transfer function relates the output transfer function with the input one as shown in Eq. 148.

$$Y(s) = G(s)U(s) \quad \text{Eq. 148}$$

Figure 5.4-1 represents in a schematic way the process.

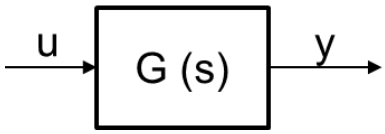

Figure 5.4-1 Graphic representation of a process

The process transfer function can be then identified in Eq. 147 as:

$$G(s) = [C(sI - A)^{-1}B + D] \quad \text{Eq. 149}$$

The matrices A,B, C and D are obtained through the “Linearize” command in Dymola. (see Appendix C to see how this command is used). Therefore, the process transfer function can be known. As the combined cycle mGT+ORC is a multiple input and multiple output (MIMO) system, particularly, it has three inputs (i.e. fuel mass flow, rotational speed of the mGT turbomachinery and ORC fluid mass flow) and three outputs (i.e. the total produced electric power, the mGT turbine outlet temperature and the ORC turbine inlet temperature), the transfer function of the process is a 3x3 matrix. In order to reduce the non-linearities of the plant when controlling it, virtual control variables have been used, instead of the values of the inputs themselves. These variables are dimensionless and they are a deviation from the variable which they are substituting with respect to their equilibrium value. Each element of the matrix is a transfer function which indicates how one of the output changes with a variation of one of the inputs. Eq. 150 shows each correlation among the inputs and outputs of the analyzed system.

$$G(s) = \begin{bmatrix} \frac{\Delta P_{el,total}(s)}{\delta \dot{m}_{fuel}(s)} & \frac{\Delta P_{el,total}(s)}{\delta N(s)} & \frac{\Delta P_{el,total}(s)}{\delta \dot{m}_{ORC}(s)} \\ \frac{\Delta T_5(s)}{\delta \dot{m}_{fuel}(s)} & \frac{\Delta T_5(s)}{\delta N(s)} & \frac{\Delta T_5(s)}{\delta \dot{m}_{ORC}(s)} \\ \frac{\Delta T_{11}(s)}{\delta \dot{m}_{fuel}(s)} & \frac{\Delta T_{11}(s)}{\delta N(s)} & \frac{\Delta T_{11}(s)}{\delta \dot{m}_{ORC}(s)} \end{bmatrix} \quad \text{Eq. 150}$$

In order to simplify the notation, Eq. 151 substitutes each of the elements of Eq. 150.

$$G(s) = \begin{bmatrix} G_{11}(s) & G_{12}(s) & G_{13}(s) \\ G_{21}(s) & G_{22}(s) & G_{23}(s) \\ G_{31}(s) & G_{32}(s) & G_{33}(s) \end{bmatrix} \qquad \text{Eq. 151}$$

The model linearized is shown in Figure 5.4-2.

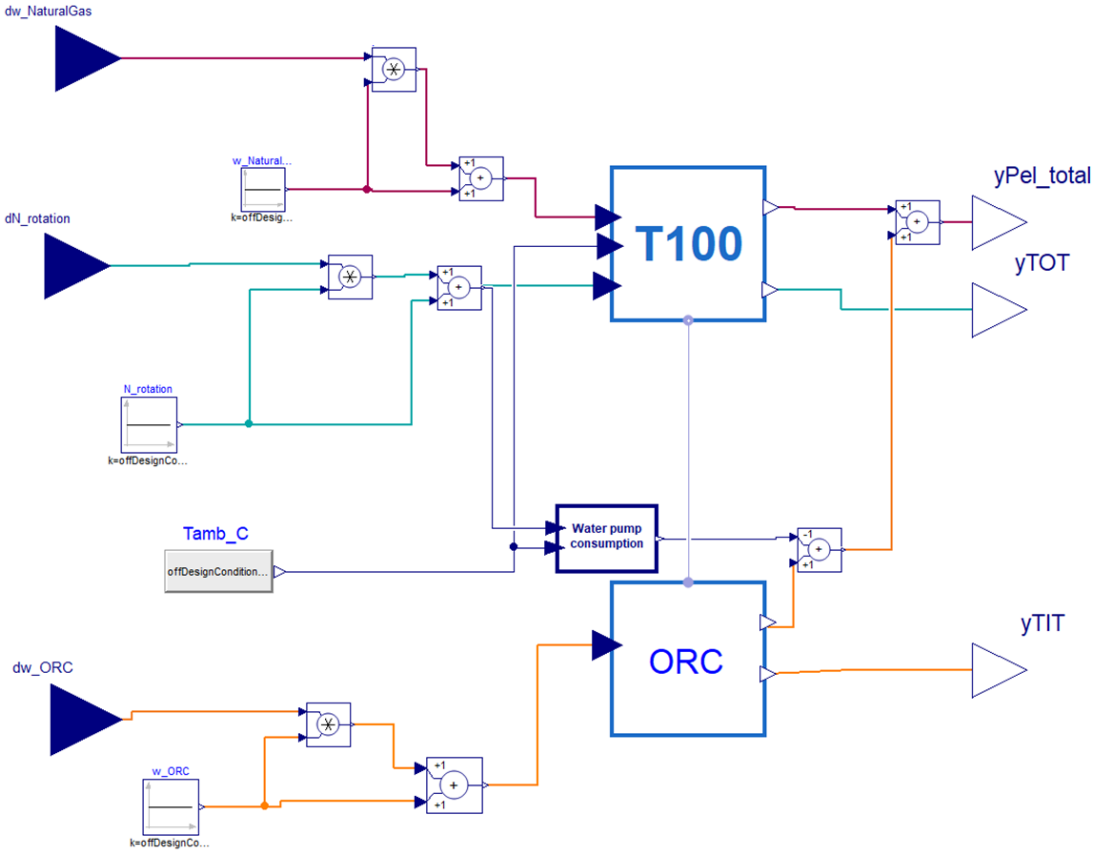

Figure 5.4-2 System for linearization in Dymola

The block T100 represents the whole scheme of the mGT (see Figure 5.3-2) and the block ORC represents the whole scheme of the ORC (see Figure 5.3-4). The vertical gray line connecting both systems is the connection of the flue gases leaving the regenerator of the mGT and entering the evaporator of the ORC. The three inputs of the manipulated variables (i.e. fuel mass flow rate, rotational speed and mass flow rate of the ORC working fluid) are shown as triangles on the left and the three outputs that should be controlled (i.e. total electric power, mGT TOT and ORC TIT) as triangles on the right. The total electric power produced is the sum of the electric power produced by the mGT and by the ORC. The power consumed by the cooling system of the ORC is computed with the module water pump consumption and it is subtracted from the total production.

As mentioned before, to reduce the non-linearities of the plant while controlling it, the outputs of the controller (i.e. inputs of the system) represent variations from a selected equilibrium point to the variable itself. The blocks on the left with the horizontal line are constant values obtained from the off-design case. The outputs of the controller modify that constant value.

Different linearizations have been performed considering different off-design conditions obtained from the steady-state model. The adopted off-design conditions are representative of the process conditions. They are 70000, 65000, 60000 and 55000 rpm at two different temperatures: 0 and 15 ºC.

5.4.3. Analysis of mutual interaction

Once the system has been linearized at different equilibrium conditions, before proceeding with the design of the controllers, an analysis of the mutual interactions should be done. The control architecture mainly depends on the mutual interaction between the manipulated and the controlled variables. The ideal process transfer function is a diagonal one, which means that the variation of one of the inputs just affects the response of one of the outputs and not the others. That would mean that the system is decoupled, and there are no mutual interactions between the manipulated and controlled variables. The analysis of the coupling among the different variables can be made through the evaluation of the Relative Gain Array (RGA) matrix [105]. This matrix also gives information about the optimal pairing between the inputs and outputs. It is defined as shown in Eq. 152.

$$\Lambda(G) = G(0) \times (G(0)^{-1})^{T} \qquad \text{Eq. 152}$$

The RGA is a normalized form of the gain matrix which describes the impact of each manipulated variable on each controlled variable. Therefore, the diagonal matrix of ones is the ideal one. Each element of the matrix can be evaluated by using the gain values of the process transfer function as shown in Eq. 153 [103].

$$\lambda_{ij} = (-1)^{i+j} \frac{g_{ij} \det G^{ij}}{\det G} \qquad \text{Eq. 153}$$

The analysis of the RGA matrix has been performed for the different equilibrium points considered to do the linearization [106]. The results are shown in section 6.4.3.1. By analyzing these results, it can be seen that the system is not decoupled. The modification of the mGT rotational speed of the turbomachinery or the fuel mass flow rate have a high influence on both the total electric power and the mGT turbine outlet temperature. Therefore, it is mandatory to design a decoupled control scheme to make it effective. The main function of a decoupler is to decompose the

multivariable process into a series of independent single-loop subsystem. If this objective can be achieved and the system can be decoupled, independent control loops can be designed and implemented [103].

Figure 5.4-3 shows the way a decoupler is introduced in the system.

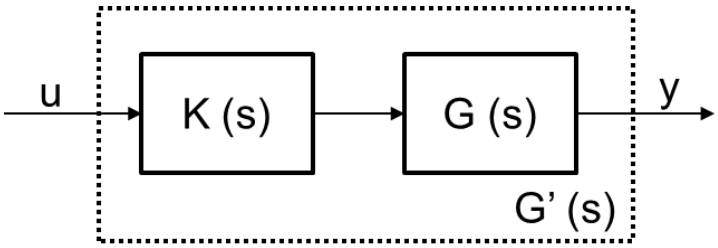

Figure 5.4-3 Reference scheme for the decoupling procedure

As it has been said before, the ideal process transfer function is a diagonal one, therefore, after adding the decoupler a diagonal matrix should be found. The process transfer function matrix is replaced by a pseudo-process matrix diagonal by construction G(s)K(s)=G'(s) [107]

$$\begin{cases} K_{11}(s) = 1 \\ K_{22}(s) = 1 \\ G_{11}(s)K_{12}(s) + G_{12}(s)K_{22}(s) = 0 \\ G_{21}(s)K_{11}(s) + G_{22}(s)K_{21}(s) = 0 \end{cases} \quad \text{Eq. 154}$$

Since the number of diagonal conditions is just two, and there are four unknown elements in the matrix K, it has been imposed that the trace of K(s) is equal to 1 [107].

$$\begin{cases} K_{11}(s) = 1 \\ K_{22}(s) = 1 \\ K_{12}(s) = -\dfrac{G_{12}(s)}{G_{11}(s)} \\ K_{21}(s) = -\dfrac{G_{21}(s)}{G_{22}(s)} \end{cases} \quad \text{Eq. 155}$$

The pseudo-process matrix is:

$$G'(s) = \begin{bmatrix} G_{11}(s)\big(1 - K_{12}(s)K_{21}(s)\big) & 0 \\ 0 & G_{22}(s)\big(1 - K_{12}(s)K_{21}(s)\big) \end{bmatrix} \quad \text{Eq. 156}$$

Considering that the dynamic decoupler may not be physically feasible, a static one has been chosen (calculated with s=0). Therefore, the transient response may vary, but the final result will deal to an uncoupled system.

$$G'(0) = \begin{bmatrix} G_{11}(0)(1 - k_{12}k_{21}) & 0 \\ 0 & G_{22}(0)(1 - k_{12}k_{21}) \end{bmatrix} \quad \text{Eq. 157}$$

where the values of the static matrix consider the gain values of the original process transfer function.

$$k_{ij} = -\frac{g_{ij}}{g_{ii}} \quad \text{Eq. 158}$$

For each linearization, the values of the static decoupler have been calculated. Figure 5.4-4 shows the decoupler scheme implemented in Dymola. The name of the block of the decoupler in Dymola is Ks.

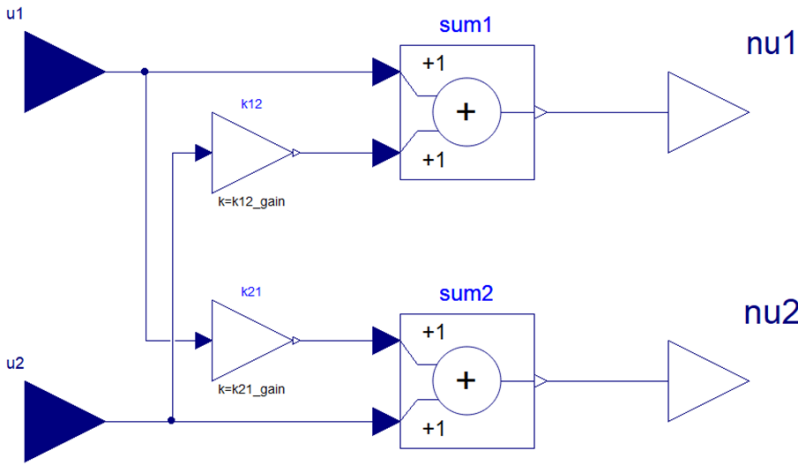

Figure 5.4-4 Decoupler scheme in Dymola

Average values have been considered taking into account the different linearizations. The final values implemented are shown in section 6.4.3.1. The final scheme of the overall system that should be controlled is shown in Figure 5.4-5. The Figure 5.4-5 is the same as Figure 5.4-2 but in this case, it can be seen the presence of the decoupler separating the effects of the two inputs of the mGT.

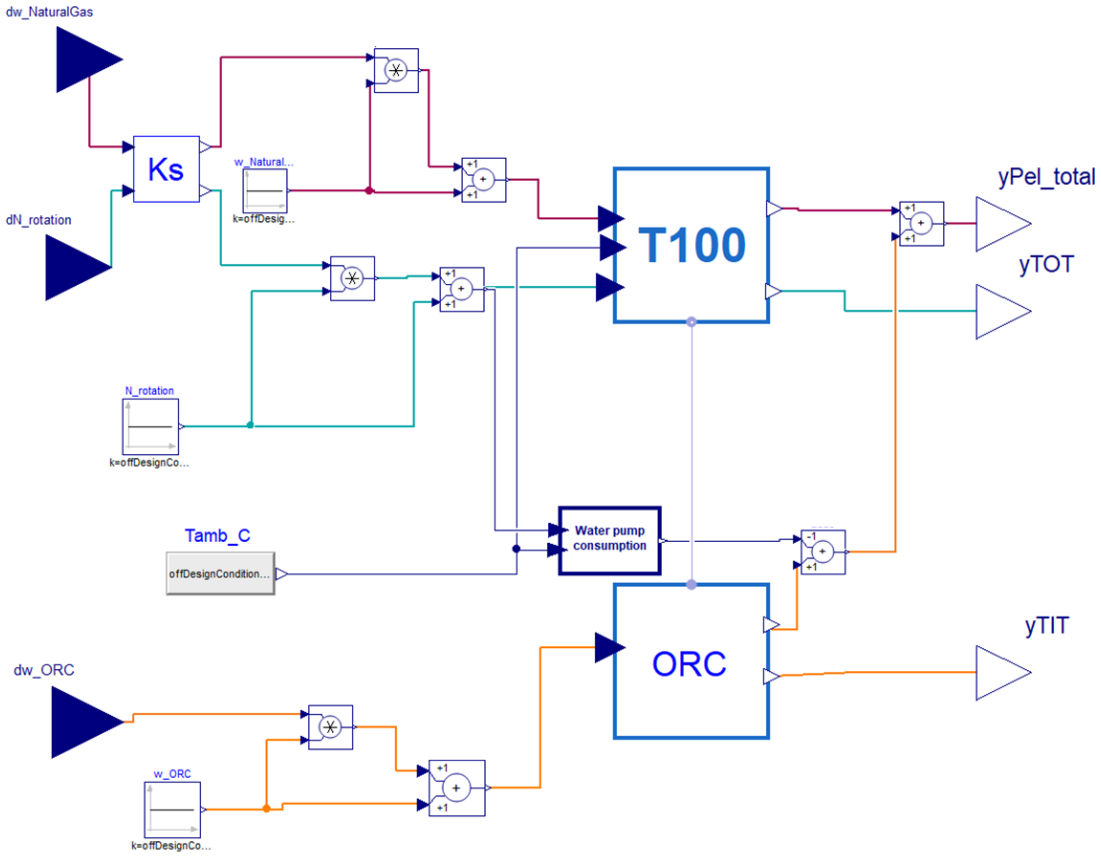

Figure 5.4-5 System for linearization and control in Dymola

5.4.4. PID controller

PID controllers are the simplest but most commonly used control architecture in industry. Therefore, they have been selected to control the three variables of interest (i.e. total electric power, mGT TOT and ORC TIT).

The PID controller, in the time domain, is given by:

$$u(t) = k_p e(t) + \frac{k_p}{T_i}\int_0^t e(\tau)d\tau + k_p T_d \frac{de(t)}{dt} \qquad \text{Eq. 159}$$

Where u is the control signal and e is the control error (i.e. the difference between the set point and the actual value of the controlled variable). The control signal is the sum of three terms: a proportional term, and integral term and a derivative term. The proportional action produces an output value that is proportional to the current error value. Generally, the higher the proportional gain, the faster is the controller dynamics. However, the closed-loop system may suffer of oscillating response or even of instability issues if the proportional gain is too high. The integral action depends on both the actual and the previous values of the error. The introduction of

an integral action guarantees zero-error conditions in steady-state. The derivative action improves the settling time of the system, but it is rarely used in practice because of variable impact on system stability. In this work, the derivative action was not implemented as it created an instable system, decreasing the controllability of the energy system.

As PI controllers have been adopted, the proportional gain (k_p) and the integral time constant (T_i) have to be determined for each PI controller. In order to do that, the *PID tuner* tool from Matlab® has been used. It allows tuning the parameters while analyzing the step response of the system. The process transfer functions obtained from Dymola are introduced in the PID tuner of Matlab®. By modifying the response time and the transient behavior, different controller configurations may be obtained. The response time can be slower or faster, depending on the requirements of the process. A faster controller allows reaching faster the value of the set point indicated, but it has the consequence of bigger overshoots. The transient behavior can be set to be more aggressive or more robust. An aggressive controller would increase the disturbances rejection; however, it has the consequence of higher overshoots. A balance should be found in both response time and transient behavior to obtain the desired behavior: fast enough but also with not so high value of overshoot.

Figure 5.4-6 represents the generic way in which the system is controlled. SP is the set point indicating the desired value of the controlled variable (y) and the error is the difference between the SP and the actual value of the controlled variable. C(s) represents the PI controller, K(s), the decoupler and G(s), the process.

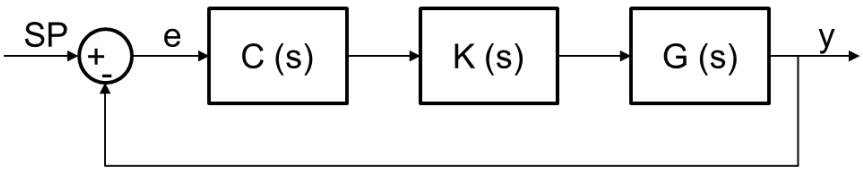

Figure 5.4-6 Reference scheme of the control system with decoupler

5.4.5. Control system layout

Once the controllers have been tuned, the whole system has been modeled as shown in Figure 5.4-7.

The overall scheme consists in three feedback loops with one controller for each one of the loops. The mGT+ORC block aggregates all the elements in Figure 5.4-5.

The magenta loop represents the loop controlling the electric power by modifying the fuel mass flow rate. In the figure, the electric requirement block represents the actual electric demand. However, the mGT+ORC system has not been designed to fulfill all the electric demand, but most of it. Therefore, taking into account the results from the steady-state model at different temperatures, there is a maximum power output that

the mGT+ORC system can give at the nominal rotational speed (i.e. 70000 rpm) at the actual ambient temperature. Moreover, it has been set that the system cannot give less than the 30% of the maximum power, in order to respect the limitation of the minimum mGT power. Therefore, the block SP_filter shown in the figure limits the set point of the electric demand considering the physical limitations of the system.

The cyan loop represents the one controlling the mGT TOT, manipulating the number of revolutions of the mGT turbomachinery. The set point is kept constant at the value of 645 ºC in every condition.

The orange loop represents the one controlling the ORC TIT by manipulating the mass flow of the ORC working fluid. In this case, the set point of the ORC TIT is not constant, but it varies with the partial load degree of the system. As stated in the Chapter 4. , while performing the off-design simulations, the value of the temperature could not be fixed to the nominal one when the conditions were far away from the nominal ones. Therefore, the steady-state results have been introduced to fix the right set point in the dynamic model considering the actual ambient temperature and rotational speed.

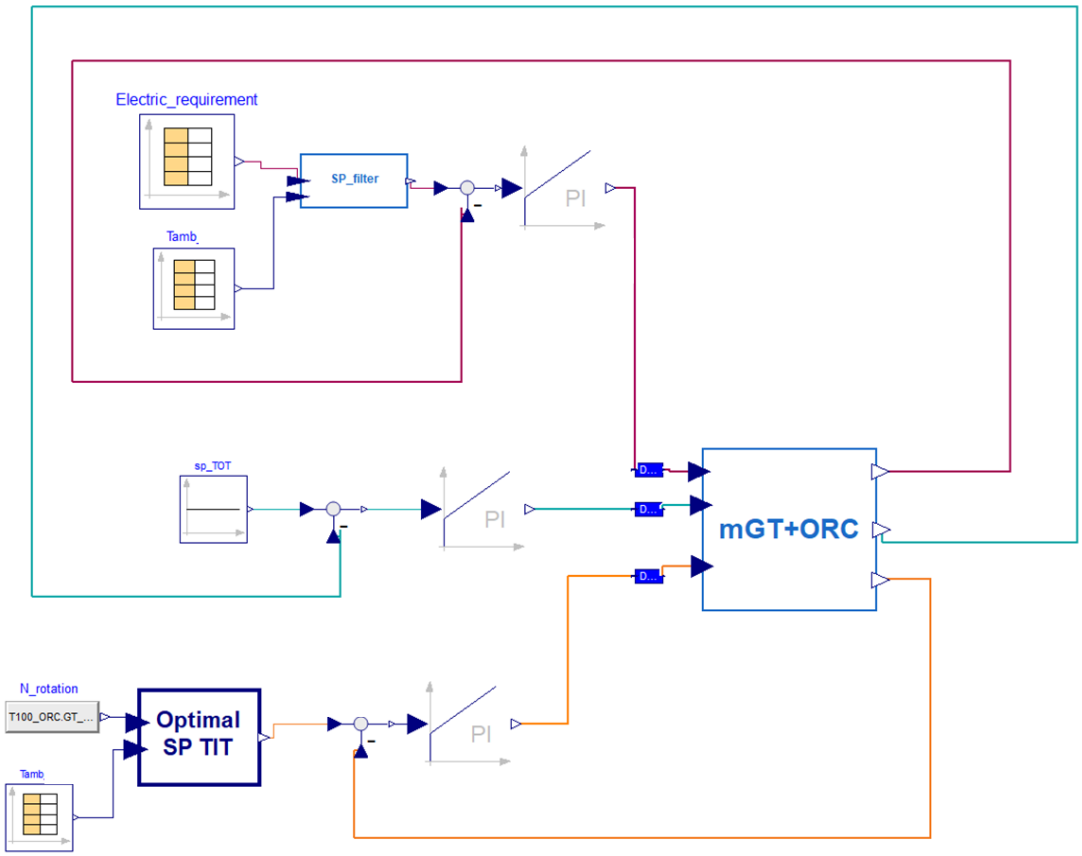

Figure 5.4-7 Overall system with the control architecture

Chapter 6. Results

Sometimes, you don't have to work harder, you just have to expect less.

6.1. Introduction

Along this chapter, all the results obtained from the work of this thesis will be presented and discussed.

The three main sections will be here presented:

- Section 6.2 collects the results from the design, having the system working at nominal conditions.
- Section 6.3 collects the results from the part load simulations considering steady-state conditions and making a deep analysis on them.
- Section 6.4 collects the results with the dynamic modeling, including the tuning of the controllers and the dynamic response of the system while trying to satisfy the electricity demand of a set of 150 houses.

6.2. Design

In this section, the design of the system is reported. First, the nominal values adopted and obtained from the mGT working in stand-alone conditions, matching the values declared by the manufacturer, are reported. After obtaining the values of the mGT working at nominal conditions, the bottoming ORC is designed. Different fluids have been selected for this study and the best fluid within the selected ones is taken as working fluid of the ORC. Once the thermodynamic conditions characterizing the cycles are known, the geometries of the heat exchangers (i.e. regenerator of the mGT, primary heat exchanger, regenerator and condenser of the ORC) are determined.

6.2.1. Nominal conditions of the mGT

As stated in Chapter 3. , the nominal performance of the existing mGT AE-T100 in stand-alone conditions should be completely characterized for two different purposes:

- Study the effect of the addition of the bottoming heat exchanger to recover heat from the flue gases with the bottoming ORC

- Analyze the part load performance when the conditions differ from the nominal ones.

In order to obtain the nominal conditions, the model described in 3.2 is implemented, considering the nominal parameters collected in Table 6.2-1 [17]–[19] and the characteristic maps describing the performance of the compressor (Figure 3.2-3) and turbine (Figure 3.2-4).

Table 6.2-1 Assumptions taken at nominal conditions of the mGT

$\varepsilon_{regenerator}$ [%]	88.9
$\dot{m}_{air}$ [kg/s]	0.8
N [rpm]	70000
TOT [ºC]	645
p_{amb} [bar]	1.01
T_{amb} [°C]	15
$\Delta p_{comb}/p_3$ [%]	5.9
η_{comb} [%]	99

The pressure drops of the components are modified iteratively (as shown in Figure 3.2-2) to get a proper match with the performance declared by the manufacturer. The best match obtained with the different iterations is depicted in Table 6.2-2.

Table 6.2-2 Performance of the mGT at nominal conditions

η_{comp} [%]	78.58
η_{turb} [%]	85.09
Q_{in} [kW]	339.06
P_{mech} [kW]	116.95
P_{loss}[kW]	16.93
P_{el} [kW]	100.03
η_{el} [%]	29.50

The electric power obtained is 100 kW, working in stand-alone conditions, with an electric efficiency of 29.50%. The values of these two parameters correspond with the ones specified by the manufacturer (the declared electric power is 100±3 kW and the declared electric efficiency 30±2%) [17]. The thermodynamic properties characterizing the thermodynamic cycle states are collected in Table 6.2-3.

Table 6.2-3 Thermodynamic properties of the mGT at nominal conditions

	p [bar]	T [ºC]	h [kJ/kg]	s [kJ/kgK]	ρ [kg/m^3]
0	1.01	15.00	-10.05	6.82	1.24
1	1.01	15.00	-10.05	6.83	1.22
2	4.58	210.93	188.44	6.92	3.29
3	4.49	597.19	601.68	7.55	1.80
4	4.22	935.58	549.66	8.05	1.21
5	1.10	645.45	208.13	8.12	0.41
6	1.01	274.70	-201.32	7.57	0.64

After analyzing the thermodynamic properties, it can be said that the values of pressure drops obtained in the components are reasonable as they have the same order of magnitude as the ones declared in other works [18], [28], [108], as well as the temperatures across the components. The only value which differs from the ones declared is the TIT, which is slightly lower (936 °C vs 945°C). However, this value is always declared as an approximative one as the only one which can be measured is the TOT, fixed at 645 ºC. Therefore, these conditions are the ones taken to characterize the AE-T100 and the ones taken to implement the bottoming ORC.

6.2.2. Optimization of the ORC

After obtaining the performance of the mGT working in stand-alone conditions, the bottoming ORC cycle has been designed to produce the maximum power output.

6.2.2.1. Performance of the selected fluids

Different candidates as working fluid have been selected in order to have a representative sample. Among them, some refrigerants and some hydrocarbons have been considered. On one hand, the main criteria for pre-selecting the refrigerants was to have a condensation pressure above 0.8 bar at a temperature of 15ºC. This criterion aims to avoid infiltrations in the condenser. On the other hand, the main criteria for selecting the hydrocarbons were to explore different fluids with low environmental impact, previously studied as working fluids in an ORC module and with different critical temperature among them, giving the possibility of exploring a higher variability of working conditions. The main reason of selecting two different criteria stands on increasing the number of possible suitable fluids.

The properties of the candidates as working fluid are shown in Table 6.2-4 [109], [110] and the T-s diagrams for each fluid is depicted in Figure 6.2-1.

Table 6.2-4 Properties of the working fluid candidates of the ORC module

Fluid	T_{critic} [ºC]	p_{critic} [bar]	T_{cond} at 1bar [ºC]	p_{cond} at 15 ºC [bar]	ODP	GWP	Flammable
R245fa	154.01	36.51	14.81	1.01	0	950	No
R1233zd	165.60	35.73	17.97	0.89	0	1	No
R21	178.33	51.81	8.52	1.28	0.01	210	Yes
Pentane	196.55	33.70	35.68	0.46	0	0	Yes
Cyclohexane	280.45	40.81	80.28	0.08	0	0	Yes
Butane	151.98	37.96	-0.84	1.76	0	20	Yes

The selected refrigerants were: R245fa [49], [68], [79], [111]–[114], R1233zd [115]–[117] and R21[118]. While the selected hydrocarbons were: pentane [49], [111], [119]–[122], cyclohexane [123], [124] and butane [49], [122], [125]. Among them, the R245fa and the R1233zd are refrigerants with similar properties (i.e. critical temperature and pressure and almost isentropic fluids); however, in terms of GWP, the R1233zd has a lower environmental impact in terms of GWP (1 vs 950), that is the reason why the R1233zd is getting more relevance as a substitute of the R245fa [115], [116]. In addition, the R1233zd is competitive with respect to R245fa in terms of prize (20-25€/kg for the R1233zd vs 30-35€/kg for the R245fa) [116]. The R21 is a refrigerant which satisfies the requirement of a higher condensation pressure at 15ºC (1.28 bar), but it is a wet fluid (as it can be seen in Figure 6.2-1), which may have the problem of a wet expansion in the turbine. All the hydrocarbons are dry fluids (as it can be seen in Figure 6.2-1).

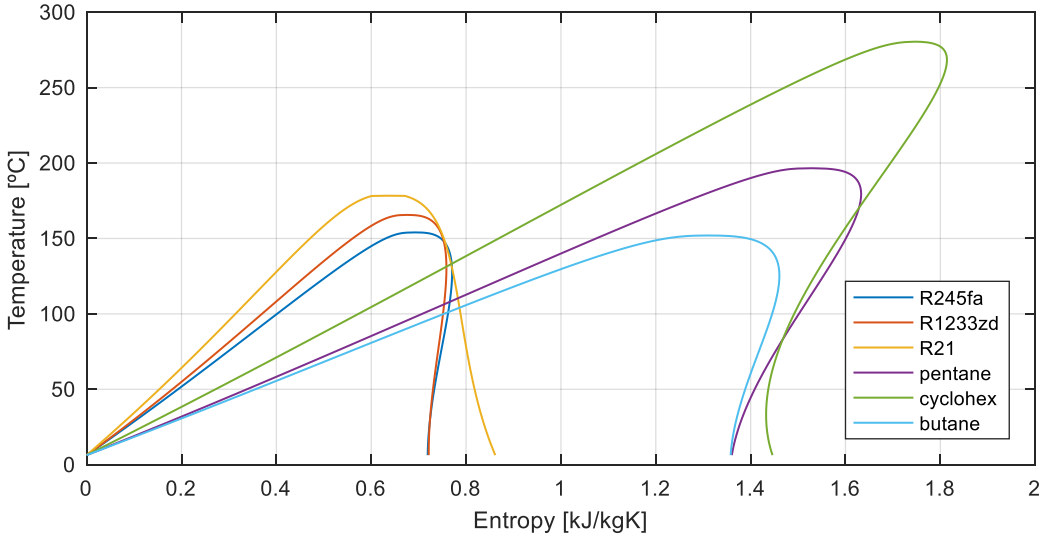

Figure 6.2-1 T-s diagram of the studied working fluids for the ORC

Once different fluids have been selected for the study, the optimization of the cycle has been implemented considering the model described in 4.2, adopting the pinch-point temperature difference at nominal conditions indicated in Table 6.2-5.

Table 6.2-5 Assumptions of pinch-point temperature difference at nominal conditions

$\Delta T_{pp,PHE}$ [ºC]	25
$\Delta T_{pp,reg}$ [ºC]	5
$\Delta T_{pp,cond}$ [ºC]	3

After optimizing the cycle with the different selected fluids, the maximum power that can be obtained is shown in Figure 6.2-2. The fluids which have the maximum power output are R21 (26.90 kWe), R1233zd (25.77 kWe) and butane (25.52 kWe). As the differences on the maximum power output are small, R1233zd has been selected as working fluid for the designed ORC module. The motivations driving this decision are the consideration of the environmental impact of it (i.e. ODP equal to 0, GWP equal to 1) and its non-flammability, with almost the same performance as the best fluid in terms of power output.

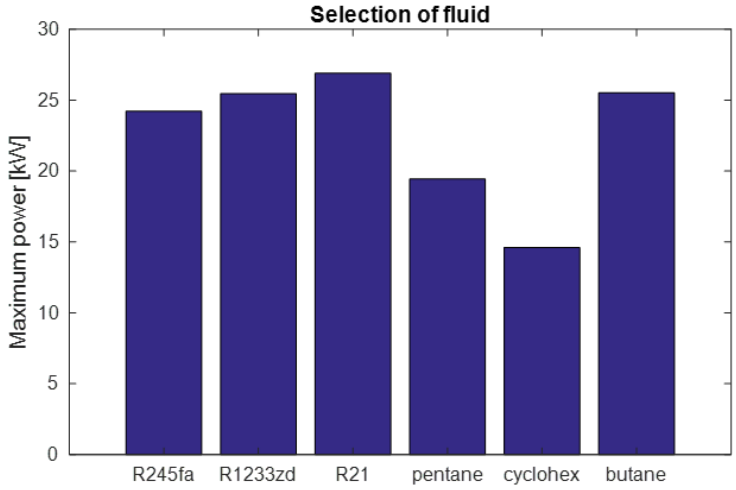

Figure 6.2-2 Optimization of the nominal ORC performance for the different working fluids

6.2.2.2. Nominal cycle

The main focus of this section is to present the characteristics of the designed ORC. The optimized ORC module is a regenerative superheated subcritical one, as it can be seen in Figure 6.2-4-a. Table 6.2-6 collects the performance of the ORC at design conditions.

Table 6.2-6 Performance of the ORC at nominal conditions

$\dot{m}_{ORC}$ [kg/s]	0.70
$P_{turb,ORC}$ [kW]	28.05
$P_{pump,ORC}$ [kW]	1.05
$P_{pump,water}$ [kW]	1.22
$P_{el,ORC}$ [kW]	25.77
$\dot{m}_{cooling\ water}$ [kg/s]	8.16
$\eta_{turb,ORC}$ [%]	83.19
$\eta_{el,ORC}$ [%]	15.55
η_{turb} [%]	84.99

Table 6.2-7 shows the thermodynamic properties of each stream in the ORC (following the same numeration as shown in Figure 4.2-1), Figure 6.2-3 shows the optimal design for the single-stage radial-inflow turbine and Figure 6.2-4 shows the T-s diagram of the whole cycle (a), the T-Q diagram of the primary heat exchanger (b), the T-Q diagram of the condenser (c) and the T-Q diagram of the regenerator (d).

The mass flow of working fluid is equal to 0.70 kg/s, producing a nominal electric power output equal to 25.77 kW with a cycle efficiency equal to 15.55%. By looking at Table 6.2-7, the minimum temperature of the cycle is 26.75ºC, condensing at a pressure of 1.38 bar, higher than the atmospheric pressure; therefore, there is no risk of fluid infiltration from the outside. The condensation temperature is guaranteed with a mass flow rate of 8.16 kg/s of water in design conditions. The maximum temperature of the working fluid is equal to 139.82 ºC, which is an acceptable value to avoid thermal decomposition [126], [127].

Table 6.2-7 Thermodynamic properties of the ORC at nominal conditions

	p [bar]	T [ºC]	h [kJ/kg]	s [kJ/kgK]	ρ [kg/m^3]
8	1.38	26.75	233.05	1.12	1258.56
9	15.97	27.52	234.49	1.12	1261.14
10	15.47	56.78	271.28	1.23	1186.85
11	14.38	139.82	506.88	1.85	68.82
12	1.44	75.72	465.79	1.88	6.68
13	1.41	32.52	428.63	1.77	7.62

The design of the single-stage radial-inflow turbine is pushed to the maximum volume ratio affordable by the turbine, equal to 9.98, with a size parameter equal to 0.0214

m, with an efficiency equal to 83.19% and rotating at a nominal speed equal to 52278 rpm. The fact that the optimal design has the volume ratio at the maximum value that the turbine can give may indicate that a multi-stage radial-inflow turbine could be used to increase the maximum volume ratio and thus, giving the possibility of a higher enthalpy difference in the turbine. However, as the increment of stages in the turbine increases the complexity of the turbine and the contribution for this particular case is limited, it has been considered to keep the design as a single-stage radial-inflow turbine.

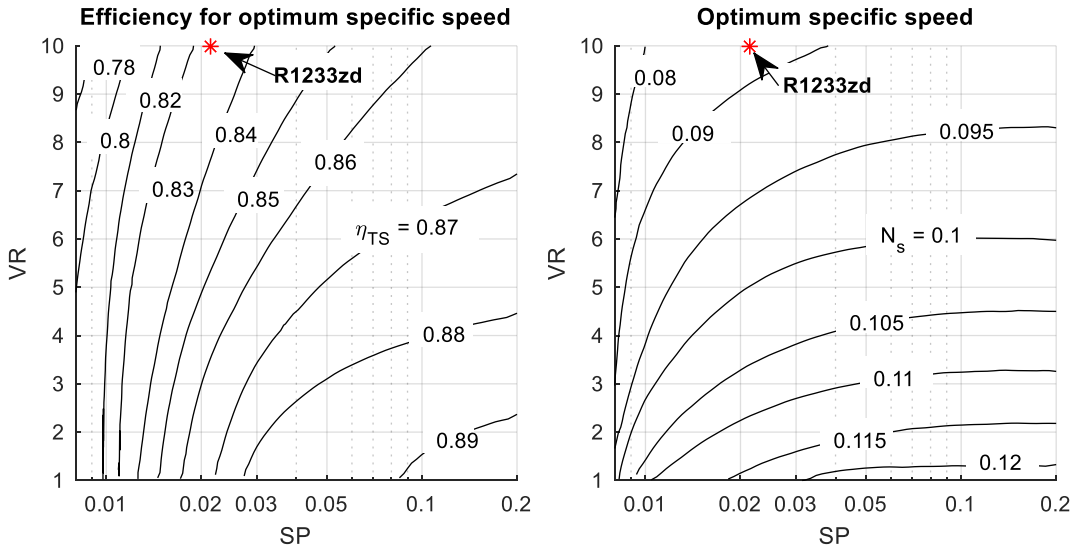

Figure 6.2-3 Efficiency prediction (left) and optimum specific speed (right) at nominal conditions for a single-stage radial inflow turbine using R1233zd as working fluid.

In Figure 6.2-4-a, the T-s diagram of the organic cycle is reported, including also the variation of temperature of the flue gases of the mGT and the cooling water. Figure 6.2-4-b represents the T-Q diagram of the primary heat exchanger (i.e. how the temperature varies with the exchanged heat). In this graphic, the three sections of heating up the working fluid can be clearly identified: the liquid heats up till it starts evaporating, when it evaporates, the temperature remains almost constant (not completely constant due to the pressure drops) and after the evaporation, the saturated vapor heats up till superheated vapor. Figure 6.2-4-c shows the T-Q diagram of the condenser. The working fluid cools down from superheated vapor till saturated vapor and it starts condensing at almost constant temperature till reaching the condition of saturated liquid, this process happens by releasing the heat to the cooling fluid, namely water. Finally, in Figure 6.2-4, the T-Q diagram of the regenerator is shown. The hot fluid exiting the turbine preheats the cold fluid before entering the primary heat exchanger.

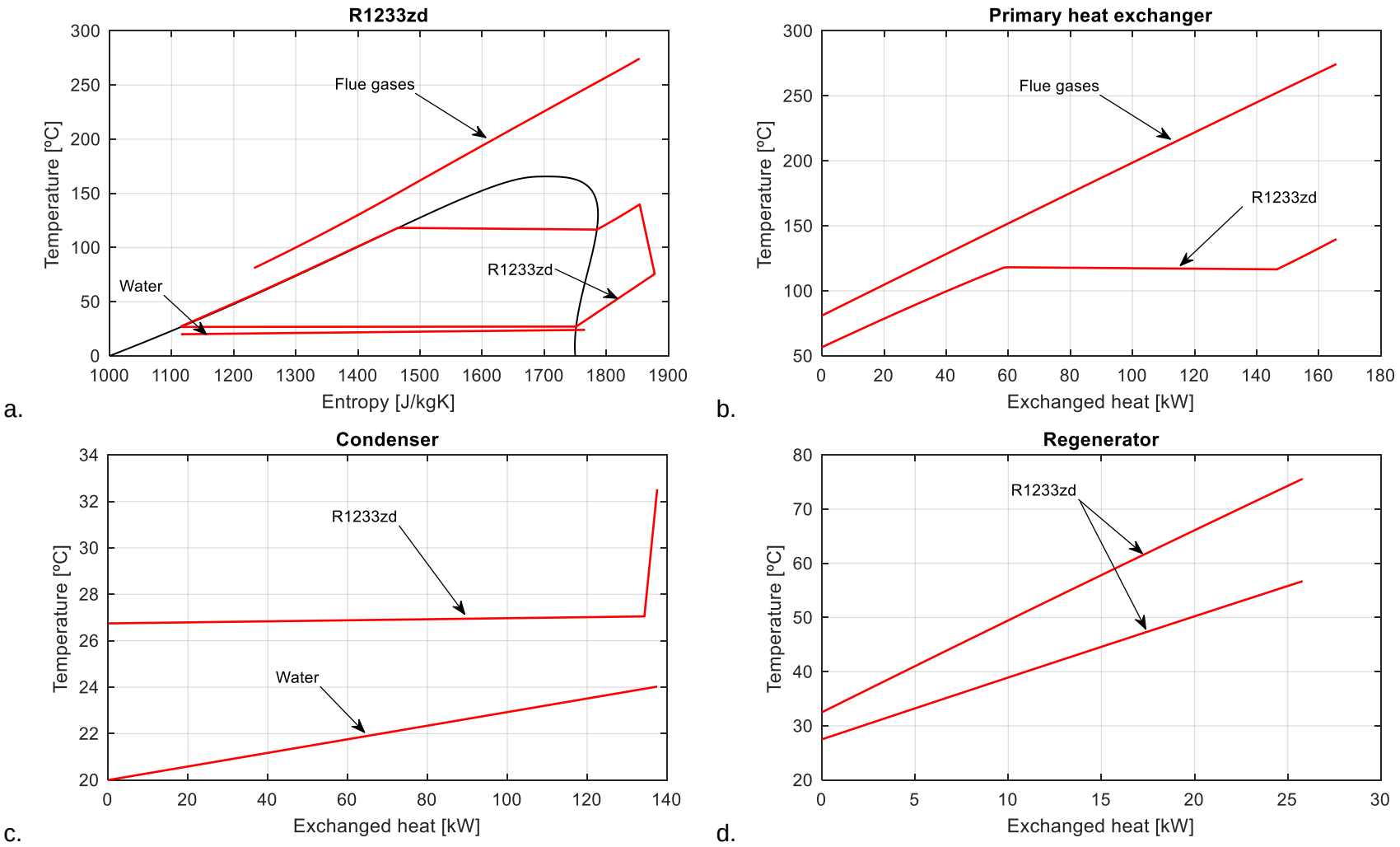

Figure 6.2-4 T-s diagram (a), T-Q diagram of the primary heat exchanger (b), condenser (c) and regenerator (d) of the ORC at nominal conditions

6.2.3. Overall system

Both technologies have been presented in the sections mentioned before. However, the performance of the mGT indicated in the section 6.2.1 is related to stand-alone conditions, which is not the case under study. The addition of the bottoming heat exchanger to recover the remaining heat from the flue gases adds a pressure drop (in this case equal to the 3% of the inlet pressure) to the mGT system, worsening its performance.

After introducing the bottoming heat exchanger, the thermodynamic properties of the mGT are the ones reported in Table 6.2-8. It can be seen that the pressure ratio in the turbine has been decreased, as well as the TIT, with the consequence of a lower electric power output in comparison with the mGT without the bottoming cycle, from 100 kWe to 93.89 kWe (as it can be seen in Table 6.2-9). Table 6.2-9 collects the main information about the performance of the mGT working at nominal conditions but with the effect of the bottoming heat exchanger. The efficiency of the mGT by itself is decreased from 29.5 % to 28.26 %.

Table 6.2-8 Thermodynamic properties of the mGT at nominal conditions with the bottoming ORC

	p [bar]	T [ºC]	h [kJ/kg]	s [kJ/kgK]	ρ [kg/m^3]
0	1.01	15.00	-10.05	6.77	1.30
1	1.01	15.00	-10.05	6.83	1.22
2	4.58	210.85	188.36	6.92	3.29
3	4.48	596.67	601.09	7.55	1.80
4	4.22	928.26	550.04	8.04	1.22
5	1.12	645.00	216.94	8.11	0.42
6	1.04	274.45	-192.09	7.56	0.64
7	1.01	81.04	-393.14	7.12	0.99

Table 6.2-9 Performance of the mGT at nominal conditions with the bottoming ORC

η_{comp} [%]	78.57
η_{turb} [%]	84.99
Q_{in} [kW]	332.28
P_{mech} [kW]	110.28
P_{loss}[kW]	16.39
P_{el} [kW]	93.89
η_{el} [%]	28.26

Even if the electric power output is reduced, with the bottoming cycle the overall electric power output is increased from 100 kWe to 119.66 kWe, with an increment of the electric efficiency from 29.5% to 36% because of the additional power output of the ORC. In Table 6.2-10, the performance of the overall system is shown, indicating the contributions of each engine.

Table 6.2-10 Performance of the overall system at nominal conditions

Q_{in} [kW]	332.28
$P_{el,mGT}$ [kW]	93.89
$P_{el,ORC}$ [kW]	25.77
P_{total} [kW]	119.66
$\eta_{el,total}$ [%]	36.01

6.2.4. Heat exchangers

After presenting the thermodynamic properties at nominal conditions, the design of the heat exchangers is done. In order to study the dynamic behavior of the system, it is mandatory to know the geometries of the heat exchangers. For this purpose, in this section, the results of the designed heat exchangers are presented.

6.2.4.1. Regenerator of the mGT

The regenerator of the mGT is an existing one, as it has been mentioned before, therefore, the values needed for the dynamic model (i.e. the surface exchanging heat, the volume of the channel of the fluid and the mass of the heat exchanger) should be calculated as described in section 3.4. The results are shown in Table 6.2-11, where A_{plate} is the surface exchanging heat of each plate, A_{total} is the sum of all the exchanging surfaces, $V_{channel\ fluid}$ is the volume of passage of the fluid between two plates, $V_{total\ channel}$ is the volume of passage of the fluid between two plates but considering all the channels in the heat exchanger for both hot and cold sides and M_{total} is the total mass of the heat exchanger.

Table 6.2-11 Physical values of the mGT regenerator

A_{plate} [m^2]	0.12
A_{total} [m^2]	93.31
$V_{channel\ fluid}$ [m^3]	$6.37 \cdot 10^{-5}$
$V_{total\ channel}$ [m^3]	$2.45 \cdot 10^{-2}$
M_{total} [kg]	295.86
UA_{nom} [kW/K]	5940

Figure 6.2-5 shows a zoom of three plates of the 3-D heat exchanger designed in Matlab®. It can be clearly seen the disposition of the plates as well as the space of the channels through which the fluid flows.

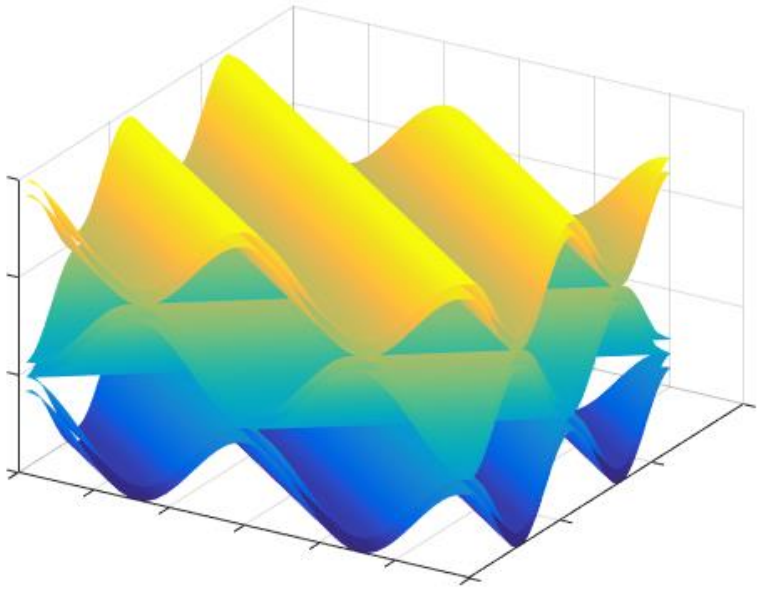

Figure 6.2-5 3-D zoom of three plates of the mGT regenerator

6.2.4.2. ORC heat exchangers

The heat exchangers of the ORC module have to be designed completely by using specialized software for that, as explained in section 4.4. For that purpose, Aspen Exchanger Design & Rating has been used. The type of heat exchanger (plate fin heat exchanger) and the nominal thermodynamic properties have been specified. Table 6.2-12 collects the relevant information from the design of each heat exchanger obtained with the software after performing the dimensioning of them.

Table 6.2-12 Physical parameters of the ORC heat exchangers

		V [m^3]	A [m^2]	M [kg]
Primary heat exchanger	Hot side	0.0994	66.9	93.5
	Cold side	0.0152	24.5	
Condenser	Hot side	0.0301	40.6	70.7
	Cold side	0.016	24.7	
Regenerator	Hot side	0.0994	66.9	38.2
	Cold side	0.0152	24.5	

6.3. Steady-state part load performance

In this section, the part load performance of the designed system is depicted. Before starting with the analysis of the part load performance of the system itself, simulations of the part load conditions of the heat exchangers of the ORC have been performed in order to establish the off-design parameters characterizing how the heat transfer coefficients change with the variation of the mass flow of working fluids. After analyzing the heat transfer coefficients variation, the variation of the main characteristics of both technologies is shown. First, the performance of the mGT; second, the performance of the ORC and third, the performance of the overall system itself are shown.

6.3.1. ORC heat exchangers part load

To study the part load of the ORC module, it is mandatory to know how the heat transfer coefficients change when the mass flow of the working fluid changes. In order to establish a correlation which relates the heat transfer coefficient (γ) in part load conditions with the mass flow rate of fluid (see Eq. 160) with an exponent coefficient (α), different simulations have been performed. The software Aspen Exchanger Design & Rating allows simulating the performance of an already designed heat exchanger by varying the working conditions.

$$\gamma = \gamma_{nom} \left(\frac{\dot{m}}{\dot{m}_{nom}} \right)^{\alpha} \qquad \text{Eq. 160}$$

Simulations have been performed for each heat exchanger of the ORC (i.e. regenerator, primary heat exchanger and condenser). For each side of the heat exchanger (namely hot and cold side), the evaluation of the effective heat transfer coefficient has been performed by varying the mass flow rate of the working fluid of the side under study by keeping constant the working fluid mass flow rate of the other side. For example, to evaluate how the heat transfer coefficient of the flue gases varies in the primary heat exchanger, the mass flow of the flue gases has been reduced but the mass flow rate of the R1233zd has been kept constant. Oppositely, staying with the same example of the primary heat exchanger, to evaluate the variation of the heat transfer coefficient of the R1233zd, its mass flow rate has been varied but the mass flow rate of the flue gases has been kept constant at the nominal value. The only exception is made in the ORC regenerator because the mass flow rate of working fluid is the same on both sides; in particular, to analyze the part load performance, the mass flow rate of both sides has been changed.

For simplification purposes, even if the effective heat transfer coefficient varies along the heat exchanger due to the different thermodynamic conditions, which influence

the fluid thermophysical properties, average values have been considered. The only distinction that has been done is splitting the values of the heat transfer coefficient if there is a phase change of the fluid.

Figure 6.3-1 shows the variation of the effective heat transfer coefficient (i.e. the actual heat transfer coefficient considering that the efficiency of the fins (η_{Fin}) varies) of the vapor flowing along the hot side of the ORC regenerator while Figure 6.3-2 shows the variation of the effective heat transfer coefficient of the liquid flowing along the cold side of the heat exchanger. The x-axes represent the heat exchanged. There is a temperature profile along the heat exchanger, thus, there is a variation of the properties of the fluid, including the effective heat transfer coefficient. That is the reason why the effective heat transfer coefficient does not remain constant. However, the approximation of an averaged value has been taken. The variation of this value is relatively low when there is no phase change.

Table 6.3-1 collects the average results of the simulations shown in Figure 6.3-1, while Table 6.3-2 collects the average results of the simulations shown in Figure 6.3-2. The first row indicates the nominal conditions, while the rest, the part load ones. With each performed simulation, an exponent coefficient has been computed through Eq. 109. An average of that exponent coefficient has been computed. For each case, the values that should be introduced in Eq. 109 to evaluate the effective heat transfer coefficient in the off-design ORC heat exchangers' model is shown in light yellow. The values introduced in the model are the nominal value of the effective heat transfer coefficient and the average exponent coefficient.

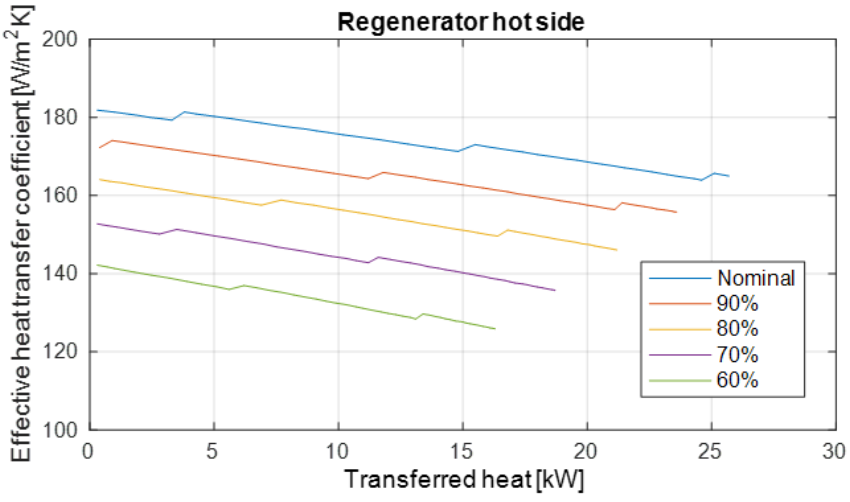

Figure 6.3-1 Effective heat transfer coefficient variation in the hot side of the regenerator at different reductions of the mass flow rate with respect to the nominal one

Table 6.3-1 Heat transfer coefficient analysis of the hot fluid in the regenerator by varying the mass flow of working fluid

Hot side - Vapor						
	$\dot{m}_{hot\ side}$ [kg/s]	$\dot{m}_{cold\ side}$ [kg/s]	$\gamma_{hot\ side}$ [W/m^{2}K]	η_{Fin} [-]	$\gamma_{effective.hot\ side}$ [W/m^{2}K]	α
100%	0.70	0.70	233.29	0.74	173.41	
90%	0.63	0.63	214.49	0.76	162.73	0.60
80%	0.56	0.56	198.61	0.77	153.28	0.55
70%	0.49	0.49	182.10	0.78	142.91	0.54
60%	0.42	0.42	164.79	0.80	132.08	0.53
Average						0.56

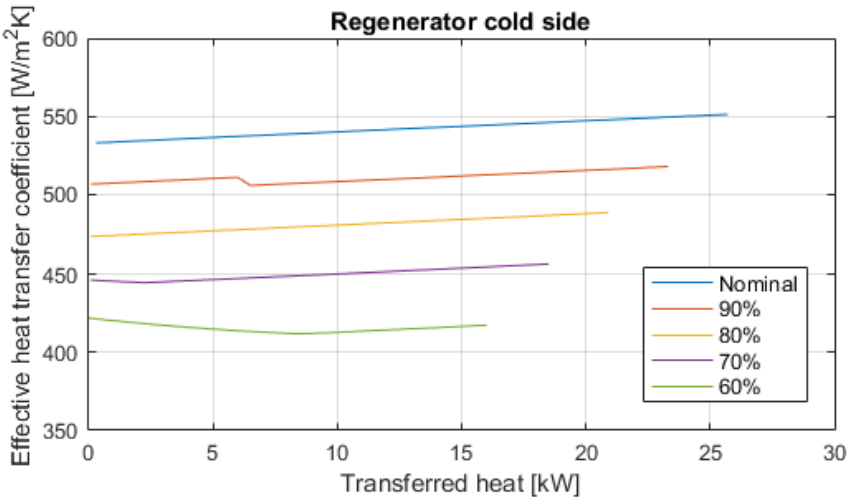

Figure 6.3-2 Effective heat transfer coefficient variation in the cold side of the regenerator at different reductions of the mass flow rate with respect to the nominal one

Table 6.3-2 Heat transfer coefficient analysis of the cold fluid in the regenerator by varying the mass flow of working fluid

Cold side - Liquid						
	$\dot{m}_{hot\ side}$ [kg/s]	$\dot{m}_{cold\ side}$ [kg/s]	$\gamma_{cold\ side}$ [W/m^{2}K]	η_{Fin} [-]	$\gamma_{effective.cold\ side}$ [W/m^{2}K]	α
100%	0.70	0.70	602.31	0.90	542.08	
90%	0.63	0.63	564.02	0.90	510.07	0.58
80%	0.56	0.56	526.37	0.91	479.00	0.55
70%	0.49	0.49	487.59	0.92	448.59	0.53
60%	0.42	0.42	452.80	0.92	416.57	0.52
Average						0.54

The same study performed with the regenerator has been done with the condenser. However, in this case, the hot side of the condenser is split into two zones, namely the de-superheating section and the condensing section. Figure 6.3-3 and Figure 6.3-4 show the variation of the effective heat transfer coefficient with the exchanged heat in vapor and two-phase conditions, respectively. Figure 6.3-5 shows the variation of the effective heat transfer coefficient of the cooling water in part load conditions. As it can be seen in Figure 6.3-4, the variation of the effective heat transfer coefficient is abrupt. This happens because the fluid is changing phase, thus, the heat transfer improves. This also happens in the primary heat exchanger (Figure 6.3-8). In this case, the average differs more from the actual value along the heat exchanger in comparison with the cases in which there is no phase change. However, as the heat transfer coefficient is so high, the heat exchange is limiting by the other fluid. Thus, the impact of taking the average in the overall heat transfer coefficient is negligible.

Table 6.3-3 collects the average results from the simulations shown in Figure 6.3-3 and Figure 6.3-4, while Table 6.3-4, the ones from the simulations shown in Figure 6.3-5.

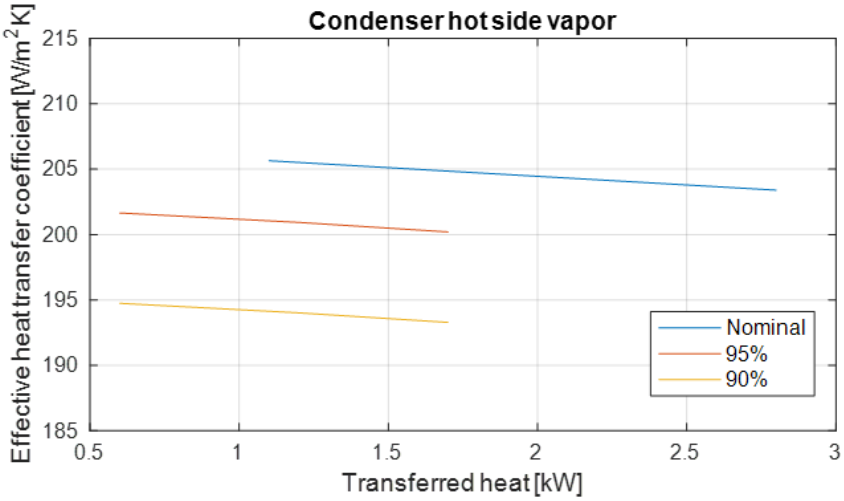

Figure 6.3-3 Effective heat transfer coefficient variation in vapor conditions along the hot side in the condenser at different reductions of the mass flow rate with respect to the nominal one

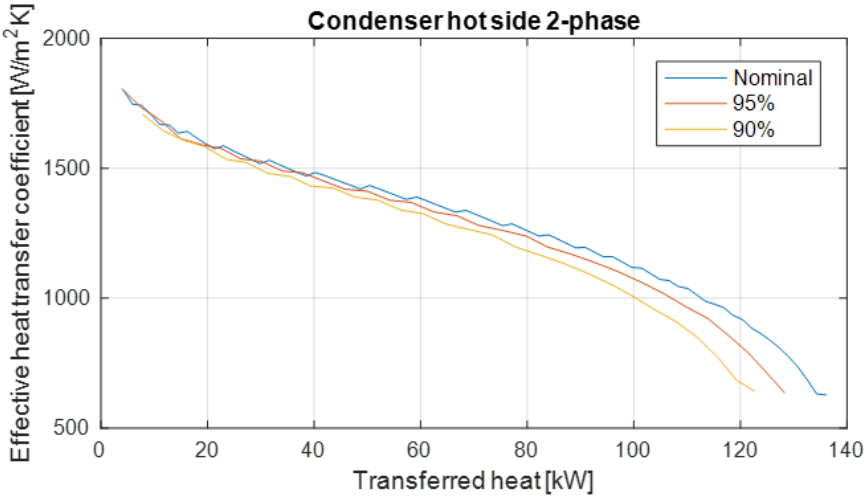

Figure 6.3-4 Effective heat transfer coefficient variation in condensing section in the hot side of the condenser at different reductions of the mass flow rate with respect to the nominal one

As it can be seen in Figure 6.3-4, the variation of the effective heat transfer coefficient is abrupt. This happens because the fluid is changing phase, thus, the heat transfer improves. This also happens in the primary heat exchanger (Figure 6.3-8). In this case, the average differs more from the actual value along the heat exchanger in comparison with the cases in which there is no phase change. However, as the heat transfer coefficient is so high, the heat exchange is limiting by the other fluid. Thus, the impact of taking the average in the overall heat transfer coefficient is negligible.

Table 6.3-3 Heat transfer coefficient analysis of the hot fluid in the condenser by varying the mass flow of working fluid and keeping constant the mass flow of the cooling fluid

Hot fluid - Vapor						
	$\dot{m}_{hot\ side}$ [kg/s]	$\dot{m}_{cold\ side}$ [kg/s]	$\gamma_{hot\ side}$ [W/m²K]	η_{Fin} [-]	$\gamma_{effective.hot\ side}$ [W/m²K]	α
100%	0.70	8.09	228.08	0.90	205.27	
95%	0.67	8.09	220.80	0.91	200.93	0.42
90%	0.63	8.09	213.20	0.91	194.01	0.54
Average						0.48
Hot fluid - 2-phase						
100%	0.70	8.09	2325.89	0.57	1329.12	
95%	0.67	8.09	2337.47	0.57	1335.28	-0.09
90%	0.63	8.09	2231.42	0.58	1294.22	0.25
Average						0.08

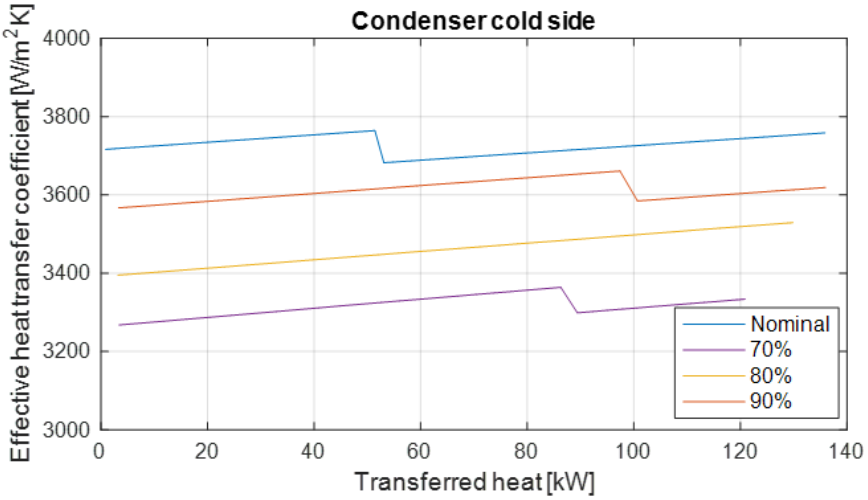

Figure 6.3-5 Effective heat transfer coefficient along the cold side in the condenser at different reductions of the mass flow rate with respect to the nominal one

Table 6.3-4 Heat transfer coefficient analysis of the hot fluid in the condenser by varying the mass flow of cooling fluid while keeping constant the mass flow of the working fluid

Cold fluid - Liquid						
	$\dot{m}_{hot\ side}$ [kg/s]	$\dot{m}_{cold\ side}$ [kg/s]	$\gamma_{cold\ side}$ [W/m²K]	η_{Fin} [-]	$\gamma_{effective.cold\ side}$ [W/m²K]	α
100%	0.70	8.09	8401.53	0.44	3728.98	
90%	0.70	7.28	7908.38	0.46	3610.17	0.31
80%	0.70	6.47	7380.78	0.47	3468.96	0.32
70%	0.70	5.66	6827.92	0.49	3318.37	0.33
Average						0.32

The last component to be evaluated is the primary heat exchanger. This case is more similar to the condenser, as the cold fluid changes phase. In this case, the flue gases exiting the mGT flow through the hot side; while the R1233zd flows through the cold side. First, the ORC working fluid enters as liquid and it heats up till saturated conditions. Second, it starts evaporating being in two-phase conditions. Third, it reaches superheated vapor conditions. Therefore, three sections need to be identified.

Figure 6.3-6 shows the variation of the flue gases effective heat transfer coefficient with the exchanged heat; while Figure 6.3-7, Figure 6.3-8 and Figure 6.3-9 show the ones of the ORC working fluid along the different sections divided according to the state of the fluid: vapor, two-phase and liquid, respectively. Table 6.3-5 collects the

information of the performed simulations shown in Figure 6.3-6, and Table 6.3-6 collects the information of the performed simulations shown in Figure 6.3-7, Figure 6.3-8 and Figure 6.3-9.

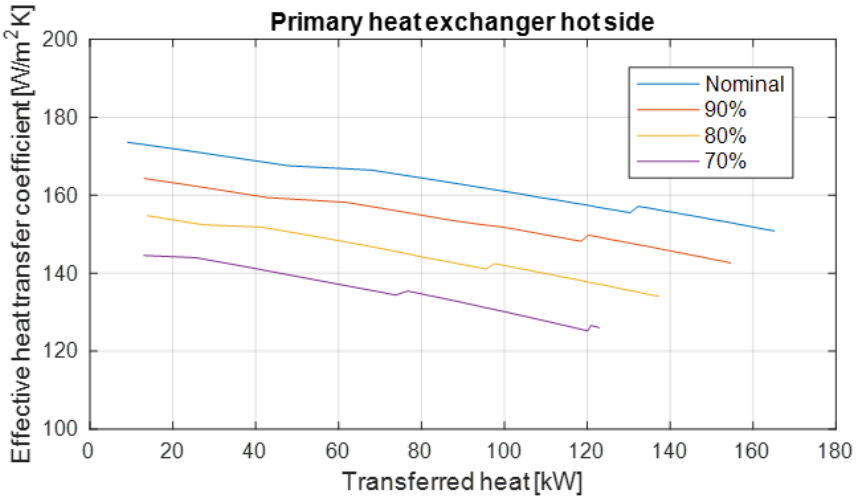

Figure 6.3-6 Effective heat transfer coefficient variation along the hot side in the PHE at different reductions of the mass flow rate with respect to the nominal one

Table 6.3-5 Heat transfer coefficient analysis of the hot fluid in the PHE by varying the mass flow of the flue gases while keeping constant the mass flow of the working fluid

Hot fluid - Vapor						
	$\dot{m}_{hot\ side}$ [kg/s]	$\dot{m}_{cold\ side}$ [kg/s]	$\gamma_{hot\ side}$ [W/m^{2}K]	η_{Fin} [-]	$\gamma_{effective.hot\ side}$ [W/m^{2}K]	α
100%	0.81	0.70	203.57	0.77	157.59	
90%	0.73	0.70	189.78	0.79	149.00	0.53
80%	0.65	0.70	176.20	0.80	140.32	0.52
70%	0.57	0.70	161.53	0.81	130.72	0.52
Average						0.53

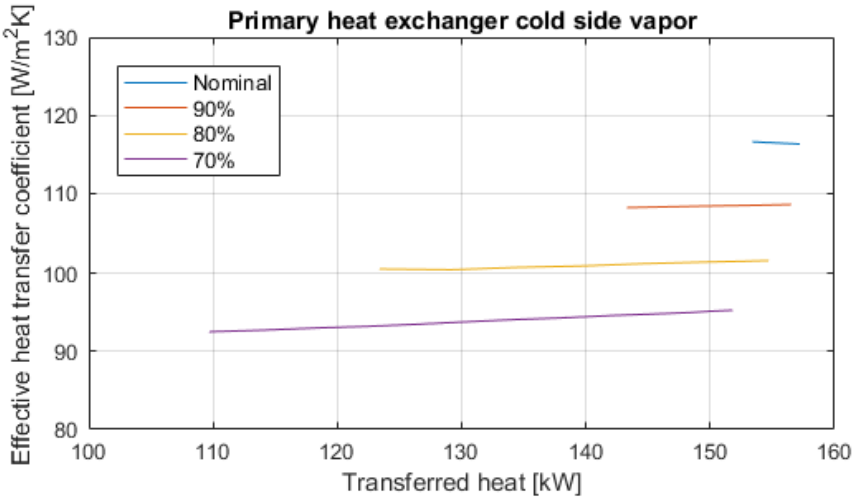

Figure 6.3-7 Effective heat transfer coefficient variation in vapor conditions in the cold side of the PHE at different reductions of the mass flow rate with respect to the nominal one

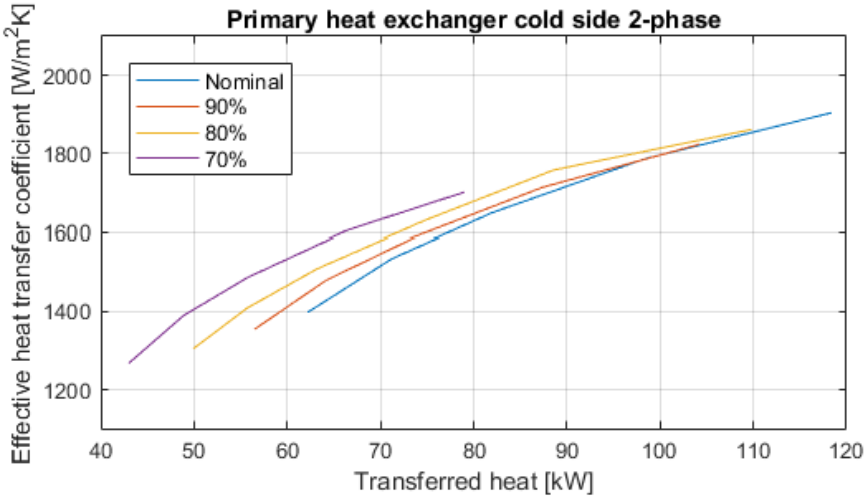

Figure 6.3-8 Effective heat transfer coefficient variation in two-phase conditions in the cold side of the PHE at different reductions of the mass flow rate with respect to the nominal one

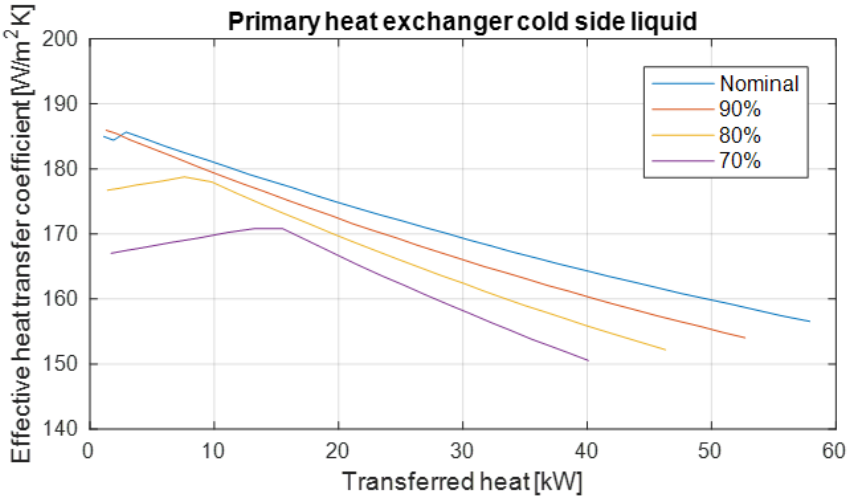

Figure 6.3-9 Effective heat transfer coefficient variation in liquid conditions in the cold side of the PHE at different reductions of the mass flow rate with respect to the nominal one

Table 6.3-6 Heat transfer coefficient analysis of the cold fluid in the PHE by varying the mass flow of the working fluid while keeping constant the mass flow of the flue gases

	$\dot{m}_{hot\ side}$ [kg/s]	$\dot{m}_{cold\ side}$ [kg/s]	$\gamma_{cold\ side}$ [W/m^{2}K]	η_{Fin} [-]	$\gamma_{effective.cold\ side}$ [W/m^{2}K]	α
Cold fluid - Liquid						
100%	0.81	0.70	176.74	0.97	171.33	
90%	0.81	0.63	174.31	0.97	169.08	0.13
80%	0.81	0.56	171.46	0.97	166.31	0.13
70%	0.81	0.49	167.62	0.97	162.59	0.15
Average						0.14
Cold fluid - 2-phase						
100%	0.81	0.70	2177.98	0.72	1558.50	
90%	0.81	0.63	2107.68	0.72	1527.94	0.19
80%	0.81	0.56	1883.06	0.72	1352.81	0.63
70%	0.81	0.49	2051.90	0.73	1504.41	0.10
Average						0.14
Cold fluid - Vapor						
100%	0.81	0.70	118.85	0.98	116.47	
90%	0.81	0.63	110.63	0.98	108.41	0.68
80%	0.81	0.56	103.13	0.98	101.06	0.64
70%	0.81	0.49	95.90	0.98	93.98	0.60
Average						0.64

It needs to be highlighted that in Table 6.3-6 there is one exponent (indicated in dark red) that clearly differs from the rest as the average of the effective heat transfer coefficient for that simulation is much lower than the rest. That result has not been considered as it is clearly wrong.

After the deep analysis on how the effective heat transfer coefficients vary, the off-design simulations can be performed including the results here obtained.

6.3.2. mGT

The part load performance of the system has been evaluated by simulating the system at different values of ambient temperature (from 0 ºC to 30 ºC) and the mGT rotating at different rotational speed (from 52000 rpm to 71000 rpm). All these simulations cover the whole range of interest under study and they are useful to know how the system behaves and to predict its steady-state result before proceeding with the dynamic simulations.

In this section, the main focus is to analyze how the performance of the mGT changes with respect to the nominal conditions.

On one hand, Figure 6.3-10 shows all the part load results (in light green) and the nominal point (in red) of all the performed simulations plotted in the compressor maps. On the left, it is shown how the pressure ratio changes with respect to the reduced mass flow at different values of reduced rotational speed. All the operating conditions are far from the surge line, guaranteeing good stability in the working conditions in the compressor. On the right, the variation of the efficiency of the compressor is shown with respect to the reduced mass flow.

On the other hand, Figure 6.3-11 shows all the part load results (in light green) and the nominal point (in red) of all the performed simulations plotted in the turbine maps. On the left, it is shown how the reduced mass flow changes with respect to the pressure ratio at different values of reduced rotational speed. For high values of pressure ratio, the turbine almost works in chocked conditions, with small variations of the reduced mass flow. On the right, how the efficiency changes with the pressure ratio at different values of reduced rotational speed is depicted. It can be highlighted that all the efficiency values are quite high, without entering a zone of high reduction of efficiency for both turbomachinery: turbine and compressor.

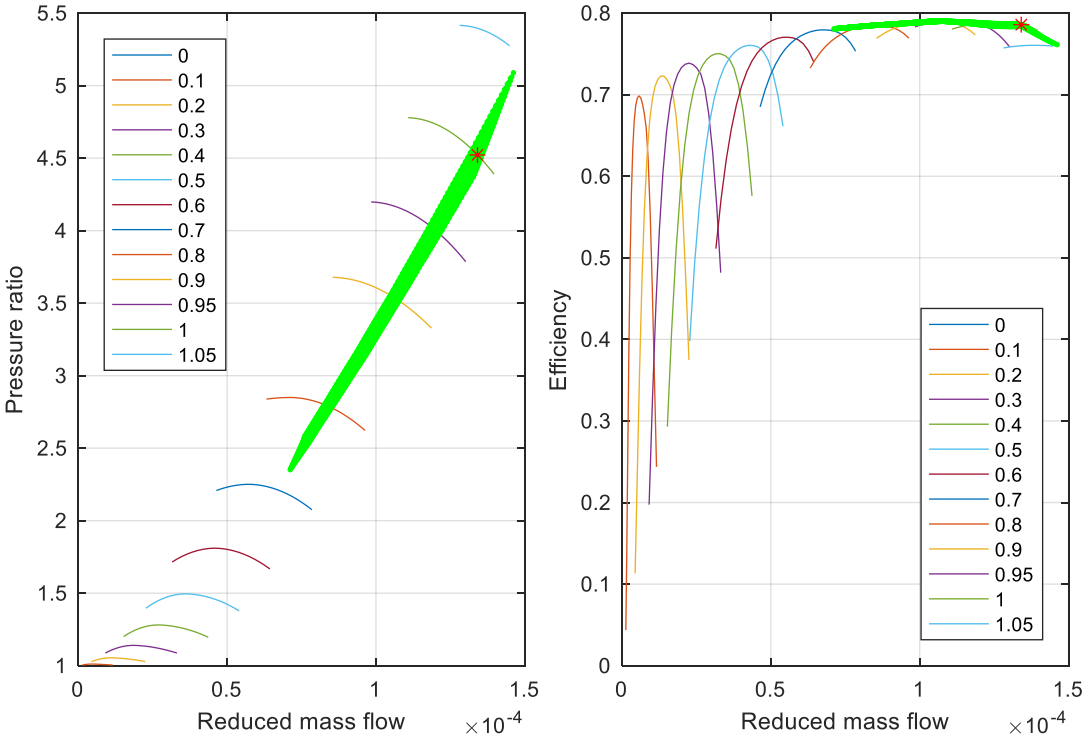

Figure 6.3-10 Part load (light green) and nominal (red) conditions shown in the characteristic map of the centrifugal compressor (left) and efficiency trend (right)

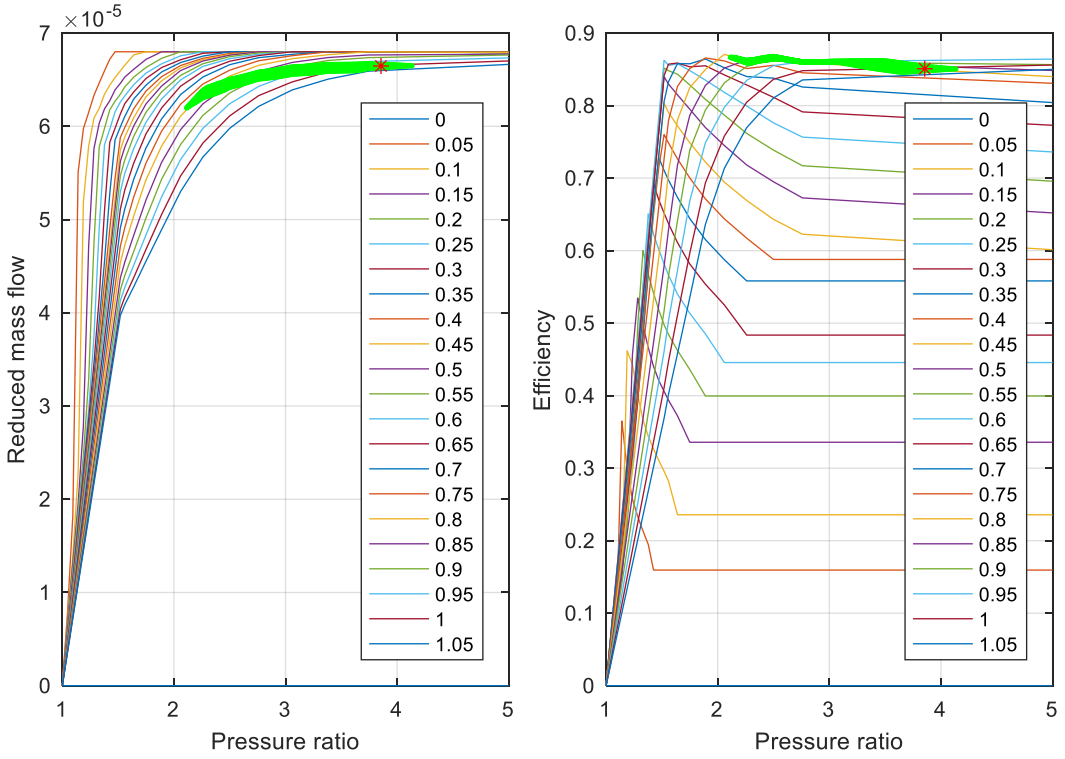

Figure 6.3-11 Part load (light green) and nominal (red) conditions shown in the characteristic map of the turbine (left) and efficiency trend (right)

Showing the operating points represented in the characteristics maps gives an overall view of all the simulations, but it cannot be appreciated the influence of both of the parameters modified to study the part load analysis, namely the ambient temperature and the rotational speed. However, showing the characteristics maps is fundamental to the deep understanding of the results.

Figure 6.3-12 represents the variation of the pressure ratio with respect to the ambient temperature and the rotational speed for both turbine (black lines) and compressor (red lines) and Figure 6.3-13 represents the variation of the reduced mass flow rate with respect to the ambient temperature and rotational speed for both turbine (black lines) and compressor (red lines).

If a horizontal line is taken to analyze the parameters on Figure 6.3-12 and Figure 6.3-13 (so just analyzing how the rotational speed affects to the parameters at a constant value of temperature), it can be seen that a reduction of a rotational speed yields to a reduction of both pressure ratio and reduced mass flow rate of both turbomachinery. This occurs as a consequence of a reduction of the reduced rotational speed. By looking at Figure 6.3-10 at the graphic on the left, if the reduced rotational speed is decreased, the curve correlating pressure ratio and reduced mass flow rate is displaced to a lower one, implying lower values of pressure ratio and reduced mass flow rate. By taking a vertical line in Figure 6.3-12 and Figure 6.3-13, it can be seen that the increment of the ambient temperature has qualitatively the same effect as decreasing the reduced rotational speed. Thus, higher ambient temperature implies lower values of pressure ration and mass flow rate. This fact is justified as the temperature is on the denominator of the reduced rotational speed, so an increment of the temperature yields to a decrease of the reduced rotational speed, thus, a reduction of pressure ratio and reduced mass flow rate. The reduction of the reduced mass flow rate has the consequence of the reduction of the intake air, as depicted in Figure 6.3-14. It can be appreciated in Figure 6.3-12 that the pressure ratio of the turbine follows the same tendency as the pressure ratio of the compressor. The difference in values is justified by the pressure drops in the cycle.

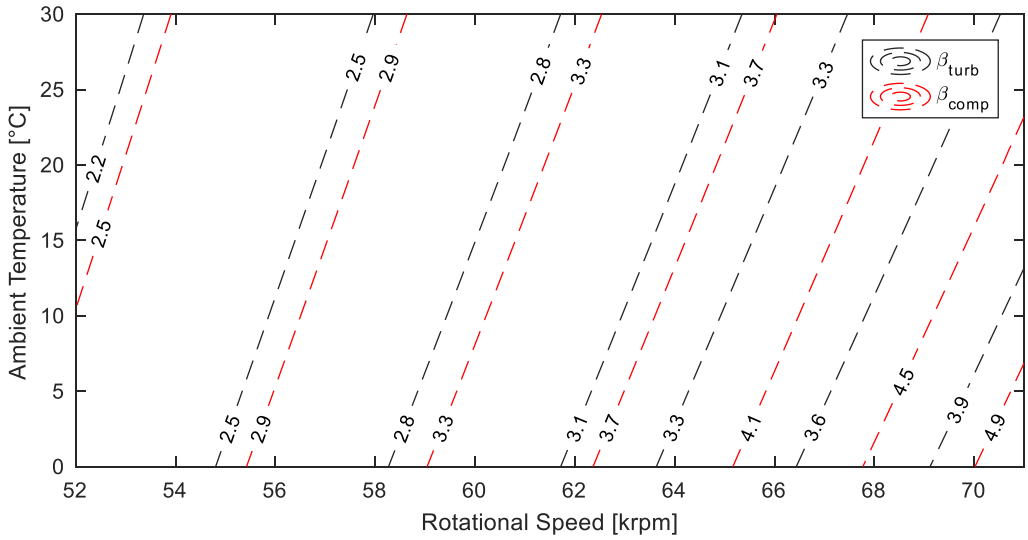

Figure 6.3-12 Variation of the pressure ratio in turbine and compressor with the ambient temperature and rotational speed

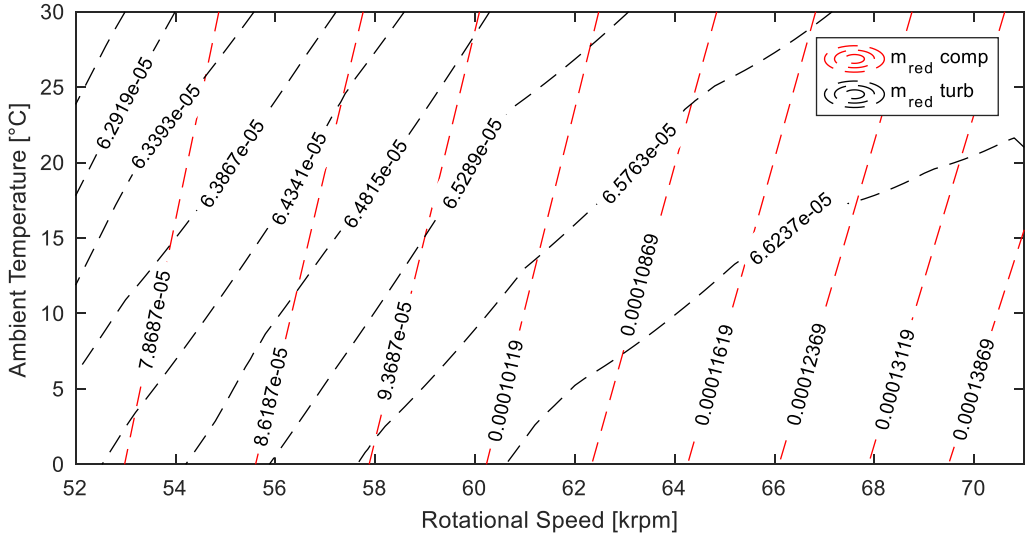

Figure 6.3-13 Variation of the reduced mass flow rate of the turbine and compressor with the ambient temperature and rotational speed

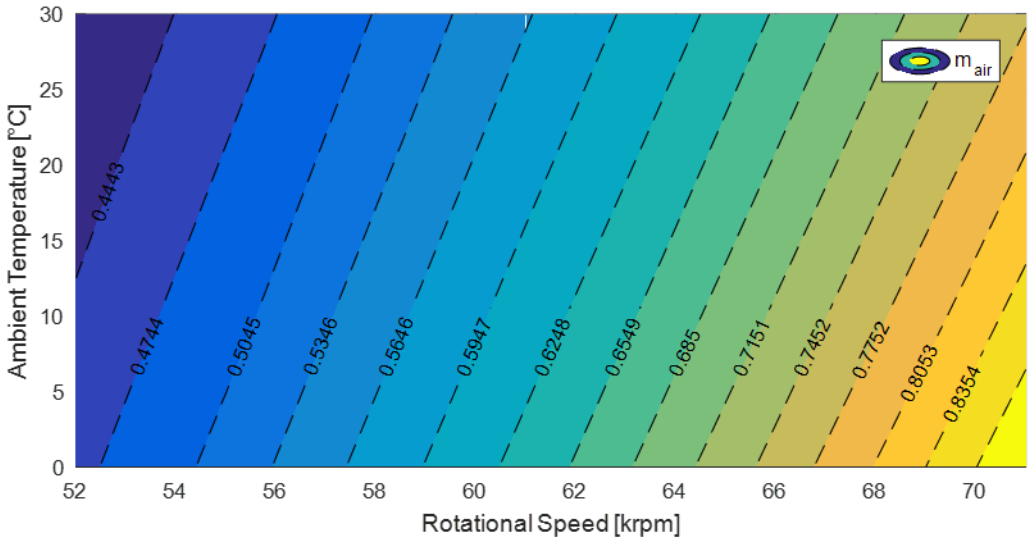

Figure 6.3-14 Variation of the air mass flow rate entering the mGT with the ambient temperature and rotational speed

Figure 6.3-15 represents the variation of the effectiveness of the regenerator with the ambient temperature and the rotational speed. The discussion about the effectiveness follows the opposite tendency of the mass flow rate. As a consequence of the reduction of the intake air mass flow rate, the regenerator is oversized, therefore, its effectiveness increases.

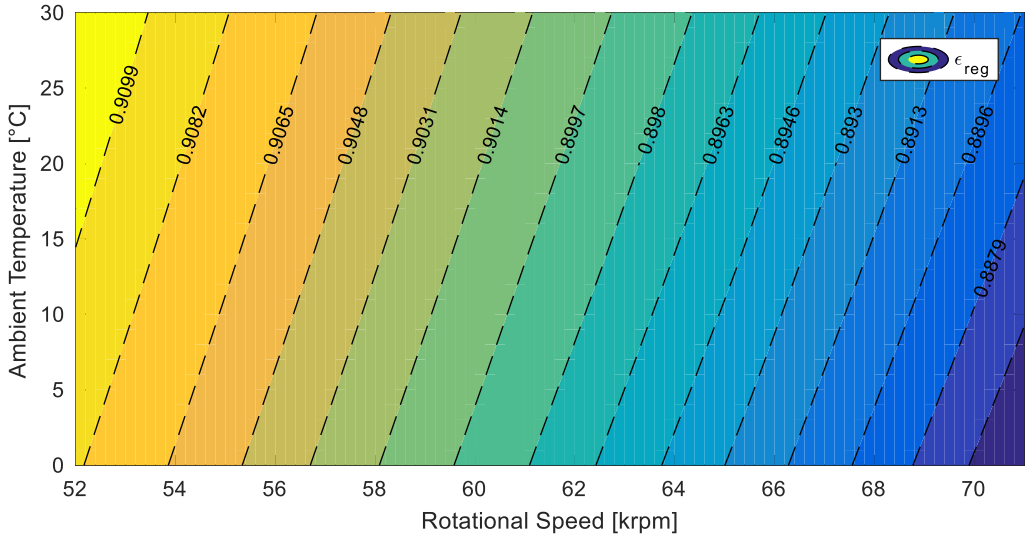

Figure 6.3-15 Variation of the effectiveness of the mGT regenerator with the ambient temperature and rotational speed

Figure 6.3-16 shows the map in which the variations of electric power (black line), electric efficiency (dashed red line) and the TIT (color map) are represented with respect to the ambient temperature and the rotational speed.

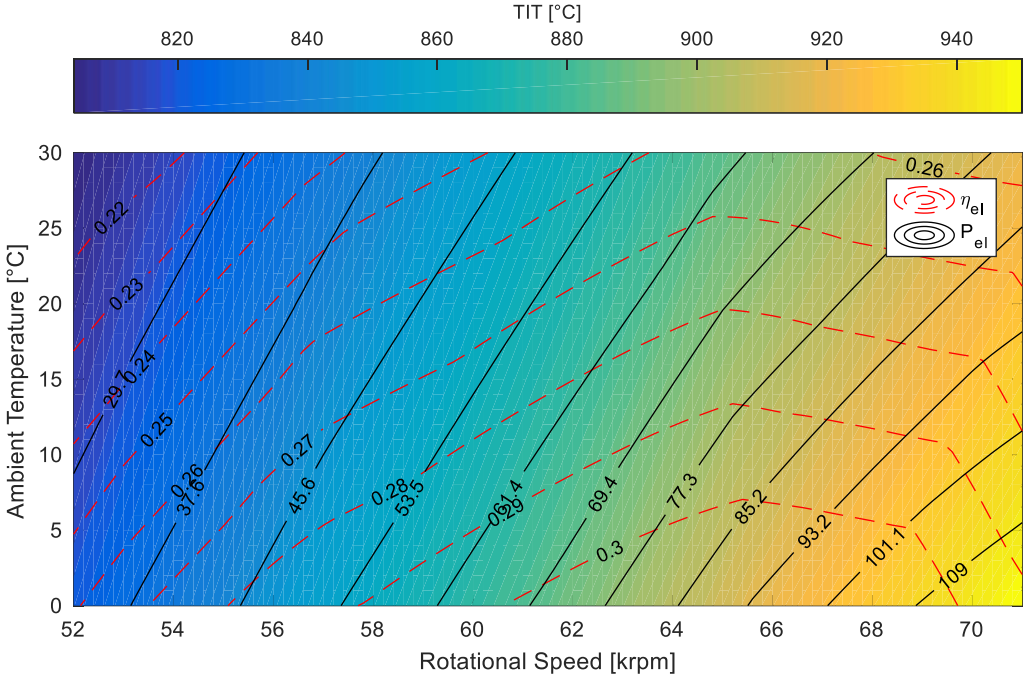

Figure 6.3-16 Variation of the mGT electric power and electric efficiency with the ambient temperature and rotational speed

Figure 6.3-17 shows a different type of map in which, in this case, the study is made not with the simulations done by varying the ambient temperature and the rotational speed, but this latter one is substituted with the electric power, and the electric efficiency (dashed red line), the rotational speed of the turbomachinery (dashed black line), the heat input (dashed blue line) and the TIT (color map) are represented. In this case, the maximum electric power can be obtained at higher values of rotational speed and lower values of ambient temperature, thus, at the higher values of air mass flow rate, the TIT and the pressure ratio. As the axes have been changed, there are not enough simulated cases for the whole projected map, therefore, there are some white zones in which the rotational speed would correspond to values out of the range between 52 and 70krpm.

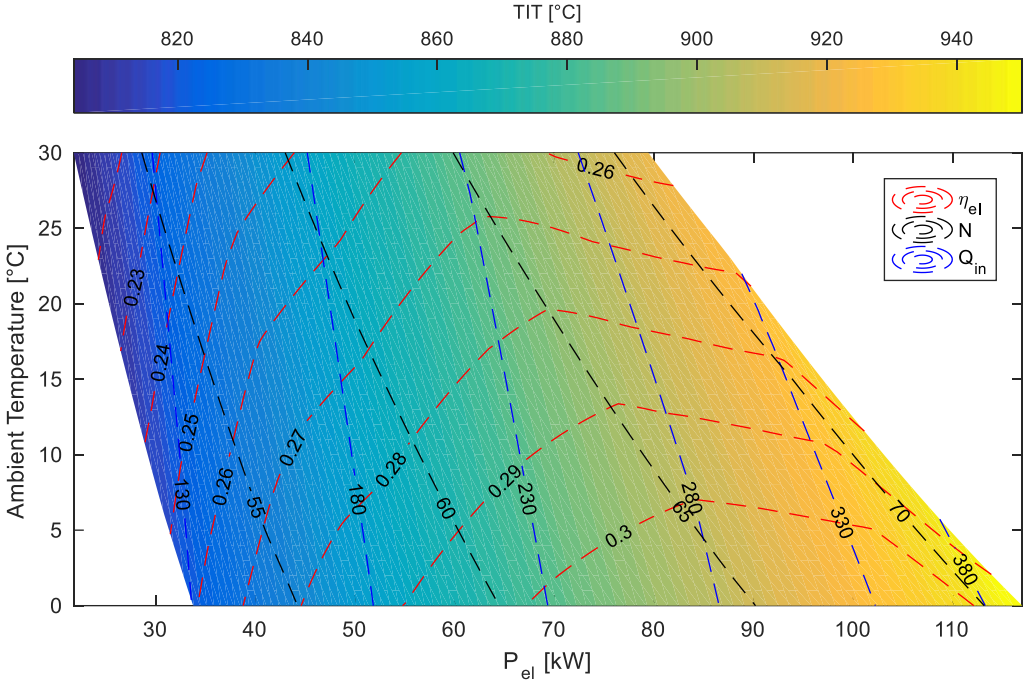

Figure 6.3-17 Variation of the mGT electric efficiency, the heat input and the rotational speed with the ambient temperature and electric power produced

6.3.3. ORC

After analyzing how the performance of the mGT changes with a variation of the ambient temperature and rotational speed, some analysis should be done to know how the performance of the ORC changes.

The description of the performance of the ORC module differs from how the performance of the mGT has been exposed. In this case, instead of studying the overall maps, the main focus will be done considering the variation of the cycle in terms of the T-s diagram and the T-Q diagrams of each heat exchanger of the ORC module.

Three analyses are shown here. These three analyses will be explained in the next lines. In all of them, the red line indicates the nominal case (i.e the conditions at which the ORC module has been designed while the mGT works at 70000 rpm and the ambient temperature is equal to 15 °C).

The first study case is shown in Figure 6.3-18 (see Table 6.3-7 for further numeric details). It consists in analyzing the performance of the ORC when the turbomachinery is rotating at 60000 rpm and at ambient temperature equal to 15°C, considering two different types of control of the condensation pressure of the ORC working fluid: keeping the condensation pressure fixed by varying the mass flow rate of cooling water (dashed line) and letting the condensation pressure varies in sliding

mode by fixing the mass flow rate of cooling fluid (dot-dashed line). As the only parameter which is modified is the way of controlling the condensation pressure of the ORC system, there is no variation of the performance of the mGT between the two cases.

In this case, the T-s diagram of the ORC keeps almost the same, so the variations of the cycle are minimal from one case to the other. The most important graphic for this analysis is the T-Q diagram of the condenser. In this case, when keeping the mass flow rate of cooling fluid as a constant value and working in sliding pressure mode, as the ORC working fluid mass flow rate is reduced in part load, the tendency is to lower down the condensation pressure, lowering the temperature difference. Varying the condensation pressure would allow a higher pressure ratio in the turbine, yielding to a higher power produced with it. In the case in which the condensation pressure is kept as a constant value by modifying the mass flow rate of the cooling fluid, the pressure ratio could be limited in comparison with the previous case. However, the reduction of the cooling fluid has the consequence of a lower consumption of the pump. Therefore, the net produced power should be computed numerically in order to get a clear conclusion. In this particular case, by analyzing the numerical results reported in Table 6.3-7, in the case in which the ORC is working in condensation sliding pressure mode, the electric production of the ORC turbine is 13.61 kWe, which is higher than the produced power if the constant pressure is kept constant (13.03 kWe). However, the mass flow rate of the cooling fluid decreases from 8.16 kg/s to 2.87 kg/s, yielding to a reduction of the electric consumption of the pump from 1.22 kWe to 0.05 kWe. As the reduction of the power consumed by the pump is much higher than what is gained with the turbine, it is more convenient to keep the condensation pressure constant, producing a net electric power of 12.67 kWe instead of 12.08 kWe in condensation sliding pressure mode. This is an example case which is representative of most of the simulated cases. Therefore, for the next analysis, the condensation pressure has been kept constant. Moreover, this consideration allows the simplification of the dynamic model, as the condenser can be modeled as a constant pressure one (see section 5.3.6).

The second study case is shown in Figure 6.3-19 (see Table 6.3-8 for further numeric details). It consists in analyzing how the performance of the ORC changes when the ambient temperature is equal to 15ºC but the mGT turbomachinery varies its rotational speed from 55000 rpm (darkest blue) till 71000 rpm (lightest blue).

As the consequence of the partial load of the mGT, in which the temperature and mass flow rate of the flue gases are reduced (it can be appreciated qualitatively in the T-Q diagram of the primary heat exchanger with the slope of the curves and the maximum temperature and quantitatively in Table 6.3-8), the heat entering the ORC module is reduced. By decreasing the heat input, the evaporating pressure also

decreases (considering the two limiting cases of 71000 rpm and 55000 rpm, from 15.35 bar to 7.05 bar). Moreover, the TIT of the ORC is kept at the nominal value (i.e. 139.82 ºC) if the physical conditions allow it (i.e. the temperature and mass flow of the flue gases is high enough); if not, it is reduced till reaching the convergence of the system. This can be seen in the case in which the mGT turbomachinery rotates at 55000 rpm, in which the TIT is reduced till a value of 115.82ºC. By reducing the load of the ORC, the electric efficiency varies, but it stays in the range of 15%, however, if the heat load coming from the mGT is so low that the TIT has to be reduced, the efficiency of the cycle drops to values lower than 12.5%. By analyzing qualitatively the T-Q of the condenser, it can be seen how the mass flow rate of the cooling fluid is decreased (the slope increases) with the part load conditions to keep the same condensation pressure. Quantitatively, the mass flow rate of the cooling fluid decreases from 9.91 kg/s to 2.11 kg/s in the two limit cases (i.e. 71000 rpm and 55000 rpm).

The third study case is shown in Figure 6.3-20 (see Table 6.3-7 and Table 6.3-9 for further numeric details). In this case, the study consists in varying the ambient temperature (two limit cases have been considered at 0 and 30ºC) but keeping the rotational speed constant at 60000 rpm. The differences between these two cases are just small in comparison with the previous studied cases. When working at higher temperature, the mass flow of the flue gases is clearly reduced (as seen in section 6.3.2) from 0.62 kg/s at 0ºC to 0.55 kg/s at 30ºC; however, the temperature of the flue gases is increased from 210.96ºC at 0ºC to 232.74 ºC at 30 ºC (it can be seen qualitatively in the T-Q diagram of the primary heat exchanger). This is a consequence of the fact that the intake air enters in the mGT compressor at a higher temperature, exiting also at a higher temperature. Therefore, as the mGT TOT is kept constant at 645ºC, if the lower temperature of the cold side is higher, the temperature exiting the regenerator will be higher, so hotter flue gases exiting the mGT. The increment of the flue gases temperature has the consequence of a higher ORC working fluid mass flow rate: 0.37 kg/s at 0ºC and 0.39 kg/s at 30ºC and an increment of the evaporation pressure: 8.56 bar at 0ºC and 8.85 bar at 30ºC. This has the overall effect of a slightly higher electricity production of the ORC when the ambient temperature is reduced. However, the increment of the electricity production with the ORC (from 12.24 kWe at 0ºC to 12.96 kWe at 30 ºC) is really small in comparison with the effect of the increment of the ambient temperature in the reduction of the electric power produced by the mGT (from 66.78 kWe at 0ºC to 44.58 kWe at 30 ºC).

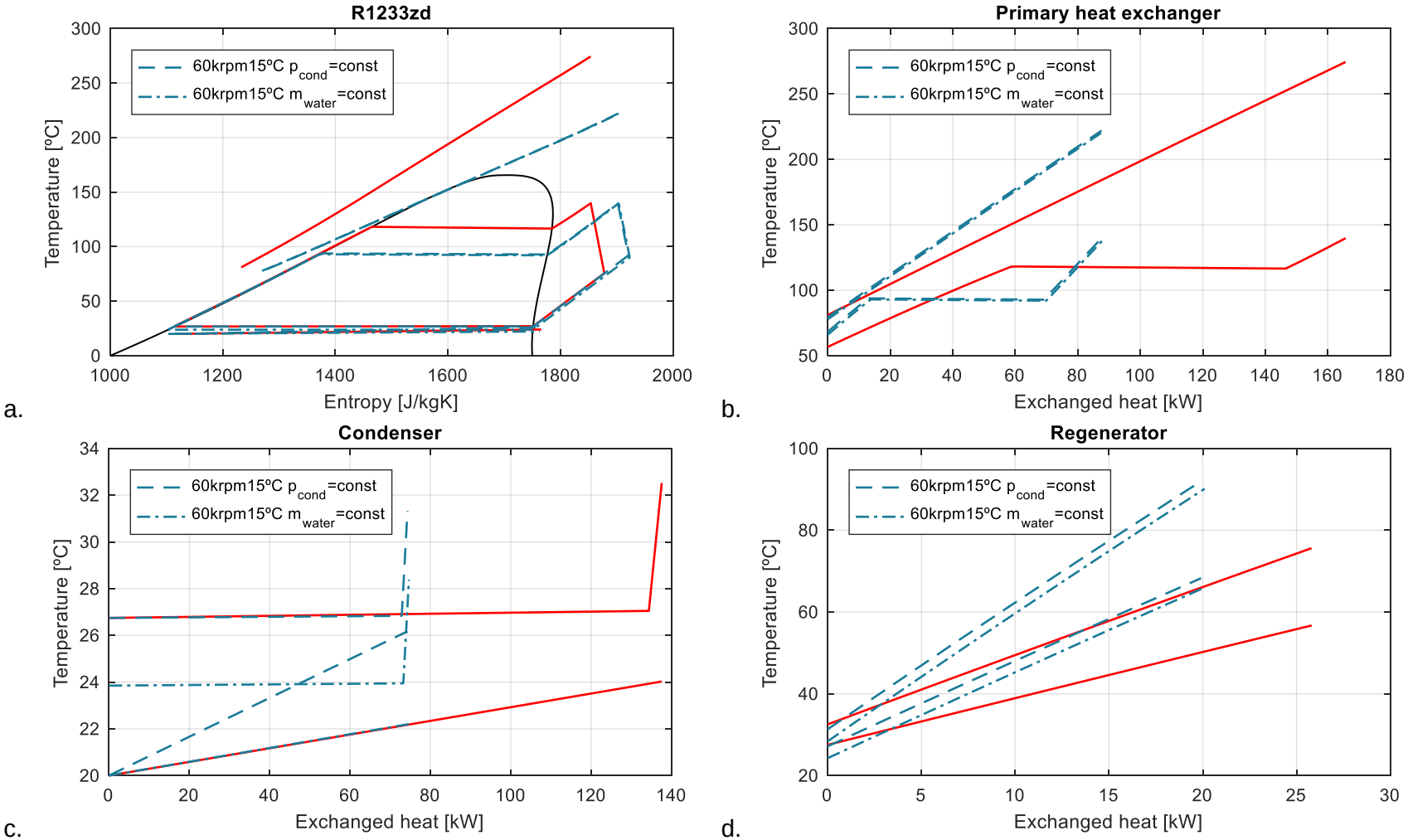

Figure 6.3-18 T-s diagram (a), T-Q diagram of the primary heat exchanger (b), condenser (c) and regenerator (d) of the ORC varying the type of control of the condenser: fixed condensation pressure (dashed line) / fixed cooling fluid mass flow rate (dash-dotted line)

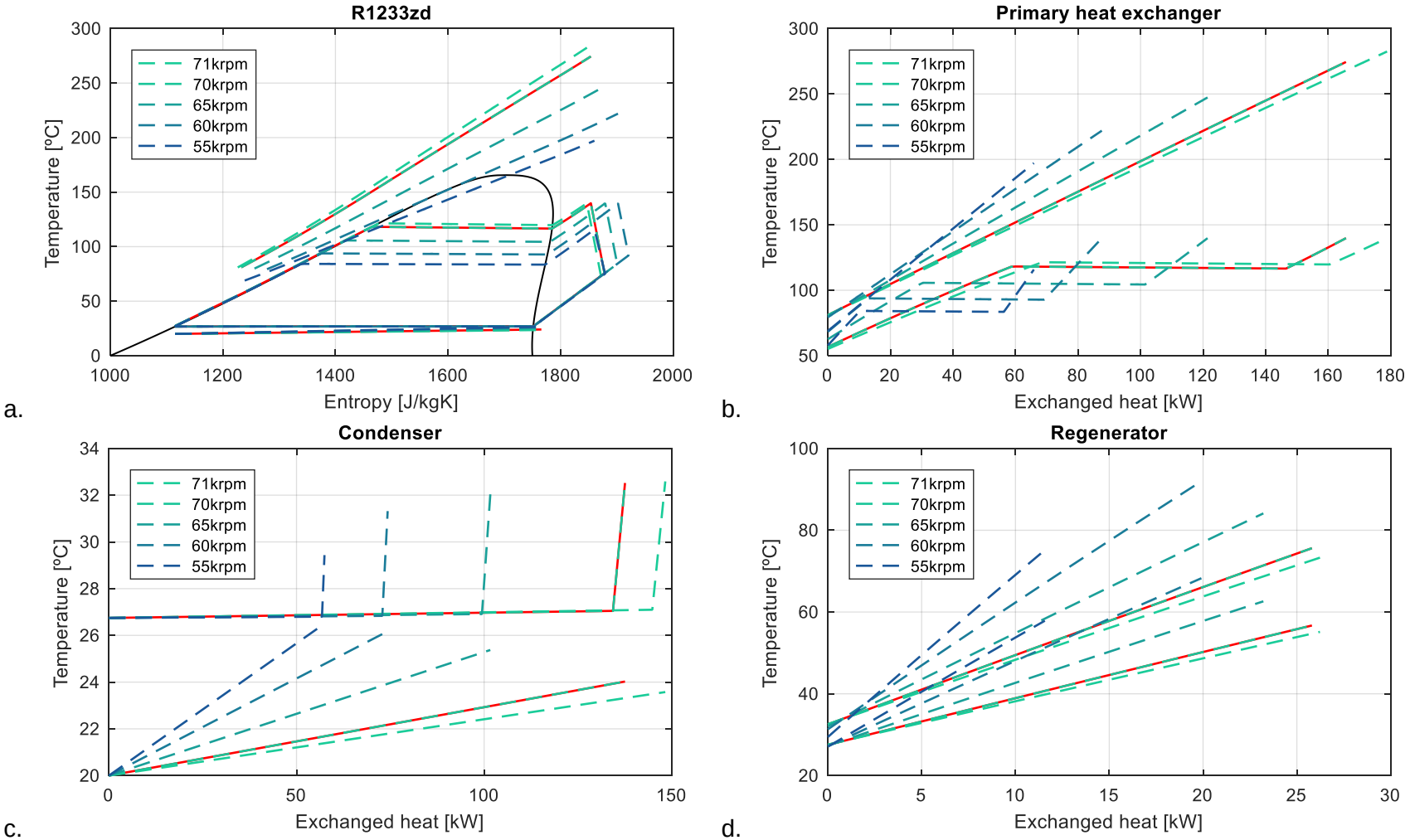

Figure 6.3-19 T-s diagram (a), T-Q diagram of the primary heat exchanger (b), condenser (c) and regenerator (d) of the ORC varying the mGT rotational speed with an ambient temperature of 15ºC

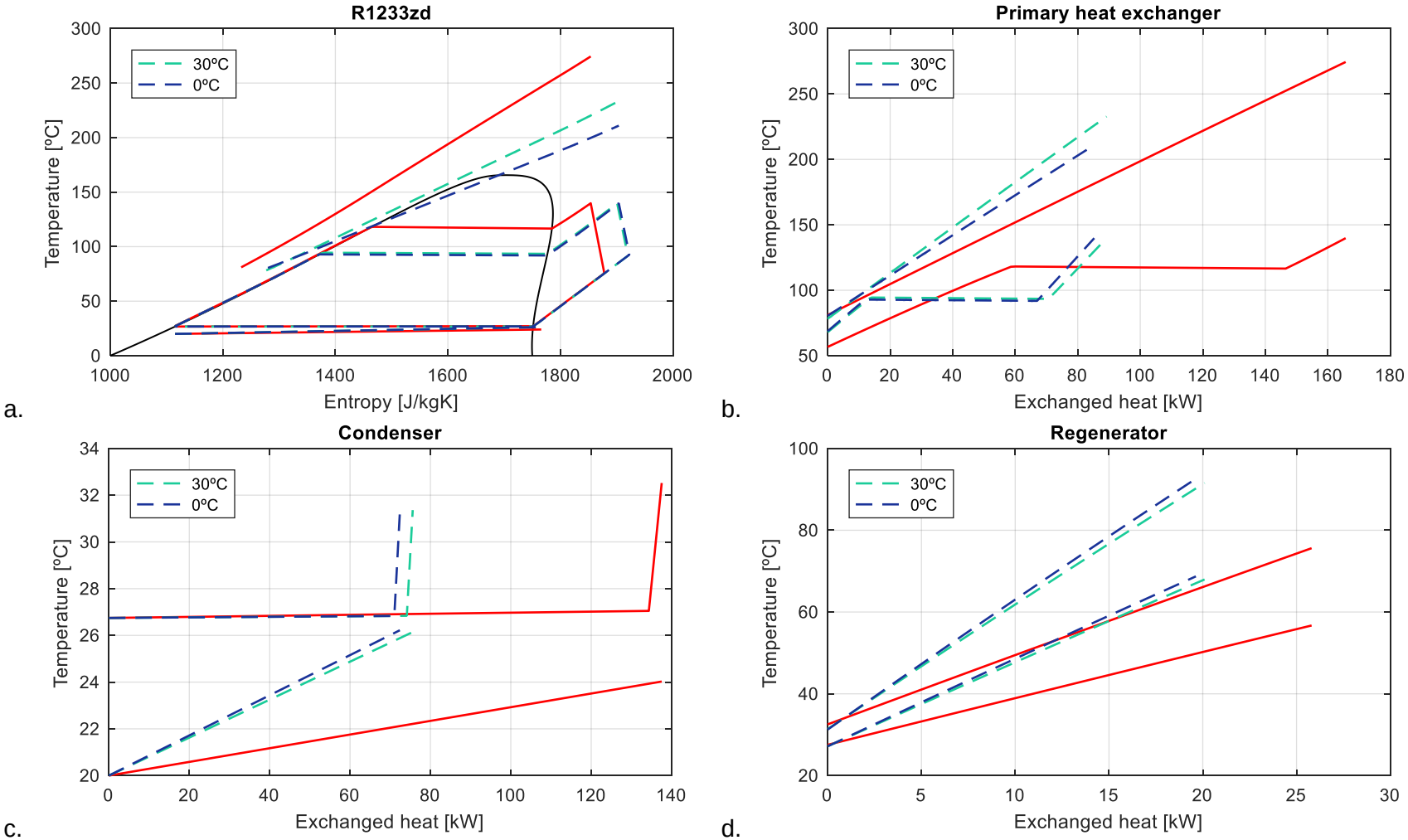

Figure 6.3-20 T-s diagram (a), T-Q diagram of the primary heat exchanger (b), condenser (c) and regenerator (d) of the ORC varying the ambient temperature with the mGT rotating at 60000rpm

Table 6.3-7 Performance of the overall system changing the condensation pressure control

	Nominal	Constant p_{cond}	Constant $\dot{m}_{water}$
N_{mGT} [rpm]	70000	60000	60000
T_{amb} [ºC]	15	15	15
$\varepsilon_{reg,mGT}$ [%]	88.87	90.10	90.10
$\eta_{comp,mGT}$ [%]	78.57	78.80	78.80
$\eta_{turb,mGT}$ [%]	84.99	86.02	86.02
T_{fg} [ºC]	274.45	221.95	221.95
$\dot{m}_{fg}$ [kg/s]	0.81	0.58	0.58
$\dot{m}_{ORC}$ [kg/s]	0.70	0.38	0.38
$P_{turb,ORC}$ [kW]	28.05	13.03	13.61
$P_{pump,ORC}$ [kW]	1.05	0.31	0.31
$P_{pump,water}$ [kW]	1.22	0.05	1.22
$P_{el,ORC}$ [kW]	25.77	12.67	12.08
$\dot{m}_{water}$ [kg/s]	8.16	2.87	8.16
p_8 [bar]	1.38	1.38	1.24
p_{11} [bar]	14.43	8.73	8.57
T_{cond} [ºC]	26.75	26.75	23.85
TIT_{ORC} [ºC]	139.82	139.82	139.82
$\eta_{turb,ORC}$ [%]	83.19	83.77	83.94
$\eta_{el,ORC}$ [%]	15.55	14.46	13.67
$P_{el,mGT}$ [kW]	93.89	52.76	52.76
$\eta_{el,mGT}$ [%]	28.26	27.33	27.33
P_{total} [kW]	119.66	65.42	64.87
$\eta_{el,total}$ [%]	36.01	33.90	33.61
$P_{el,\ stand\text{-}alone\ mGT}$ [kW]	99.89	54.73	54.73
$\eta_{el,\ stand\text{-}alone\ mGT}$ [%]	29.48	28.02	28.02

Table 6.3-8 Performance of the overall system changing the rotational speed of the mGT

N_{mGT} [rpm]	70000	71000	65000	60000	55000
T_{amb} [ºC]	15	15	15	15	15
$\varepsilon_{reg,mGT}$ [%]	88.87	88.72	89.52	90.10	90.69
$\eta_{comp,mGT}$ [%]	78.57	77.62	78.87	78.80	78.41
$\eta_{turb,mGT}$ [%]	84.99	84.81	86.13	86.02	86.40
T_{fg} [ºC]	274.45	282.46	247.33	221.95	197.14
$\dot{m}_{fg}$ [kg/s]	0.81	0.84	0.69	0.58	0.49
$\dot{m}_{ORC}$ [kg/s]	0.70	0.76	0.52	0.38	0.30
$P_{turb,ORC}$ [kW]	28.05	30.55	19.51	13.03	8.25
$P_{pump,ORC}$ [kW]	1.05	1.22	0.58	0.31	0.18
$P_{pump,water}$ [kW]	1.22	2.19	0.21	0.05	0.02
$P_{el,ORC}$ [kW]	25.77	27.14	18.73	12.67	8.04
$\dot{m}_{water}$ [kg/s]	8.16	9.91	4.52	2.87	2.11
p_8 [bar]	1.38	1.38	1.38	1.38	1.38
p_{11} [bar]	14.43	15.35	11.24	8.73	7.05
T_{cond} [ºC]	26.75	26.75	26.75	26.75	26.75
TIT_{ORC} [ºC]	139.82	139.82	139.82	139.82	115.82
$\eta_{turb,ORC}$ [%]	83.19	83.01	83.66	83.77	81.39
$\eta_{el,ORC}$ [%]	15.55	15.17	15.42	14.46	12.21
$P_{el,mGT}$ [kW]	93.89	96.90	73.82	52.76	35.66
$\eta_{el,mGT}$ [%]	28.26	27.64	28.72	27.33	25.28
P_{total} [kW]	119.66	124.04	92.55	65.42	43.71
$\eta_{el,total}$ [%]	36.01	35.39	36.00	33.90	30.98
$P_{el,\ stand\text{-}alone\ mGT}$ [kW]	99.89	103.63	77.21	54.73	36.82
$\eta_{el,\ stand\text{-}alone\ mGT}$ [%]	29.48	28.96	29.59	28.02	25.84

Table 6.3-9 Performance of the overall system changing the ambient temperature

N_{mGT} [rpm]	70000	60000	60000
T_{amb} [ºC]	15	30	0
$\varepsilon_{reg,mGT}$ [%]	88.87	90.28	89.92
$\eta_{comp,mGT}$ [%]	78.57	78.67	78.92
$\eta_{turb,mGT}$ [%]	84.99	86.20	85.97
T_{fg} [ºC]	274.45	232.74	210.96
$\dot{m}_{fg}$ [kg/s]	0.81	0.55	0.62
$\dot{m}_{ORC}$ [kg/s]	0.70	0.39	0.37
$P_{turb,ORC}$ [kW]	28.05	13.34	12.59
$P_{pump,ORC}$ [kW]	1.05	0.32	0.29
$P_{pump,water}$ [kW]	1.22	0.06	0.06
$P_{el,ORC}$ [kW]	25.77	12.96	12.24
$\dot{m}_{water}$ [kg/s]	8.16	2.94	2.78
p_8 [bar]	1.38	1.38	1.38
p_{11} [bar]	14.43	8.85	8.56
T_{cond} [ºC]	26.75	26.75	26.75
TIT_{ORC} [ºC]	139.82	139.82	139.82
$\eta_{turb,ORC}$ [%]	83.19	83.78	83.75
$\eta_{el,ORC}$ [%]	15.55	14.52	14.35
$P_{el,mGT}$ [kW]	93.89	42.99	64.46
$\eta_{el,mGT}$ [%]	28.26	24.92	29.81
P_{total} [kW]	119.66	55.95	76.70
$\eta_{el,total}$ [%]	36.01	32.43	35.47
$P_{el,\ stand\text{-}alone\ mGT}$ [kW]	99.89	44.58	66.78
$\eta_{el,\ stand\text{-}alone\ mGT}$ [%]	29.48	25.56	30.50

6.3.4. Overall system

The performance of the overall system is a conclusion of the analysis performed in the sections described before (6.3.2 and 6.3.3), and to deepen into detail, the reader should refer to them. In Table 6.2-10 of section 6.2.3 the main parameters of the overall system at nominal conditions are reported.

Here, how the electric power produced by the mGT working in stand-alone conditions changes with respect to a system in which the mGT is combined with a bottoming cycle to recover the remaining heat is shown. Figure 6.3-21 represents the electric power that the mGT can produce by working in stand-alone conditions for different values of ambient temperature and rotational speed. Figure 6.3-22 shows how the electric power produced by the mGT by its own is decreased if it is coupled with a bottoming heat exchanger. Finally, Figure 6.3-23 represents the total power produced by the overall system formed by the mGT and the ORC designed in this work, for different values of ambient temperature and rotational speed.

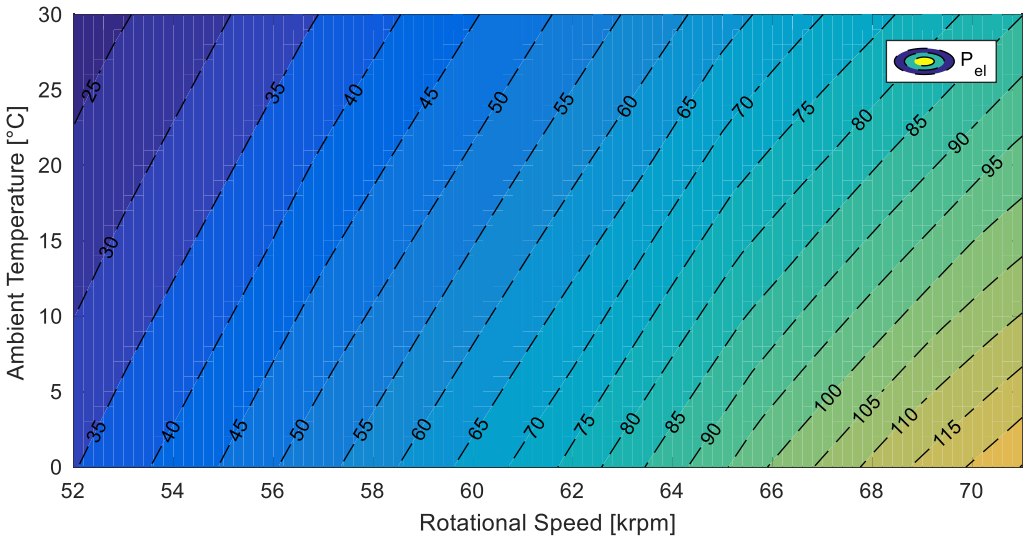

Figure 6.3-21 Variation of the mGT electric power with the ambient temperature and rotational speed

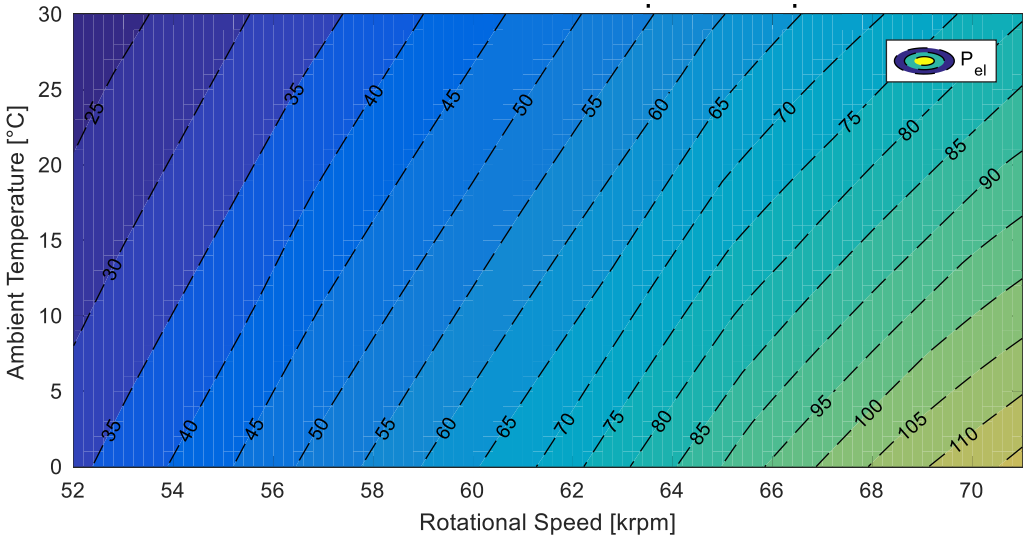

Figure 6.3-22 Variation of the mGT electric power with the ambient temperature and rotational speed considering the effect of the primary heat exchanger of the bottoming ORC

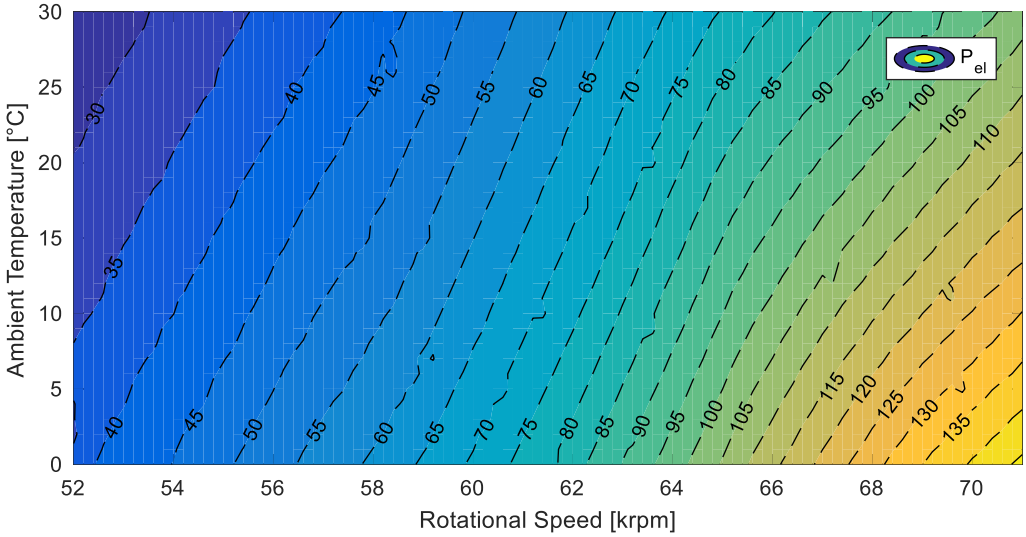

Figure 6.3-23 Variation of the power produced by the overall system mGT+ORC with the ambient temperature and rotational speed.

6.4. Dynamic performance

Along this section, the dynamic results will be presented.

First, a validation in steady-state conditions with both models is done. The comparison is between the results at part load conditions from the steady-state model implemented in Matlab® and the results from the dynamic model implemented in Dymola.

Second, the results from open-loop simulations, in which the rotational speed is reduced by a step of 5% without modifying any other parameter, are shown.

Third, the analysis of the couplings among manipulated variables (i.e. fuel mass flow rate, rotational speed and mass flow rate of the ORC working fluid) is performed and the tuning of the PI controllers to be implemented is done.

Fourth, in order to analyze the flexibility of the whole system and study the dynamic response, the electricity-demand profile is applied to the system. The profile collects the electricity demand of a set of 150 houses in Cologne, Germany. The relevance of the study does not stand on studying the whole year demand, but on analyzing how well the system composed by the mGT with ORC responds to the variations. Therefore, it has been decided to perform the dynamic simulations of the two most critical days of the year (i.e. maximum and minimum load).

6.4.1. Validation

As stated in the Chapter 5. , the dynamic simulations have been performed by using a specific software by implementing dynamic models and using its libraries. As all the steady-state simulations have been performed with an ad-hoc model implemented in Matlab® which differs from the dynamic model, before performing the dynamic analysis, a validation with the steady-state results has been completed. In order to do this validation, different operating conditions have been taken into account considering the range in which the final dynamic analysis will be performed. These operating conditions are two different temperatures (i.e. 0 and 15 ºC) and four different values of rotational speed (i.e. 55, 60, 65 and 70 krpm). As the dynamic model is been tested, the values of fuel mass flow rate and ORC working fluid mass flow rate (which are manipulated variables in the dynamic system as indicated in section 5.4) have been imposed to the ones obtained with the steady-state model. After imposing those values, the reached steady-state conditions obtained with the dynamic model in Dymola are compared to the ones obtained with the steady-state model in Matlab®. Table 6.2-1 shows the results of the total electric power output, which is the parameter selected for the validation. It can be highlighted that the difference of the electric power produced with both models is less than 1%.

Therefore, it can be said that both models are coherent, and the steady-state conditions of the dynamic model are guaranteed.

Table 6.4-1 Comparison of the produced electric power with the steady-state model in Matlab® and the dynamic model in Dymola

N [krpm]	T_{amb} [ºC]	P_{el} [kW] (steady-state model)	P_{el} [kW] (dynamic model)	Difference [%]
70	15	119.66	118.93	-0.617%
65	15	92.55	92.05	-0.549%
60	15	65.42	65.66	0.369%
55	15	43.71	43.84	0.295%
70	0	139.31	139.73	0.301%
65	0	108.79	107.86	-0.854%
60	0	76.70	76.62	-0.107%
55	0	51.86	51.89	0.046%

6.4.2. Open-loop simulations

After validating the dynamic model with the steady-state one, some simulations have been performed by varying one of the manipulated variables in step, without modifying the rest. In this section, a reduction of the 5% of the rotational speed is done. This simulation aims to analyze what happens if one variable is modified in open-loop conditions without any kind of control system.

At the very beginning of the case under study, the system is working at nominal conditions, imposed with the results of the steady-state model. After 1000 s, the rotational speed is reduced following a step of 5% of the nominal value. As no other variables are modified to compensate that variation, the reduction of the rotational speed yields to a reduction of the intake air mass flow rate (as explained in section 6.3.2). If there is a reduction of the intake air mass flow rate but the fuel mass flow rate is not modified, the heat input is so high that the TIT increases considerably, provoking structural damages to the heat exchanger and potentially to the turbine. Therefore, a control system is needed to avoid this kind of situations in which the controlled variables stay at the value imposed. Even if there are some perturbations on the system, the control system should guarantee good conditions. The implemented control system will be presented in the next sections.

Figure 6.4-1 shows the time response of the intake air mass flow rate (orange) with a step reduction of the 5% of the mGT turbomachinery rotational speed (blue). Figure

6.4-2 represents the time response of the mGT TIT (orange) with a step reduction of the 5% of the mGT turbomachinery rotational speed (blue).

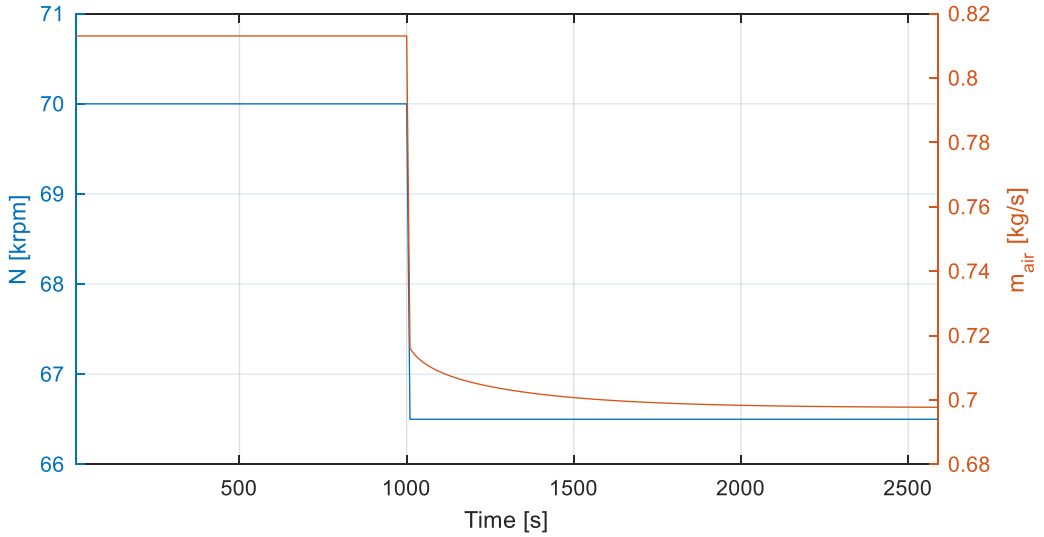

Figure 6.4-1 Response of air mass flow rate with the reduction of 5% of the rotational speed

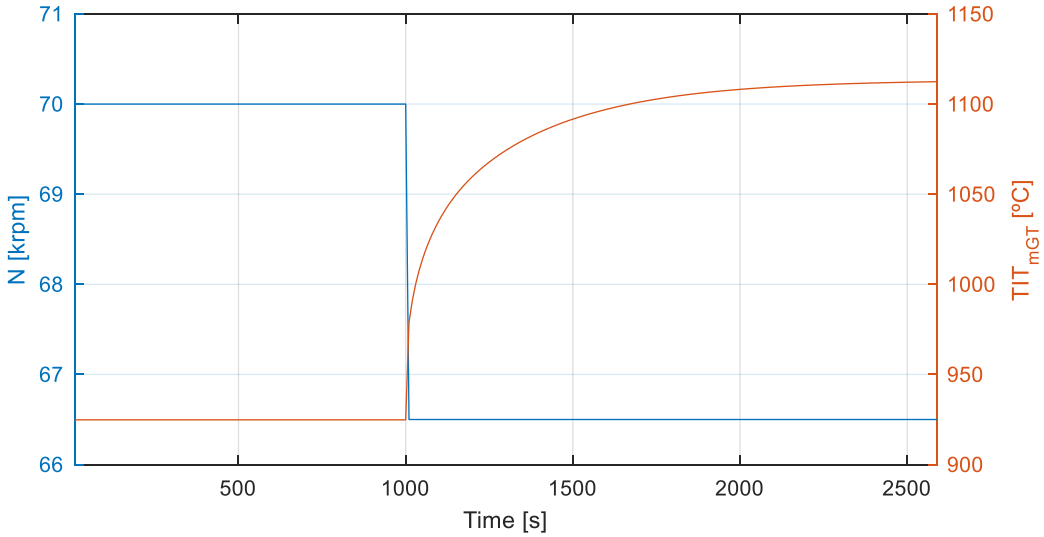

Figure 6.4-2 Response of mGT TIT with the reduction of 5% of the rotational speed

6.4.3. Control

After demonstrating that a control system is needed, it is mandatory to analyze the mutual interactions between the manipulated variables and their effect in the controlled variables. After performing the analysis of the mutual interactions, the tuning of the controllers is made.

6.4.3.1. Analysis of the couplings

To evaluate the proper match of the manipulated variables (i.e. fuel mass flow rate, mGT rotational speed and ORC working fluid mass flow rate) with the controlled variables (i.e. total electric power, mGT TOT and ORC TIT) and the mutual interactions among them, the RGA matrix should be evaluated. For this evaluation, linearization nearby different equilibrium points should be made (see section 5.4.3 for more information).

As explained in the section 5.4.2, the linearization of the system has been done for 8 different cases which are representative of the operating conditions that will be studied dynamically. These cases consider two different temperatures (0 and 15 ºC) and four different rotational speeds (55, 60, 65 and 70 krpm). The reader should refer to the Section 5.4.2 and Appendix C to understand how the linearization was made. After performing the linearization nearby the equilibrium points indicated by imposing the conditions of the steady-state model, the transfer functions have been obtained through specific commands in Matlab® indicated in the Appendix C. Once the transfer functions have been obtained, the gain matrix can be computed for each performed linearization. After computing the gain matrix, it is possible to evaluate the RGA matrix, which describes the impact of each manipulated variable on each controlled variable, as explained in section 5.4.3. For each linearization a 3x3 function transfer matrix is obtained, leading to a 3x3 gain matrix and a 3x3 RGA matrix, which correlates the three inputs (i.e. fuel mass flow rate, mGT rotational speed and ORC working fluid mass flow rate) with the three outputs (i.e. total electric power, mGT TOT and ORC TIT). Figure 6.4-3 shows the diagonal elements of the RGA matrix of the different linearization points studied. As explained in section 5.4.3, the diagonal elements of the RGA matrix should be as close as 1 as possible. This is an indicator of a good coupling between input and output (i.e. each controlled variable reacts to the effect of each manipulated variable separately).

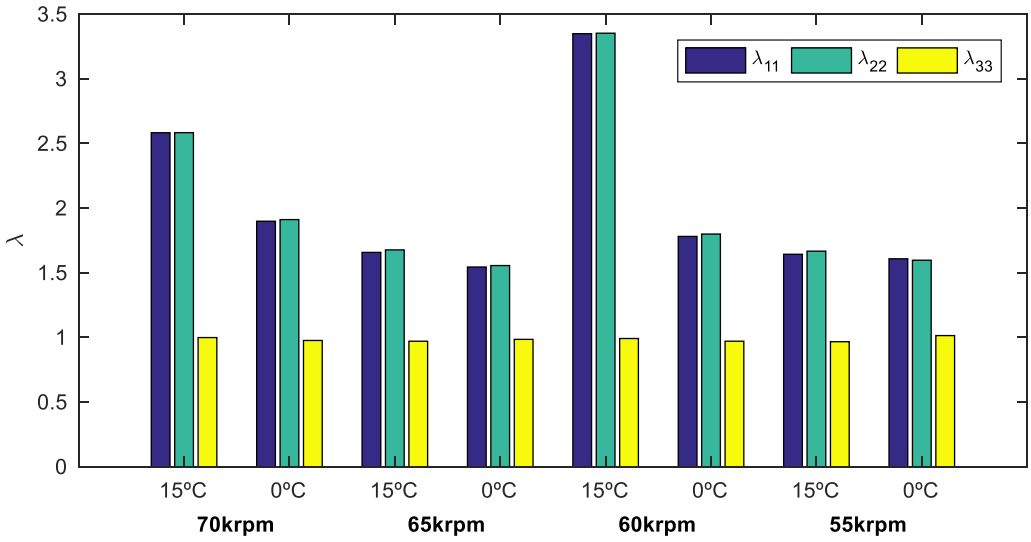

Figure 6.4-3 Diagonal elements of the RGA matrix of the system

In this case, by looking at Figure 6.4-3, the pair formed by the manipulated and controlled variables defined by ORC working fluid mass flow rate and ORC TIT, respectively, shows a perfect match, with no interactions (λ_{33} is equal to 1). However, the couples formed by fuel mass flow rate with total electric power and mGT rotational speed with mGT TOT show a high interaction between them (λ_{11} and λ_{22} are much higher than 1). This high interaction implies that manipulating one of the variables (e.g. the fuel mass flow rate) has a high impact on both controlled variables (i.e. total electric power, mGT TOT). This fact affects negatively the control, as for control purposes, one manipulated variable should just modify one controlled variable.

Therefore, as anticipated in the section 5.4.3, a decoupler is needed. This decoupler is a static one (i.e. it considers de gain part of the process transfer function and it compensates the steady-state response), and in order to evaluate it, the results of the gain matrix are needed. For each linearized case, the elements of the matrix forming the decoupler have been computed. As just one decoupler can be implemented, the average values of each element of the matrix have been taken. It has to be highlighted that the decoupler is just needed for two variables, not all three; thus, a decoupler is a 2x2 matrix. As overall result, the decoupler is:

$$K = \begin{bmatrix} 1 & 1.6892 \\ 0.2825 & 1 \end{bmatrix}$$

After implementing the decoupler in the dynamic model in Dymola (see Figure 5.4-4 and Figure 5.4-5), new linearizations have been made nearby the same equilibrium points as indicated before. Also in this case, the transfer functions matrix has been obtained, the gain matrix computed and the RGA matrix evaluated to verify whether there is still the presence of couplings or not. Figure 6.4-4 shows the diagonal elements of the RGA matrix of the system including the decoupler.

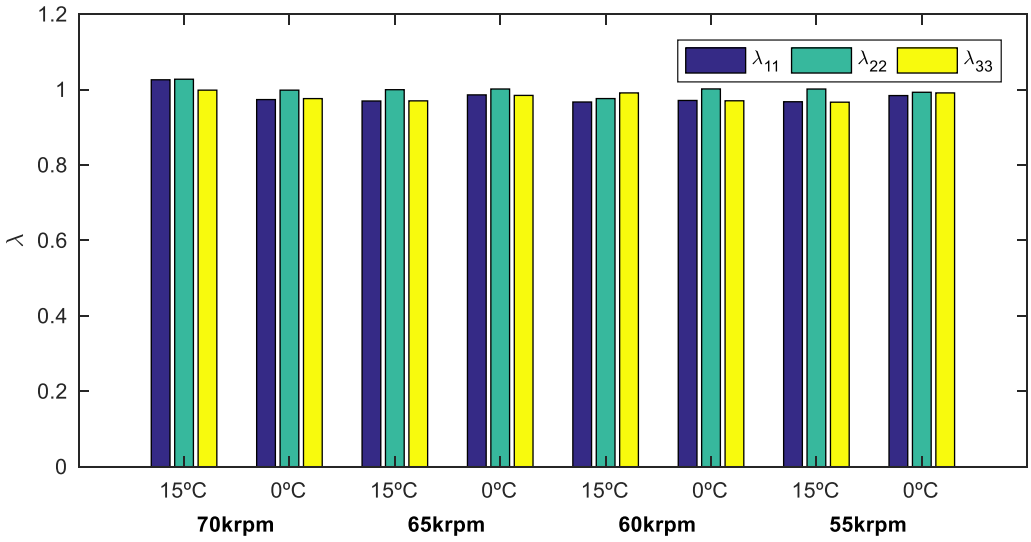

Figure 6.4-4 Diagonal elements of the RGA matrix of the system with the presence of the decoupler

By looking at Figure 6.4-4, all the diagonal elements are closed to 1, indicating the proper relation between manipulated and controlled variables.

As mentioned in the section 5.4.2, to reduce the non-linearities of the plant while controlling it, the outputs of the controller (i.e. inputs to the system) represent variations from a selected equilibrium point. The selected equilibrium point is the one given at 65 krpm and 15ºC.

In order to have a physical meaning of what has been shown with the RGA matrix and justify physically the implementation of the decoupler, two studies have been performed starting from the equilibrium point conditions selected (i.e. 65 krpm and 15ºC). The first study consists in imposing a step of the 3% of the rotational speed (which is one of the manipulated variables presenting the coupling) and studying its influence on both controlled variables, namely total electric power (Figure 6.4-5) and mGT TOT (Figure 6.4-6), for both cases, with (red line) and without (blue line) decoupler implemented. The second study consists in imposing a step of the 3% of the fuel mass flow rate (which is the other manipulated variable presenting the coupling) and studying its influence on both controlled variables, namely total electric power (Figure 6.4-7) and mGT TOT (Figure 6.4-8), for both cases, with (red line) and without (blue line) decoupler implemented.

By analyzing Figure 6.4-5, with the decoupler, the variation of the response of the electric power with a manipulation of the rotational speed is almost zero; which is not the case without decoupler. Both controlled variables are modified when the decoupler is not present (see Figure 6.4-5 and Figure 6.4-6), but with the decoupler, the manipulation of the rotational speed only influences the variable which should

control, namely the mGT TOT. As it is a static decoupler, the dynamic transition is still present.

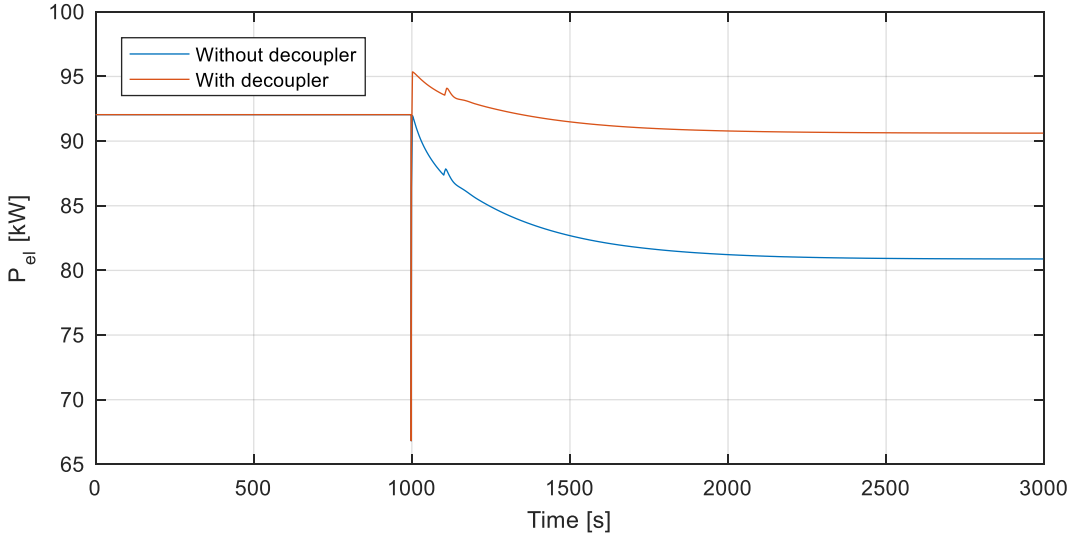

Figure 6.4-5 Effect of the decoupler in the total electric power produced by a 3% increase of the rotational speed

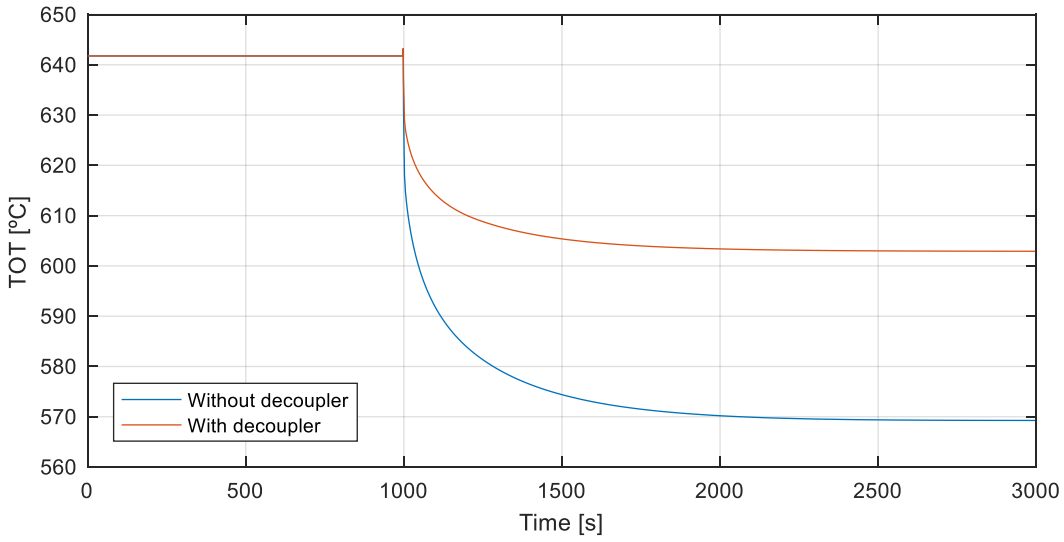

Figure 6.4-6 Effect of the decoupler in the mGT TOT by a 3% increase of the rotational speed

By manipulating the fuel mass flow rate, it is expected that it only has an effect on the total electric power produced. By analyzing Figure 6.4-8, it can be seen the effect of the decoupler, with which the mGT TOT remains almost unaffected by the manipulation of the fuel mass flow rate. This fact completely differs when the decoupler is not present.

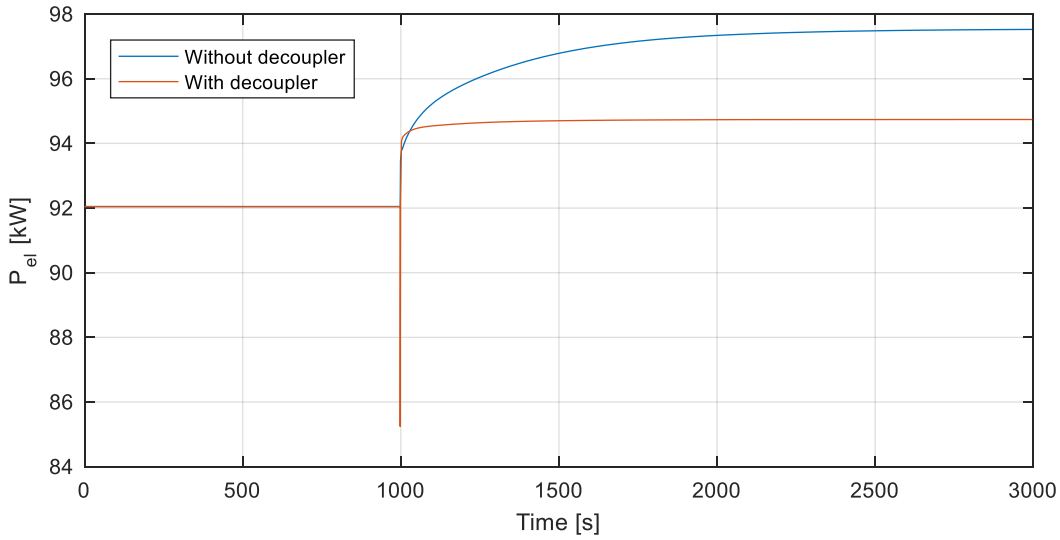

Figure 6.4-7 Effect of the decoupler in the total electric power produced by a 3% increase of the fuel mass flow rate

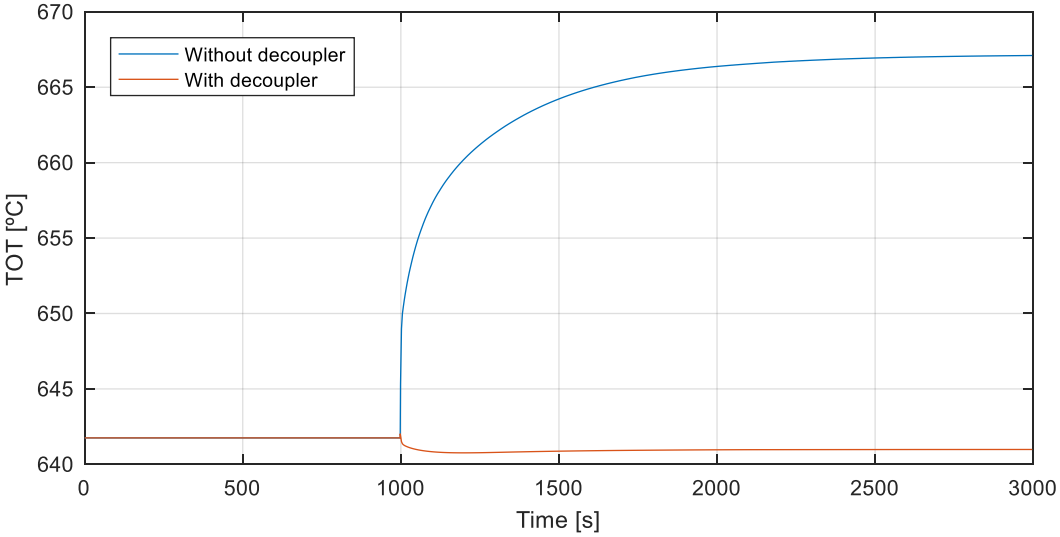

Figure 6.4-8 Effect of the decoupler in the mGT TOT by a 3% increase of the fuel mass flow rate

With both studied cases, it can be concluded that the fuel mass flow rate uniquely affects the total electric power produced and the rotational speed only affects the mGT TOT.

Therefore, the decoupler is well designed and its need is justified by the fact that it allows the complete separation of the effects of the manipulated variables in the controlled variables which are not supposed to control.

6.4.3.2. Tuning of the controllers

After performing the linearization of the system and study the mutual interactions, it is possible to proceed with the tuning of the controllers. For that purpose, the PID Tuning tool from Matlab® has been used. To use that tool, the transfer functions obtained from the linearization are needed. With the tool, it is possible to study the step response of the controlled variable by modifying the parameters of the controller automatically, selecting the response time (slower or faster) and the transient behavior (aggressive or robust) through a slide bar. A faster response decreases the settling time (i.e. the time that takes to the output to reach and to stay within an error band from the steady-state value after applying a step in the input) but increases the overshoot (i.e. the maximum deviation of the output with respect to the steady-state final value) and a robust behavior increases the rise and settling time but decreases the overshoot. The optimal response would be the fastest and with less overshoot. As that cannot be possible, a good compromise should be found. Different controllers have been implemented and tested; however, the most suitable ones are the ones reported in Table 6.4-2. At the beginning, PID controllers were tried to be implemented, however, the derivative part creates so much instabilities, that the author has decided to use PI controllers.

Table 6.4-2 Tuning of the PI controllers

	Controller 1	Controller 2	Controller 3
Controlled variable	Electric power	mGT TOT	ORC TIT
Manipulated variable	Fuel mass flow	Rotational speed	ORC mass flow rate
Kp	$5.17 \cdot 10^{-8}$	$-2.242 \cdot 10^{-4}$	$-5.0153 \cdot 10^{-3}$
Ti	$3.01 \cdot 10^{-2}$	$7.79 \cdot 10^{-1}$	32.19
Rise time [s]	15.2	11.9	32.9
Settling time [s]	24.7	69.8	127.0
Overshoot	1.58%	8.55%	1.77%

By looking at Table 6.4-2, the controller which controls the electric power is the fastest one with the lowest value of overshoot. Figure 6.4-9 shows the step response of the tuning of the controller which controls the electric power. On that figure, it can be appreciated the smooth response of the controlled variable.

The second controller, namely the one controlling the mGT TOT, has a bigger overshoot, equal to 8.55%, but it is accepted to lower down the settling time. Figure 6.4-10 shows the step response of the tuning of the controller which controls the mGT

TOT. Another controller has been tested with a lower settling time, but the overshoot was so high that the TOT reached unaffordable values.

Finally, the third controller, namely the one which controls the ORC TIT, presents the biggest settling time with not so high overshoot. This is expected as the inertia of the ORC is higher due to the number of heat exchangers involved. Figure 6.4-11 represents the step response of the tuning of the controller of the ORC TIT. With the action of the controller, the controlled variable has a steep inverse response at the beginning. As the dynamic system under study changes fast (in less than a minute), the settling time should be minimized, but that effect must be considered. The controller indicated in Table 6.4-2, is the fastest one that can be implemented.

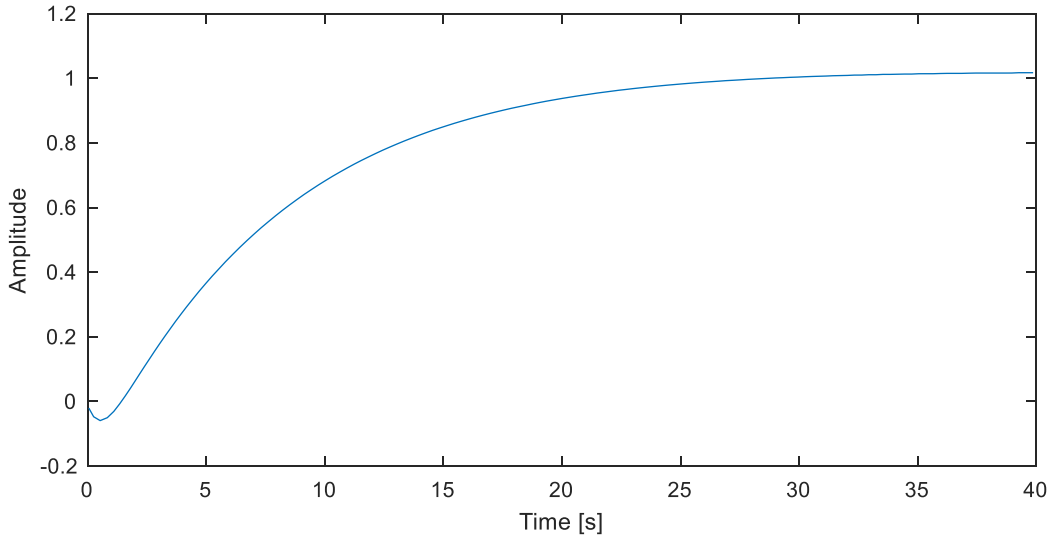

Figure 6.4-9 Step response for tuning the PI controller of the produced electric power

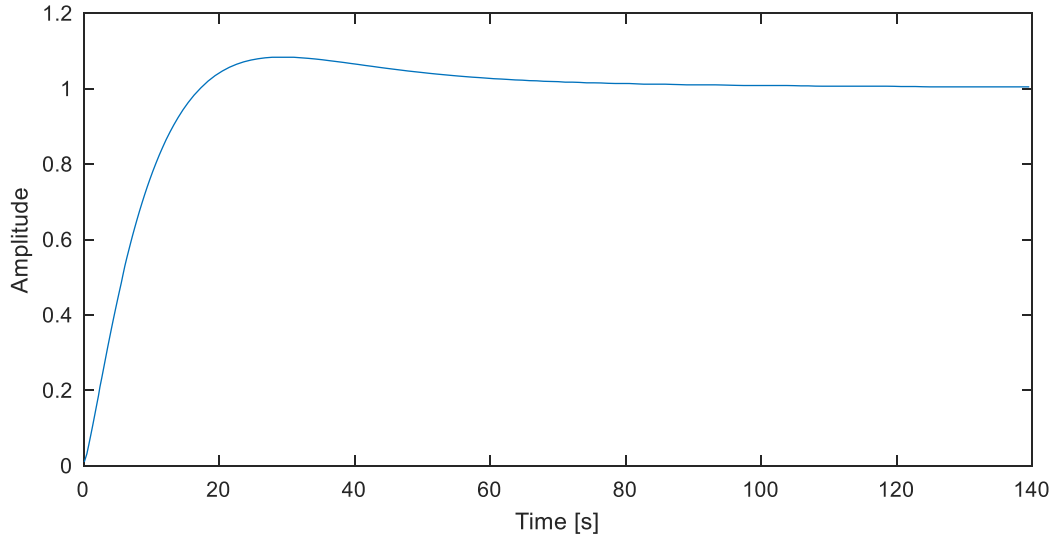

Figure 6.4-10 Step response for tuning the PI controller of the mGT TOT

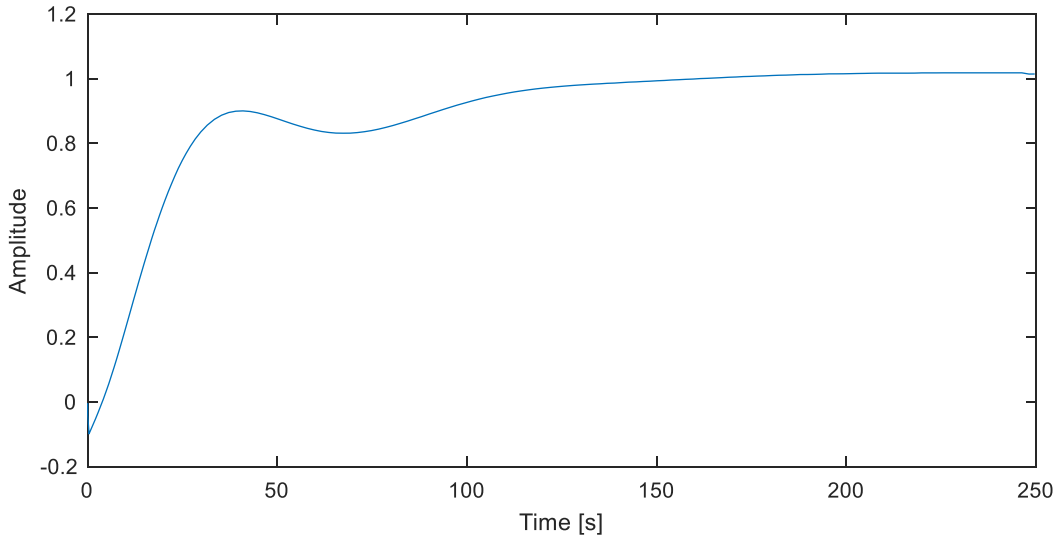

Figure 6.4-11 Step response for tuning the PI controller of the ORC TIT

6.4.4. Overall analysis

The selected case study considers that the designed system aims following the electric demand of a group of 150 houses placed in Cologne, Germany [128]. The annual electric load profile is shown in Figure 6.4-12, representing the required peaks of power for each second of the year.

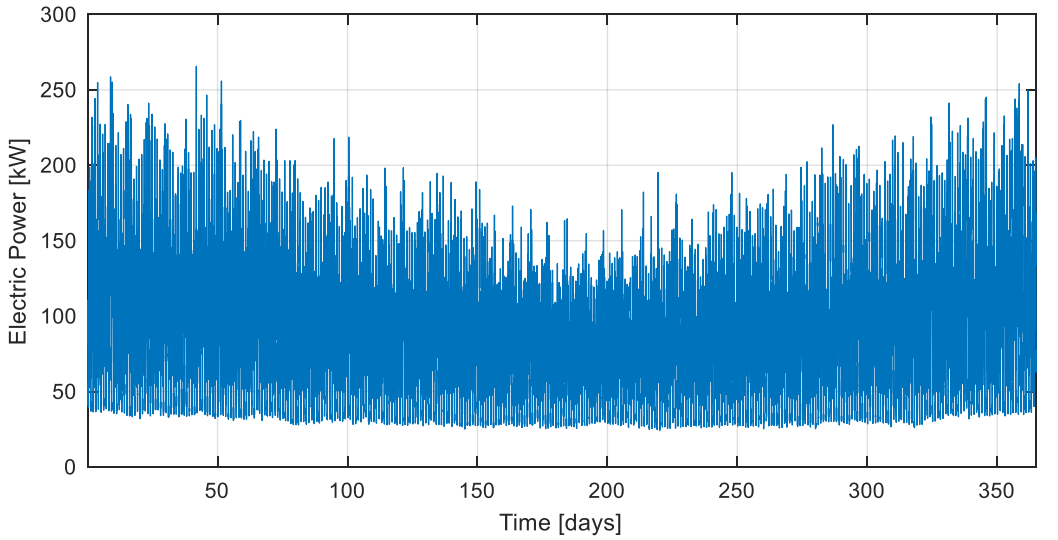

Figure 6.4-12 Power peaks along a whole year

It can be appreciated that the electric demand is higher in winter than in summer. This fact is explained since the heating system consists in a group of heat pumps. In order to stay as less intrusive as possible, it has been decided to integrate a system in parallel with the grid which just feeds the electricity requirements and not the heat ones, so no cogeneration is considered.

The dynamic analysis here described aims to know whether the system composed by the mGT and ORC can fulfill adequately the electric demand, when it is possible. That last remark indicates that the system has some physical limits (i.e. maximum and minimum power output) because the system has not been designed to satisfy the whole request, but to work in high load conditions along the year. Therefore, even if the electric demand is high, the system has a maximum of production at the ambient temperature in which is working. Moreover, it has been established that the system cannot work in conditions lower than the 30% in part-load conditions. Thus, taking the steady-state results, limits on the set point of the required demand are imposed. Those limits are the maximum, given by the mGT rotating at 70000 rpm at the different ambient temperatures, and the minimum, which is the 30% of the maximum value. Those values limit the operating range of the energy system at different ambient temperature. The limits on the set point are shown in Figure 6.4-13. Those limits indicate that if the request is higher than the maximum limit, the system will be asked to give its maximum and not more. The rest demanded electricity should be given by another system, which could be a battery or the grid itself. Oppositely, if the request is lower than the established minimum, the system will give the minimum in order not to stop the system. Hence, the overproduction should be transferred to another system, which could be a battery or the grid.

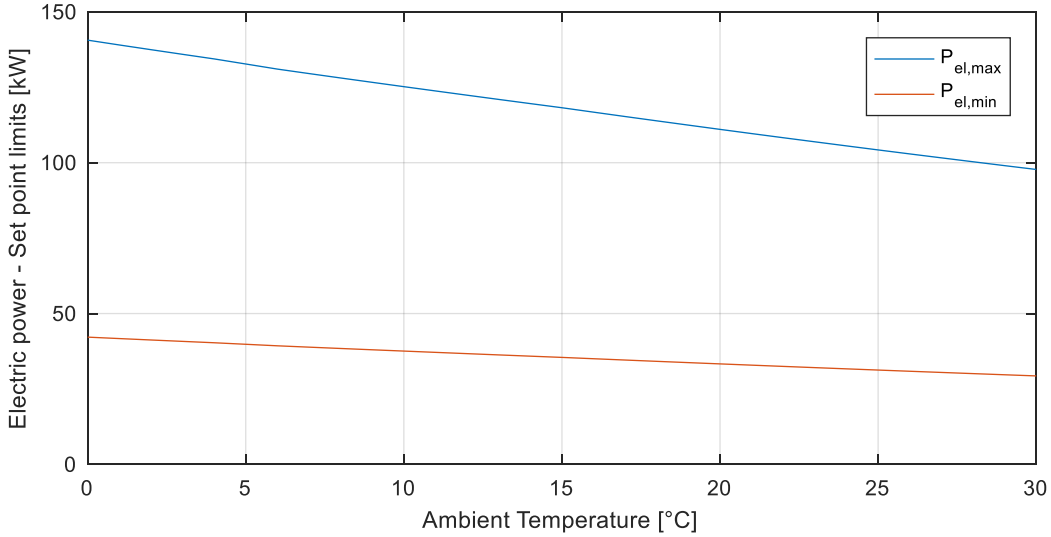

Figure 6.4-13 Limits of the produced electric power at different ambient temperature

As the dynamic analysis will be performed, the set points of the controllers have to be set. As mentioned above, the set point imposed for the total produced electric power, which is the first controlled variable and the most important one, is given by the electric demand imposed by the set of houses (if that demand is within the limits indicated in Figure 6.4-13; if not, the physical limits impose the set point). The set point of the second controlled variable, which is the mGT TOT, is fixed to the value

of 645 ºC. Finally, the set point of the third controlled variable, namely the ORC TIT, is fixed by the results obtained with the steady-state model. It is considered that the TIT should be fixed at the nominal value when possible, but, as described in section 6.3.3, not always is possible to keep that temperature when the part load of the mGT is too low and the temperature and mass flow of the flue gases drop. Figure 6.4-14 shows the results coming from the steady-state model, satisfying the mass and energy balances trying to keep the maximum possible TIT. The discontinuities at the end of the flat part in which the TIT is kept as its maximum value are due to numerical issues. The variation with respect to the nominal value is 1°C.

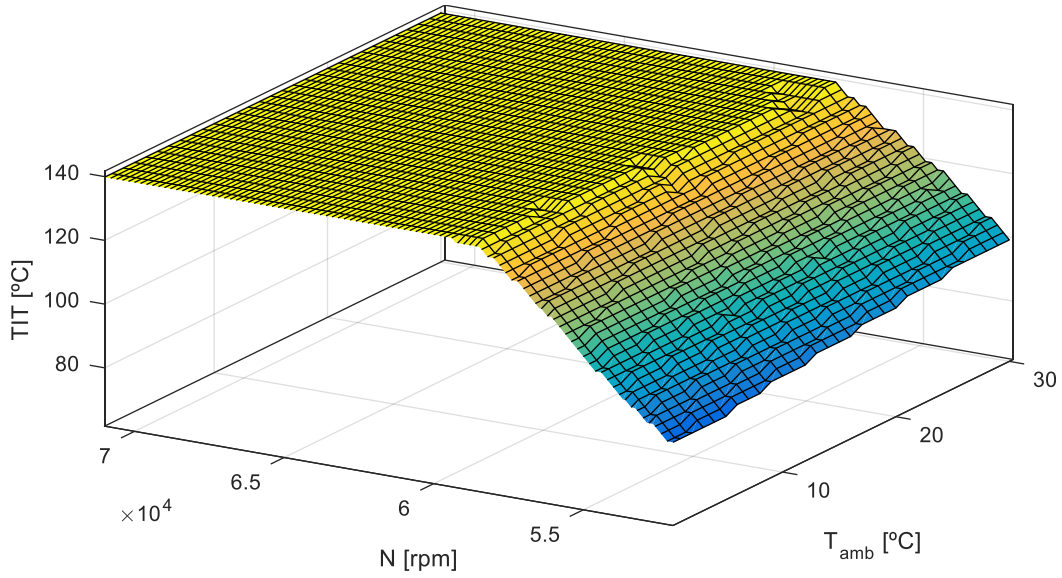

Figure 6.4-14 ORC TIT set point with respect to the rotational speed and ambient temperature

Once the limits on the set points have been imposed, to analyze the dynamic response, the two most critical days in terms of electricity demand have been simulated: the one with the highest (winter day, January 9th) and the lowest (summer day, July 1st) electricity demand.

As the performance varies with the ambient temperature, the profiles of both days have been taken from the database of Cologne in [129]. The ambient temperature profile of a day in January is shown in Figure 6.4-15; while the ambient temperature profile of a day in July is shown in Figure 6.4-16.

As stated before, two critical days have been studied, but they have been studied in two different ways. The first way considers that the electricity demand is the real one each second; hence, the simulation of the system aims to follow the actual electricity demand. The second way considers that following the peaks is not feasible for this system, thus a filtered demand is considered by taking an average value for each

minute of the day. These last simulations are made after realizing that the peaks on the actual value of the variable cannot follow the real demand.

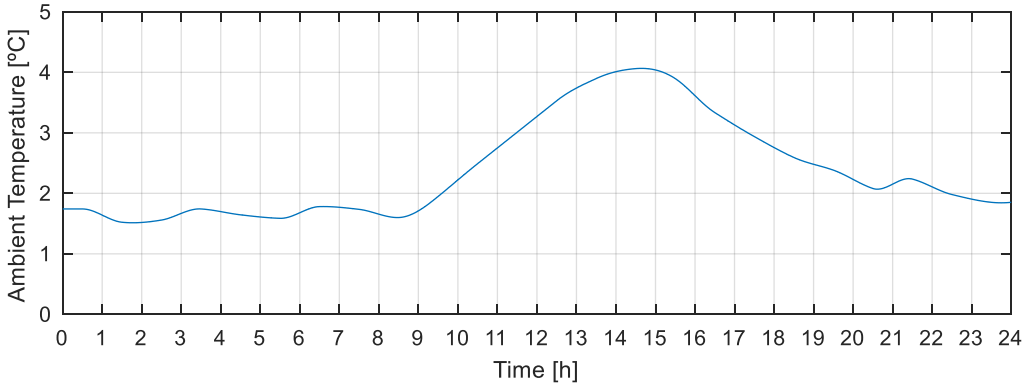

Figure 6.4-15 Ambient temperature of the day with the highest electricity demand (January)

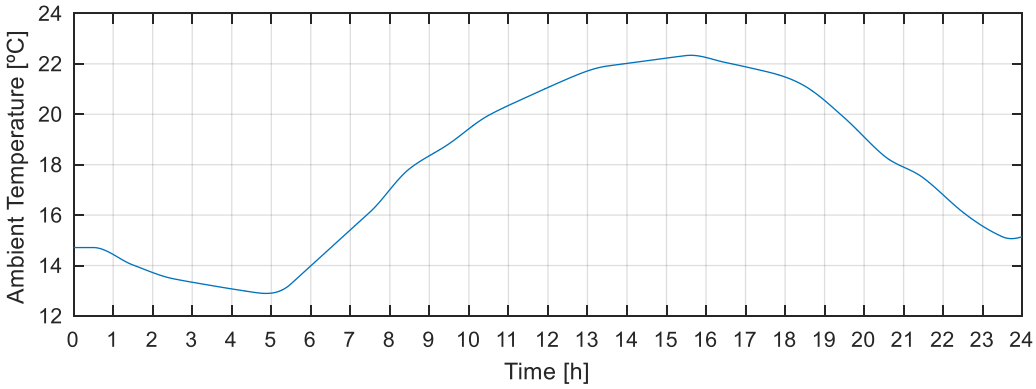

Figure 6.4-16 Ambient temperature of the day with the lowest electricity demand (July)

In the next pages, the controlled variables resulting for the simulations of each day are presented. Figure 6.4-17 shows the three controlled variables (i.e. Total electric power, mGT TOT and ORC TIT) of the day with the highest electricity demand; while Figure 6.4-18 shows the results of the simulations of the same day but considering a one-minute averaged electricity demand. Figure 6.4-19 shows how the three controlled variables behave on the day with the lowest electricity demand and Figure 6.4-20 shows the same three controlled variables considering a one-minute averaged electricity demand. Finally, after presenting the results of the whole day, an ampliation of the most critical minutes detected are presented to properly see how the controlled variable follows the imposed set point. Figure 6.4-21 shows the ampliation considering the real demand while Figure 6.4-22 shows the ampliation of the results of the filtered simulation. In all the figures mentioned in this paragraph, in magenta the real electricity demand is shown; in red, the set point imposed to the controller; and in blue, the actual value of the controlled variable. It can be seen that the set point of the electric power differs from the real electricity demand when the limits are overpassed, as explained before.

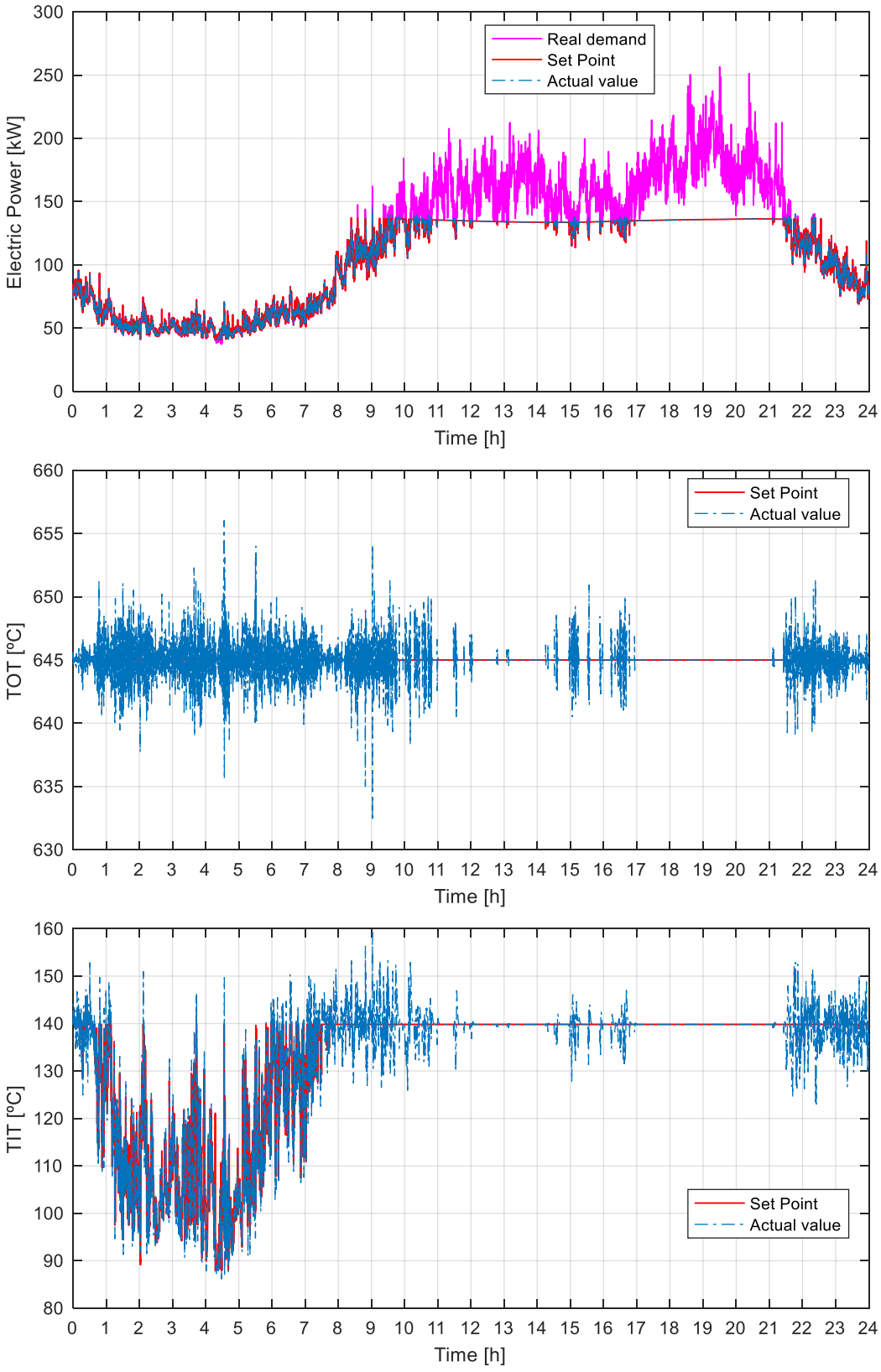

Figure 6.4-17 Electric power request (top), mGT TOT (middle) and ORC TIT (bottom) for the day with the highest electricity demand

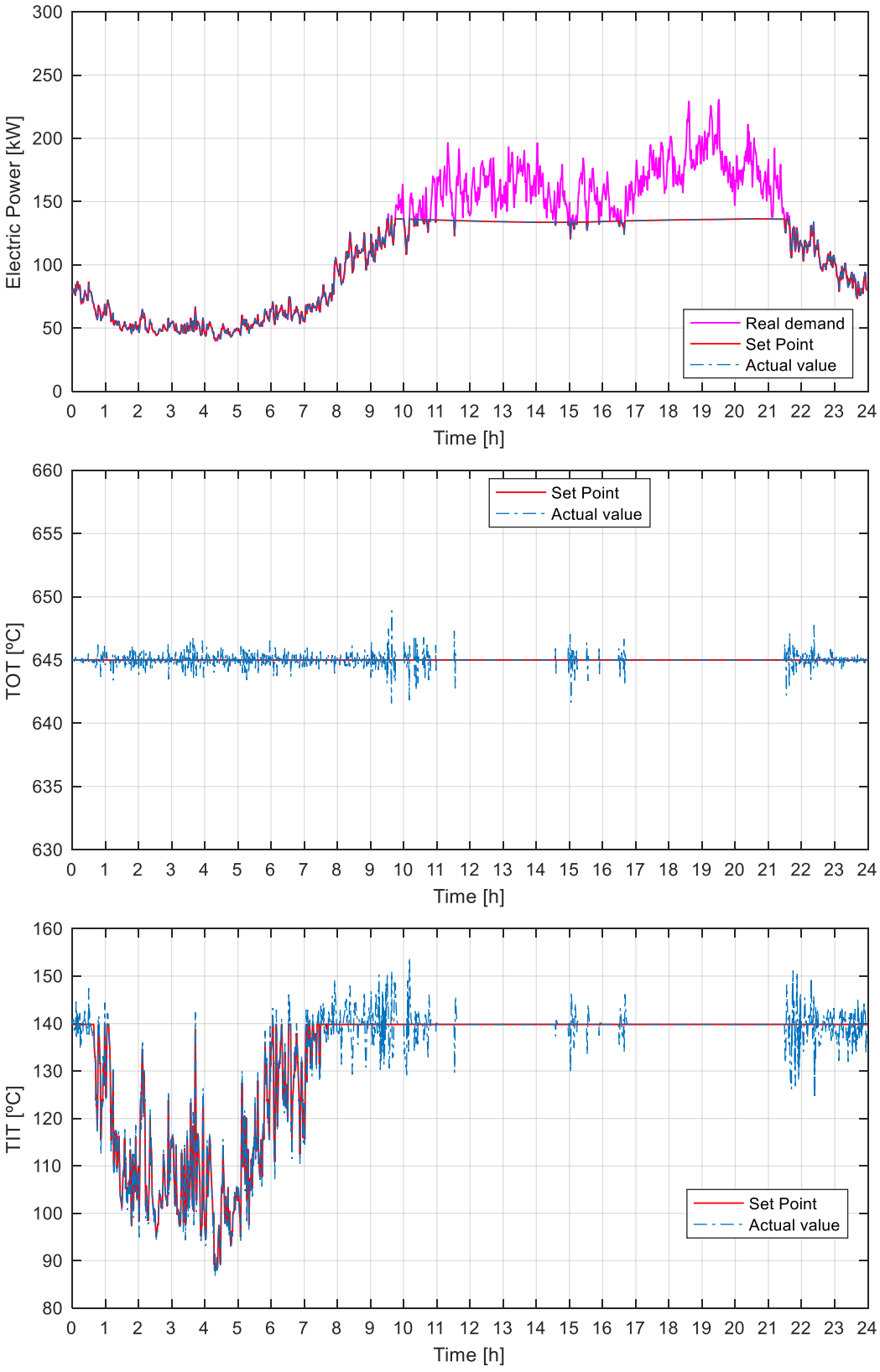

Figure 6.4-18 Electric power request (top), mGT TOT (middle) and ORC TIT (bottom) for the day with the highest electricity demand (one-minute average filtered demand)

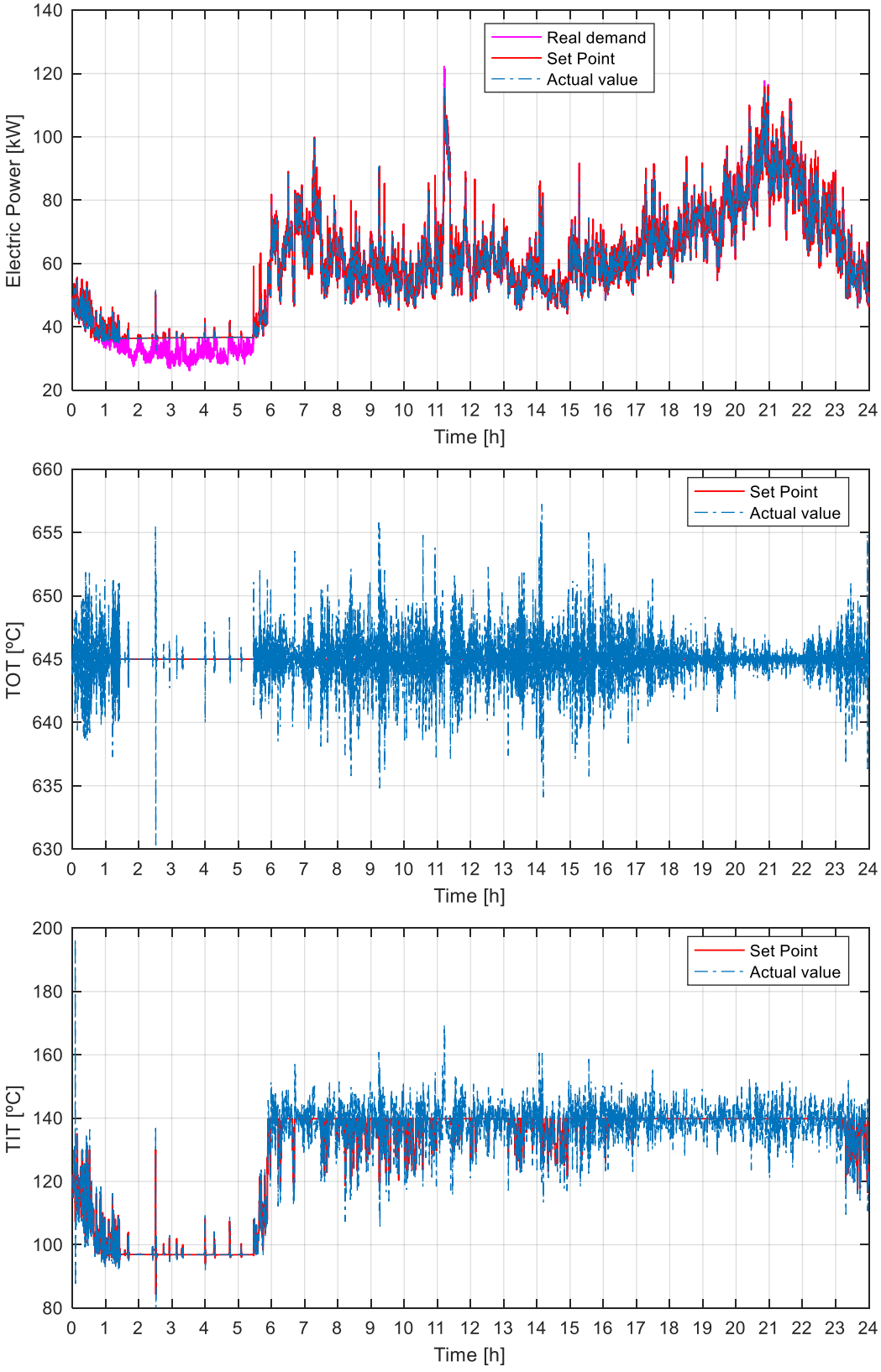

Figure 6.4-19 Electric power request (top), mGT TOT (middle) and ORC TIT (bottom) for the day with the lowest electricity demand

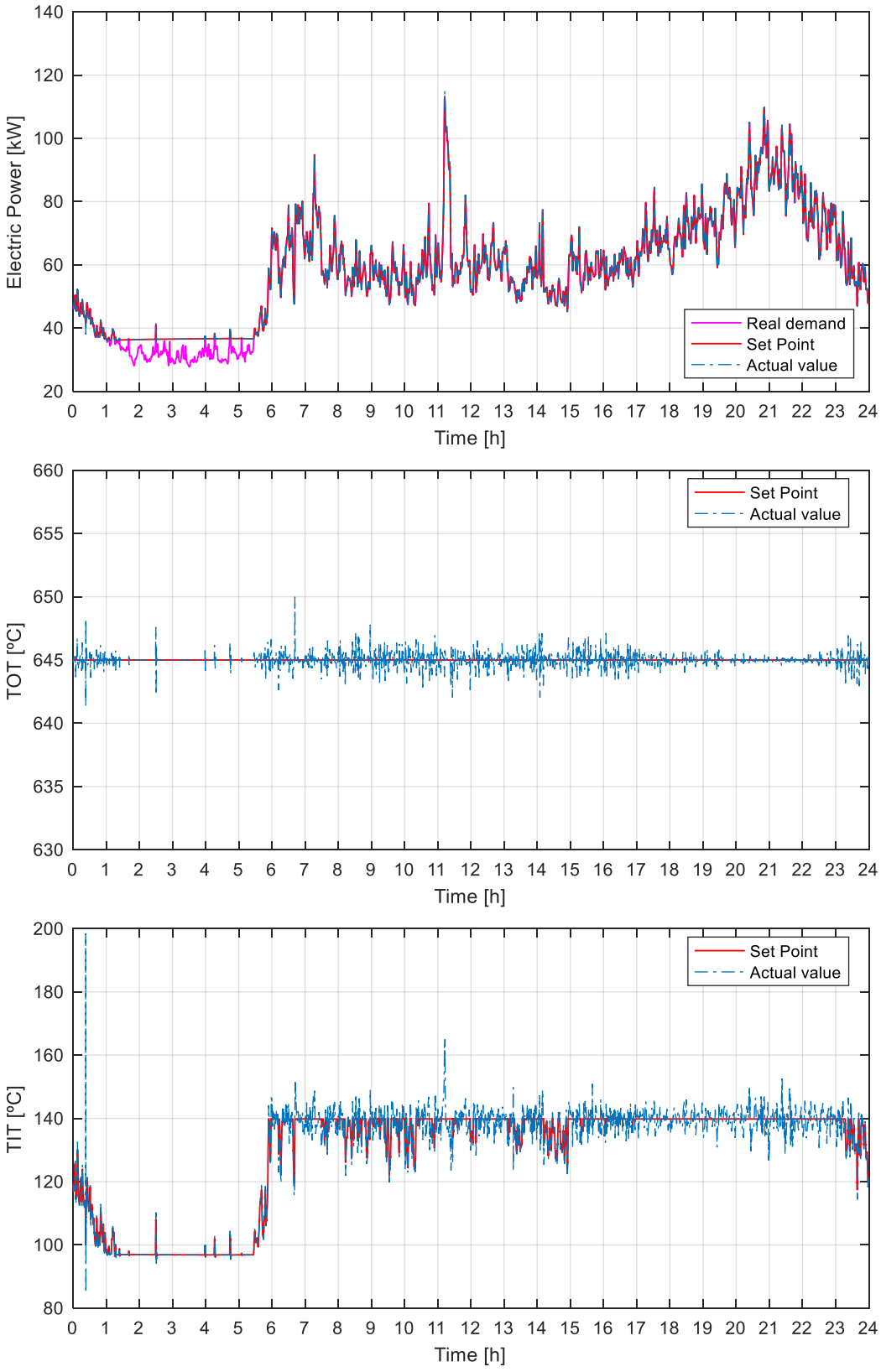

Figure 6.4-20 Electric power request (top), mGT TOT (middle) and ORC TIT (bottom) for the day with the lowest electricity demand (one-minute average filtered demand)

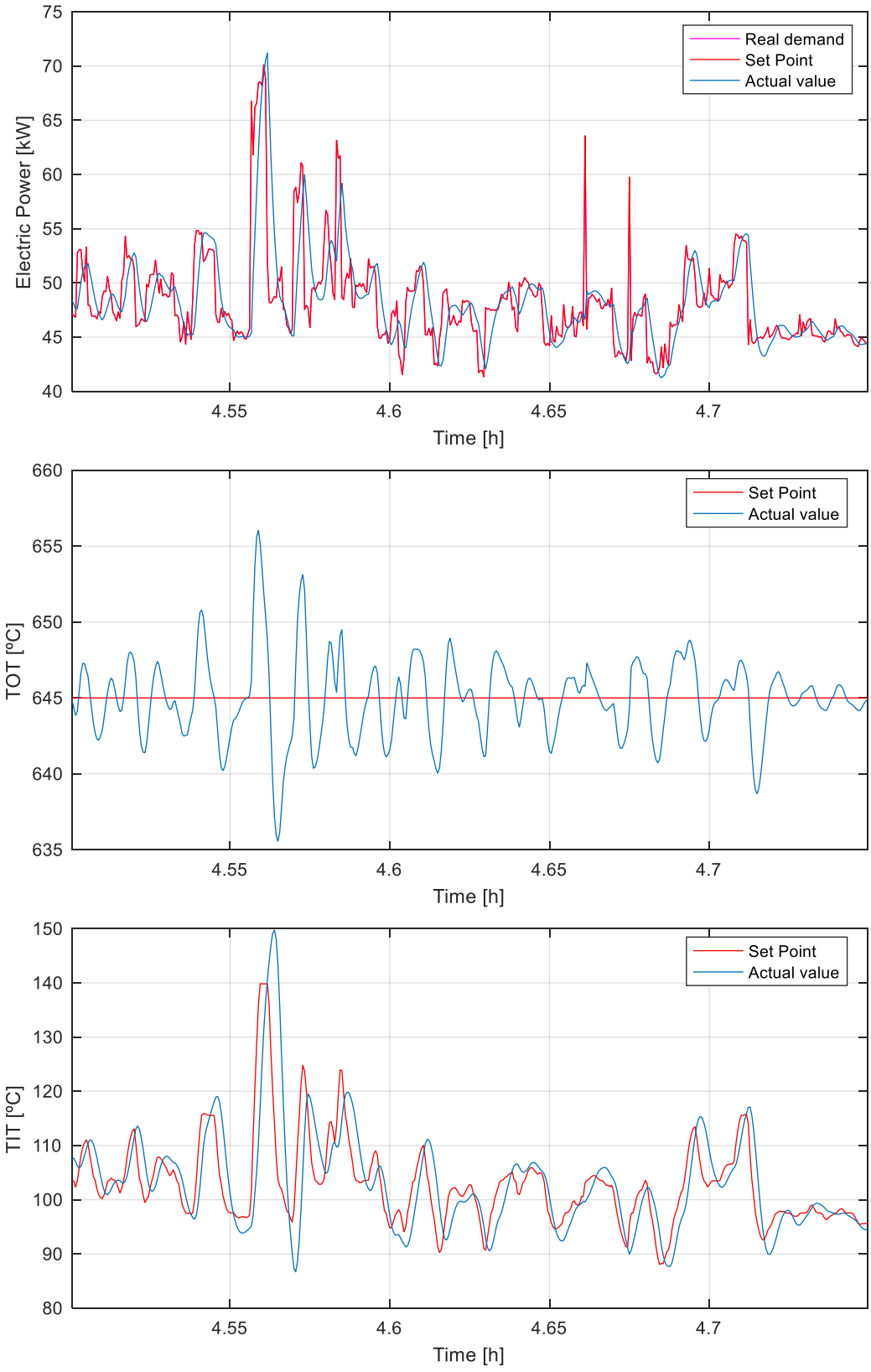

Figure 6.4-21 Ampliation of electric power request (top), mGT TOT (middle) and ORC TIT (bottom) for the day with the highest electricity demand

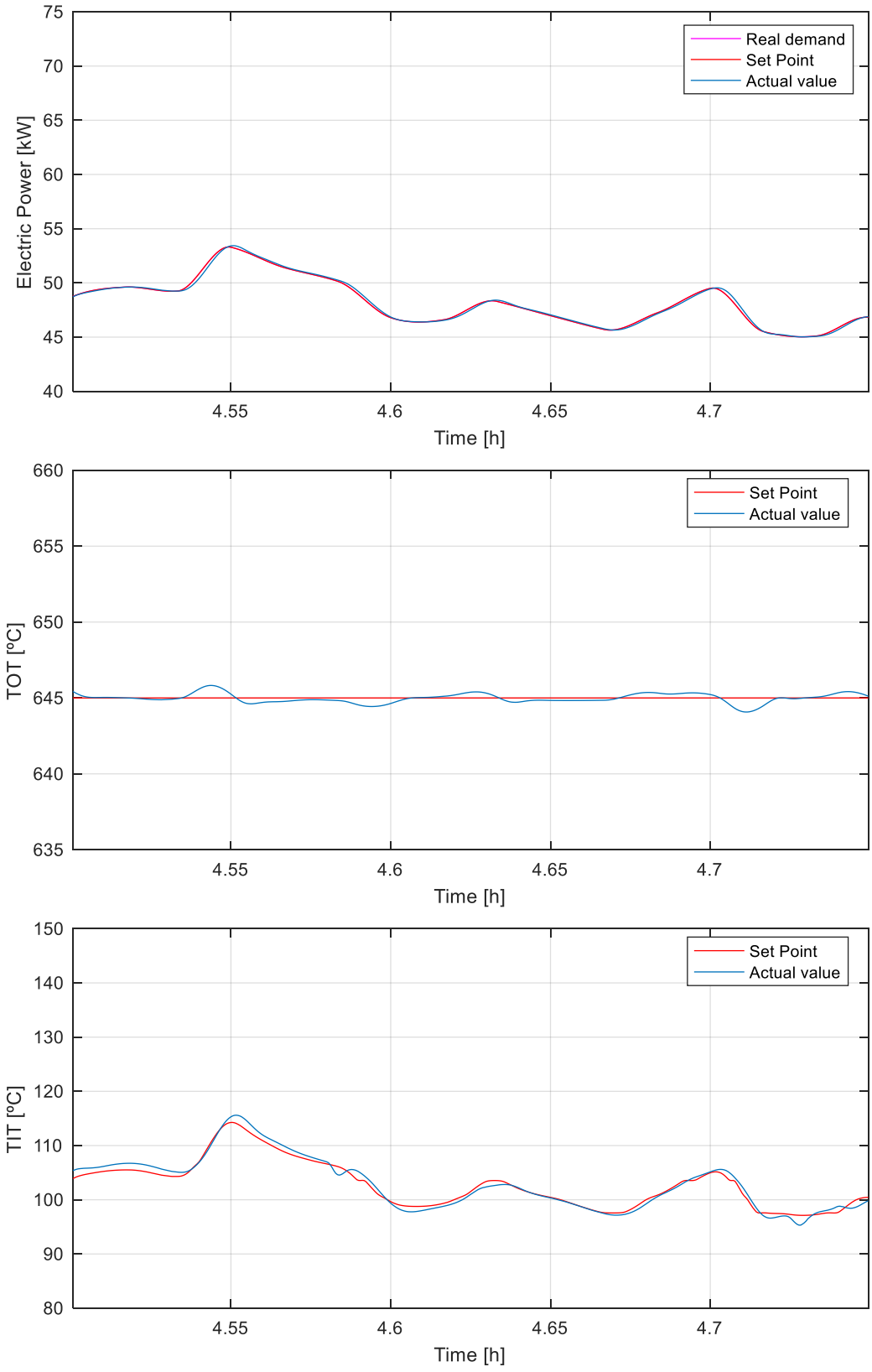

Figure 6.4-22 Ampliation of electric power request (top), mGT TOT (middle) and ORC TIT (bottom) for the day of the highest electricity demand (one-minute average filtered demand)

While comparing the performance of the system considering the filtered demand or the non-filtered one, it can be seen that with the non-filtered one, the system is not able to completely follow the request. This fact has been expected from the beginning when analyzing the settling time of the controllers (Table 6.4-2). Even if the PI controller which controls the electric power is the fastest one, it still needs 24.7 s to reach the steady-state solution. This time, combined with the peaks on the request (therefore peaks on the set point), causes that the system cannot follow completely what it is demanded so the exchange of energy with the grid is needed. The average differences with the demanded energy with respect to the set point are 1.92 % in the case in which it is asked to the system the real electricity demand and 0.30 % in the case in which that demand is filtered considering one-minute average, presenting the maximum error peaks equal to 69.06 % and 7.95 %, respectively. This indicates that the system cannot follow the real demand when it is needed, so a parallel system (like a grid or a battery) should be introduced to satisfy the differences and to receive and give energy when the system works on its limits.

With the real demand, the electricity peaks are so high, that also the other controlled variables suffer big peaks. By looking at the response of the controlled variables in Figure 6.4-21 and Figure 6.4-22, it can be clearly appreciated these differences. The peaks present in the electric demand disappear if it is considered a one-minute average demand, giving as a result a smoother behavior. The controlled variables follow better the set point with a filtered demand.

In addition, by analyzing the temperature peaks, a heat exchanger may not withstand the peaks that appear with the real demand, because they can cause thermal stresses to the component.

Summing up, as a parallel system is needed anyway because the system formed by the mGT and ORC cannot satisfy the real demand, it is better to impose a filtered set point on the electric demand rather than consider the real one, to make smoother transitions and guaranteeing the proper performance, as well as reducing thermal stresses in the components.

Chapter 7. Conclusions and recommendations

It's better to feel the rain on your skin rather than to look at the sun through the window

7.1. Conclusions

The PhD work deals with the study of the steady-state and transient response of a system formed by a commercial mGT and an optimized bottoming ORC, which aims to satisfy the electricity demand of a set of 150 houses in Cologne (Germany). The research project aims to develop simulation models to evaluate the performance of the overall system.

The first part of the research aims to study how the system behaves in nominal conditions. For that part of the research, two main models are developed in Matlab®: one to evaluate the performance of a commercial mGT and another one to optimize the design of the bottoming ORC module in terms of electric power output. As regards the ORC, different working fluids are investigated and the most promising one in term of electric power output and environmental impact is the R1233zd. This fluid seems the perfect alternative to R245fa in terms of environmental impact and cost (20-25€/kg for the R1233zd vs 30-35€/kg for the R245fa) [116]. Introducing the bottoming ORC results in an increment of the electricity production from 100 kWe to almost 120 kWe, increasing the efficiency of the overall system from 29.5% to 36%. In order to complete the design, the geometries of the heat exchangers are determined. The determination of the geometries is mandatory to evaluate the mass and volume of each heat exchanger, which rule the dynamic behavior of them. Two different procedures are used here according to the heat exchanger that has to be simulated. For the regenerator of the mGT, a 3D model is developed in Matlab® to recreate the existing heat exchanger with the dimensions available in the literature. The heat exchangers of the ORC are designed by using the commercial software Aspen Exchanger Design & Rating®. Plate-fin heat exchangers are the most optimal ones in terms of compactness.

The second part of the research aims to study how the system behaves in steady-state off-design conditions. This is a mandatory part for the transition in the study of the system behavior from nominal conditions to dynamic conditions. This part is exhaustively described in the section 6.3. It is needed to deeply analyze how the system behaves when the ambient temperature changes and the demanded electric

power is not the nominal one. The off-design conditions obtained from the steady-state models in Matlab® are then used for the study of the dynamic behavior in different ways. These results are the basis to validate the performance of the dynamic model developed with Dymola by imposing different operating conditions and checking the final steady-state results from the dynamic model. Moreover, for control purposes, the off-design steady-state conditions are used in two different ways. The first one consists in imposing a physical limit to the required electric power (i.e. the controller cannot ask to the system more than what is physically possible) and imposing the set point of the ORC TIT, aiming to maximize the ORC power output. The second one consists in detecting different off-design equilibrium points in which the system will be linearized to proceed with the design of the control system.

Once the steady-state models, simulations and results are concluded, the third part of the research aims to move forward the steady-state conditions and analyze the dynamic response. For this purpose, dynamic models are developed by using Dymola. As mentioned before, the steady-state results obtained with the dynamic models are validated with the off-design steady-state results. After that validation, open loop (i.e. without a control system) simulations are performed. These simulations bring to the conclusion that a control system is needed for studying the dynamic response, aiming to guarantee good operational conditions, which do not occur if the system works in open-loop conditions. Therefore, a simple control system is designed using the most common controllers in the market, PI controllers. The controllers are designed using the PID Tuner tool of Matlab®, looking for a compromise in the response in terms of fast response and overshoot. The dynamic behavior is then analyzed by studying the electricity demand profiles of the two most critical days of the year: the one with the highest and the lowest load profile. The simulations are performed considering a time step of one second, however, two type of profiles are imposed: real demand conditions and one-minute averaged demand conditions. Those profiles are imposed as set points in the electric power controller. After analyzing the transient response, it is concluded that the proposed system formed by the mGT and ORC cannot work in stand-alone conditions to satisfy the demand instantaneously, as there is a difference in the demanded electricity and the given electricity. As the system is not able to fulfill the demand by its own, and a parallel system should be needed, the results show that taking an averaged profile helps to get considerably smoother results, therefore, the equipment would suffer less as the temperature gradients are lower. Taking an averaged profile is unrealistic if the proposed system formed by mGT and ORC has to work on its own, but it could be very efficient when working with a parallel system consisting of a battery or the electric grid itself, which allows peaks to be satisfied.

7.2. Recommendations

After analyzing the dynamic behavior of the system, it is concluded that the proposed system formed by the mGT and ORC cannot work in stand-alone conditions to fulfill the demand instantaneously without being coupled with a parallel system (e.g. the grid, battery). The author has identified some points that could be further studied.

Three recommendations are given here to deepen more into detail and to optimize the performance of the cycle.

First, if the overall system aims to fulfill completely the demand, then, different considerations should be taken into account to try to satisfy that requirement. The number of houses should be reduced, in order to be able to satisfy all the peaks, which is not the case under study here. Moreover, if the purpose is to follow the demand without a parallel system, then the system power output cannot be reduced till the 30%, but the study of stronger partial loads should be done. As it has been shown through the dynamic analysis, following the demand instantaneously cannot be made with the implemented controllers; therefore, more sophisticated controllers should be considered (e.g. model predictive controllers). These suggestions need to be further studied because there are no guarantees that with these recommendations, the system would be able to satisfy the demand.

Second, as the dynamics of the mGT are much faster than the bottoming ORC, still considering the suggestions given before, it could be studied a way to couple and decouple the bottoming ORC. This could give another degree of freedom increasing the flexibility. However, the author expects that this could give more flexibility to reduce the load drastically, by avoiding the ORC; but it would be more critical increasing the load, as the ORC should be warmed up. Nevertheless, this is an interesting study that could be performed.

Third, taking for granted that the system formed by the mGT and ORC here studied cannot satisfy the demand (as demonstrated with the dynamic analysis) and thus, a parallel system is needed, an optimization of the performance of the system can be done. The author considers this solution as the best one among those mentioned. The proposed solution consists in optimizing the load of the system by imposing optimized set points to the electric load instead of the real demand. As it has been seen with the dynamic results considering one-minute averaged values, the behavior is smoother, reducing the error between the set point and the actual value, as well as the overshoots. The optimization here proposed aims to guarantee a smooth transition as well as to optimize the energy exchange with the battery or with the grid. In the case that the energy exchange is done with the grid, then an economic optimization should be performed, aiming to satisfy the overall electricity demand of the set of houses but considering the benefits and uncertainties of selling and buying

electricity to and from the grid, respectively. This optimization could be implemented with more sophisticated controllers as well.

A. Turbomachinery extrapolation method

The procedure used for the sub-idle extrapolation is based on the basic principles of the similarity laws while taking into consideration the compressibility effects. This method has been validated for both steady state and dynamic conditions [130], [131].

Usually, the characteristics of the turbine and compressor (i.e. mass flow rate, $\dot{m}$, pressure ratio, PR, and efficiency, η) are given by terms of a percentage of reduced relative speed ($\%N$) and a beta value[4].

$$(\dot{m}, PR, \eta) = f(\%N, \beta_{line})$$

The extrapolation method considers the two speed lines which correlate the efficiency, reduced mass flow and pressure ratio at the lowest values of percentage of relative speed that is available. The speed lines taken as reference are at the lowest values because the extrapolation is done for the sub-idle region. This method uses a reference value of the variable which is going to be extrapolated, as start point for the calculation of the variable, and another lower speed line in order to calculate the similarity law exponents.

Figure A-1shows the relation between pressure ratio and reduced mass flow for the centrifugal compressor of the AE-T100 at different percentages of reduced rotational speed. Continuous lines represent the information given by the manufacturer, while dashed lines represent the extrapolated curves for the sub-idle region, following the procedure here described. On one hand, the curve in red represents the value of 60% of reduced rotational speed, and it is taken as the reference speed line in the procedure (subscript *ref* in the equations). On the other hand, the curve in magenta represents the value of 50% of reduced rotational speed (subscript *aux* in the equations). Once the information given by the manufacturer is collected, the values that are going to be extrapolated are the pressure ratio, the reduced mass flow and the efficiency, for both turbine and compressor. Each of these values requires a different expression and different similarity law exponents.

[4] A beta value is an unique value of a beta line. A beta line is an auxiliary line with no physical meaning which correlates the pressure ratio with the mass flow. The usefulness of these lines stays in the fact that they provide unique intersections with speed lines.

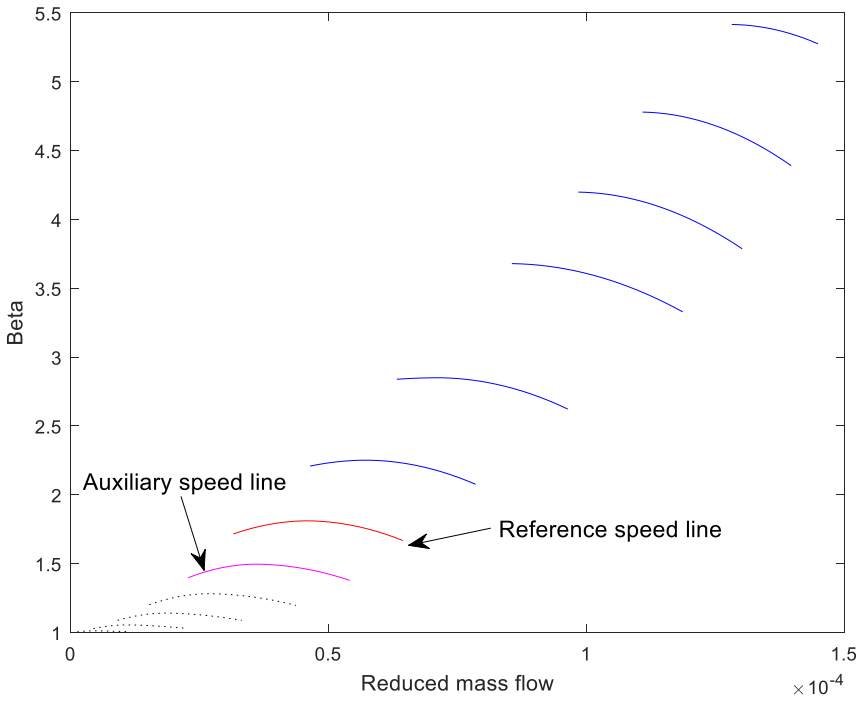

Figure A-1 Characteristic map of the compressor-Explanation of reference speed lines

Compressor

The equations used to extrapolate the values for the compressor, following [130], are:

Pressure ratio ($\beta_{comp\,x}$):

$$\beta_{comp\,x} = \left(1 + \left(\beta_{ref\ comp}^{\frac{\gamma-1}{\gamma}} - 1\right) \cdot \left(\frac{\%N_x}{\%N_{ref\ comp}}\right)^{\kappa_{\beta\ comp}}\right)^{\frac{\gamma}{\gamma-1}} \qquad \text{Eq. 161}$$

Similarity law exponent coefficient for the pressure ratio ($\kappa_{\beta\ comp}$):

$$\kappa_{\beta\ comp} = \frac{\log_{10}\left(\frac{\beta_{aux}^{\frac{\gamma-1}{\gamma}} - 1}{\beta_{ref\ comp}^{\frac{\gamma-1}{\gamma}} - 1}\right)}{\log_{10}\left(\frac{\%N_{aux}}{\%N_{ref\ comp}}\right)} \qquad \text{Eq. 162}$$

Reduced mass flow rate ($mr_{comp\,x}$):

$$mr_{comp\,x} = mr_{ref\ comp} \cdot \left(\frac{\%N_x}{\%N_{ref\ comp}}\right)^{\kappa_{mr\ comp}} \qquad \text{Eq. 163}$$

Similarity law exponent coefficient for the reduced mass flow rate ($\kappa_{mr\ comp}$):

$$\kappa_{mr\ comp} = \frac{\log_{10}\left(\frac{mr_{aux}}{mr_{ref\ comp}}\right)}{\log_{10}\left(\frac{\%N_{aux}}{\%N_{ref\ comp}}\right)} \quad \text{Eq. 164}$$

Efficiency ($\eta_{comp\,x}$):

$$\eta_{comp\,x} = \eta_{ref\ comp} \cdot \left(\frac{\%N_x}{\%N_{ref\ comp}}\right)^{\kappa_{mr\ comp}+\kappa_{\beta\ comp}-\kappa_{\eta\ comp}} \quad \text{Eq. 165}$$

Similarity law exponent coefficient for the efficiency ($\kappa_{\eta\ comp}$):

$$\kappa_{\eta\ comp} = \kappa_{\beta\ comp} + \kappa_{mr\ comp} - \frac{\log_{10}\left(\frac{\eta_{aux}}{\eta_{reference}}\right)}{\log_{10}\left(\frac{\%N_{aux}}{\%N_{ref\ comp}}\right)} \quad \text{Eq. 166}$$

Turbine

The equations used to extrapolate the values for the turbine slightly differ than the ones of the compressor, so those differences have to be taken into account in order to properly perform the extrapolation. By following [130], those equations are:

Pressure ratio ($\beta_{turb\,x}$):

$$\beta_{turb\,x} = \frac{1}{\left(1 - \left(\left(1 - \left(\frac{1}{\beta_{ref\ turb}}\right)^{\frac{\gamma-1}{\gamma}}\right) \cdot \left(\frac{\%N_x}{\%N_{ref\ turb}}\right)^{\kappa_{\beta\ turb}}\right)\right)^{\frac{\gamma}{\gamma-1}}} \quad \text{Eq. 167}$$

Similarity law exponent coefficient for the pressure ratio ($\kappa_{\beta\ turb}$):

$$\kappa_{\beta\ turb} = \frac{\log_{10}\left(\frac{1 - \left(\frac{1}{\beta_{aux}}\right)^{\frac{\gamma-1}{\gamma}}}{1 - \left(\frac{1}{\beta_{ref\ turb}}\right)^{\frac{\gamma-1}{\gamma}}}\right)}{\log_{10}\left(\frac{\%N_{aux}}{\%N_{ref\ turb}}\right)} \quad \text{Eq. 168}$$

Reduced mass flow rate ($mr_{turb\,x}$):

$$mr_{turb\,x} = mr_{ref\ turb} \cdot \left(\frac{\%N_x}{\%N_{ref\ turb}} \right)^{\kappa_{mr\ turb}} \quad \text{Eq. 169}$$

Similarity law exponent coefficient for the reduced mass flow rate ($\kappa_{mr\ turb}$)

$$\kappa_{mr\ turb} = \frac{\log_{10}\left(\frac{mr_{aux}}{mr_{ref\ turb}} \right)}{\log_{10}\left(\frac{\%N_{aux}}{\%N_{ref\ turb}} \right)} \quad \text{Eq. 170}$$

Efficiency ($\eta_{turb\,x}$):

$$\eta_{turb\,x} = \eta_{ref\ turb} \cdot \left(\frac{\%N_x}{\%N_{ref\ turb}} \right)^{\kappa_{\eta\ turb} - \kappa_{mr\ turb} - \kappa_{\beta\ turb}} \quad \text{Eq. 171}$$

Similarity law exponent coefficient for the efficiency ($\kappa_{\eta\ turb}$):

$$\kappa_{\eta\ turb} = \kappa_{\beta\ turb} + \kappa_{mr\ turb} + \frac{\log_{10}\left(\frac{\eta_{aux}}{\eta_{ref\ turb}} \right)}{\log_{10}\left(\frac{\%N_{aux}}{\%N_{ref\ turb}} \right)} \quad \text{Eq. 172}$$

B. Calculation of properties using the NASA coefficients

In order to speed up the simulations while still obtaining the real values of the properties of the fluids, for the fluids working in the gas turbine (i.e. air, natural gas and flue gas) the properties have been calculated using the NASA polynomials [132]. For this purpose, the equations used are:

$$C_p(T) = R(a_1 + a_2T + a_3T^2 + a_4T^3 + a_5T^4) \quad \text{Eq. 173}$$

$$h(T) = RT\left(a_1 + \frac{a_2T}{2} + \frac{a_3T^2}{3} + \frac{a_4T^3}{4} + \frac{a_5T^4}{5} + \frac{b_1}{T}\right) \quad \text{Eq. 174}$$

$$s(T) = R\left(a_1 lnT + a_2T + \frac{a_3T^2}{2} + \frac{a_4T^3}{3} + \frac{a_5T^4}{4} + b_2\right) \quad \text{Eq. 175}$$

The Table B- 1 collects the information of the enthalpy and entropy of formation at 25°C of each component participating in the reactions of combustion with the used fuel. Moreover, the molecular masses of each component is also reported.

Table B- 1 Molecular mass, enthalpy and entropy of formation of the components.

	h^of [J/mol]	s^of [J/molK]	MM [kg/kmol]
Ar	0	$1.54\cdot10^5$	39.94
CH_4	$-7.49\cdot10^7$	$1.86\cdot10^5$	16.043
CO_2	$-3.94\cdot10^8$	$2.14\cdot10^5$	44.009
C_2H_6	$-8.47\cdot10^7$	$2.29\cdot10^5$	30.07
C_3H_8	$-1.04\cdot10^8$	$2.70\cdot10^5$	44.09
H_2O (vap)	$-2.42\cdot10^8$	$1.89\cdot10^5$	18.01
N_2	0	$1.92\cdot10^5$	28.013
O_2	0	$2.05\cdot10^5$	31.999
C_4H_{10}	$-1.26\cdot10^5$	$-3.66\cdot10^2$	58.124

Table B- 2 and Table B- 3 collect the coefficients that should be introduced in Eq. 173, Eq. 174 and Eq. 175 to evaluate the different properties. Table B- 2 is used when the temperature at which the properties are going to be evaluated is lower than 1000 K and Table B- 3 when the temperature is higher than 1000 K.

Table B- 2 NASA coefficients to be applied when the temperature is lower than 1000K

	a_1	a_2	a_3	a_4	a_5	b_1	b_2
Ar	2.50	0	0	0	0	$-7.45\cdot10^{2}$	4.37
CH_4	2.93	$2.57\cdot10^{-3}$	$7.84\cdot10^{-6}$	$-4.91\cdot10^{-9}$	$2.04\cdot10^{-13}$	$-1.01\cdot10^{4}$	4.63
CO_2	2.40	$8.74\cdot10^{-3}$	$-6.61\cdot10^{-6}$	$2.00\cdot10^{-9}$	$6.33\cdot10^{-16}$	$-4.84\cdot10^{4}$	9.70
C_2H_6	1.46	$1.55\cdot10^{-2}$	$5.78\cdot10^{-6}$	$-1.26\cdot10^{-8}$	$4.59\cdot10^{-12}$	$-1.12\cdot10^{4}$	$1.44\cdot10^{1}$
C_3H_8	$8.97\cdot10^{-1}$	$2.67\cdot10^{-2}$	$5.43\cdot10^{-6}$	$-2.13\cdot10^{-8}$	$9.24\cdot10^{-12}$	$-1.40\cdot10^{4}$	$1.94\cdot10^{1}$
H_2O	4.17	$-1.81\cdot10^{-3}$	$5.95\cdot10^{-6}$	$-4.87\cdot10^{-9}$	$1.53\cdot10^{-12}$	$-3.03\cdot10^{4}$	$-7.31\cdot10^{-1}$
N_2	3.70	$-1.42\cdot10^{-3}$	$2.87\cdot10^{-6}$	$-1.20\cdot10^{-9}$	$-1.40\cdot10^{-14}$	$-1.06\cdot10^{3}$	2.23
O_2	3.78	$-3.02\cdot10^{-3}$	$9.95\cdot10^{-6}$	$-9.82\cdot10^{-9}$	$3.30\cdot10^{-12}$	$-1.06\cdot10^{3}$	3.64
C_4H_{10}	2.41	$3.39\cdot10^{-2}$	$-1.58\cdot10^{-6}$	$-1.14\cdot10^{-8}$	$4.11\cdot10^{-12}$	$-1.89\cdot10^{4}$	$-5.38\cdot10^{1}$

Table B- 3 NASA coefficients to be applied when the temperature is higher than 1000K

	a_1	a_2	a_3	a_4	a_5	b_1	b_2
Ar	2.50	0	0	0	0	$-7.45\cdot10^{2}$	4.37
CH_4	2.36	$8.73\cdot10^{-3}$	$-2.84\cdot10^{-6}$	$4.05\cdot10^{-10}$	$-2.05\cdot10^{-14}$	$-1.03\cdot10^{4}$	6.03
CO_2	4.46	$3.10\cdot10^{-3}$	$-1.24\cdot10^{-6}$	$2.27\cdot10^{-10}$	$-1.55\cdot10^{-14}$	$-4.90\cdot10^{4}$	$-9.86\cdot10^{-1}$
C_2H_6	4.83	$1.38\cdot10^{-2}$	$-4.56\cdot10^{-6}$	$6.72\cdot10^{-10}$	$-3.60\cdot10^{-14}$	$-1.27\cdot10^{4}$	-5.24
C_3H_8	7.53	$1.89\cdot10^{-2}$	$-6.28\cdot10^{-6}$	$9.18\cdot10^{-10}$	$-4.81\cdot10^{-14}$	$-1.65\cdot10^{4}$	$-1.78\cdot10^{1}$
H_2O	2.61	$3.16\cdot10^{-3}$	$-9.30\cdot10^{-7}$	$1.33\cdot10^{-10}$	$-7.47\cdot10^{-15}$	$-2.99\cdot10^{4}$	7.21
N_2	2.85	$1.60\cdot10^{-3}$	$-6.29\cdot10^{-7}$	$1.14\cdot10^{-10}$	$-7.81\cdot10^{-15}$	$-8.90\cdot10^{2}$	6.40
O_2	3.61	$7.49\cdot10^{-4}$	$-1.98\cdot10^{-7}$	$3.37\cdot10^{-11}$	$-2.39\cdot10^{-15}$	$-1.20\cdot10^{3}$	3.67
C_4H_{10}	2.41	$3.39\cdot10^{-2}$	$-1.58\cdot10^{-6}$	$-1.14\cdot10^{-8}$	$4.11\cdot10^{-12}$	$-1.89\cdot10^{4}$	$-5.38\cdot10^{1}$

C. Linearization using Dymola

One huge feature that Dymola has is the possibility to linearize the whole system nearby a fixed steady-state point. This powerful tool is very useful for control purposes, but a non-straight-line procedure has to be followed in order to do it properly.

The Jacobian matrices can be obtained through the "Linearize" command of Dymola: for a given set of variables values at equilibrium. Therefore, the first step is to reach the convergence nearby the equilibrium point in which it is desired to do the linearization. In order to do that, a similar schema of the one in the figure should be implemented in Dymola. In that schema, the inputs and outputs are included in the model without being connected to an external source/sink respectively. The conditions of the equilibrium point at which the linearization is going to be performed is imposed by the constant blocks.

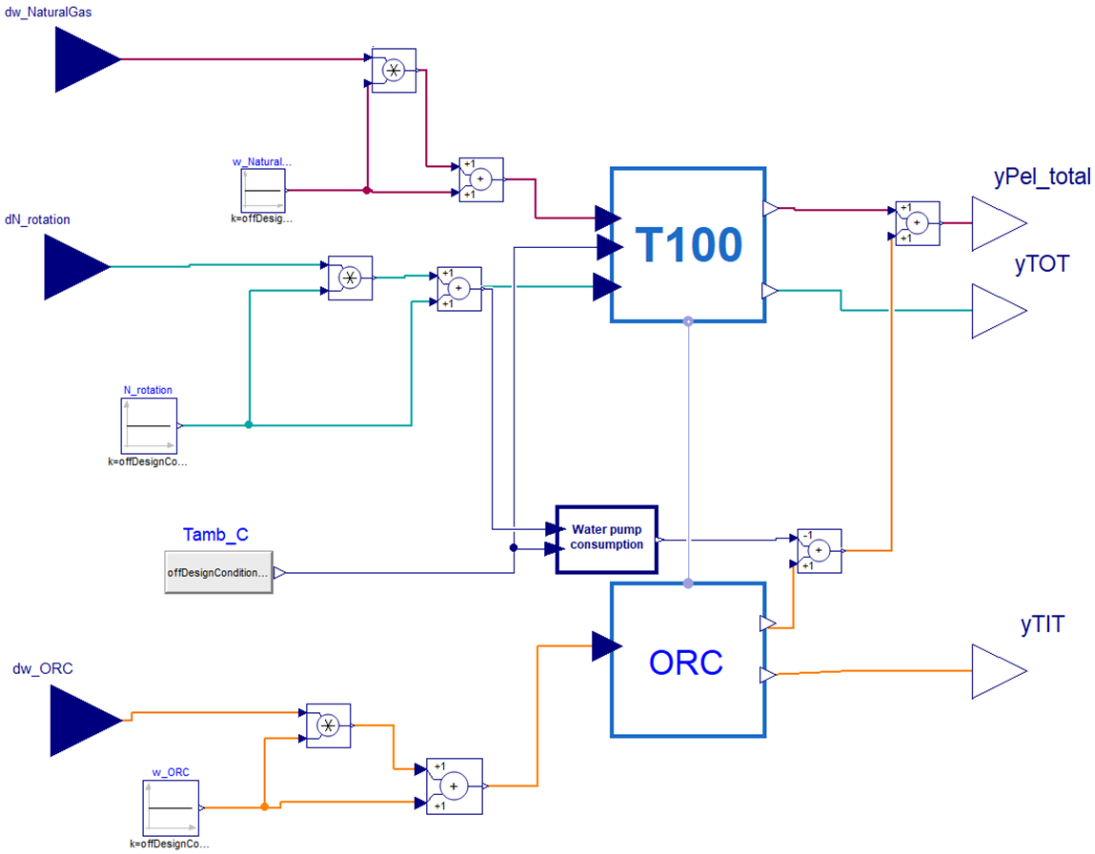

The procedure is here explained:

1. Impose the points at which the linearization at equilibrium conditions will be performed.

2. Run the simulation for a long time till steady-state conditions are reached. In the folder of the simulation file, a file called ¨dsfinal¨ should have been created.
3. Run steady-state conditions of the system by importing the final conditions of the ¨dsfinal¨ file (Simulation →Continue→Import initial).
4. Proceed with the linearization (Modeling→Linear Analysis→Linearize)
5. A new Matlab® file is created in the folder in which the results are being stored.

The Matlab® file storages 4 variables:

- ABCD
- Aclass
- XuyName
- nx

Through the command ¨Linearize¨, Dymola evaluates numerically the Jacobian and stores the results in a (n + p) x (n + m) matrix: matrix ABCD. The size of the matrix is defined by. n, which is the system order (i.e. the number of state variables), p, which is the number of outputs and m, which is the number of inputs.

In order to work with the process transfer function, it is mandatory to extract first the data.The Matlab® code to extract the matrices is:

```
NameLin = 'dslin';      % This is the name of the file with the linearization data
                        % generated with Dymola
load(strcat(NameLin)); % Load of the data
% Extraction of the different matrices of the system.
A = ABCD(1:nx,1:nx);
B = ABCD(1:nx,nx+1:end);
C = ABCD(nx+1:end,1:nx);
D = ABCD(nx+1:end,nx+1:end);
% Process transfer function in state space.
G = ss(A,B,C,D);
```

References

[1] International Energy Agency, “Energy balances & global energy statistics,” 2019. [Online]. Available: https://www.iea.org/. [Accessed: 19-May-2019].

[2] International Energy Agency, “World Energy Balances: an overview,” 2018.

[3] European Parliament, “Energy Policy: General Principles.” 2019.

[4] European Parliament, “Renewable energy.” pp. 1–5, 2019.

[5] European Commission, “Good practice in energy efficiency for a sustainable, safer and more competitive Europe,” Brussels, Belgium, 2016.

[6] European Parliament, “Directive 2012/27/EU of the European Parliament and of the council of 25 October 2012 on energy efficiency, amending Directives 2009/125/EC and 2010/30/EU and repealing Directives 2004/8/EC and 2006/32/EC,” no. L 315/2. Official Journal of the European Union, pp. 1–56, 2012.

[7] European Parliament, “Energy efficiency.” 2019.

[8] Odyssee-mure, “Energy efficiency policies,” 2019. [Online]. Available: http://www.measures-odyssee-mure.eu/topics-energy-efficiency-policy.asp. [Accessed: 05-May-2019].

[9] Sweco, “Study on the effective integration of Distributed Energy Resources for providing flexibility to the electricity system,” 2015.

[10] Smart grid task force, “Regulatory Recommendations for the Deployment of Flexibility: Refinement of Recommendations,” 2015.

[11] European Commission, “METIS Studies-Study S07: The role and need of flexibility in 2030,” 2016.

[12] P. B. Meherwan, *Gas Turbine Engineering Handbook*, Third. Gulf Professional Publishing, 2006.

[13] P. P. Walsh and P. Fletcher, *Gas Turbine Performance*, Second. Blackwell, 2004.

[14] Ansaldo Energia, “Cogenerazione con microturbine a gas: l’esperienza Ansaldo Energia col biogas.” Milan (Italy), 2016.

[15] Turbec Spa, “T100 Microturbine System - Technical description,” 2009.

[16] Turbec Spa, “Installation Manual Turbec T100,” 2006.

[17] Ansaldo Energia, “AE-T100NG,” Genoa, 2018.

[18] M. Hohloch, J. Zanger, A. Widenhorn, and M. Aigner, “Experimental Characterization of a Micro Gas Turbine Test Rig,” *Proc. ASME Turbo Expo 2010*, 2010.

[19] M. L. Ferrari, P. Silvestri, M. Pascenti, F. Reggio, and A. F. Massardo, “Experimental dynamic analysis on a T100 microturbine connected with

different volume sizes," *Proc. ASME Turbo Expo*, vol. 3, no. February, pp. 1–12, 2017.

[20] L. Larosa and A. Traverso, "GT2016-57312 Dynamic analysis of a recuperated mGT cycle for fuel cell hybrid systems," pp. 1–12, 2016.

[21] I. Rossi, A. Traverso, M. Hohloch, A. Huber, and D. Tucker, "Physics-Based Dynamic Models of Three SOFC/GT Emulator Test Rigs," *J. Eng. Gas Turbines Power*, vol. 140, no. 5, pp. 1–10, 2018.

[22] W. De Paepe, M. Montero Carrero, S. Bram, A. Parente, and F. Contino, "Experimental characterization of a T100 micro gas turbine converted to full humid air operation," *Energy Procedia*, vol. 61, pp. 2083–2088, 2014.

[23] G. Lozza, *Turbine a gas e cicli combinati*, Third. Bologna: Esculapio, 2016.

[24] A. Giostri and E. Macchi, "An advanced solution to boost sun-to-electricity efficiency of parabolic dish," *Sol. Energy*, vol. 139, pp. 337–354, 2016.

[25] F. Caresana, L. Pelagalli, G. Comodi, and M. Renzi, "Microturbogas cogeneration systems for distributed generation: Effects of ambient temperature on global performance and components' behavior," *Appl. Energy*, vol. 124, pp. 17–27, 2014.

[26] M. L. Ferrari, M. Pascenti, L. Magistri, and A. F. Massardo, "Micro Gas Turbine Recuperator: Steady-State and Transient Experimental Investigation," *J. Eng. Gas Turbines Power*, vol. 132, no. 2, p. 022301, 2010.

[27] Fluxys, "Average composition of the natural gas," 2017. [Online]. Available: https://www.fluxys.com/belgium/en/services/servicesforconnectedcompanies/operationaldata/operationaldata. [Accessed: 15-Sep-2017].

[28] M. Henke, N. Klempp, M. Hohloch, T. Monz, and M. Aigner, "Validation of a T100 micro gas turbine steady-state simulation tool," pp. 1–10, 2017.

[29] M. Henke, T. Monz, and M. Aigner, "Introduction of a New Numerical Simulation Tool to Analyze Micro Gas Turbine Cycle Dynamics," *J. Eng. Gas Turbines Power*, vol. 139, no. 4, p. 042601, 2016.

[30] M. L. Ferrari, M. Pascenti, L. Magistri, and A. F. Massardo, "Hybrid System Test Rig: Start-up and Shutdown Physical Emulation," *J. Fuel Cell Sci. Technol.*, vol. 7, no. 2, p. 021005, 2010.

[31] W. De Paepe, S. Abraham, P. Tsirikoglou, F. Contino, A. Parente, and G. Ghorbaniasl, "Operational Optimization of a Typical micro Gas Turbine," *Energy Procedia*, vol. 142, pp. 1653–1660, 2017.

[32] F. Baina, A. Malmquist, L. Alejo, B. Palm, and T. H. Fransson, "Analysis of a high-temperature heat exchanger for an externally-fired micro gas turbine," *Appl. Therm. Eng.*, vol. 75, pp. 410–420, 2015.

[33] G. Höök, "Networks and Niches for Microturbine Technology in Europe and U . S . - A Strategic Niche Management Analysis of Microturbines Networks and Niches for Microturbine Technology in Europe and U . S .," 2007.

[34] G. Lagerström and M. Xie, "High performance & cost effective recuperator for

micro-gas turbines," in *ASME Turbo Expo 2002*, 2002, no. June 2002, pp. 1–5.

[35] G. Xiao *et al.*, "Recuperators for micro gas turbines: A review," *Appl. Energy*, vol. 197, pp. 83–99, 2017.

[36] J. N. G and L. Shailendra, "Heat Transfer Analysis of Corrugated Plate Heat Exchanger of Different Plate Geometry: A Review," *Int. J. Emerg. Technol. Adv. Eng.*, vol. 2, no. 10, pp. 110–115, 2012.

[37] M. Asadi and R. H. Khoshkhoo, "Effects of Chevron Angle on Thermal Performance of Corrugated Plate Heat Exchanger," *Int. J. Eng. Pract. Res.*, vol. 3, no. 1, p. 8, 2014.

[38] E. Utriainen and B. Sundén, "Evaluation of the Cross Corrugated and Some Other Candidate Heat Transfer Surfaces for Microturbine Recuperators," *J. Eng. Gas Turbines Power*, vol. 124, no. 3, p. 550, 2002.

[39] A. A. Fahmy, "Flat Plate Heat Exchanger Design for MTR Reactor Upgrading," vol. 4, no. 1, 2013.

[40] C. S. Fernandes, R. P. Dias, J. M. Nóbrega, and J. M. Maia, "Laminar flow in chevron-type plate heat exchangers: CFD analysis of tortuosity, shape factor and friction factor," *Chem. Eng. Process. Process Intensif.*, vol. 46, no. 9 SPEC. ISS., pp. 825–833, 2007.

[41] J. Stasiek, M. W. Collins, M. Ciofalo, and P. E. Chew, "Investigation of flow and heat transfer in corrugated passages—I. Experimental results," *Int. J. Heat Mass Transf.*, vol. 39, no. 1, pp. 149–164, 1996.

[42] G. Strang, *Calculus*. Cambridge: Wellesley-Cambridge Press, 2001.

[43] J. Hejcík and M. Jícha, "CFD modeling of cross corrugated microturbine recuperator," in *ASME International Mechanical Engineering Congress*, 2003, pp. 1–6.

[44] E. Macchi and M. Astolfi, *Organic Rankine Cycle (ORC) Power Systems: Technologies and Applications*, 1st ed. Woodhead Publishing, 2016.

[45] P. Colonna *et al.*, "Organic Rankine Cycle Power Systems: From the Concept to Current Technology, Applications, and an Outlook to the Future," *J. Eng. Gas Turbines Power*, vol. 137, no. 10, p. 100801, 2015.

[46] E. Casati, A. Desideri, F. Casella, and P. Colonna, "Preliminary Assessment of a Novel Small CSP Plant Based on Linear Collectors , ORC and Direct Thermal Storage," *SolarPaces Conf.*, no. October 2015, 2012.

[47] S. Karellas and K. Braimakis, "Energy – exergy analysis and economic investigation of a cogeneration and trigeneration ORC – VCC hybrid system utilizing biomass fuel and solar power," *ENERGY Convers. Manag.*, 2015.

[48] B. F. Tchanche, G. Lambrinos, A. Frangoudakis, and G. Papadakis, "Low-grade heat conversion into power using organic Rankine cycles - A review of various applications," *Renew. Sustain. Energy Rev.*, vol. 15, no. 8, pp. 3963–3979, 2011.

[49] K. Braimakis, M. Preißinger, D. Brüggemann, and S. Karellas, “Low grade waste heat recovery with subcritical and supercritical Organic Rankine Cycle based on natural refrigerants and their binary mixtures,” *Energy*, 2015.

[50] C. Sprouse III and C. Depcik, “Review of organic Rankine cycles for internal combustion engine exhaust waste heat recovery,” *Appl. Therm. Eng.*, vol. 51, no. 1–2, pp. 711–722, 2013.

[51] S. Lecompte, H. Huisseune, M. van den Broek, S. De Schampheleire, and M. De Paepe, “Part load based thermo-economic optimization of the Organic Rankine Cycle (ORC) applied to a combined heat and power (CHP) system,” *Appl. Energy*, vol. 111, pp. 871–881, 2013.

[52] S. Lecompte, H. Huisseune, M. van den Broek, B. Vanslambrouck, and M. De Paepe, “Review of organic Rankine cycle (ORC) architectures for waste heat recovery,” *Renew. Sustain. Energy Rev.*, vol. 47, pp. 448–461, 2015.

[53] S. L. Gómez-Aláez, V. Brizzi, D. Alfani, P. Silva, A. Giostri, and M. Astolfi, “Off-design study of a waste heat recovery ORC module in gas pipelines recompression station,” *Energy Procedia*, vol. 129, pp. 567–574, 2017.

[54] F. Vélez, J. J. Segovia, M. C. Martín, G. Antolín, F. Chejne, and A. Quijano, “A technical, economical and market review of organic Rankine cycles for the conversion of low-grade heat for power generation,” *Renew. Sustain. Energy Rev.*, vol. 16, no. 6, pp. 4175–4189, 2012.

[55] B. T. Liu, K. H. Chien, and C. C. Wang, “Effect of working fluids on organic Rankine cycle for waste heat recovery,” *Energy*, vol. 29, no. 8, pp. 1207–1217, 2004.

[56] J. Bao and L. Zhao, “A review of working fluid and expander selections for organic Rankine cycle,” *Renew. Sustain. Energy Rev.*, vol. 24, pp. 325–342, 2013.

[57] S. Solomon and D. J. Wuebbles, “Ozone Depletion Potentials , Global Warming Potentials , and Future Chlorine/Bromine Loading Lead,” 2012.

[58] EPA, “Understanding Global Warming Potentials.” [Online]. Available: https://www.epa.gov/ghgemissions/understanding-global-warming-potentials. [Accessed: 12-Oct-2018].

[59] M. Astolfi *et al.*, “Testing of a new supercritical ORC technology for efficient power generation from geothermal low temperature resources Enel today,” in *2nd International Seminar in ORC Power Systems*, 2013, no. October.

[60] C. Spadacini, L. Centemeri, L. G. Xodo, M. Astolfi, M. C. Romano, and E. Macchi, “A new configuration for Organic Rankine Cycle power systems,” in *1st International Seminar on ORC Power Systems*, 2011.

[61] G. Kosmadakis, D. Manolakos, and G. Papadakis, “Experimental investigation of a lowerature organic Rankine cycle (ORC) engine under variable heat input operating at both subcritical and supercritical conditions,” *Appl. Therm. Eng.*, vol. 92, pp. 1–7, 2016.

[62] K. Braimakis and S. Karellas, “Integrated thermoeconomic optimization of standard and regenerative ORC for different heat source types and

capacities," *Energy*, 2017.

[63] K. Braimakis and S. Karellas, "Exergetic optimization of double stage Organic Rankine Cycle (ORC)," *Energy*, 2018.

[64] K. Braimakis and S. Karellas, "Energetic optimization of regenerative Organic Rankine Cycle (ORC) configurations," *Energy Convers. Manag.*, vol. 159, no. September 2017, pp. 353–370, 2018.

[65] S. Quoilin, M. Van Den Broek, S. Declaye, P. Dewallef, and V. Lemort, "Techno-economic survey of organic rankine cycle (ORC) systems," *Renew. Sustain. Energy Rev.*, vol. 22, pp. 168–186, 2013.

[66] R. H. Aungier, *Turbine aerodynamics: Axial-Flow and Radial-Flow Turbine Design and Analysis*, First. ASME, 2006.

[67] L. Da Lio, G. Manente, and A. Lazzaretto, "A mean-line model to predict the design efficiency of radial inflow turbines in organic Rankine cycle (ORC) systems," *Appl. Energy*, vol. 205, no. July, pp. 187–209, 2017.

[68] K. Rahbar, S. Mahmoud, R. K. Al-Dadah, and N. Moazami, "Modelling and optimization of organic Rankine cycle based on a small-scale radial inflow turbine," *Energy Convers. Manag.*, vol. 91, pp. 186–198, 2015.

[69] D. Hu, S. Li, Y. Zheng, J. Wang, and Y. Dai, "Preliminary design and off-design performance analysis of an Organic Rankine Cycle for geothermal sources," *Energy Convers. Manag.*, vol. 96, pp. 175–187, 2015.

[70] V. Mounier, L. E. Olmedo, and J. Schiffmann, "Small scale radial inflow turbine performance and pre-design maps for Organic Rankine Cycles," *Energy*, vol. 143, pp. 1072–1084, 2018.

[71] L. L. de Rijk, R. H. L. Eichhorn, M. D. Boot, and D. M. J. Smeulders, "Flow Analysis of a Radial-Inflow Variable Geometry Turbine Stator Vane Ring Using Particle Image Velocimetry," *J. Flow Vis. Image Process.*, vol. 19, no. 3, pp. 195–213, 2012.

[72] J. F. Suhrmann, D. Peitsch, M. Gugau, T. Heuer, and U. Tomm, "Validation and development of loss models for small size radial turbines," in *Proceedings of ASME Turbo Expo 2010: Power for Land, Sea and Air*, 2010, pp. 1–13.

[73] A. Perdichizzi and G. Lozza, "Design Criteria and Efficiency Prediction for Radial Inflow Turbines," *Gas Turbine Conf. Exhib. Anaheim, California, May 31-June4*, pp. 1–9, 1987.

[74] M. Astolfi, M. C. Romano, P. Bombarda, and E. Macchi, "Binary ORC (Organic Rankine Cycles) power plants for the exploitation of medium-low temperature geothermal sources - Part A: Thermodynamic optimization," *Energy*, vol. 66, pp. 423–434, 2014.

[75] M. Astolfi, M. C. Romano, P. Bombarda, and E. Macchi, "Binary ORC (Organic Rankine Cycles) power plants for the exploitation of medium-low temperature geothermal sources - Part B: Techno-economic optimization," *Energy*, vol. 66, pp. 435–446, 2014.

[76] S. Karellas, A. Schuster, and A. Leontaritis, "Influence of supercritical ORC

parameters on plate heat exchanger design," *Appl. Therm. Eng.*, vol. 33–34, pp. 70–76, 2012.

[77] W. Jansen and E. B. Qvale, "A Rapid Method for Predicting the Off-Design Performance of Radial-Inflow Turbines A Rapid Method for Predicting the Off-Design Performance of Radial-Inflow Turbines," in *ASME 1967 Winter Annual Meeting*, 1967.

[78] M. White, "The One-Dimensional Meanline Design of Radial Turbines for Small Scale Low Temperature Organic Rankine Cycles," *Turbine Tech. Conf. Expo.*, pp. 1–12, 2015.

[79] M. White and A. I. Sayma, "System and component modelling and optimisation for an efficient 10 kWe low-temperature organic Rankine cycle utilising a radial inflow expander," *Proc. Inst. Mech. Eng. Part A J. Power Energy*, vol. 229, no. 7, pp. 795–809, 2015.

[80] M. White and A. I. Sayma, "The Application of Similitude Theory for the Performance Prediction of Radial Turbines Within Small-Scale Low-Temperature Organic Rankine Cycles," *J. Eng. Gas Turbines Power*, vol. 137, no. 12, p. 122606, 2015.

[81] M. White, "The design and analysis of radial inflow turbines implemented within low temperature organic Rankine cycles." City, University of London Institutional Repository Citation:, pp. 55–76, 2012.

[82] M. White and A. I. Sayma, "Improving the economy-of-scale of small organic rankine cycle systems through appropriate working fluid selection," *Appl. Energy*, vol. 183, pp. 1227–1239, 2016.

[83] P. Tochon, J. F. Fourmigue, P. Mercier, and B. Thonon, "Large eddy simulation of turbulent flow and heat transfer in compact heat exchangers," in *Sixth International Conference on Advanced Computational Methods in Heat Transfer: Heat Transfer 2000*, 2000, pp. 477–486.

[84] K. M. Lunsford, "Advantages of brazed heat exchangers in the gas processing industry," *Proceedings, Annu. Conv. - Gas Process. Assoc.*, pp. 218–226, 1996.

[85] E. Feru, B. de Jager, F. Willems, and M. Steinbuch, "Two-phase plate-fin heat exchanger modeling for waste heat recovery systems in diesel engines," *Appl. Energy*, vol. 133, pp. 183–196, 2014.

[86] J. Galindo *et al.*, "Experimental and thermodynamic analysis of a bottoming Organic Rankine Cycle (ORC) of gasoline engine using swash-plate expander," *Energy Convers. Manag.*, vol. 103, pp. 519–532, 2015.

[87] J. Wen and Y. Li, "Study of flow distribution and its improvement on the header of plate-fin heat exchanger," *Cryogenics (Guildf).*, vol. 44, no. 11, pp. 823–831, 2004.

[88] S. Sanaye and H. Hajabdollahi, "Thermal-economic multi-objective optimization of plate fin heat exchanger using genetic algorithm," *Appl. Energy*, vol. 87, no. 6, pp. 1893–1902, 2010.

[89] C. Ranganayakulu and K. N. Seetharamu, "The combined effects of

longitudinal heat conduction, flow nonuniformity and temperature nonuniformity in crossflow plate-fin heat exchangers," *Int. Commun. Heat Mass Transf.*, vol. 26, no. 5, pp. 669–678, 1999.

[90] P. Ahmadi, H. Hajabdollahi, and I. Dincer, "Cost and Entropy Generation Minimization of a Cross-Flow Plate Fin Heat Exchanger Using Multi-Objective Genetic Algorithm," *J. Heat Transfer*, vol. 133, no. 2, p. 021801, 2011.

[91] a. L. London, "Offset Rectangular Plate-Fin Surfaces—Heat Transfer and Flow Friction Characteristics," *J. Eng. Gas Turbines Power*, vol. 90, no. 3, p. 218, 1968.

[92] F. Casella, *Object-oriented modelling of power plants: A structured approach*, vol. 42, no. 9. IFAC, 2009.

[93] Modelica Association, "ModelicaTM - A Unified Object-Oriented Language for Physical Systems Modeling: Language Specification," *ReVision*, pp. 1–71, 2000.

[94] F. Casella and C. Richter, "ExternalMedia: A Library for Easy Re-Use of External Fluid Property Code in Modelica," in *6th International Modelica Conference*, 2008, pp. 157–161.

[95] F. Casella and P. Milano, "The ThermoPower Library."

[96] F. Casella and A. Leva, "Object-Oriented Modelling & Simulation of Power Plants with Modelica," in *Proceedings of the 44th IEEE Conference on Decision and Control*, 2005, pp. 7597–7602.

[97] F. Casella, "Modelica open library for power plant simulation: design and experimental validation," *Proc. 3rd Int. Model. Conf.*, pp. 41–50, 2003.

[98] F. Casella, T. Mathijssen, P. Colonna, and J. van Buijtenen, "Dynamic Modeling of Organic Rankine Cycle Power Systems," *J. Eng. Gas Turbines Power*, vol. 135, no. 4, p. 042310, 2013.

[99] R. A. Roberts, I. Rossi, and A. Traverso, "Dynamic simulation of energy systems: Comparison of a physics-based against time constant based approach applied to a microturbine test rig," in *Proceedings of ASME Turbo Expo 2015: Turbine Technical Conference and Exposition*, 2015, pp. 1–8.

[100] F. Schiavo and F. Casella, "Object-oriented modelling and simulation of heat exchangers with finite element methods," *Math. Comput. Model. Dyn. Syst.*, vol. 13, no. 3, pp. 211–235, 2007.

[101] N. S. Nise, *Control Systems Engineering*, 6th editio. Pomona: John Wiley & Sons, 2010.

[102] K. M. Hangos, J. Bokor, and G. Szederk, *Analysis and control of nonlinear process systems*, vol. 42, no. 10. Springer, 2006.

[103] S. Skogestad and I. Postlethwaite, *Multivariable feedback control. Analysis and design*, 2nd ed. John Wiley & Sons, 2001.

[104] L. Ljung, *System Identification: Theory for User*, vol. 25. New Jersey: Prentice Hall, 1987.

[105] E. H. Bristol, “On a new measure of interaction for multivariable process control,” *IEEE Trans. Automat. Contr.*, vol. 11, no. 1, pp. 133–134, 1966.

[106] S. Trabucchi, C. De Servi, F. Casella, and P. Colonna, “Design, Modelling, and Control of a Waste Heat Recovery Unit for Heavy-Duty Truck Engines,” *Energy Procedia*, vol. 129, pp. 802–809, 2017.

[107] S. Trabucchi, “Design, Modelling, and Control of a Waste Heat Recovery Unit for Heavy-Duty Truck Engines,” Politecnico di Milano, 2014.

[108] M. L. Ferrari, M. Pascenti, L. Magistri, and A. F. Massardo, “A Micro Gas Turbine Based Test Rig for Educational Purposes,” *J. Eng. Gas Turbines Power*, vol. 132, no. 2, p. 024502, 2010.

[109] G. Restrepo, M. Weckert, R. Brüggemann, S. Gerstmann, and H. Frank, “Ranking of Refrigerants,” *Environ. Sci. Technol.*, vol. 42, no. 8, pp. 2925–2930, 2008.

[110] AGA, “R1233zd refrigerant (Solstice zd). Ultra low GWP solution .”

[111] E. Sauret and A. S. Rowlands, “Candidate radial-inflow turbines and high-density working fluids for geothermal power systems,” *Energy*, vol. 36, no. 7, pp. 4460–4467, 2011.

[112] R. Capata and E. Zangrillo, “Preliminary design of compact condenser in an organic rankine cycle system for the low grade waste heat recovery,” *Energies*, vol. 7, no. 12, pp. 8008–8035, 2014.

[113] L. Da Lio, G. Manente, and A. Lazzaretto, “A mean-line model to predict the design efficiency of radial inflow turbines in organic Rankine cycle (ORC) systems,” *Appl. Energy*, vol. 205, no. July, pp. 187–209, 2017.

[114] E. A. Bufi, S. M. Camporeale, and P. Cinnella, “Robust optimization of an Organic Rankine Cycle for heavy duty engine waste heat recovery,” *Energy Procedia*, vol. 129, pp. 66–73, 2017.

[115] B. V Datla, “Comparing R1233zd And R245fa For Low Temperature ORC Applications,” 2014.

[116] S. Eyerer, C. Wieland, A. Vandersickel, and H. Spliethoff, “Experimental study of an ORC (Organic Rankine Cycle) and analysis of R1233zd-E as a drop-in replacement for R245fa for low temperature heat utilization,” *Energy*, vol. 103, pp. 660–671, 2016.

[117] M. A. Chatzopoulou and C. N. Markides, “Thermodynamic optimisation of a high-electrical efficiency integrated internal combustion engine-Organic Rankine cycle combined heat and power system,” *Appl. Energy*, vol. 226, no. July, pp. 1229–1251, 2018.

[118] S. Douvartzides and I. Karmalis, “Working fluid selection for the Organic Rankine Cycle (ORC) exhaust heat recovery of an internal combustion engine power plant,” in *IOP Conference Series: Materials Science and Engineering*, 2016, vol. 161, no. 1.

[119] O. Nurhilal, C. Mulyana, N. Suhendi, and D. Sapdiana, “The Simulation of Organic Rankine Cycle Power Plant with n-Pentane Working Fluid,” in *AIP*

Conference Proceedings, 2016, vol. 1712, pp. 040003-1-040003–5.

[120] M. Khennich and N. Galanis, “Optimal design of ORC systems with a low-temperature heat source,” *Entropy*, vol. 14, no. 2, pp. 370–389, 2012.

[121] Y. Jang and J. Lee, “Optimizations of the organic Rankine cycle-based domestic CHP using biomass fuel,” *Energy Convers. Manag.*, vol. 160, no. January, pp. 31–47, 2018.

[122] O. A. Oyewunmi, C. J. W. Kirmse, A. M. Pantaleo, and C. N. Markides, “Performance of working-fluid mixtures in ORC-CHP systems for different heat-demand segments and heat-recovery temperature levels,” *Energy Convers. Manag.*, vol. 148, pp. 1508–1524, 2017.

[123] J. Song and C. Gu, “Analysis of ORC (Organic Rankine Cycle) systems with pure hydrocarbons and mixtures of hydrocarbon and retardant for engine waste heat recovery,” *Appl. Therm. Eng.*, vol. 89, no. October 2015, pp. 693–702, 2017.

[124] M. Kolahi, M. Yari, S. M. S. Mahmoudi, and F. Mohammadkhani, “Case Studies in Thermal Engineering Thermodynamic and economic performance improvement of ORCs through using zeotropic mixtures : Case of waste heat recovery in an offshore platform,” *Case Stud. Therm. Eng.*, vol. 8, pp. 51–70, 2016.

[125] S. Glover, R. Douglas, L. Glover, and G. Mccullough, “Preliminary analysis of organic Rankine cycles to improve vehicle efficiency,” no. August 2014, 2015.

[126] Honeywell, “Solstice ® ZD , Solstice ® 1233zd (E),” no. 1907. pp. 1–12, 2015.

[127] OARS WEEL, “trans-1-Chloro-3,3,3-Trifluoropropene (1233zd(E)),” 2013.

[128] T. Tjaden, J. Bergner, J. Weniger, and V. Quaschning, “Representative electrical load profiles of residential buildings in Germany with a temporal resolution of one second,” *Dataset, HTW Berlin - Univ. Appl. Sci. Res.*, pp. 1–7, 2015.

[129] National Renewable Energy Laboratory, “System Advisor Model.” 2017.

[130] S. R. Gaudet and J. E. D. Gauthier, “A Simple Sub-idle Component Map Extrapolation Method,” *ASME Turbo Expo 2007*, pp. 1–9, 2007.

[131] W. R. Sexton, “A Method to Control Turbofan Engine Starting by Varying Compressor Surge Valve Bleed,” Virginia Polytechnic Institute, 2001.

[132] B. J. Mcbride, M. J. Zehe, and S. Gordon, “NASA Glenn Coefficients for Calculating Thermodynamic Properties of Individual Species,” 2002.